UNIVERSIDADE DE BRASÍLIA
INSTITUTO DE GEOCIÊNCIAS
PROGRAMA DE PÓS-GRADUAÇÃO EM GEOLOGIA

O CONTEXTO LATERÍTICO DO SUDESTE DO ESTADO DO AMAZONAS: UMA ABORDAGEM MINERALÓGICA, GEOQUÍMICA, AEROGEOFÍSICA E GEOCRONOLÓGICA.

Tese n° 142

MÁRCIO FERNANDO DOS SANTOS ALBUQUERQUE

BRASÍLIA, 9 DE MARÇO DE 2018

UNIVERSIDADE DE BRASÍLIA
INSTITUTO DE GEOCIÊNCIAS
PROGRAMA DE PÓS-GRADUAÇÃO EM GEOLOGIA

MÁRCIO FERNANDO DOS SANTOS ALBUQUERQUE

Tese apresentada junto ao Programa de Pós Graduação em Geologia da Universidade de Brasília, como requisito para obtenção de título de Doutor em Geologia

O CONTEXTO LATERÍTICO DO SUDESTE DO ESTADO DO AMAZONAS: UMA ABORDAGEM MINERALÓGICA, GEOQUÍMICA, AEROGEOFÍSICA E GEOCRONOLÓGICA.

Área de concentração: Geoquímica

Banca examinadora

_____

Adriana Maria Coimbra Horbe (IG/UnB- Orientadora)

_____

Rômulo Simões Angélica (IG/UFPA)

_____

Marly Babinski (IGC/USP)

_____

Jérémie Garnier (IG/UnB)

BRASÍLIA, 9 DE MARÇO DE 2018

AGRADECIMENTOS

Agradeço a Deus pela força, perseverança e saúde.
Agradeço por fazer parte do sonho dos meus pais. Muito obrigado por tudo, Antônio Albuquerque e Zenilda Albuquerque, só vocês sabem o valor dessa caminhada, desde a infância de vocês no Paraná de Dona Rosa, passando por Juruti, Óbidos, Porto Trombetas... Até me lançarem à Manaus e Brasília. Se cheguei até aqui, devo tudo isso a vocês. Não posso deixar de citar meus irmãos Ricardo, Vinicius e Vitor pela amizade e irmandade de sempre, amo vocês.
À orientadora Profa. Dra Adriana Horbe, pela paciência, conselhos e respeito.
À Universidade de Brasília pela infraestrutura.
À CAPES pela concessão de bolsa no Brasil e no exterior.
Aos amigos da pós-graduação da UnB.
Ao geólogo Marco Horbe pelo auxílio nas etapas de campo.
Ao professor Fred Jourdan (orientador no exterior) e aos demais colegas de Curtin University (Hugo Olierook, Adam Frew, Celia Mayers e Zdenka).
Aos professores Martin Danisik e João Orestes Santos por auxiliarem nas análises de (U-Th)/He e MEV, respectivamente.
Aos housemates de Perth, aquele abraço.
Aos amigos da geologia UFAM (poucos, mas fiéis), especialmente os frequentadores do Ceará.
Aos amigos da geologia UnB, com menção honrosa ao grupo LDP (HueBr), aos frequentadores e moradores da antiga república (que descanse em paz), geocervas e dos complexos ébrios 410/411 e 408/409.

Salve!

Epígrafe

Vamo acordar, vamo acordar porque o sol não espera. Demorô, vamo acordar!
O tempo não cansa. Ontem à noite você pediu... Você pediu... Uma oportunidade
Mais uma chance, como Deus é bom, né não nego? Olha aí, mais um dia todo seu.
Que céu azul louco hein?
Vamo acordar, vamo acordar, agora vem com a sua cara, sou mais você nessa guerra.
A preguiça é inimiga da vitória, o fraco não tem espaço e o covarde morre sem tentar.
Não vou te enganar, o bagulho tá doido e eu não confio em ninguém.
Nem em você. Os inimigos vêm de graça.
É a selva de pedra, eles matam os humildes demais.
Você é do tamanho do seu sonho, faz o certo, faz a sua.
Vamo acordar, vamo acordar. Cabeça erguida, olhar sincero, tá com medo de quê?
Nunca foi fácil, junta os seus pedaços e desce pra arena.
Mas lembre-se: Aconteça o que aconteça, nada como um dia após outro dia

"Sou mais você"- Racionais Mc's

…in the morning
they're out there
making money:
judges, carpenters,
plumbers, doctors,
newsboys, policemen,
barbers, car washers,
dentists, florists,
waitresses, cooks,
cabdrivers…
and you turn over
to your left side
to get the sun
on your back
and out
of your eyes.

Poem for my 43rd birthday - Charles Bukowski

LISTA DE ABREVIAÇÕES

A1 e A2- Grauvacas manganesíferas do Grupo Beneficente
A3- Grauvaca manganesífera do Grupo Vila do Carmo
B1, B2, B3 e B4- Crosta manganesífera vermiforme do perfil Beneficente
B1A e B1C- Bauxitas pisolíticas desenvolvidas sobre o Grupo Beneficente
Bx- Bauxita maciça desenvolvida sobre os tufos do Grupo Vila do Carmo
C- Criptomelana
C.C- Média crustal de Taylor & McLennan (1985)
C1, C3, C4 e C6- Crostas ferruginosas desenvolvidas sobre as rochas do Grupo Alto Tapajós
C2- Crosta ferruginosa desenvolvida sobre as rochas do Grupo Beneficente
C7- Crosta ferruginosa desenvolvida sobre os tufos do Grupo Vila do Carmo
Ca- Caulinita
CH- Condrito de Taylor & McLennan (1985)
Co- Coronadita
G1, G2, G4,G5 e G6- Grauvacas do Grupo Alto Tapajós
Gb- Gibbsita
Gt- Goethita
H1, H2, H3 e H4- Crosta manganesífera vermiforme do perfil Holanda
M1- Crosta manganesífera maciça do perfil Novo Natal
ML- Camada manganesífera do perfil Holanda
Pi1 e Pi2- Crosta Mn-Al-Fe pisolítica do perfil Novo Natal
Pi6- Horizonte pisolítico do perfil Beneficente
Pp1 e Pp2- Crosta manganesífera protopisolítica do perfil Novo Natal
PS- Siltito rosado do Grupo Vila do Carmo
Py- Pirolusita
Q- Quartzo
Q1 e Q3-Quartzo arenitos do Grupo Vila do Carmo
Q4- Quartzo arenito do Grupo Alto Tapajós
QA e Q2 - Quartzo arenitos do Grupo Beneficente
R e V- Tufos do Grupo Vila do Carmo
R/ An- Rutilo/ Anatásio
Ro- Romanechita
S1, S2, S3, S4, S5, S6 e S7- Solos
VB e VT- Crosta Mn-Al-Fe vermiforme do perfil Apuí
Z1, Z2, Z3, Z4, Z5, Z6, Z7 e Z8- Fragmentos coluvionares do Perfil Zé Julião

LISTA DE FIGURAS

Figura 1: Regiões de ocorrência de lateritos no mundo, com ênfase aos depósitos supergênicos de maior porte na Amazônia. Modificado de Bardossy & Aleva (1990) e Costa (1991) 19

Figura 2: Principais tipos de perfis lateríticos na região Amazônica (Costa, 1991) 23

Figura 3: Mapa de localização da região de estudo e de pontos coletados. 30

Figura 4: Região estudada enquadrada no Escudo Brasileiro, Província Rondônia-Juruena, Domínio Roosevelt-Juruena do cráton Amazonas (Santos et al. 2006). 37

Figura 5: Mapa geológico da região estudada (CPRM 2014; 2015). Retângulo vermelho está relacionado ao mapeamento em andamento da região sudeste do Amazonas 38

Figura 6: A- Principais domínios geomorfológicos do estado do Amazonas. B- Mapa altimétrico da região sudeste do Amazonas (Dantas & Maia, 2010). 41

Figura 7: Tipos de relevo da região estudada. A- serras alongadas e platôs; B- colinas com topo suave e arredondado; C- crostas lateríticas que sustentam o relevo colinoso e D- vales em formato de U. 42

Figura 8: A- Colúvios falhados pela neotectônica (Silva, 2009). B e C- Exposição de linhas de pedra e horizonte mosqueado 43

Figura 9: Mapa mostrando a posição altimétrica das amostras datadas por (U-Th)/He, bem como perfil topográfico e substrato rochoso. B e C- Composição mineralógica obtida por meio de difratometria por raios-X. K- caulinita. Gb-gibbsita. Gt-goethita. An- anatásio. R-rutilo. Q-quartzo. He-hematita. 141

Figura 10: Principais aspectos macroscópicos e microscópicos das amostras analisadas. A- Bauxita pisolítica (B1A) composta por pisólitos de hematita (He), cortéx de goethita (Gt) e plasma de gibbsita (Gb) e caulinita (K). Em amarelo o detalhe da foto B. B- Relação de contato entre o pisólito hematítico e diversas gerações de goethita. C- Crosta Fe-Al (C6) composta por pisólitos de hematita e gibbsita. Em amarelo detalhe da foto D. D- Detalhe do núcleo e borda do pisólito. E- Diminutos gãos angulosos de gibbsita nos núcleos do pisólito. F- Cortéx goethítico com inclusões de gibbsita e zircão (Zr). 142

Figura 11: Relações He (ncc) vs Idade em Ma e Th/U vs idade em Ma das hematitas e goethitas datadas 144

Figura 12: Idades obtidas em goethitas e hematitas por U-Th-He e em minerais do grupo da hollandita por Ar-Ar em diversas regiões do mundo 147

Figura 13: Arcabouço das grauvacas do Grupo Alto Tapajós compostas por matriz de muscovita (Ms), illita (Il) e quartzo (Q) com grãos de feldspato potássico (FK) e zircão (Zr). 148

LISTA DE TABELAS

Tabela 1: Principais tipos de crostas lateríticas descritas na região Amazônica (Costa, 1991; Kotschoubey et al., 2005; Costa et al. 2005; Costa, 2007; Peixoto & Horbe, 2008; Albuquerque & Horbe, 2015; Castro, 2015) 24

Tabela 2: Principais características dos principais depósitos de bauxita da região Amazônica, segundo Boulangé & Carvalho (1997), Kotschoubey et al. (2005), Lucas (1997), DNPM (2010), Costa et al. (2014) e Oliveira et al. (2016). 28

Tabela 3: Localização dos perfis e demais pontos amostrados utilizados para determinação mineralógica e análises químicas, totalizando 56 amostras. X- realizadas, x*- realizadas apenas as amostras A2, B2 e S6, N- não realizadas 32

Tabela 4: Pontos amostrados em que não foram realizadas análises químicas e mineralógicas . 33

Tabela 5: Resultados da datação (U-Th)/He em goethitas e hematitas. 143

SUMÁRIO

LISTA DE ABREVIAÇÕES 5
LISTA DE FIGURAS 6
LISTA DE TABELAS 7
RESUMO 10
ABSTRACT 12
CAPÍTULO I: APRESENTAÇÃO, INTRODUÇÃO E OBJETIVOS 14
1 APRESENTAÇÃO 15
2 INTRODUÇÃO 15
3 OBJETIVOS GERAIS E ESPECÍFICOS 16
CAPÍTULO II: REVISÃO BIBLIOGRÁFICA 18
4 REVISÃO BIBLIOGRÁFICA 19
4.1 Localização, estrutura, formação e posicionamento topográfico dos horizontes e paisagens lateríticas 19
4.2 Métodos geocronológicos, termocronológicos e paleomagnéticos aplicados à datação de crostas lateríticas 24
4.3 Histórico dos principais depósitos de manganês e bauxita da Amazônia 26
4.3.1 Manganês 26
4.3.2 Bauxita 27
CAPÍTULO III: LOCALIZAÇÃO E ACESSO, MATÉRIAS E MÉTODOS CONTEXTO GEOLÓGICO E GEOMORFOLÓGICO LOCAL. 29
5 LOCALIZAÇÃO E ACESSO 30
6 MATERIAIS E MÉTODOS 31
6.1 Composição mineral, químico-mineral e geoquímica 31
6.2 Métodos radiométricos Sr-Sr, Sm-Nd e Pb-Pb 33
6.3 Termocronologia (U-Th)/He 34
6.4 Aerogeofísica 35
6.5 Elaboração de mapas e perfis topográficos 36
7 CONTEXTO GEOLÓGICO E GEOMORFOLÓGICO LOCAL 36
CAPÍTULO IV: ARTIGO 1- GENESIS OF MANGANESE DEPOSITS IN SOUTHWESTERN AMAZONIA: MINERALOGY, GEOCHEMISTRY AND PALEOENVIROMENT 44
CAPÍTULO V: ARTIGO 2- NEODYMIUM, STRONTIUM AND LEAD ISOTOPES: AN INSIGHT OF PROVENANCE AND BEHAVIOR UNDER EXTREME WEATHERING CONDITIONS 75
CAPÍTULO VI: ARTIGO 3- USING AIRBORNE RADIOMETRIC DATA TO IDENTIFY LATERITIC DURICRUST AND SUPERGENE DEPOSITS IN SOUTHWESTEN AMAZONIA 116
CAPÍTULO VII: APRESENTAÇÃO DE DADOS E DISCUSSÕES DA GEOCRONOLOGIA (U-Th)/He 139
8 GEOCRONOLOGIA (U-Th)/He 140
8.1 Discussões das idades (U-Th)/He 144

CAPÍTULO VIII: CONSIDERAÇÕES FINAIS DA TESE E REFERÊNCIAS BIBLIOGRÁFICAS 149
9 REFERÊNCIAS BIBLIOGRÁFICAS 157

RESUMO

A região sudeste do Amazonas é composta por embasamento vulcânico do Grupo Colíder (1,80-1,78 Ga), recoberto por sequência vulcano-sedimentar (Supergrupo Sumaúma), subdivida nos grupos Vila do Carmo (1,76-1,74 Ga) e Beneficente (1,43-1,08 Ga), corpos graníticos reunidos nas suítes intrusivas Teodósia (1,756 Ga), Igarapé das Lontras (1,754 Ga) e Serra da Providência (1,57-1,53 Ga) e diábasio Mata-Matá (1,57 Ga). Sobrepondo estas unidades há sucessão sedimentar Siluro-Devoniana do Grupo Alto Tapajós.

O Supergrupo Sumaúma têm alto conteúdo de MnO em grauvacas e siltitos, ao passo que o Grupo Alto Tapajós concentra P_2O_5 nas grauvacas, o que implica em fontes distintas. Além disso, arenitos do Supergrupo Sumaúma com grãos de quartzo bem esféricos e arredondados miram contribuição de fontes distais. Já os grãos de quartzo subarredondados e subesféricos dos arenitos e alto teor de K_2O nas grauvacas, indicam fontes proximais para o Grupo Alto Tapajós. As fontes do Supergrupo Sumaúma, reveladas pelos isótopos de Nd, estão atreladas à Província Rondônia Juruena. Além disso, as províncias Tapajós-Parima e Amazônia Central supriram o Grupo Vila do Carmo, e fontes distais relativas às províncias Carajás e Sunsás fomentaram sedimentos para o Grupo Beneficente. Vale ressaltar que o Grupo Vila do Carmo foi fonte para o Grupo Beneficente, prova disso é a discordância angular entre as unidades, altos conteúdos de Fe_2O_3, TiO_2, rutilo, Ti-magnetita e população de zircão entre 1,76 e 1,74 Ga nos arenitos do Grupo Beneficente. As mesmas fontes do Supergrupo Sumaúma foram identificadas pelos isótopos de Nd para o Grupo Alto Tapajós, contudo boas correlações entre $^{87}Sr/^{86}Sr$ vs CIA e $^{87}Sr/^{86}Sr$ vs Rb/Sr atestaram seu caráter autóctone e intraformacional relacionado à incisão do Grabén do Cachimbo no Supergrupo Sumaúma e Grupo Colíder serviram de fontes para o Grupo Alto Tapajós.

A exposição destas rochas formou espessas crostas Mn, Mn-Al-Fe, bauxíticas, Fe, Fe-Al-Fe e colúvios, recobertos por latossolos. Os protólitos de Mn estão relacionados aos grupos Vila do Carmo e Beneficente, Supergrupo Sumaúma. Contudo, há diferenças mineralógicas e geoquímicas entre eles, enquanto os do Grupo Vila do Carmo são caracterizados pela presença de Pb-hollandita, coronadita e criptomelana e altos conteúdos de Pb e Cu, aqueles do Grupo Beneficente têm romanechita como fase dominante e Ba mais elevado. Crostas Mn e Mn-Al-Fe maciças, vermiformes, protopisolíticas, pisolíticas e colúvios foram formadas a partir destas rochas. Assim como nos protólitos, crostas Mn desenvolvidas sobre o Grupo Vila do Carmo também formaram hollandita, Pb-hollandita, criptomelana e coronadita e têm altos teores de K_2O, Ag, Cu, Pb e Tl, já aquelas do Grupo Beneficente formaram romanechita supergênica.

A presença de galena, Ag nativa, coronadita, Pb-hollandita, alto Cu, Tl e anomalias positivas de Gd nas crostas Mn desenvolvidas sobre o Vila do Carmo são similares aos conteúdos de gossans, minérios sulfetados e depósitos de Mn de origem hidrotermal. Além do mais, a fonte hidrotermal do Mn do Grupo Vila do Carmo, a mesma que originou os sulfetos, é a ratificada pelas relações $^{206}Pb/^{207}Pb$ vs $^{208}Pb/^{206}Pb$, (Zn x Ni)/MnO_2 vs (Cu/Zn)/Fe_2O_3 e pelos altos teores de Cu, Pb e Zn, similar aos Gossans Australianos, e pode classificar o Mn supergênico como dubhito. Por outro lado, o Mn do Grupo Beneficente tem assinatura sedimentar e pode ser classificado como supergênico marinho.

A relação Rb/Sr vs εNd permitiu agrupar rochas, crostas lateríticas (Mn,Mn-Al-Fe, bauxíticas, Fe e Fe-Al) e solos desenvolvidos a partir dos grupos Vila do Carmo, Beneficente e Alto Tapajós, o que ratifa o uso de crostas lateríticas no mapeamento de rochas mães. A razão ETR/(Zr+Hf) ≥1 indica controle por minerais de Mn e cerianita.

Ao passo que, ETR/(Zr+Hf) ≤ 1 atesta que minerais pesados como zircão controlam a variação dos ETR ao longo do perfil laterítico. A redistribuição de minerais em todo o perfil laterítico com concentração residual de zircão ou lixiviação de minerais de Mn (coronadita, holandita e criptomelana) e fixação na cerianita, controla a assinatura isotópica de Nd.

As razões isotópicas de Sr apresentaram dois tipos de comportamento distintos: 1- A razão $^{87}Sr/^{86}Sr$ aumenta em direção ao topo dos perfis onde predominam crostas Fe e Mn-Fe-Al, sugerindo a entrada de Sr proveniente da atmosfera, água da chuva e lençol freático. 2- A intensa lixiviação que resultou na formação de caulinita e gibbsita liberou Sr dos protólitos em solução e diminuiu a razão $^{87}Sr/^{86}Sr$ em direção aos solos.

As razões isotópicas de Pb são mais elevadas nas crostas lateríticas e solos do que nos protólitos, como não são afetadas pelo intemperismo, essa diferença pode estar relacionada ao decaimento do ^{238}U para o ^{206}Pb ou misturas de fontes. A excelente correlação entre $^{143}Nd/^{144}Nd$, $^{206}Pb/^{207}Pb$ e $^{208}Pb/^{206}Pb$ no balanço de massa dos perfis P1 e P2 ratifica o não francionamento dos isótopos de Pb durante a intemperismo extremo.

A gammaespectometria aliada a altimetria e métodos estatísticos como Booleano e Fuzzy, designaram áreas favoráveis às ocorrências de crostas lateríticas. Os dois modelos apresentaram boa correlação para bauxitas, crostas manganesíferas e solos, apesar de que o Booleano é capaz de identificar 67% das crostas ferruginosas, 20% a mais que os modelos Fuzzy. No entanto, os modelos Fuzzy foram eficientes em descartar pedras de ferro localizadas na porção oeste da área. A combinação relevo, eTh fuzzy (índice Kappa-0.8), estratigrafia e mapa de solos permitiu sugerir 100 Km^2 de áreas propícias à ocorrência de Mn, 700 Km^2 para bauxitas e 83 Km^2 para crostas fosfáticas.

A datação U-Th-He indicou que o início da lateritização remete ao Permiano e se estende até o Jurássico-Cretáceo com agradação de crosta ferruginosa maciça. A ausência de dados Ar-Ar em crostas manganesíferas impede afirmar sua época precisa de formação, no entanto, por correlação de crostas manganesíferas em Burkina Faso, Carajás e Quadrilátero ferrífero, apontam para o fim do Cretáceo (~70 Ma) o início de formação dessas crostas, se estendendo até o fim do Mioceno. Neste contexto, na região de Apuí houve a segunda fase de agradação de crosta ferruginosa (Oligoceno médio ao início do Mioceno). A partir de então, houve dois intervalos distintos de degradação de crostas lateríticas (formação de goethita); o primeiro entre 22,5±2,3 e 17,1±1,7 Ma e segundo entre 13,1±1,3 e 16.6 ±1,7 Ma.

Palavras chave: Lateritização, isótopos, Fuzzy, Booleano, dubhito

ABSTRACT

The southestern of Amazonas state is composed by volcanic basement related to Colíder Group (1.80-1.78 Ga), followed by two volcano-sedimentary sequences related to Vila do Carmo (1.76-1.74 Ga) and Beneficente (1.43-1.08 Ga) groups, framed into Sumaúma Supergroup; granitic bodies gather into Teodósia (1.756Ga), Igarapé das Lontras (1,754) and Serra da Providência (1.57-1.53 Ga) intrusive suites and Mata-Matá diabase sills (1.57 Ga). Overlapping these units there is a Silurian-Devonian sedimentary sucession of the Alto Tapajós Group.

The Sumaúma Supergroup has high contents of MnO in greywackes and siltstones, whereas the Alto Tapajós Group concentrates P_2O_5 in greywackes, what implies in distinct sources. Moreover, the Supergroup Sumaúma sandstones displays spherical and rounded quartz grains mirror distal source. While the subrounded and subspherical quartz grains of the sandstones and high amounts of K_2O in the greywackes indicate proximal sources to the Alto Tapajós Group. The sources of the Sumaúma Supergroup identified by Nd isotopes are assigned to Rondônia Juruena Province. Moreover, the Tapajós-Parima and Amazônia Central provinces supplied the Vila do Carmo Group, and distal sources relative to Carajás and Sunsás provinces fomented sediments to the Beneficente Group. It is worthy to be highlighted that the Vila do Carmo Group was source of the Beneficente Group, proof of that is the angular discordance between these units, high amounts of Fe_2O_3, TiO_2, rutile, Ti-magnetite and zircon population between 1.76 to 1.74 Ga in the sandstones of the Beneficente Group. The same sources of Sumaúma Supergroup have been identified by Nd isotopes to the Alto Tapajós Group, however the good correlations between $^{87}Sr/^{86}Sr$ vs CIA and $^{87}Sr/^{86}Sr$ vs Rb/Sr ratified their autochthony and intraformational signature are related to the Cachimbo graben incision in the Colíder Group and Sumaúma Supergroup, sources to the Alto Tapajós Group.

The exposure of these rocks developed thick Mn, Mn-Al-Fe, bauxitic, Fe and Fe-Al duricrusts and colluviums, overlapped by oxisols. The Mn protoliths are related to Vila do Carmo and Beneficente groups, Sumaúma Supergroup. Nevertheless, there are mineralogical and geochemical differences among them, while those from Vila do Carmo Group are characterized by Pb-hollandite, coronadite and cryptomelane and high amounts of Pb and Cu, the other ones linked to Beneficente are featured by romanechite as main phase and more Ba. Mn and Mn-Al-Fe massive, vermiforms, protopisolitic, pisolitic and colluvium have been developed from these rocks. As well as in the protoliths, Mn duricrusts developed over Vila do Carmo Group also formed hollandite, Pb-hollandite, cryptomelane and coronadite and have K_2O, Ag, Cu, Pb and Tl, whereas those from Beneficente Group formed supergenic romanechite.

Galena, native Ag, coronadite, Pb-hollandite, high Cu, Tl and positive Gd anomalies in the Mn duricrusts developed from Vila do Carmo Group are similar to the gossan contents, sulphide ores and hydrothermal Mn deposits. Besides that, the hydrothermal source of the Mn from Vila do Carmo Group is ratified by $^{206}Pb/^{207}Pb$ vs $^{208}Pb/^{206}Pb$, (Zn x Ni)/MnO_2 vs (Cu/Zn)/Fe_2O_3 ratios, and by Cu, Pb and Zn content, similar to the Australian gossans, and may classify the supergenic Mn as duhbite. By the other hand, the Mn from the Beneficente Group has sedimentary signature and may be classified as marine supergenic.

The Rb/Sr vs εNd allowed gather together rocks, lateritic duricrusts (Mn,Mn-Al-Fe, bauxitics, Fe and Fe-Al) and oxisols developed over Vila do Carmo, Beneficente and Alto Tapajós groups, what ratifies the use of lateritic duricrusts as tool of bedrocks mapping. The REE/(Zr+Hf) ratio ≥ 1 indicate control by Mn minerals and cerianite. Whereas, ≤ 1 claim that heavy minerals as zircon are risponsible by the REE variations

along the lateritic profile. The redistribution of minerals in the lateritic porfiles with residual concentration of zircon or leaching of Mn minerals (coronadite, hollandite and cryptomelane) and fixation in cerianite controls the Nd isotopic signature.

The Sr isotopic ratios displays two distinct behaviors:1- The $^{87}Sr/^{86}Sr$ increase in to the top of profiles where predominate Fe and Mn-Fe-Al duricrusts, suggesting the Sr input from the atmosphere, rainwater and groundwater. 2- The harsher leaching which culminated in the kaolinite and gibbsite formation release Sr in solution from protoliths and decrease the $^{87}Sr/^{86}Sr$ to the oxisols.

Pb isotopic ratios are higher in the lateritic duricrusts and oxisols than in the protoliths, as they are not affect by the weathering, this difference may be assingned to ^{238}U decay to ^{206}Pb or mixing of sources. The excellent correlation between $^{143}Nd/^{144}Nd$, $^{206}Pb/^{207}Pb$ and $^{208}Pb/^{206}Pb$ showed by the mass balance of the profiles P1 and P2 ratifies the Pb isotope immobility during extreme weathering

The gammaspectometry together with the altimetry, and Boolean and Fuzzy statistical methods allowed recognize favorable areas to the duricrust occurrences. Both models displayed good correlation to bauxites, manganiferous duricrusts and oxisols, despite the Boolean model be able to identify 67% of the Fe duricrusts, 20% more than Fuzzy models. However, the Fuzzy models have been efficient when they discarded ironstones located in the western of the area, once it does not have relationship with the lateritization. The combination between relief, eTh fuzzy (best kappa index- 0.8), stratigraphy and soil map allowed identify/suggest 100 Km^2 of the possible areas to Mn lateritic duricrust occurrence, 700 Km^2 to bauxites and 83 Km^2 to phosphatic duricrusts.

The beginning of lateritization refers to the Permian and extends to Jurassic-Cretaceous with aggradation of massive Fe duricrust. The absence of Ar-Ar data in manganese duricrusts in the southeastern Amazonas state prevents to assert its precise formation time; however, by correlation of manganese duricrusts in Burkina Faso, Carajás and Iron Quadrangle, they point towards the end of the Cretaceous (~ 70 Ma) of these duricrusts, extending to the end of the Miocene. In this context, there was the second phase of ferruginous duricrust aggradation (Oligocene medium at the beginning of the Miocene) in the study area. From then on, there were two distinct intervals of lateritic duricrusts degradation (goethite formation); the first one between 22.5 ± 2.3 and 17.1 ± 1.7 Ma and second between 13.1 ± 1.3 and 16.6 ± 1.7 Ma.

Keywords: Lateritization, isotopes, Fuzzy, Boolean, dubhite

CAPÍTULO I: APRESENTAÇÃO, INTRODUÇÃO E OBJETIVOS

1 APRESENTAÇÃO

A presente tese de doutorado reúne um conjunto de dados, discussões e conclusões obtidas ao longo de quatro anos de estudo. A tese está subdividida em três artigos que enfocam a composição química e isotópica (isótopos Pb, Sr e Nd) das rochas sedimentares dos grupos Vila do Carmo, Beneficente e Alto Tapajós, e das crostas lateríticas e solos desenvolvidas a partir estas unidades litoestratigráficas. Essas informações compõem o artigo publicado na *Ore Geology Reviews* n°89 (2017; páginas 270-289) e outro submetido à *Chemical Geology*. Além disso, foram abordados parâmetros geofísico-estatísticos (lógica fuzzy e booleana) que visam identificar locais favoráveis à ocorrência de crostas lateríticas (3º. Artigo em preparação). Por último, e ainda em fase preliminar, é enfocada a evolução da lateritização na região sudeste do Amazonas com base nos dados de (U-Th)/He. Para complementar esses dados foram feitas análises Ar-Ar, mas os resultados ainda não foram finalizados.

2 INTRODUÇÃO

A descoberta de matérias primas e bens minerais que possam suprir a demanda tecnológica, siderúrgica e agrícola está cada vez mais rara, de modo que, à medida que grandes depósitos minerais estão se exaurindo, a atenção tem se voltado a depósitos de pequeno porte e com mais baixo teor. No entanto, há diversos inibidores do mapeamento em detalhe de possíveis rochas mineralizadas, que incluem matas fechadas, redes de drenagem bem desenvolvidas e o intemperismo. O intemperismo, quando em regiões de clima quente e úmido com curtas estações secas promove o desenvolvimento de espessos regolitos com latossolos que alcançam dezenas de metros de espessura. Os regolitos são registros de mudanças climáticas e erosivas ocorridas ao longo do tempo geológico, configuram importantes ferramentas prospectivas e concentram metais oriundos do enriquecimento supergênico como bauxita (Al), fosfatos de alumínio, Ni, ouro, manganês, caulim, dentre outros. (Bardossy & Aleva 1990; Costa, 1990; Oliveira et al. 1992; Varentsov, 1996; Costa, 1997, Costa & Moraes, 1998; Larizzati et al. 2008; Bogatyrev et al. 2009).

O estudo dos lateritos ganhou importância na região Amazônica graças à descoberta de grandes depósitos de bauxita, ferro, caulim e manganês e rendeu inúmeros trabalhos que discutem os aspectos mineralógicos, geoquímicos e geomorfológicos independente da natureza parental sobre as quais se desenvolveram (Dennen & Norton 1977, Grubb 1979, Kronberg *et al*. 1979 e 1982, Lucas 1997,

Boulangé & Carvalho 1997, Horbe & Costa 1999, Costa 1997, Costa et al. 2005, Kotschoubey et al. 2005, Costa et al. 2014, Oliveira et al. 2016 entre vários outros). Esses estudos estão centrados na composição mineral e na geoquímica dos perfis com a definição dos padrões de distribuição dos elementos nos diferentes horizontes. Apesar dos avanços, há necessidade de estudos mais amplos, que permitam correlacionar perfis lateríticos, solucionar problemas como autoctonia e alóctonia de solos, idade de formação das crostas lateríticas e a consequente implicação na evolução geomorfológica.

Na Amazônia, são reconhecidos dois tipos perfis lateríticos classificados como imaturos e maturos, que sustentam serras, platôs e colinas (Costa, 1991; Costa, 2007). Assim, sobre rochas expostas por mais tempo ao intemperismo desenvolveu-se bauxita, enquanto nas mais jovens do Neógeno há apenas crostas ferruginosas (Lucas, 1997; Boulangé & Carvalho, 1997; Horbe & Costa, 1999; Costa, 1997; Costa et al. 2005; Kotschoubey et al. 2005; Costa et al. 2014; Oliveira et al. 2016).

Apesar dos terrenos lateríticos serem bem conhecidos e estudados na região Amazônica, há inúmeras ferramentas, técnicas analíticas e aplicações pouco exploradas que serão apresentadas nesta tese, como isótopos (Sr, Pb e Nd), aerogeofísicas e geocronológicas ((U-Th)/He).

3 OBJETIVOS GERAIS E ESPECÍFICOS

- Estudar os efeitos da lateritização nas rochas dos grupos Vila do Carmo, Beneficente e Alto Tapajós, região sudeste do Amazonas, que deram origem a oito perfis lateríticos. Dentre os quais, cinco apresentam crostas lateríticas manganesíferas à Mn-Fe-Al e em três foram desenvolvidas bauxitas e crostas Fe e Fe-Al.
- Identificar as variações mineralógicas e químicas ao longo dos perfis lateríticos
- Reconhecer a fonte do Mn, o ambiente de formação e as assembléias minerais que identificam os perfis com crosta manganesífera e Mn-Fe-Al.
- A partir dos dados mineralógicos, químicos e isotópicos, correlacionar os produtos da lateritização com as rochas mães.
- Identificar a proveniência das rochas sedimentares da região com o auxílio dos isótopos de Sr e Nd

- Compreender o comportamento dos isótopos de Nd, Pb e Sr sob intemperismo agressivo e identificar os minerais responsáveis pelas mudanças nas razões isotópicas ao longo dos perfis.
- Identificar crostas lateríticas com o auxílio da gamaespectometria aérea de acordo com os modelos estatísticos Booleano e Fuzzy.
- Propor mapa de favorabilidade para crostas lateríticas
- Designar regiões favoráveis às ocorrências minerais baseados na altimetria, estratigrafia e gamaespectometria.
- Datar as crostas ferruginosas por (U-Th)/He e estabelecer a evolução dos lateritos na região
- Ratificar o potencial dos lateritos como ferramenta de mapeamento e prospecção, de inferência de paleoambiente e de evolução geomorfológica.

CAPÍTULO II: REVISÃO BIBLIOGRÁFICA

4 REVISÃO BIBLIOGRÁFICA

4.1 Localização, estrutura, formação e posicionamento topográfico dos horizontes e paisagens lateríticas

Lateritos são abundantes e espalhados nas paisagens profundamente intemperizadas do cinturão intertropical, particularmente nas terras continentais entre latitude 35º N e 35º S onde a média da temperatura é superior a 20° C e a umidade supera 1200 mm/ano, bem como nas Américas Central e do Sul, África, parte da Ásia e Oceania (Figura 1). São formados por crostas, cascalhos e diversas impregnações resultantes de complexo intemperismo químico e físico durante longos períodos de tempo geológico. Constituem a parte superior do perfil que é tipicamente composto por rocha mãe, saprólito, mosqueado, crosta laterítica e solo.

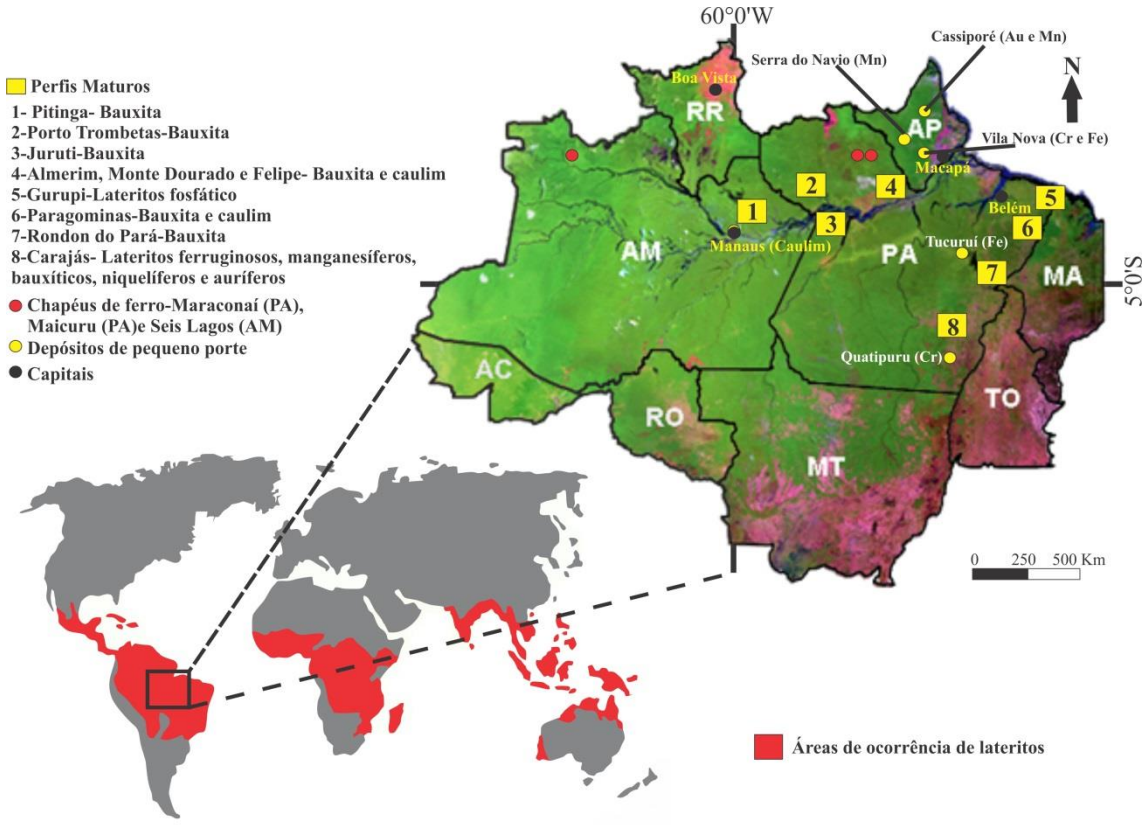

Figura 1: Regiões de ocorrência de lateritos no mundo, com ênfase aos depósitos supergênicos de maior porte na Amazônia. Modificado de Bardossy & Aleva (1990) e Costa (1991)

Na região Amazônica perfis maturos se diferenciam dos imaturos por serem mais antigos e, consequentemente, mais lixiviados, o que permitiu a formação do horizonte bauxítico e/ou de fosfato de alumínio (Costa, 1991; Costa, 2007; Figura 1 e 2). No que se refere à estruturação dos perfis, o saprólito é a parte inferior do regolito, correlato ao

horizonte C do solo. No atual modelado da paisagem, aflora em vales e/ou encostas ingrímes (Anand et al. 2002; Bitom et al. 2013), representa a rocha mãe parcialmente alterada, preserva os constituintes minerais primários do material original em coexistência com argilominerais neoformados (Anand & Paine, 2002; Costa, 2007). A parte inferior do saprólito, denominada "*saprock*" ou saprólito grosso, exibe menos que 20% dos minerais primários alterados, é constituída por grandes blocos individualizados pelo intemperismo ao longo de fraturas, falhas, acamamentos, contatos, vênulas, veios, dentre outros. Nesta interface há illita e esmectitas e ausência de oxi-hidróxidos de ferro. A porção superior, conhecida como saprólito fino ou litomarge, apresenta mais de 20% dos minerais primários alterados, além disso, os minerais primários são substituídos pseudomorficamente para a caulinita, goethita e hematita; restando apenas quartzo em estado parcial de dissolução e resistatos. Próximo ao contato com o horizonte mosqueado, à medida que a proporção de argilominerais, cimentação por sílica secundária, goethita e hematita aumentam, o saprólito tende a perder progressivamente o "*fabric*" da rocha mãe (Anand & Paine, 2002; Costa, 2007).

O horizonte mosqueado, que se sobrepõe ao saprolítico e geralmente aflora em vales ou meia encostas, representa a transição entre o saprólito e a crosta laterítica, onde isolam-se zonas esbranquiçadas ricas em caulinita (neoformadas in situ) e em quartzo (herdados da rocha mãe) de porções ferruginosas, geralmente avermelhadas a violetas (Tardy, 1993; Beauvais, 1999). De acordo com Ollier et al. (1988) e Eggleton (2001), manchas menores que 10 mm são denominadas *"minimottles/minimosquedas"* e aquelas maiores que 200 mm, "megamottles/ megamosqueadas". Sua formação está atrelada ao dissolvimento do quartzo nas zonas ricas em caulinita com aumento da porosidade, e por consequência, caulinita passa a ser substituída por hematita e goethita que formam manchas avermelhadas, violetas e amarelas (Aleva, 1994; Rosolen et al. 2002). Os "megamottles/ megamosqueadas", mais comuns sobre sedimentos que preenchem vales, têm sua origem relacionada à mobilização e segregação do Fe ao longo de sistemas radiculares antigos, resultando em "cilindros" argilosos de coloração pálida e depletados em Fe (Anand et al. 2002). Por fim, Costa (2007) sugere que o horizonte mosqueado juntamente com o saprolítico seja denominado "argiloso", uma vez que há mosqueamentos que preservam o *fabric* da rocha mãe (Anand and Paine, 2002; Anand and Butt, 2010).

A crosta laterítica é o material mais duro, denso e coeso do perfil laterítico devido à formação e recristalização de óxidos de ferro e alumínio e, quando aflorante

sustenta platôs, serras e colinas devido a sua maior resistência à erosão. A formação das crostas pressupõe longo processo de lixiviação, acúmulo de ferro e alumínio, clima sazonal e estabilidade tectônica (Valeton, 1972, Bardossy & Aleva, 1990). Na sua base ou zona inferior, quando em lateritos maturos, mais expostos ao intemperismo, há presença de fosfatos de alumínio e/ou crosta bauxítica (Costa, 2007). No topo ou zona superior, a crosta é abundante em hematita e goethita. Os principais tipos de crostas lateríticas são colunares, maciços, vermiformes, protopisolíticas/protonodulares, brechóides/fragmentada e pisolítica, nodular ou oolítica descritos na Tabela 1.

Segundo Rosolen et al. (2002) o endurecimento do topo de mosqueados oriundo da acumulação de ferro, leva à formação das crostas lateríticas. Nesse contexto, acredita-se que crosta com estrutura colunar esteja relacionada a ações de raízes, uma vez que forma prismas ou elementos cilindros posicionados na vertical ou com leve inclinação que remetem a colunas. Entre as colunas há espaços vazios que podem estar preenchidos por material friável e caulinita com filmes de goethita recobrindo poros e tubos (Castro, 2015). Ademais, este tipo de feição se sobrepõe à textura da crosta, por exemplo, há crostas colunares com textura vermiforme, maciça e pisolítica.

Na evolução do perfil laterítico é entendido que a crosta maciça se encontra no topo dos perfis e a partir da sua degradação se formam outros fácies, tal qual relatado por Théveniaut & Freyssinet (1999), Bitom et al. (2003), Beauvais (2009) e Albuquerque & Horbe (2015). Há quem afirme que crostas vermiformes, que em geral ocupam meia encosta e baixas vertentes das paisagens (Beauvais, 1991), resultam do endurecimento direto do horizonte mosqueado em clima mais quente e seco, a partir da ferruginização da caulinita e dissolução de quartzo resultando no aumento de cavidades e póros (Anand & Paine, 2002). As crostas protonodulares e protopisolíticas, ocupam os topos dos platôs e meia encosta de vertentes íngrimes que recobrem mosqueados e saprólitos, respectivamente. De acordo com Beauvais (1999), crostas protonodulares consistem de uma mistura de plasmas hematíticos e cauliníticos, onde hematita sempre apresenta Al em sua estrutura. A segregação do Al leva à formação de plasmas micronodulares de gibbsita que suportam nódulos ferruginosos. A progressiva degradação em meia encosta, geralmente sem ou com pouca cobertura vegetal leva à individualização de pisólitos e ao estabelecimento das crostas protopisolíticas (Beauvais, 2009).

Crostas brechóides e/ou fragmentadas ocupam topo dos perfis, geralmente em contato direto com o mosqueado e/ou saprólito. Anand & Paine (2002) sustentam a

hipótese que tais crostas derivam do colapso do topo de crostas vermiformes, horizontes mosqueados e saprolíticos em função do aumento de espaços vazios com subsequente cimentação dos fragmentos. Enquanto que, Anand and Butt (2003) descreveram crostas fragmentadas provenientes da bauxitização direta do "*saprock*", sem formação de caulinita, seguido de ferruginização e preservação do fabric original da rocha mãe.

Crostas nodulares resultam da individualização e endurecimento de nódulos ferruginosos em horizontes mosqueados, podendo haver cimentação por gibbsita em períodos mais quente e úmido. Os pisólitos resultam da atividade pedogênica na parte superior do perfil e são formados por lixiviação, migração e acumulação de óxidos de Fe na matriz argilosa ou em espaços vazios. Podem se formar a partir de qualquer material proveniente da segregação e ferruginização de fragmentos argilosos, ferruginosos, quartzosos ou mesmo líticos (Clarcke & Chenoweth, 1996). A mobilização, segregação e acumulação do ferro estão associadas às flutações do lençol freático que promove a formação de Fe^{3+}. Além disso, a matéria orgânica mobiliza e segrega o Fe, tais como observado na atividade de raízes que tem relação com as manchas subverticais em mosqueados. A individualização de pisólitos, nódulos e oólitos com formas concêntricas e formação de cutans de goethita, estão relacionados à degradação in situ da crosta laterítica. Posteriormente esses nódulos, pisólitos e oólitos podem ser cimentados por plasmas ricos em ferro ou Al (Anand & Paine, 2002; Anand et al. 2002). Anand & Butt (2003) também advogam que pisólitos também podem ser transportados, depositados e em seguida cimentados.

O horizonte nodula e/ou pisolítico, que se sobrepõe à crosta laterítica, são comuns na região Amazônica e recebem o nome de horizonte desmantelado. Os nódulos podem ser irregulares e ovalados, enquanto que os pisólitos podem ser subdivididos em homogêneos, líticos, pseudomórficos (compostos por minerais secundários como argilominerais e gibbsita) e concêntricos (múltiplos cutans) (Anand et al. 1989).

Os latossolos amarelos a avermelhados, também denominados "Argila de Belterra" (Sombroek, 1966), são os principais tipos de solos que recobrem crostas lateríticas na Amazônia. Tratam-se de solos espessos (até dezenas de metros), isotrópicos, ricos em caulinita, goethita e anatásio/rutilo com quantidades razoáveis de quartzo e, por vezes, concreções de gibbsita (Horbe & Costa, 1999). Sua origem é controversa, enquanto Sombroek (1966) sugere fonte andina e deposição em ambiente lacustre durante o Plioceno-Pleistoceno; Klammer (1971) e Dennen & Norton (1977) consideram-na como horizonte A do perfil de solo derivados das crostas aluminosas

sotopostas. Grubb (1979) também atesta a relação da "Argila de Belterra" com as crostas aluminosas, no entanto, credita sua origem a depósitos coluvionares, devido à presença de nódulos de gibbsita na base do solo. Truckenbrodt & Kotshoubey (1981), na mesma linha de pensamento de Sombroek (1966) sugerem exposição subárea das sequências lateríticas e deposição da "Argila de Belterra" por fluxos de lama ou *"sheet flows"*. No entanto, podem simplesmente representar o retrabalhamento in situ das bauxitas adjacentes e/ou sobrepostas, das crostas ferruginosas ou mesmo de saprólitos expostos (Horbe & Costa, 1999 e 2005).

Contudo, em Carajás e Maicuru no Pará, Seis Lagos no Amazonas e ao longo do rio Madeira em Rondônia há sedimentos lacustres recobrindo crostas lateríticas (Costa, 1991; Correa, 1996; Costa et al. 2005b; Figura 2).

Há ainda perfis truncados pela neotectônica, que expõem linhas de pedras e demarcam superfícies erosivas (Horbe & Horbe, 2005, Figura 2).

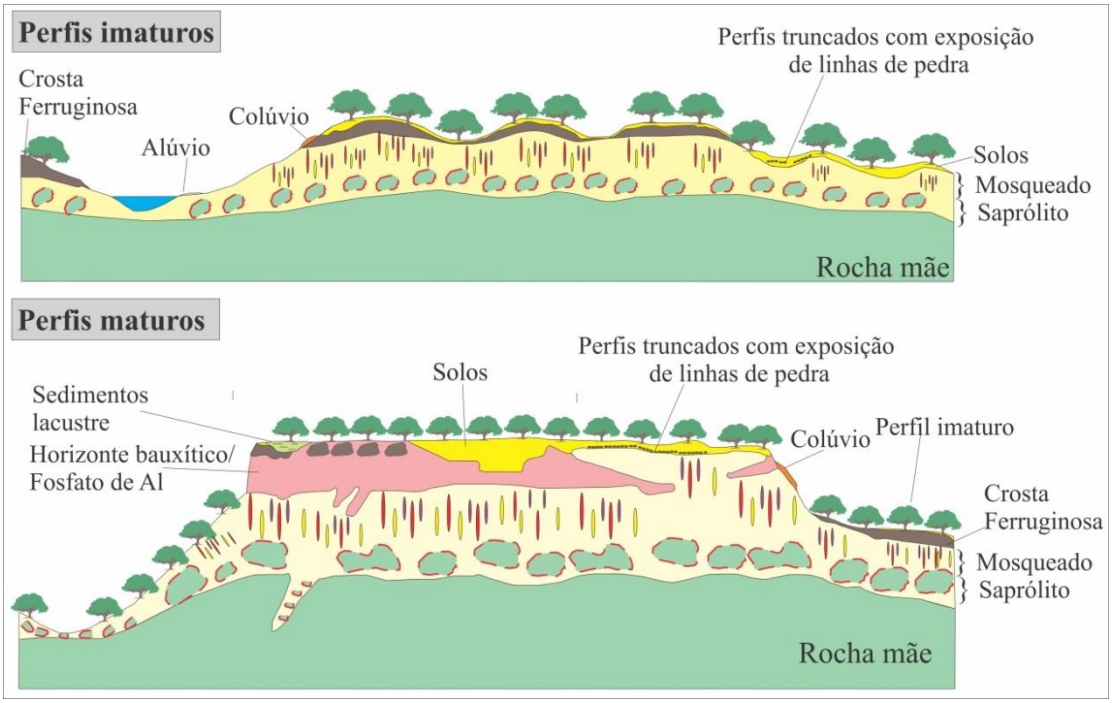

Figura 2: Principais tipos de perfis lateríticos na região Amazônica (Costa, 1991)

Tabela 1: Principais tipos de crostas lateríticas descritas na região Amazônica (Costa, 1991; Kotschoubey et al., 2005; Costa et al. 2005; Costa, 2007; Peixoto & Horbe, 2008; Albuquerque & Horbe, 2015; Castro, 2015)

Tipo de crosta/ estrutura	Descrição
Maciça	Apresenta textura homogênea, sem nódulos, pisólitos ou oólitos, ou elementosgeométricos definidos. Pode apresentar póros, vesículas e tubos preenchidos por argilominerais e quartzo. Além disso, pode apresentar variação de cores dependendo da composição mineral.
Vermiforme	Assemelha-se a favos-de-mel, geralmente é a mais friável dos tipos de crosta. Apresenta "esqueleto" frequentemente composto por hematita e goethita ou óxidos e hidróxidos de manganês, e póros, tubos e cavidades parcialmente preenchidos por material argiloso a arenoso.
Protopisolítica/ Protonodulares	Crostas protopisolíticas/protonodulares são aquelas na qual há individualização incipiente dos pisólitos/nódulos. Podem se desenvolver em crostas maciças e vermiformes, por exemplo.
Brechóide/Fragmentada	Este tipo de crosta exibe fragmentos angulosos que podem ser ferruginosos, manganesíferos e aluminosos cimentados por plasma. O plasma também pode variar desde o gibbsítico, passando pelo manganesífero e ferruginoso. Há ainda, casos em que o plasma tem composição oolítica, o que confere a crosta maior porosidade. Nos fragmentos é comum a presença de córtex goethítico.
Nodular/Pisolítica/oolítica	Assemelham-se às crostas brechóides/fragmentadas, no entanto, pisólitos e oólitos são ovalados ou apresentam forma elipsoidal, enquanto que os nódulos podem ter forma irregular. Diferenciam-se pelo tamanho dos componentes, de modo que, nódulo (>64mm)> pisólito (2- 64mm)> oólito (0,25-2mm)

4.2 Métodos geocronológicos, termocronológicos e paleomagnéticos aplicados à datação de crostas lateríticas

Segundo Retallack (2010) a idade de crostas lateríticas pode ser inferida por condições estratigráficas específicas, como por exemplo, quando há formação de crostas em meio a sedimentos pantanosos, calcários fossilíferos e em meio a derrames basálticos. No entanto, a aplicação dos métodos Ar-Ar e (U-Th)/He em óxidos de Mn e Fe, respectivamente, tem evoluído ao longo das décadas e os resultados mostram-se correlatos nas diversas regiões do mundo onde foram aplicados.

O primeiro trabalho realizado na Amazônia a utilizar o método Ar-Ar em crostas lateríticas foi o de Vasconcelos et al. (1996). As idades obtidas em crostas manganesíferas atestaram que a lateritização na região de Carajás iniciou em 72 Ma e a partir de então houve precipitação episódica de óxidos de manganês em 65-69, 51-56, 40-43, 33-35, 20, 24, 12-17 Ma, refletindo alternâncias climáticas e as condições intempéricas da região. Ruffet et al. (1996) e Costa et al. (2005) também empregaram métodos geocronológicos nas crostas manganesíferas da Mina do Azul que ratificaram as idades de Vasconcelos et al. (1996) comprovando a eficácia da datação de

criptomelana por ^{39}Ar -^{40}Ar. O método (U-Th)/He em goethita e hematita, foi utilizado em crostas lateríticas ferruginosas de Carajás (Shuster et al. 2005) e no nordeste do Brasil (Lima, 2008) ambos obtiveram idades de 61 a 8 Ma e 31,4 ± 1 Ma e 0,8± 0,4 Ma, respectivamente. Esses dois métodos também foram utilizados em crostas lateríticas de outras regiões do Brasil, África, Austrália e Índia (Hécnoque et al. 1998; Pidgeon et al. 2004; Colin et al. 2005; Spier et al. 2006; Beauvais et al. 2008; Bonnet et al. 2014 e Monteiro et al. 2015), os resultados obtidos mostram-se correlatos à aqueles encontrados em crostas lateríticas da região Amazônica.

Há, contudo, dificuldades analíticas na utilização desses métodos relacionadas às características dos minerais das crostas lateríticas. Os minerais de Fe e Mn lateríticos por serem produtos da transformação de minerais primários têm contaminantes que devem ser removidos durante a fase de preparação das amostras, além disso, por formarem diminutos agregados de minerais, separar fases puras, seja de goethita, hematita, holandita e criptomelana torna-se um desafio a ser superado (Lima, 2008). Por exemplo, Lima (2008) ressalta a importância da remoção de argilominerais impregnados na goethita, uma vez que estes trazem consigo resíduos de Th e implicam em contaminação da amostra e em idades espúrias. Vasconcelos et al. (1996), Ruffet et al. (1996) e Costa et al. (2005) relatam problemas relacionados à perda de ^{40}Ar e/ou contaminação e Vasconcelos (1999) e Lima (2008) discutem que o aquecimento gradual permite testar a presença de argônio herdado ou em excesso, separar gases atmosféricos dos gases radiogênicos e detectar as várias gerações do mineral datável.

Outros métodos também surgem como alternativa para se estabelecer idades em crostas lateríticas da Amazônia, tais como o paleomagnetismo. Neste método, a idade das crostas lateríticas é estimada pela comparação dos pólos paleomagnéticos obtidos nas crostas em relação ao *South American apparent polar Wander path* (APWP). Diante disto, Théveniaunt & Freyssinet (1999) e Théveniaunt & Freyssinet (2002) identificaram dois eventos de lateritização na região da Guiana Francesa e Suriname: o primeiro denominado Ciclo Sulamericano de lateritização é bem demarcado do Paleoceno ao Eoceno (60 e 40 Ma), e o segundo correspondente ao Neo-Mioceno estabelece ciclos entre 13 e 5 Ma. Posteriomente, Horbe (2014) estudou sete perfis que abrangeram boa parte da região Amazônica. Os dados indicaram que a lateritização se deu entre 80 e 10 Ma (Neo-Cretáceo ao Eo-Paleoceno), e mostrou correlação com os dados de Ar-Ar obtidos por Vasconcelos et al. (1996), Ruffet et al. (1996) e Costa et al. (2005) em crostas manganesíferas de Carajás. Além disso, demonstraram que as crostas

ferruginosas e bauxitas datam entre 70 e 80 Ma e corresponde a primeira fase de bauxitização, no entanto, entre 28 e 50 Ma a segunda fase de bauxitização está atrelada às bauxitas porcelanadas de topo de perfis. A autora ainda advoga que são necessários 50 Ma de anos para a formação de bauxita na região Amazônica.

4.3 Histórico dos principais depósitos de manganês e bauxita da Amazônia

Na atual conjectura, o Brasil é um dos grandes produtores de manganês e bauxita. Detém cerca de 4,6 bilhões de toneladas de manganês, 10% das reservas mundiais, atrás apenas da Ucrânia (24%), África do Sul (22%) e Austrália (16%); e 7,5 bilhões de toneladas de bauxitas, terceira maior reserva mundial, atrás de Guiné (25 bilhões de toneladas) e Austrália (9,8 bilhões de toneladas) (DNPM, 2017)

Na Amazônia, a corrida mineral teve início em 1945 com a descoberta de manganês na Serra do Navio, no Amapá; ouro, no Tapajós, e, 1957 com o ferro de Carajás, no Pará. Em meados da década de 1960, grandes depósitos de bauxitas foram reconhecidos sobre rochas siliciclásticas da bacia do Amazonas e Parnaíba (Paragominas, Almerim, Porto Trombetas e Juruti), alguns destes operam até hoje.

4.3.1 Manganês

O Mn hospedado em rochas sedimentares ou associado à BIFs tende a formar depósitos grandes a gigantes (média de 51 Mt e 31% de MnO) (Roy, 2006; Maynard, 2010). Quando sequências sedimentares manganesíferas são metamorfizadas, minerais primários são convertidos em silicatos ou carbonatos de Mn (p. Ex., rodonita, espessartita, Mn calcita, tefroíta) e podem formar depósitos pequenos ou grandes (<1 Mt a 43 Mt) (Roy & Purkait , 1968; Rodrigues et al., 1986; Nicholson et al., 1997; Chisonga et al., 2012). Contudo, a ação do intemperismo sobre o minério primário aumenta os teores de MnO, produz novos minerais e/ou os remobiliza em ambiente supergênico dando origem a uma segunda fase de precipitação.

Deste modo, os principais depósitos de Mn da Amazônia (Mina do Azul, Serra do Navio e Buritirama) estão associados a sequências sedimentares Proterozoicas depositadas em ambiente marinho (Formação Águas Claras, Formação Serra do Navio e Grupo Buritirama, respectivamente), que permaneceram inalterados ou foram submetidas a metamorfismo de fácies anfibolito. O manganês da mina do Azul (65 Mt de MnO), região de Carajás, Pará, está hospedado em arenitos finos e siltitos brancos a vermelhos com camadas lenticulares de siltito cinza a folhelhos ricos em matéria orgânica, MnO e rodocrosita (Anderson et al. 1974; Costa et al. 2005). De acordo com

Costa et al. (2005), o minério primário é composto em ordem de abundância por criptomelana, todorokita e hollandita, o que lhes confere assinatura química com média de 40% de MnO; 10% de Al_2O_3; 6% de Fe_2O_3, e 1,5% de K_2O. Sobrepondo o minério primário, os produtos do enriquecimento supergênico que contém manganês são o saprólito e a crosta laterítica de caráter brechóide, nodular e maciça. Enquanto no saprólito, criptomelana, hollandita, todorokita, nsutita e pirolusita são os principais minerais, na crosta laterítica a litioforita é mais abundante. Nestes horizontes a composição química média é de 63-50% de MnO; 11-7% de Al_2O_3; 13-4% de Fe_2O_3, e 1,5-1% de K_2O.

O manganês das minas de Serra do Navio e Buritirama estão relacionados a xistos, mármores e gonditos. Em resumo, o intemperismo de gonditos portadores de granadas com Mn (espessartita), xistos com silicatos de Mn (tefroíta e rodonita) e mármores ricos em rodocrosita formou 50-60m de alteração supergênica com 44-48% de MnO e cerca de 31Mt (Rodrigues et al. 1986; Scarpelli & Horikava, 2017). O principal mineral de minério no pacote supergênico é criptomelana, enquanto que pirolusita, manganita e litioforita ocorrem subordinados (Valarelli, 1967).

A mina de Buritirama é a de menor porte dentre as duas últimas, com reserva estimada em 19Mt e teor de MnO superior a 40%. O protominério é classificado como do tipo gondito com componente silicático significativo, em contraposição ao minério carbonático denominados “queluzíticos” de Serra do Navio (Machamer, 1987). A paragênese mais frequente no protominério é ampla e envolve braunita (Mn_2O_3), bixbyita ($(Mn,Fe)_2O_3$), hausmanita(MnO_4), carbonato (Mn calcita e Mn-Kutnahorita), piroxenóides manganesíferos (piroxmangita e rodonita), alabandita (MnS), tefroíta, pirofanita e espessartita (Bello, 1978). Apesar da variedade mineralógica portadora de Mn no protominério, o minério oxidado, supergênico, é composto por criptomelana, litioforita e nsutita.

4.3.2 Bauxita

As primeiras ocorrências de bauxitas na região Amazônica foram reportadas em meados de 1950 quando as empresas Kaiser Aluminium Company e Rio Tinto Zinc Company intensificaram as pesquisas de bauxitas na região oeste do Pará e Paragominas. Os depósitos de grande porte de bauxita provêm de rochas siliciclásticas das formações Alter do Chão e Itapecuru/Ipixuna, enquanto que os de menor porte

associam-se a granitos, riolitos, basaltos, xistos e gnaisses proterozóicos (Costa et al. 1997; Peixoto & Horbe, 2008; Costa, 2007).

Segundo Dennen & Norton (1977), Grubb (1979), Kotschoubey & Truckenbrodt (1981) e Kotschoubey et al. (2005) a formação dos perfis bauxíticos está associada a evolução polifásica em dois eventos de bauxitização distintos: i) bauxitização completa das rochas sedimentares seguido de ferruginazação em condições podzólicas e uma segunda fase de bauxitização nas zonas de fratura; ii) formação e retração parcial do saprólito e da crosta ferro-aluminosa com posterior desenvolvimento do horizonte bauxítico com quatro fácies de bauxita que se formaram a partir do zoneamento regional. Kotschoubey et al. (2005) advoga que a primeira fase de bauxitização em Paragominas está situada entre o Paleógeno até o início do Oligoceno, enquanto a segunda se estende do final do Oligoceno até o início do Mioceno, por outro lado, Horbe (2014) afirma com base em paleomagnetismo que o fim do Cretáceo, há cerca de 80 Ma, é o início da formação do perfis bauxíticos.

O maior depósito de bauxita da região amazônica em operação é de Paragominas, com 1249 Mt em reserva, seguido de Porto Trombetas (955 Mt), Rondon do Pará (642Mt) e Juruti (196Mt) (DNPM, 2010; Oliveira et al. 2016). Os principais constituintes mineralógicos dos perfis bauxíticos são gibbsita, goethita, hematita, caulinita, anatásio e rutilo, por isso, estes depósitos têm entre 31 a 61% de Al_2O_3; 3 a 35% de Fe_2O_3, 1 a 30 % de SiO_2 e até 2% de TiO_2 (Tabela 2).

Tabela 2: Principais características dos principais depósitos de bauxita da região Amazônica, segundo Boulangé & Carvalho (1997), Kotschoubey et al. (2005), Lucas (1997), DNPM (2010), Costa et al. (2014) e Oliveira et al. (2016).

Depósitos	**Paragominas**	**Porto Trombetas**	**Rondon do Pará**	**Juruti**
Litoestratigrafia	Formação Itapecuru	Formação Alter do Chão	Formação Itapecuru	Formação Alter do Chão
Bacia	Paranaíba	Amazonas	Parnaíba	Amazonas
Tonelagem	1249 Mt	955 Mt	642 Mt	196 Mt
Al_2O_3	31-54%	47-61%	39-52%	44-54%
Fe_2O_3	3-35%	5-25%	15-35%	4-23%
SiO_2	7-30%	1-8,5%	4-11%	7-17%
TiO_2	1,3-2%	0,7-2,7%	1,-1,4%	1,5-2%

CAPÍTULO III: LOCALIZAÇÃO E ACESSO, MATÉRIAS E MÉTODOS CONTEXTO GEOLÓGICO E GEOMORFOLÓGICO LOCAL.

5 LOCALIZAÇÃO E ACESSO

A área do presente estudo, com cerca de 19000 Km^2, localiza-se no sudeste do estado do Amazonas, é delimitada por um polígono que compreende as coordenadas 7º45’S e 6°45’S e 61° e 59°30’ W inserido nas folhas Sumáuma (SB.20-Z-D), Mutum (SB.20-Z-B), Rio Acari (SB.21-Y-C) e Vila Porto Franco (SB.21-Y-A) entre os municípios de Apuí e Nova Aripuanã (Figura 3). O acesso, partindo de Manaus (505 Km), é feito via táxi aéreo até a cidade de Apuí. Apuí se liga ao restante do Brasil pela BR-230 (Transamazônica), essa estrada, a AM-174 (Apuí-Nova Aripuanã) e vicinais adjacentes, o rio Aripuanã e afluentes foram percorridos para estudar a região.

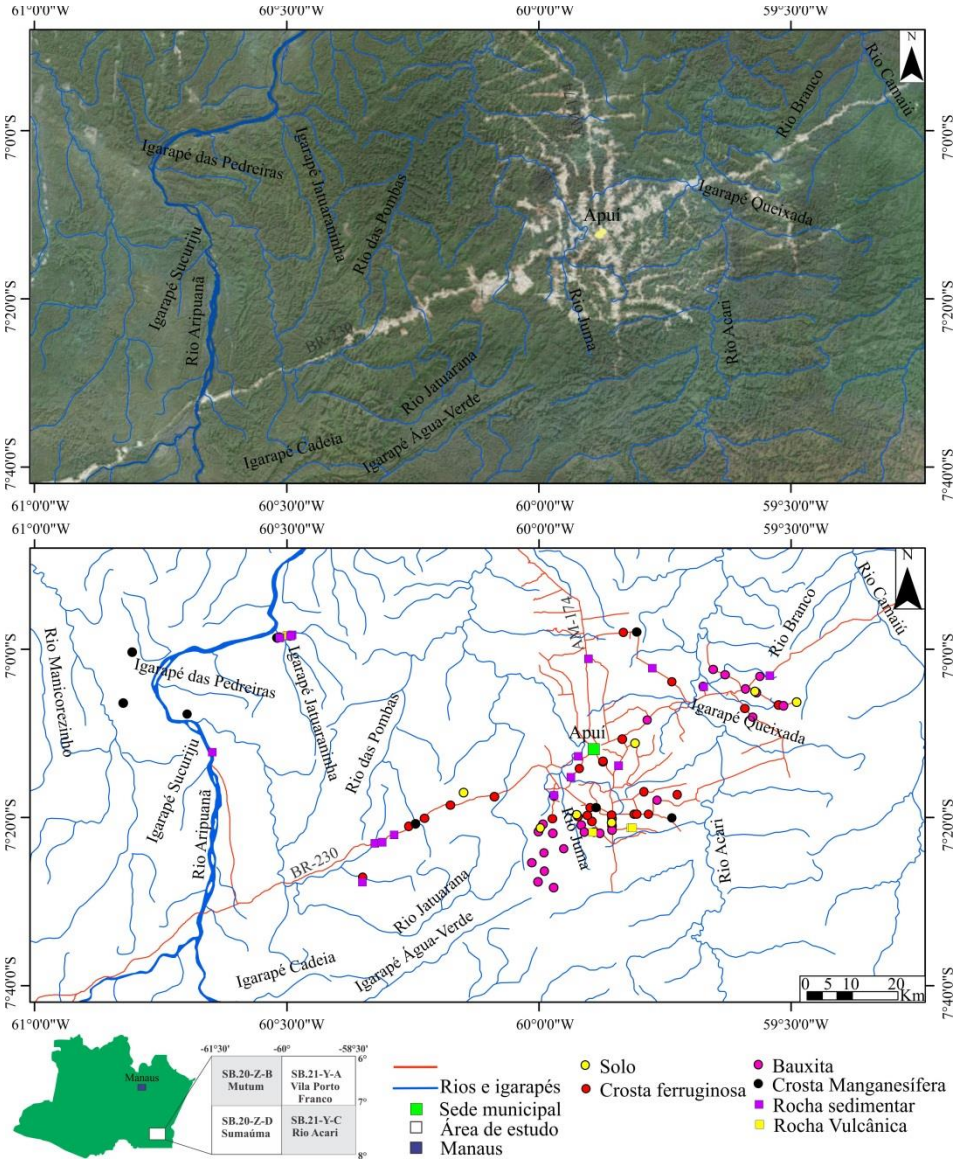

Figura 3: Mapa de localização da região de estudo e de pontos coletados.

6 MATERIAIS E MÉTODOS

6.1 Composição mineral, químico-mineral e geoquímica.

O mapeamento laterítico da região sudeste do Amazonas consistiu na coleta de 121 amostras de rochas vulcânicas, arenitos, siltitos, crostas lateríticas e solos (Tabela 3 e 4) ao longo da BR-230, das vicinais adjacentes à cidade de Apuí e dos rios Aripuanã e Jatuaraninha. Destas amostras, foram selecionadas 56 para estudo de detalhe. A composição mineral foi determinada por microscopia ótica, difração de raios-x foi realizada no Departamento de Geociências da Universidade Federal do Amazonas, enquanto que as análises de microscópio eletrônico de varredura (MEV) e microssonda eletrônica (ME) foram realizadas no Instituto de Geociências da Universidade de Brasília. Nas determinações mineralógicas por difração de raios-X (DRX) foi utilizado o método do pó em amostra total em difratômetro (Shimadzu XRD-6000) equipado com tubo de cobre acoplado, com ângulo de varredura entre 5 e 60° 2θ. A morfologia e a composição química (semi-quantitativa) foram obtidas por MEV (Quanta FEI 250), após montagem dos fragmentos de rochas e crostas em stubs de alumínio e metalização por Au-Pd. As determinações da química mineral foram realizadas por microssonda eletrônica (ME) após confecção de seções polidas, metalização por carbono e análise percentual de SiO_2, Al_2O_3, Fe_2O_3, MgO, CaO, Na_2O, K_2O, MnO_2, P_2O_5, CuO, CoO, BaO, PbO e V_2O_5 presentes em cada fase mineral.

As análises químicas foram determinadas em 56 amostras realizadas no laboratório Acmelab, Vancouver Canadá (Tabela 3). Os elementos maiores e menores (SiO_2, Al_2O_3, Fe_2O_3, MgO, CaO, Na_2O, K_2O, TiO_2, P_2O_5 e MnO) foram determinados e quantificados por ICP-ES em fusão com metaborato de lítio e digestão com HNO_3, a perda ao fogo por gravimetria, os traços (As, Ag, Ba, Be, Co, Cu, Ga, Hf, Mo, Nb, Ni, Pb, Rb, Sc, Sr, Ta, Th, U, V, Y, Zn, Zr, La, Ce, Pr, Nd, Sm, Gd, Tb, Dy, Ho, Er, Tm, Yb e Lu) por ICP-MS em fusão com metaborato/tetraborato de lítio.

O fracionamento dos ETR foi normalizado em relação ao condrito de Taylor e McLennan (1985) e as razões Eu/Eu*, Ce/Ce*, Tb/Tb* e Gd/Gd* de acordo com as equações:

$$1: Eu/Eu^* = (Eu/0.087)/[(Sm/0.231)x(Gd/0.306)]^{1/2}$$

$$2: Ce/Ce^* = (Ce/0.957)/[(La/0.367)x(Pr/0.137)]^{1/2}$$

$$3: Tb/Tb^* = (Tb/0.06)/[(Gd/0.31)x(Dy/0.38)]^{1/2}$$

$$4: Gd/Gd^* = (Gd/0.31)/[(Eu/0.087)x(Tb/0.06)]^{1/2}$$

5: (La/Yb)n= (La/0.367)/(Yb/0.250)

6 : (Gd/Yb)n= (Gd/0.31)/ (Yb/0.250)

Tabela 3: Localização dos perfis e demais pontos amostrados utilizados para determinação mineralógica e análises químicas, totalizando 56 amostras. X- realizadas, x*- realizadas apenas as amostras A2, B2 e S6, N- não realizadas

Sigla da amostra	Tipo de amostra	Latitude	Longitude	Análises químicas e mineralógicas	Isótopos de Sr e Nd	Isótopos de Pb
Perfil P1 ou Novo Natal (9 amostras)						
S7	Solo	6°58'35.4"	60°30'51.55"	x	x	x
Pi2	Crosta Mn	6°58'40.3"	60°31'8.7"	x	x	x
Pi1	Crosta Mn	6°58'36"	60°31'2.4"	x	x	x
Pp2	Crosta Mn	6°58'42.2"	60°31'6.3"	x	x	x
Pp1	Crosta Mn	6°58'42.6"	60°32'7"	x	x	x
M1	Crosta Mn	6°58'36.7"	60°30'52.5"	x	x	x
A3	Grauvaca Mn	6°58'26.3"	60°29'35.3"	x	x	x
PS	Siltito Mn	6°58'29.3"	60°29'38.3"	x	x	x
R	Rocha vulcânica	6°58'22"	60°30'3"	x	x	x
Perfil P2 ou Apuí (3 amostras)						
Perfil Apuí ou P2 (VB, VT e S5)	Crosta Mn-Fe-Al e solo	6°58'28.1"	60°29'36.5"	x	x	x
Perfil P3 ou Beneficente (6 amostras)						
Perfil Beneficente ou P3 (A2, B1, B2, B3, B4, S6 e S6)	Grauva Mn, Crosta Mn e solo	7°5'21"	60°45'46"	x	x*	N
Perfil composto P4 (5 amostras)						
C3	Crosta ferruginosa	7°19'38.2"	59°48'38.4"	x	x	N
Bx, C7 e S4	Bauxita/Crosta Fe/Solo	7°21'54"	59°52'42.7"	x	x	N
V	Rocha vulcânica	7°21'14.2"	59°48'54"	x	x	N
Perfil composto P5 (7 amostras)						
S3	Solo	6°58'2"	59°49'57"	x	x	N
C2	Crosta ferruginosa	6°58'0.8"	59°49'54.9"	x	x	N
B1A e S2 (parte do perfil composto P5)	Bauxita e solo	07°8'6.79"	59°34'32.4"	x	x	N
Q2, B1C e S2	Rocha sedimentar, bauxita e solo	7°2'42.9"	59°34'32.4"	x	x	N
Perfil composto P6 (9 amostras)						
C4	Crosta ferruginosa	7°17'27.8"	59°58'12.8"	x	x	N
C1	Crosta ferruginosa	7°8'27.9"	59°47'4.3"	x	x	N
C6	Crosta ferruginosa	7°17'32.7"	60°5'16.6"	x	x	N
Q4	Rocha sedimentar	7°1'5.4"	59°54'7.9"	x	x	N
G6	Rocha sedimentar	7°17'21.7"	59°58'13.7"	x	x	N
G5	Rocha sedimentar	7°27'40.8"	60°21'1.5"	x	x	N
G4	Rocha sedimentar	7°22'3.6"	60°17'17.4"	x	x	N
G2	Rocha sedimentar	7°15'12.5"	59°56'15"	x	x	N
G1	Rocha sedimentar	7°13'48.9"	59°50'33.5"	x	x	N
Perfil Holanda (6 amostras)						
Perfil Holanda (A1, ML, H1, H2, H3 e H4)	Grauva Mn, Crosta Mn e solo	7°8'27"	60°42'26"	x	N	N
Perfil Zé Julião (8 amostras)						
Perfil Zé Julião (Z1 a Z8)	Colúvio Mn	6°57'59.5"	59°48'20.8"	x	N	N
Outras amostras coletadas (3 amostras)						
Q1	Rocha sedimentar	7°3'6.7"	59°32'33.5"	x	x	N
QA	Rocha sedimentar	7°12'14"	60°38'54.3"	x	x	N
Q3	Rocha sedimentar	7°2'15.5"	59°46'33.9"	x	x	N

Tabela 4: Pontos amostrados em que não foram realizadas análises químicas e mineralógicas

Pontos de controle (65 amostras)					
Tipo de amostra	Latitude	Longitude	Tipo de amostra	Latitude	Longitude
Crosta Mn-Fe-Al	7°18'53"	59°53'12.5"	Rocha vulcânica	7°21'46.2"	59°53'37.7"
Crosta ferruginosa	7°7'4.1"	59°35'29.8"	Crosta Mn	7°19'44"	60°11'32.4"
Crosta ferruginosa	7°21'0.2"	59°51'18.1"	Crosta Mn	6°58'36.7"	60°30'58"
Crosta ferruginosa	7°19'38"	59°48'22.2"	Crosta Mn	6°58'37.3"	60°30'53.5"
Crosta ferruginosa	7°19'39"	59°46'56.3"	Crosta Mn	6°58'36.1"	60°30'53.4"
Crosta ferruginosa	7°17'17.2"	59°43'30.6"	Crosta Mn	7°20'8.2"	60°7'5.3"
Crosta ferruginosa	7°16'56.8"	59°47'28.7"	Crosta Mn	7°20'5.5"	59°44'7"
Crosta ferruginosa	7°13'26.3"	59°52'21.2"	Bauxita	7°21'32.19"	59°51'18.4"
Crosta ferruginosa	7°13'21"	59°52'22.5"	Bauxita	7°17'58.9"	59°45'55"
Crosta ferruginosa	7°19'56.5"	59°55'21.21"	Bauxita	7°21'32.18"	59°51'18.39"
Crosta ferruginosa	7°21'46.15"	59°53'23.8"	Bauxita	7°20'54.85"	59°54'58.1"
Crosta ferruginosa	7°20'30.2"	59°53'41.3'	Bauxita	7°21'46.76"	59°54'34.8"
Crosta ferruginosa	7°19'47"	59°54'13.4'	Bauxita	7°3'4.3"	59°37'51.7"
Crosta ferruginosa	7°20'10.3"	59°51'18"	Bauxita	7°2'26.7"	59°39'41"
Crosta ferruginosa	7°19'45.3"	59°51'19.9"	Bauxita	7°3'17"	59°33'41"
Crosta ferruginosa	7°18'51.1"	59°53'53.4"	Bauxita	7°4'43.1"	59°35'24.4"
Crosta ferruginosa	7°20'10.5"	59°58'22.8"	Bauxita	7°6'43.1"	59°30'53.5"
Crosta ferruginosa	7°3'53.7"	59°44'8.8"	Bauxita	7°5'11.29"	59°34'5.6"
Crosta ferruginosa	7°10'43"	59°50'3.8"	Bauxita	7°20'50.6"	59°59'29.9"
Crosta ferruginosa	7°6'37.6"	59°31'28.9"	Bauxita	7°21'44"	60°0.4'
Crosta ferruginosa	7°14'12.8"	59°55'9.6"	Bauxita	7°21'54"	59°58'21"
Crosta ferruginosa	7°18'34"	60°10'30.2"	Bauxita	7°23'47"	59°57'
Crosta ferruginosa	7°20'8.7"	60°13'34.9"	Bauxita	7°24'16"	59°59'23"
Crosta ferruginosa	7°21'4.9"	60°15'26.8"	Bauxita	7°25'25"	60°0.8'
Crosta ferruginosa	7°27'9.4"	60°20'56.4"	Bauxita	7°26'24"	59°59'20.4"
Crosta ferruginosa	6°58'23"	60°29'34"	Bauxita	7°27'39.6"	60°0.12'
Rocha sedimentar	7°23'4.9"	60°32'34.2"	Bauxita	7°23'22.8"	59°58'15.6"
Rocha sedimentar	7°23'5"	60°194'34.6"	Solo	7°20'37.96"	59°51'19.7"
Rocha sedimentar	7°22'55.5"	60°18'41.3"	Solo	7°19'42.9"	59°55'30.2"
Rocha sedimentar	6°58'16.5"	60°29'25"	Solo	7°11'11"	59°48'32.3"
Rocha vulcânica	7°21'12.7"	59°49'6.3"	Solo	7°6'18.9"	59°29'20.4"
Rocha vulcânica	6°58'19"	60°29'52"	Solo	7°21'16.5"	59°59'48.8"
			Solo	7°5'0.2"	59°34'17.2"

6.2 Métodos radiométricos Sr-Sr, Sm-Nd e Pb-Pb

36 amostras de rochas vulcânicas, crostas lateríticas e solos relativas aos perfis P1, P2, P3, P4, P5 e P6 e três quartzo arenitos (Q1, QA e Q3)(Tabela 3) foram escolhidas para análises de Nd e Sr. As concentrações de Sm e Nd e dos isótopos de Sr e Nd foram quantificadas por TIMS (Thermo - Ionization Mass Spectrometry) obedecendo os procedimentos de Gioia & Pimentel (2000). O processo consiste na separação de 20 a 40 mg de amostra, seguidos de dois estágios de dissolução ácida em chapa aquecedora, para isto utiliza-se HNO_3 e HF na primeira fase e 6N HCl na segunda. Sr e ETR foram separados em colunas de troca catiônica, com auxilio de resina AG50W-X8. O Nd foi isolado dos ETR em resina AG50-X2. Sr, Nd e Sm foram medidos separadamente em filamento de tungstênio com solução de TaF. Nd foi depositado em filamento duplo de rênio com H_3PO_4 (0,1 M) e medido como metal Nd^+. As medidas de $^{143}Nd/^{144}Nd$ são apresentadas em partes por 104 (unidades) de

$^{143}Nd/^{144}Nd$ CHUR como medidas atuais: $\varepsilon Nd(0) = [(^{143}Nd/^{144}Nd)_{amostra}/I_{CHUR(0)} - 1] * 10^4$, de modo que, $^{143}Nd/^{144}Nd_{amostra}$ é a razão atual medida e $I_{CHUR(0)}$ (0,512638) representa a razão $^{143}Nd/^{144}Nd$ no reservatório CHUR no presente (Jacobsen & Wasserburg, 1980). A incerteza analítica é de 0,0004% e 0,05% para $^{143}Nd/^{144}Nd$ e $^{147}Sm/^{144}Nd$, respectivamente.

Para as análises dos isótopos de Pb ($^{206}Pb/^{204}Pb$, $^{207}Pb/^{204}Pb$ e $^{208}Pb/^{204}Pb$), foram selecionadas onze amostras dos perfis P1 e P2 (Tabela 3), dentre crostas manganesíferas, mangano-alumino-ferruginosas e solos, todas analisadas no Centro de Pesquisas Geocronológicas da Universidade de São Paulo (USP), São Paulo, Brasil. Alíquotas de 20-40 mg de amostras foram digeridas a quente com HF/HNO_3 e HCl 6N. O Pb foi purificado com resina aniônica BioRad AG1-X8 condicionada em HBr e, após secar, foi misturada a sílica gel e ácido fosfórico e depositada em filamento de Re e quantificado num espectrômetro de massa com ionização térmica (TIMS) modelo Finnigan MAT 262. Baseado em múltiplas análises de um padrão de Pb (NBS-981), as amostras foram corrigidas para o fracionamento de massa de 0.13% por unidade de massa atômica. Para o desvio padrão (1s) foi utilizado $^{206}Pb/^{204}Pb = 16,898 \pm 0,008$; $^{207}Pb/^{204}Pb = 15,439 \pm 0,010$ e $^{208}Pb/^{204}Pb = 36,535 \pm 0,032$.

6.3 Termocronologia (U-Th)/He

Para a datação por (U-Th)/He foram selecionadas duas amostras, a crosta lateríticas Fe-Al brechóide (C6) e da bauxita pisolítica (B1A). A escolha das amostras foi definida com base no substrato sobre as quais foram desenvolvidas, tendo em vista que a crosta lateríticas Fe-Al brechóide (C6) se formou a partir das rochas sedimentares do Grupo Alto Tapajós, e a bauxita pisolítica (B1A) tem por protólito as rochas sedimentares do Grupo Beneficente.

Após a caracterização mineralógica, pisólitos hematíticos e córtex goethíticos foram separados das crostas lateríticas com auxílio martelo geológico. Os fragmentos de hematita e goethita dos núcleos e cortéx dos pisólitos foram desagregados cautelosamente em almofariz de ágata e peneirados no intervalo de 150 a 212 μm, a fim de eliminar o efeito de ejeção alfa reportado por Farley et al. (1996). Cerca de 40 fragmentos foram selecionados e levados para ultrassom onde foram lavados com água tri destilada e etanol absoluto (1 hora cada), e secos sob lâmpada. Após secos, seis fragmentos homogêneos de hematita e goethita de cada amostra foram escolhidos

minuciosamente em lupa binocular e montados em tubos de Nb, evitando sempre inclusões de argilominerais e outras fases minerais.

^{4}He, ^{238}U e ^{232}Th foram medidos por espectrometria de massa por diluição isotópica (quadrupolo e ICP-MS, respectivamente). ^{147}Sm, um possível produtor de partículas alfa, não foi detectado em amostras piloto e, portanto, não foi incluído na análise de rotina. A extração do ^{4}He foi realizada sob alto vácuo por laser Nd-YAG e analisado em espectrômetro de massa Pfeiffer Prisma QMS-200, no *CSIRO (Commonwealth Scientific and Industrial Research Organisation), John de Laeter Centre for Isotope Research, Perth, Australia.* A temperatura de extração dos óxidos de ferro foi estabelecida em ~500 °C (por 10 min), para evitar perda de U, mudanças mineralógicas e na composição dos isótopos pais (Boschmann, 1986; Wernicke, 1991; Bähr et al., 1994; Vasconcelos et al., 2013). Assim, todas as amostras foram desgaseificadas no primeiro ciclo de aquecimento, não restando gases residuais durante a re-extração. É importante destacar que a baixa temperatura utilizada também serviu de controle para a presença de inclusões como rutilo e zircão, uma vez que esses minerais podem ser desgaseificados acima de 500 °C e sua presença seria identificada como sinal residual de ^{4}He durante a re-extração. A re-extração (Farley, 2002) foi executada para verificar a saída completa de gás das amostras. Os resultados do gás He foram corrigidos para o analítico branco ao aquecer os tubos de Nb vazios seguindo o mesmo procedimento.

A incerteza analítica total (TAU < 6% (1 sigma) foi calculada como uma raiz quadrada da soma dos quadrados das incertezas em He e ponderadas nas medições de U e Th. As idades (U-Th) / He não foram corrigidas para a ejeção alfa (Farley et al., 1996) e para a perda difusiva (Shuster et al., 2004).

6.4 Aerogeofísica

As imagens gamaespectométricas foram obtidas pela Prospectors Aerolevantamentos e Sistemas LTDA como parte de dois projetos aregeofísicos (Aripuanã e Sucunduri) do Serviço Geológico Brasileiro (CPRM, 2010 a e b). Os levantamentos aerogeofísicos recobriram 19000 Km^2 de perfis aeromagnetométricos e aerogamaespectrométricos de alta resolução, com linhas de vôo e de controle espaçadas de 0,5 km e 10 km e orientadas nas direções N-S e E-W, respectivamente. A altura de vôo foi fixada em 100 m sobre o terreno, admitindo-se variações de mais ou menos 15 m.

O processamento dos dados foi desenvolvido no escritório sede da Prospectors Aerolevantamentos e Sistemas Ltda., Rio de Janeiro-RJ e envolveu a aplicação de rotinas do sistema Oasis Montaj versão 6.4.1, utilizado para a compilação das informações coletadas e apresentação dos resultados na forma de mapas nas escalas 1:100.000, 1:250.000 e 1:500.000, arquivos de banco de dados e grids. Os produtos que gerados pela interpolação das imagens dos canais eU, eTh e K e das razões eU/K e eTh/K e, permitiram a geração de composições ternárias de K, eTh e eU (RGB) e de Th/K, SRTM and eU/K (RGB). Para estes procedimentos foram usados os *software* ArcGIS 10.2 e Geosoft *8.3* para processar as imagens geofísicas e as composições ternarias dos canais e das razões. Os dados estatísticos serão realizados com o auxílio do software Statistica 9.

6.5 Elaboração de mapas e perfis topográficos

Mapas geológicos, de localização e topográficos foram elaborados pelo *software* Arcgis 10.1 com o auxílio de imagens SRTM (*Shuttle Radar Topography Mission*) com resolução espacial de 30 m, realizada em fevereiro de 2000. A base de dados litoestratigráfica utilizada foi a de CPRM (2006, 2013, 2014 e 2015) referente às folhas Sumáuma (SB.20-Z-D), Mutum (SB.20-Z-B), Rio Acari (SB.21-Y-C) e Vila Porto Franco (SB.21-Y-A).

7 CONTEXTO GEOLÓGICO E GEOMORFOLÓGICO LOCAL

A área de estudo está localizada na região sudoeste da Amazônia, Brasil, entre 7º45’S e 6°45’S e 61° e 59°30’ W (Figura 4 e 5). O clima é quente e úmido, e um pouco mais seco de maio a setembro. A temperatura anual média varia de 25 a 27° C, a umidade relativa é de aproximadamente 85% e a precipitação anual é de 2336 mm/ano. Está inserida nos domínios tectonoestratigráficos Juruena (1,85-1,75 Ga) e Roosevelt-Aripuanã (1,76-1,74 Ga) da Província Rondônia-Juruena (Santos et al. 2003; Santos et al. 2006) no contato do embasamento Paleoproterozoico e a Bacia Alto Tapajós de idade siluro-devoniana (Reis, 2006; Reis et. al 2013) (Figura 4).

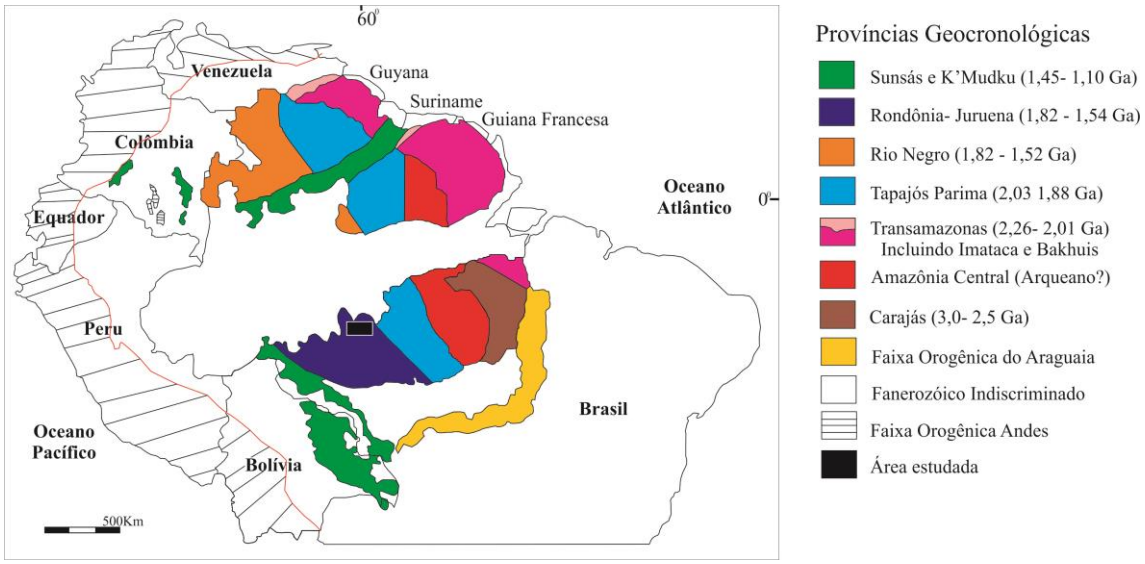

Figura 4: Região estudada enquadrada no Escudo Brasileiro, Província Rondônia-Juruena, Domínio Roosevelt-Juruena do cráton Amazonas (Santos et al. 2006).

Afloram rochas vulcânicas do Grupo Colíder e vulcano-sedimentares e sedimentares do Supergrupo Sumaúma e do Grupo Alto Tapajós respectivamente (Figura 5). As rochas do Grupo Colíder (idade U-Pb 1,787-1,805 Ga) ocorrem a sul e na porção noroeste da área estudada, são dominantemente vulcânicas (riolitos, dacitos e riodacitos predominantemente), com alguns corpos subvulcânicos associados (Lacerda Filho et al. 2001; CPRM, 2014 e 2015) (Figura 5). Intrusivos ao embasamento vulcânico ocorrem batólitos graníticos referentes às suítes intrusivas Teodósia e Igarapés das Lontras. A suíte intrusiva Teodósio (1,758-1,757 Ga) é subdividida nas fácies graníticas, granodiorítica-tonalítica e quartzo-diorítica com assinatura peraluminosa a metaluminosa com trend cálcio alcalino de alto K, afetadas localmente por cisalhamento dúctil (Reis et al. 2013; CPRM, 2014 e 2015, Figura 5). A suíte intrusiva Igarapé das Lontras (1,754 Ga) reúne monzo a sienogranitos com subordinados álcali-feldspato granitos, quartzo monzonitos e quartzo sienitos. Há ainda, corpos subvulcânicas e ignimbritos associados a caldeiras e raros cataclasitos, milonitos e filonitos (Reis et al. 2013; CPRM, 2015). Intrusivos a estas suítes graníticas ocorre a suíte intrusiva Serra da Providência (1,57-1,53 Ga). Nesta, predominam monzogranitos equigranulares a porfiríticos com textura rapakivi, subordinados siengranitos e raros alcáli-feldspatos granitos. Há ainda, granitóides a piroxênio deformado e gabronoritos associados (Scandolara 2013; CRPM, 2014 e 2015, Figura 5).

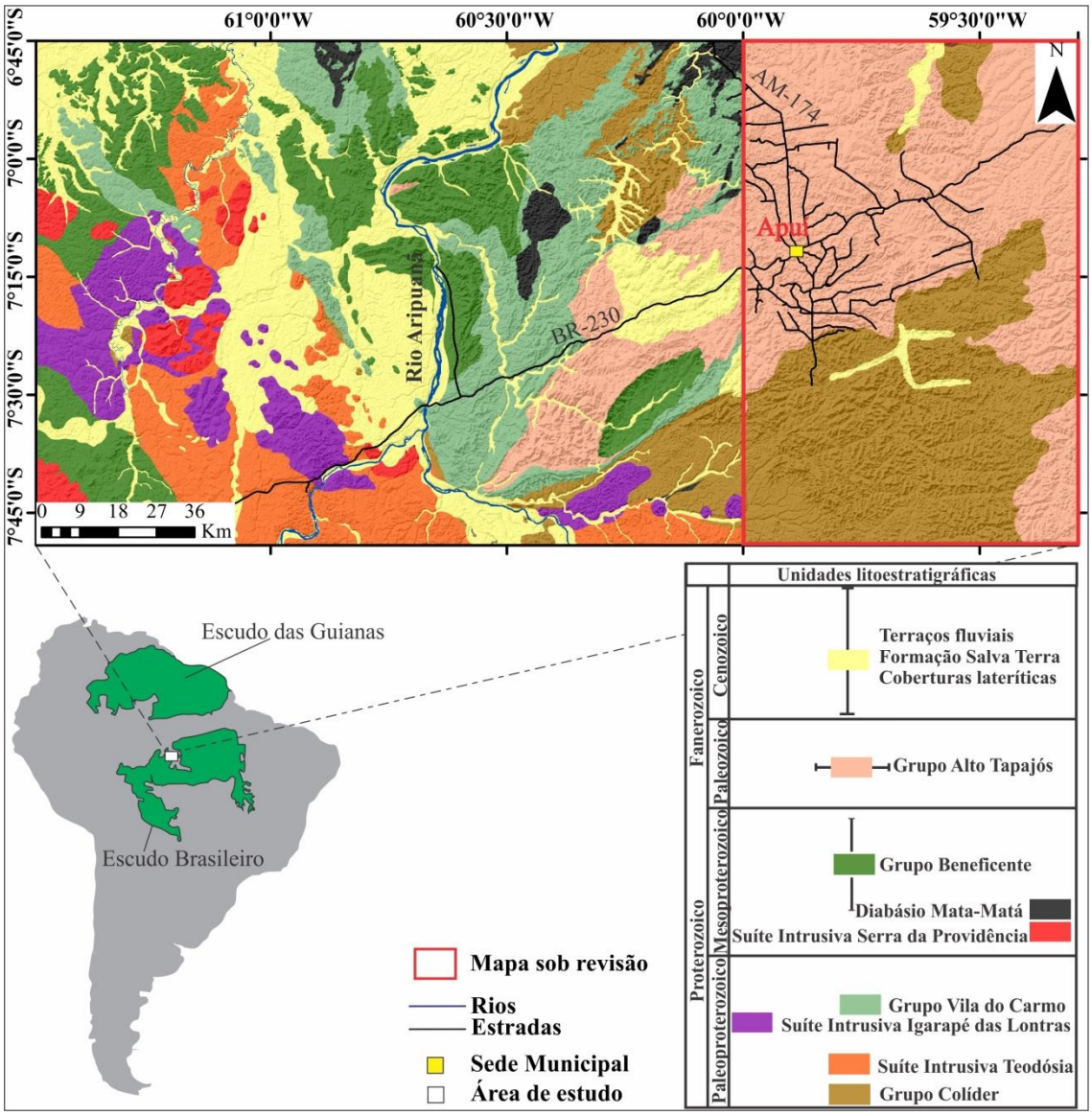

Figura 5: Mapa geológico da região estudada (CPRM 2014; 2015). Retângulo vermelho está relacionado ao mapeamento em andamento da região sudeste do Amazonas

A estruturação em grábens do Grupo Colíder e das suítes intrusivas Teodósia e Igarapé das Lontras serviu de fonte e receptáculo estrutural para a deposição das sequências vulcano-sedimentares e sedimentares proterozoicas e paleozoicas, respectivamente. O mapeamento da região está em andamento pela CPRM (Serviço Geológico do Brasil) e não há ainda integração dos resultados entre os mapas o que impede a apresentação de um mapa detalhado. Os dados disponíveis indicam que o Supergrupo Sumaúma é constituído pelos Grupos Vila do Carmo e Beneficente (Figura 5).

O Grupo Vila do Carmo, fase rifte da Bacia do Sumaúma, reúne unidades vulcanoclásticas, piroclásticas e clásticas que ocorrem sob a forma de ritmitos e quartzo arenitos (Reis et al. 2013). Reis et al. (2013) estabeleceram idade máxima entre 1,76 e

1,74 Ga ao Grupo Vila do Carmo por meio do estudo de zircão detrítico, enquanto que CPRM (2014- Folha Mutum) subdividiu a unidade nas formações Camaiú e Naldinho. A Formação Camaiú atrelada às fácies marinha rasa a deltaica distal, é constituída por ritmitos formados por rochas vulcanoclásticas, clásticas e piroclásticas inter-relacionadas. Por outro lado, a Formação Naldinho engloba arenitos róseos a esbranquiçados, médios a grossos, tabulares, com estratificações cruzadas festonadas e lobos sigmoidais, sobrejacentes em discordância angular aos ritmitos da Formação Camaiú. Soleiras e diques de olivina diabásio (Mata-Matá) e corpos de gabro com 1,57 Ga de idade, intersectam o Grupo Vila do Carmo (Betiollo et al. 2009).

O Grupo Beneficente (1,43- 1,08 Ga- pós rifte) que sobrepõe o Grupo Vila do Carmo, é constituído da base para o topo pelas formações Manicoré, Cotovelo e Prainha/Tuiuié. A Formação Manicoré foi depositada em ambiente de leques e planícies aluviais e é representada por ortoconglomerados a quartzo arenitos maciços com argilitos subordinados. A Formação Cotovelo foi depositada em ambiente de planície de maré e canais fluviais e reúne quartzo arenitos silicificados, arroxeados a róseos. As formações Prainha e Tuiuié são indivisas e compostas por arenitos sublíticos e quartzo arenitos intercalados por siltitos e argilitos, depositados em ambiente de dunas eólicas e de *washover* (Reis et al. 2013; CPRM, 2014).

A bacia do Alto Tapajós é constituída pelo Grupo Alto Tapajós (Siluriano) depositado em não conformidade sobre as rochas do Grupo Colíder e Vila do Carmo, após a incisão do gráben do Cachimbo/Alto Tapajós. Compreendem arenitos finos a médios com lentes conglomeráticas e siltitos laminados com intercalações de arenitos finos, depositados em ambiente litorâneo e lagunar enquadrados nas formações Rio das Pombas e Juma, respectivamente (CPRM, 2013; Reis et al. 2013).

Os depósitos neógenos da área são representados pela Formação Salva Terra (conglomerados, arenitos conglomeráticos, argilitos mosqueados) no alto rio Acari. Sobre as vulcânicas do Grupo Colíder, há coberturas lateríticas e colúvios formados por fragmentos de crostas lateríticas a sul do estudo e próximo à cidade de Apuí (CPRM, 2006; Reis et al. 2013). Também há crostas e colúvios manganesíferos no rio Aripuanã, ao longo da BR-230 e ao sul de Apuí (Silva et al. 2012). Os depósitos Quaternários são representados por aluviões desenvolvidos ao longo das drenagens comportando areia, cascalho, silte e argila (CPRM, 2006).

Essas unidades estabelecem dois compartimentos geomorfológicos: à direita do rio Aripuanã é classificado como Platôs Dissecados do Sul da Amazônia e à esquerda

do rio Aripuanã, as Superfícies Aplainadas da Amazônia (Figura 6A; Dantas & Maia 2010). Os pontos amostrados e a campanha de campo centraram-se na superfície denominada Platôs Dissecados do Sul da Amazônia. Estes são marcados por platôs, serras, colinas e planícies com forte dissecação pela incisão da rede de drenagem subdendrítica a dendrítica com padrões retangulares, associadas aos grandes rios, como Aripuanã, Acari e Sucunduri. Os platôs e serras, alongados na direção NE-SW e NW-SE alcançam de 186 a 290 m de altitude, têm 4 a 21 km de extensão por 2 a 10 km de largura, enquanto as colinas têm topo côncavo, 134 e 186 m de altitude, atingem até 1km de extensão e, por vezes, estão alongadas nas mesmas direções dos platôs (Figura 6B, 7A e 7B). Tanto os platôs como as colinas são sustentadas por bauxitas e crostas ferruginosas e ferro-aluminosas (Figura7). Vales em "U", encostas íngremes e colinas do entorno de Apuí têm altitude entre 0 e 134 m, e é onde predominam rochas sedimentares, vulcânicas e raras crostas manganesíferas (Figura 7D). Há também perfis truncados pela neotectônica, que expõem linhas de pedra e horizontes mosqueados nos vales (Figura 8A, B e C)

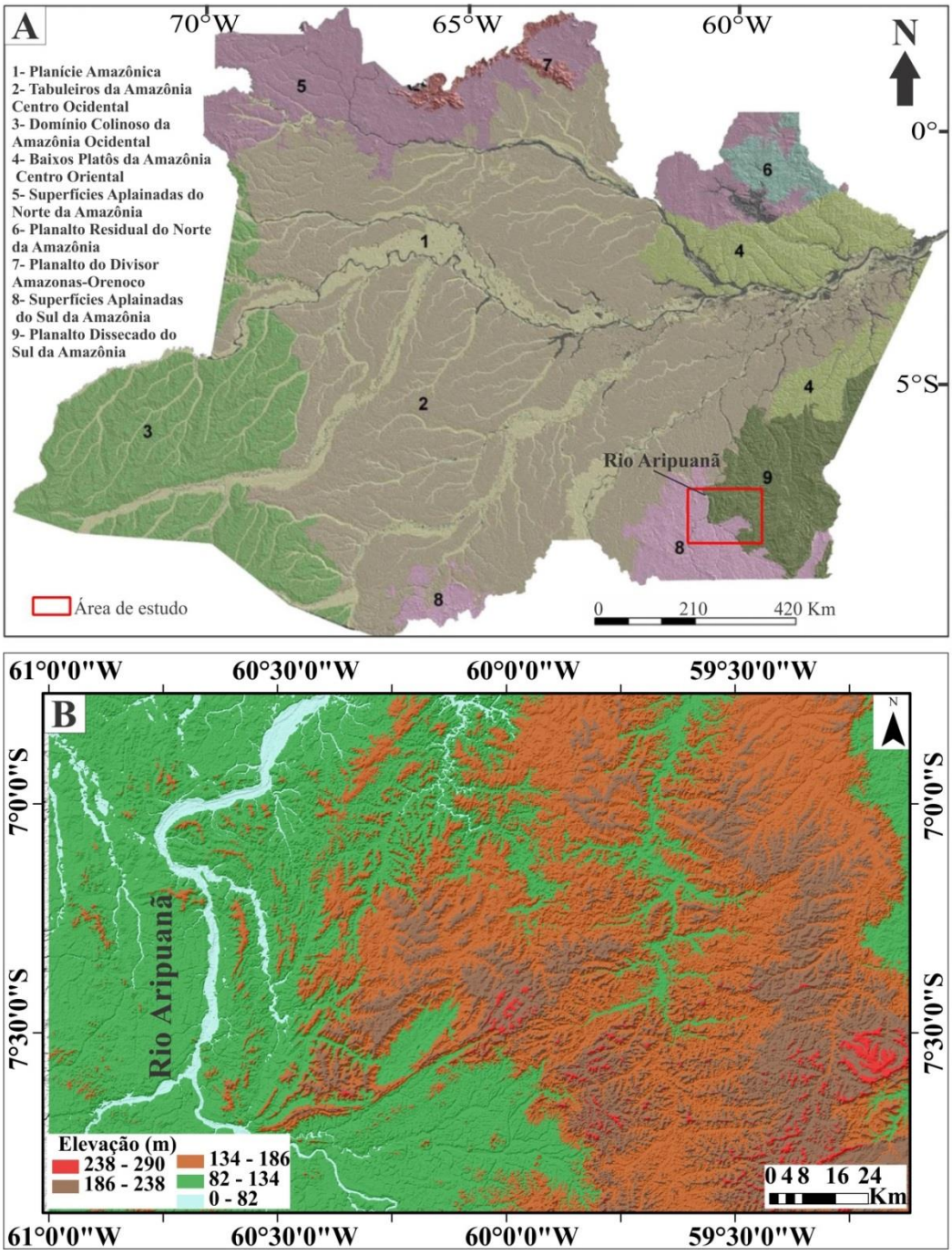

Figura 6: A- Principais domínios geomorfológicos do estado do Amazonas. B- Mapa altimétrico da região sudeste do Amazonas (Dantas & Maia, 2010).

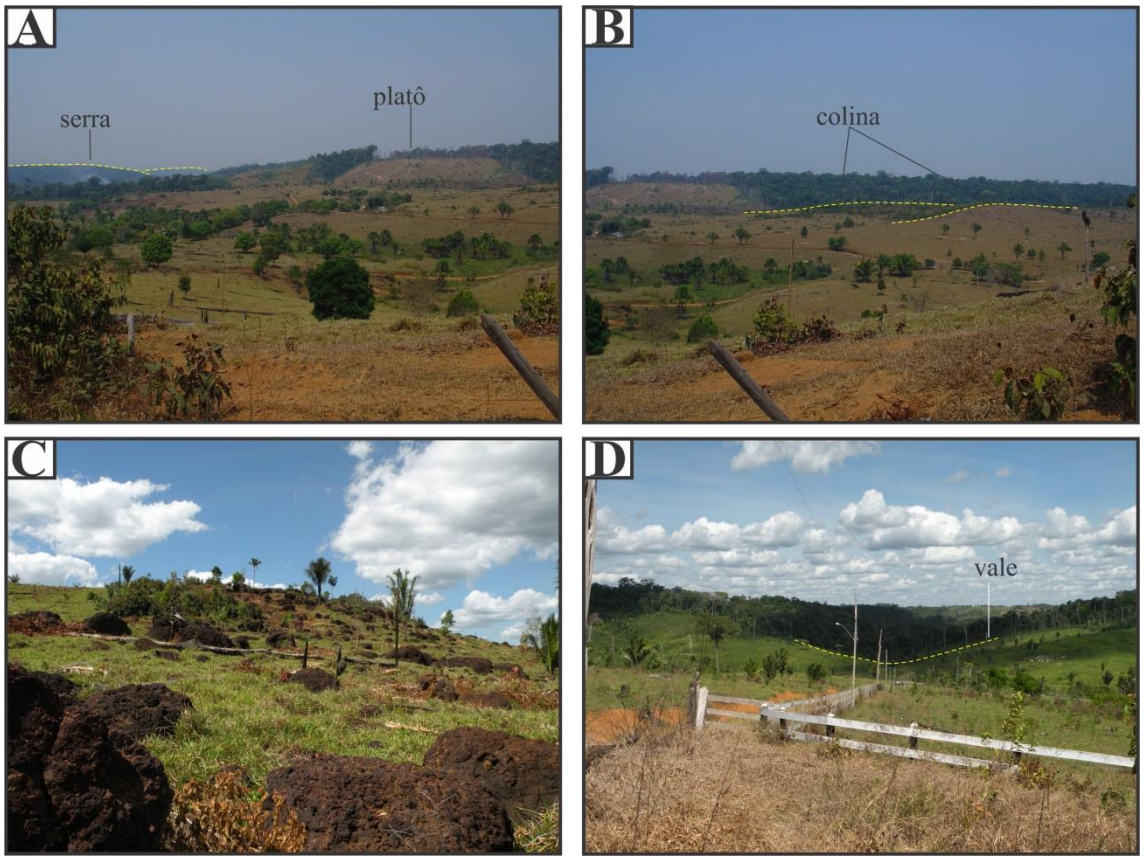

Figura 7: Tipos de relevo da região estudada. A- serras alongadas e platôs; B- colinas com topo suave e arredondado; C- crostas lateríticas que sustentam o relevo colinoso e D- vales em formato de U.

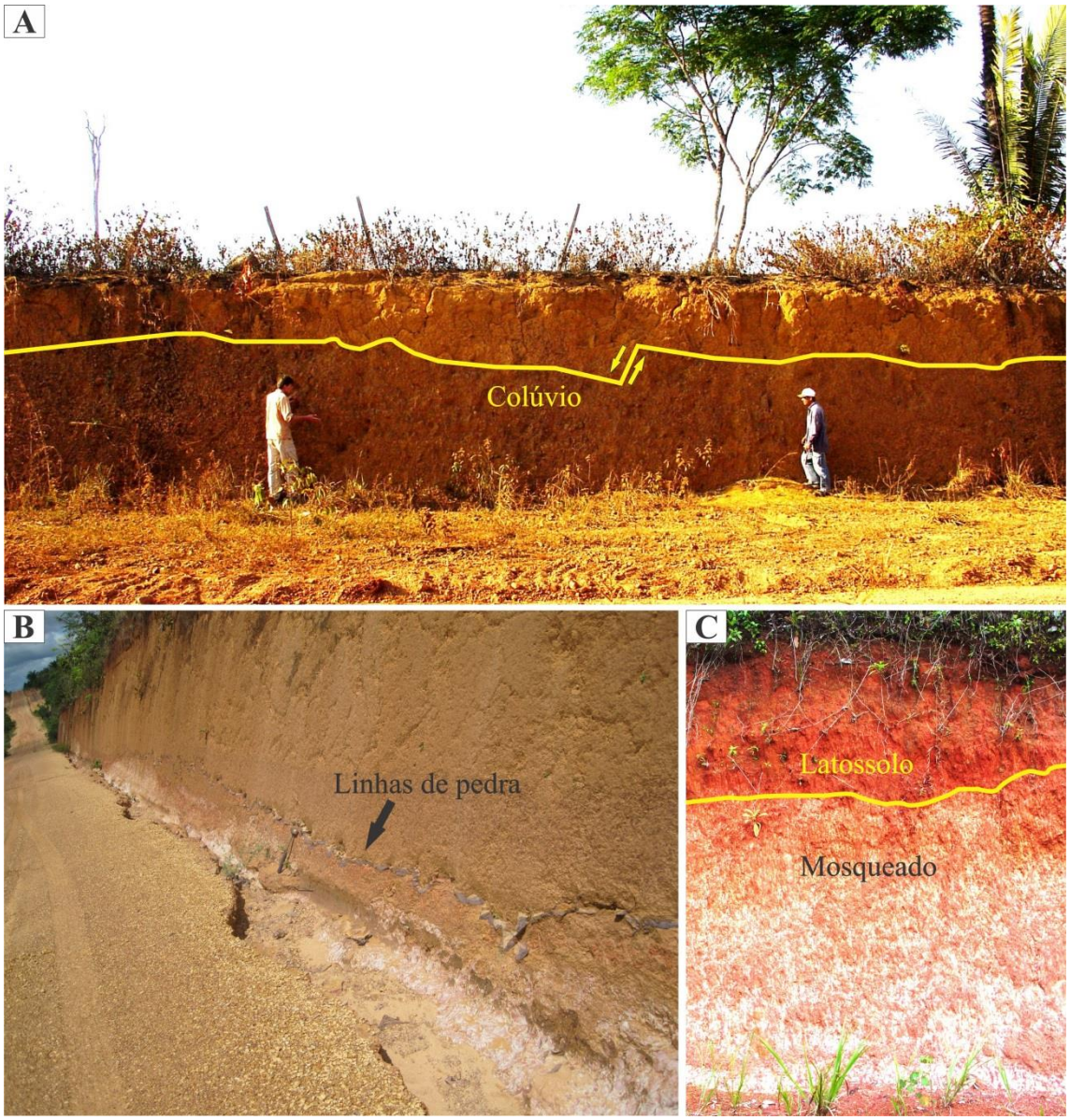

Figura 8: A- Colúvios falhados pela neotectônica (Silva, 2009). B e C- Exposição de linhas de pedra e horizonte mosqueado

CAPÍTULO IV: ARTIGO 1- GENESIS OF MANGANESE DEPOSITS IN SOUTHWESTERN AMAZONIA: MINERALOGY, GEOCHEMISTRY AND PALEOENVIROMENT

O primeiro artigo foi publicado em 2017 no periódico Ore Geology Reviews, n°89, páginas 270 a 289. Este artigo reúne dados mineralógicos, geoquímicos e de química mineral de cinco perfis lateríticos desenvolvidos sobre os Grupos Vila do Carmo e Beneficente, sudoeste do Cráton Amazonas.

Ore Geology Reviews 89 (2017) 270–289

Contents lists available at ScienceDirect

Ore Geology Reviews

journal homepage: www.elsevier.com/locate/oregeo

Genesis of manganese deposits in southwestern Amazonia: Mineralogy, geochemistry and paleoenvironment

Márcio Fernando dos Santos Albuquerque [a,*], Adriana Maria Coimbra Horbe [b], Nilson Francisquini Botelho [b]

[a] Graduate Program in Geology, Brasilia University, Geoscience Institute, Darcy Riberio University Campus, 70910-900 Brasília, Federal District, Brazil
[b] Brasilia University, Geoscience Institute, Darcy Riberio University Campus, 70910-900 Brasília, Federal District, Brazil

ARTICLE INFO

Article history:
Received 29 September 2016
Received in revised form 5 June 2017
Accepted 9 June 2017
Available online 16 June 2017

Keywords:
Coronadite
Pb-hollandite
Romanechite
Hydrothermal
Lateritic duricrust

ABSTRACT

Chemical analysis, XRD, SEM and EMPA were carried out on five manganese deposits in southwestern Amazonia, Brazil to determine their sources of Mn, their lithostratigraphic units, the environment in which Mn accumulated during the Proterozoic and the effects of weathering (since the Late Cretaceous) on the mineralization process. The sedimentary, hydrothermal and lateritic environments in this area produced a wide and complex variety of structures, textures, minerals and geochemical features, where coronadite, hollandite and romanechite, as the main Mn-minerals, changed their chemical compositions during the lateritization process. In this context, during lateritization, more mobile elements (MgO, CaO, Na_2O and K_2O) were removed, while concentrations of SiO_2, Al_2O_3, Fe_2O_3, MnO, Pb and Co increased. The high concentrations of Cu, Pb, and Tl and the presence of positive Gd anomalies, galena, and nuggets of Ag and $(Zn/Ni)/MnO_2$ in both the protoliths and duricrusts indicate that the Zé Julião, Apuí and Novo Natal deposits record the influences of sulfide and hydrothermal activity. The REE/(Zr/Hf) vs $TiO_2 \times 1000/(Co/Ni)$ ratios indicate that felsic and mafic rocks were the sources of Mn in these samples.

1. Introduction

The mineralogical and geochemical parameters of manganese minerals are useful for paleoenvironmental reconstructions of the evolution of the atmosphere, the chemical compositions of ancient oceans and the pH and Eh variations of depositional environments. Additionally, they may have implications for their geochemical environment, due to the ability of manganese to adsorb elements such as Ba, Pb, Co, Cu, Ni, Ag and Zn (Frakes and Bolton, 1992; Nicholson, 1992; Roy, 1992, 2006; Conly et al., 2011; Del Rio-Salas et al., 2013).

Mn-enriched zones are derived from sedimentary, metasedimentary and hydrothermal rocks and their weathered equivalents; they range in thickness from a few meters to over 50 m and laterally extend from a few meters to over 50 km (Force et al., 1999).

Mn that is hosted in sandstones, greywackes, shales and conglomerates and is associated with BIFs tends to form large to giant deposits (with average values of 51 Mt and 31% MnO) (Roy, 2006; Maynard, 2010). When Mn sedimentary sequences are metamorphosed, their primary minerals are converted into Mn silicates or Mn carbonates (e.g., rhodonite, spessartite, Mn calcite, tephroite) and they can form small or large deposits (<1 Mt to 43 Mt) (Roy and Purkait, 1968; Rodrigues et al., 1986; Nicholson et al., 1997; Chisonga et al., 2012). On the other hand, Mn deposits that are associated with hydrothermal environments are rather small (< 4 Mt), because they are mostly restricted to epithermal zones and occur as veins, breccias and irregular orebodies (O'Really, 1992; Glasby et al., 2001; Liakopoulos et al., 2001; Leal et al., 2008; Conly et al., 2011). The latter type of Mn deposit, which occurs in the ocean floor and within ophiolite complexes, has a particular geochemical composition and can be used to understand the behavior of Mn in plate boundary zones. The circulation of warm water through fractures removes Mn, Fe, Pb, Zn, Cu, Co and Ni from volcanic rocks, thus forming deposits with large varieties of Mn minerals (Roy, 1992, 1997; Maynard, 2014).

All of these types of Mn environments, when subjected to weathering, generate supergene Mn ores with mineralogies and geochemical compositions that are associated with the type of Mn-bedrock that was weathered (Nicholson, 1992). Generally, Mn orebodies are mined from Mn-rocks or Mn-lateritic duricrusts (Rodrigues et al., 1986; Pracejus, 1989; Pracejus and Bolton, 1992; Chisonga et al., 2012). When supergene Mn develops from a sulfide mineralization sequence, it is classified as dubhite (Nicholson,

* Corresponding author.
E-mail address: mgeoroots@gmail.com (M.F.S. Albuquerque).

http://dx.doi.org/10.1016/j.oregeorev.2017.06.012
0169-1368/

1992) and can be used as a tool for sulfide surveys, due to the formation of Mn-minerals that are enriched in trace elements, such as coronadite, hetaerolite, chalcophanite, crednerite and Pb-hollandite.

In southwestern Amazonia, Brazil, there are 261,300 ha that require examination in Mn studies, where Mn is associated with the sedimentary rocks and lateritic duricrusts of the Sumaúma Supergroup (Liberatore et al., 1972; Gonçalves and Serfaty, 1976; Fig. 1). Among them, only 179 ha have been investigated by BBM Amazonas Ltd. (using trenches, wells and galleries) in seven potential Mn-rich areas that contain 3.52 Mt of Mn (Cotovelo, Beneficente, Rosinha, Fazenda Floresta, Novo Natal, Pretinho and Zé Julião; Fig. 1). This paper describes the features of these Mn deposits and their occurrences related to sedimentary, hydrothermal and supergenic environments, which may represent the 7.8% of Mn deposits (Maynard, 2010) that have unusual mineralogies (i.e., romanechite, hollandite and coronadite) and geochemical compositions compared to the largest Mn deposits (e.g., Rodrigues et al., 1986; Okita, 1992; Pracejus and Bolton, 1992; Cornell and Schutte, 1995; Gutzmer and Beukes, 1996; Costa et al., 2005). In this study, these data facilitated the recognition of the Mn source and its mineral and chemical transformations due to the influence of lateritization. This study also discussed the genesis of Mn ore, which helped improve the geological

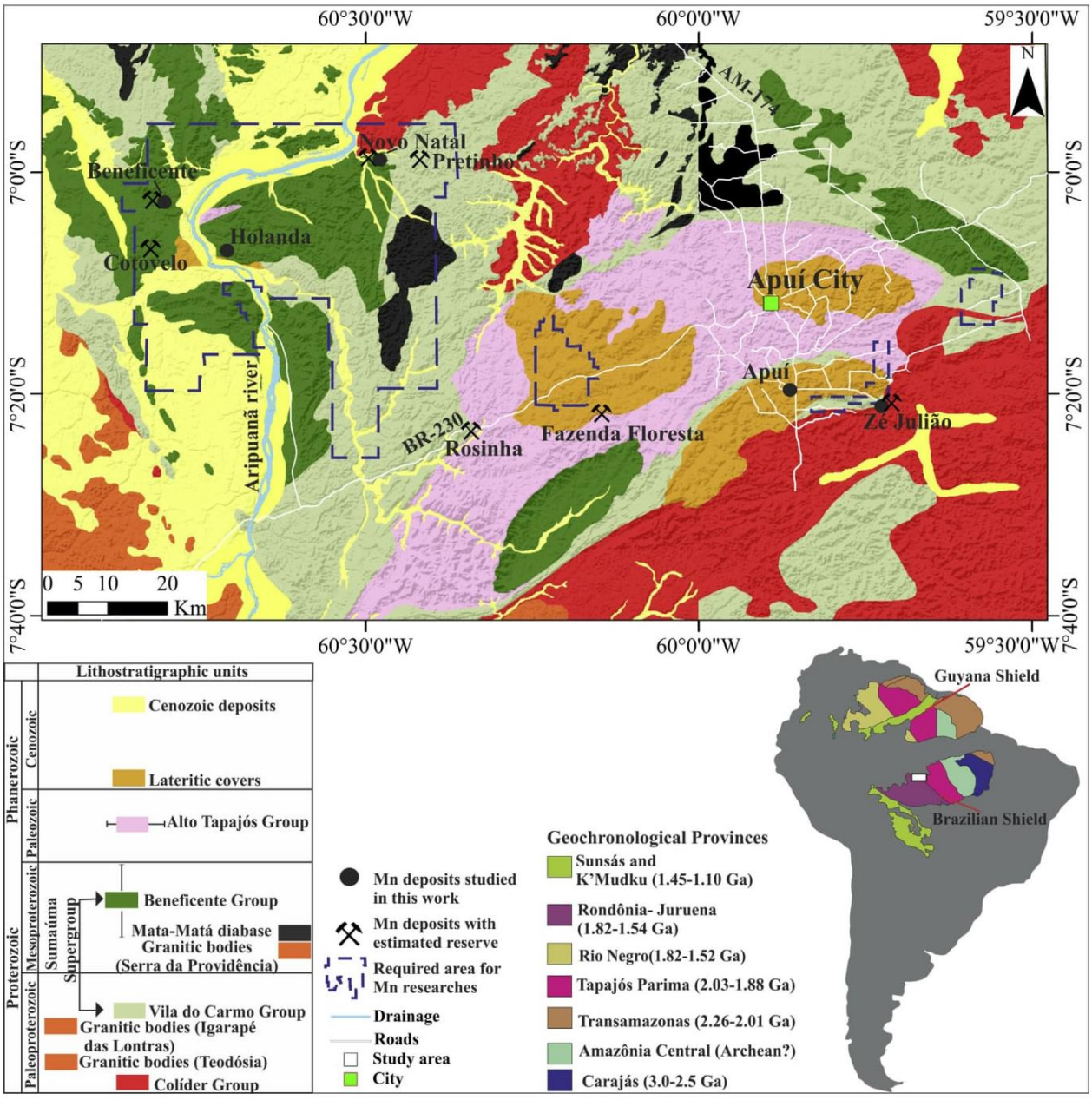

Fig. 1. Localization of study area and geological setting. Geological map carried out for CPRM (2013) (Geological Service of Brazil), still under revision (red square).

knowledge of Proterozoic rocks in Amazonia and highlight the potential of VMS mineralization in this region. Moreover, this paper proposed a new method of genetic classification and a new method to estimate the amount of Mn-minerals present using geochemical and XRD data.

2. Environmental and geological setting

The study area is located in the southwestern region of Amazonia, Brazil, between 6–13°S and 59–62°W (Fig. 1). The climate is hot and humid and is slightly drier from May to September. The mean annual temperature ranges from 25 to 27 °C, the relative humidity is approximately 85%, and the yearly rainfall is 2336 mm $year^{-1}$.

This region, which is located in the Rondonia Juruena Province (Santos et al., 2006; Fig. 1), contains a volcanic basement that is related to the Colider Group (1.78–1.80 Ga). Intruding the volcanic basement are the granitic bodies of the Teodosia (1.758–1.757 Ga) and Igarapé das Lontras (1.754 Ga) suites, all of which are intersected by the monzogranitic batholiths of the Serra da Providência suite (1.57–1.53 Ga, Santos, 2003; CPRM, 2014). Two main basins have developed over the volcanic basement and granitic bodies (Reis et al., 2013; CPRM, 2014): the first was infilled by the rocks of the Sumaúma Supergroup, which comprise a Proterozoic volcano-sedimentary sequence, while the second was infilled by the rocks of the Alto Tapajós Group, which represent a Paleozoic sedimentary sequence (Fig. 1).

According to Reis et al. (2013), the Sumaúma Supergroup is divided in the Vila do Carmo Group and the Beneficente Group. The Vila do Carmo Group (1.76–1.74 Ga) comprises the rift phase of the Sumaúma Supergroup and contains volcanoclastic, pyroclastic and clastic units and quartz-sandstones cut by the Mata-Matá diabase (1.576 Ga) (Betiollo et al., 2009; Reis et al., 2013). The post-rift phase is related to the Beneficente Group (1.43–1.08 Ga), which overlaps the Vila do Carmo Group. The Beneficente Group contains orthoconglomerates and massive quartz-sandstones with rare mudstones deposited in alluvial fans and floodplains; pinkish to purplish silicified quartz-sandstones that were deposited in tidal plains and river channels; and sublitharenites and quartz-sandstones intercalated with siltstones and mudstones that were deposited in aeolian and washover environments (CPRM, 2013; Reis et al., 2013). The Paleozoic basin (i.e., the Alto Tapajós Group) and Cenozoic deposits partially cover the older units.

Weathering has developed iron and aluminous lateritic duricrusts that sustain a strongly dissected landscape formed by plateaus and hills. On the edges of the low dissected plateaus (up to 134 m high) are where the Apuí and Zé Julião Mn deposits crop out (Fig. 2A, B); in the valleys and small hills (20–134 m high) are where the Holanda, Beneficente and Novo Natal Mn deposits crop out (Fig. 2A, B). The analysis of the drainage patterns and relief revealed that all of these Mn deposits are located along NW-SE- and NE-SW-trending structures (Fig. 2A).

3. Materials and methods

In this study, 14 samples collected from five Mn ore deposits were analyzed. Additionally, 21 other samples previously described by Silva et al. (2012) were reevaluated, and new mineralogical and geochemical data for these samples were provided. These deposits were described based on the occurrence, textures, structures and compositions of their minerals. The samples were dried at room temperature, pulverized and submitted to mineral identification using X-ray powder diffraction (Shimadzu XRD – 6000) equipped with a copper tube, as well as scanning electron microscopy (SEM, Quanta 250 FEI) following Au-Pd metallization. The electron microprobe analysis (EMPA, JEOL JXA8230) of polished thin sections provided chemical microanalysis (of SiO_2, Al_2O_3, Fe_2O_3, MgO, CaO, Na_2O, K_2O, MnO_2, P_2O_5, CuO, CoO, BaO, PbO and V_2O_5) after carbon metallization. The OH content represents the result of 100% subtracted by the bulk sum of the elements analyzed.

The bulk-rock geochemical analysis was done at Acmelab, Vancouver, Canada. The concentrations of major and minor elements (SiO_2, Al_2O_3, Fe_2O_3, MgO, CaO, Na_2O, K_2O, TiO_2, P_2O_5 and MnO) were determined using ICP-ES after lithium borate fusion. For the quantification of trace elements (Ag, As, Au, Ba, Bi, Be, Cd, Co, Cr, Cs, Cu, Ga, Hf, Hg, Mo, Nb, Ni, Pb, Rb, Sb, Sc, Se, Sn, Sr, Ta, Tl, Th, U, V, W, Y, Zn, Zr and REE), 0.25 g of each sample was heated in HNO_3, $HClO_4$, and HF until fuming and then taken to dryness. The residue was dissolved in HCl and loaded onto an ICP-MS. The loss of ignition (LOI) was analyzed by gravimetry (heated to 1000 °C).

The quantification of minerals involved stoichiometric calculations (Appendix). The mineral quantification associated with statistical analysis allowed us to relate the mineral assemblage to the trace elements. For statistical analysis, the STATISTICA 9.0 software and principal component analysis method (PCA) were used. Elements that were below detection limit in most samples (i.e., MgO and Na_2O) or that had very homogeneous contents (i.e., K_2O, Ag and V) were not used in this statistical analysis. Geology and relief maps were constructed using ArcGis 10 and Global Mapper 13.

4. Results

4.1. Novo Natal deposit

4.1.1. Pinkish siltstone and Mn-greywackes

At Novo Natal, pinkish siltstones and Mn-greywackes crop out (when Mn-greywackes and pinkish siltstone are discussed together, they are referred to as Mn-rocks). These are interbedded with acid tuffs and sometimes contain multiple quartz geodes that are up to 2 cm in diameter. The pinkish siltstone (sample PS) has a quartz framework (78% of the bulk rock) and displays a brecciated texture associated with a series of NW-SE- and NE-SW-trending fractures (Figs. 3 and 4A). The Mn-minerals that fill fractures and make up 20% of the bulk rock are coronadite (12%), hollandite (6%) and cryptomelane (approximately 2%) (Fig. 7A, Table 1). The quartz framework also contains 2% hematite and goethite (Table 1). Overlapping the pinkish siltstone is a tabular grayish Mn-greywacke (sample A3) that is fine- to medium-grained, contains well-sorted and rounded quartz grains (48%), and is supported by a matrix of romanechite (26%), hollandite (23%) and cryptomelane (1%) that is intersected by millimeter-scale veins of coronadite (1%) (Figs. 3 and 4B, Table 1). Hematite and goethite (~2%; Table 1) fill cavities and pores, while scarce nuggets of Ag (~15 μm) are widespread throughout the matrix (Fig. 8A).

4.1.2. Mn duricrusts

From the pinkish siltstones and Mn-greywackes developed a Mn lateritic duricrust that is up to 3.3 m thick. Laterally, there are some phosphatic portions of the solid solution of crandallite and goyazite (sample Pd) that preserve stratification (Figs. 4C and 7B). The duricrust is massive (sample M1), protopisolitic (samples Pp1 and Pp2) and pisolitic (samples Pi1 and Pi2) (Fig. 3). The massive duricrust has a powdery and friable framework featuring cryptomelane (34%), hollandite (25%) and pyrolusite (24%) intergrown with gibbsite (14%) (Figs. 4D and 7C, Table 1). Fractures and cracks are filled by pinkish and hard

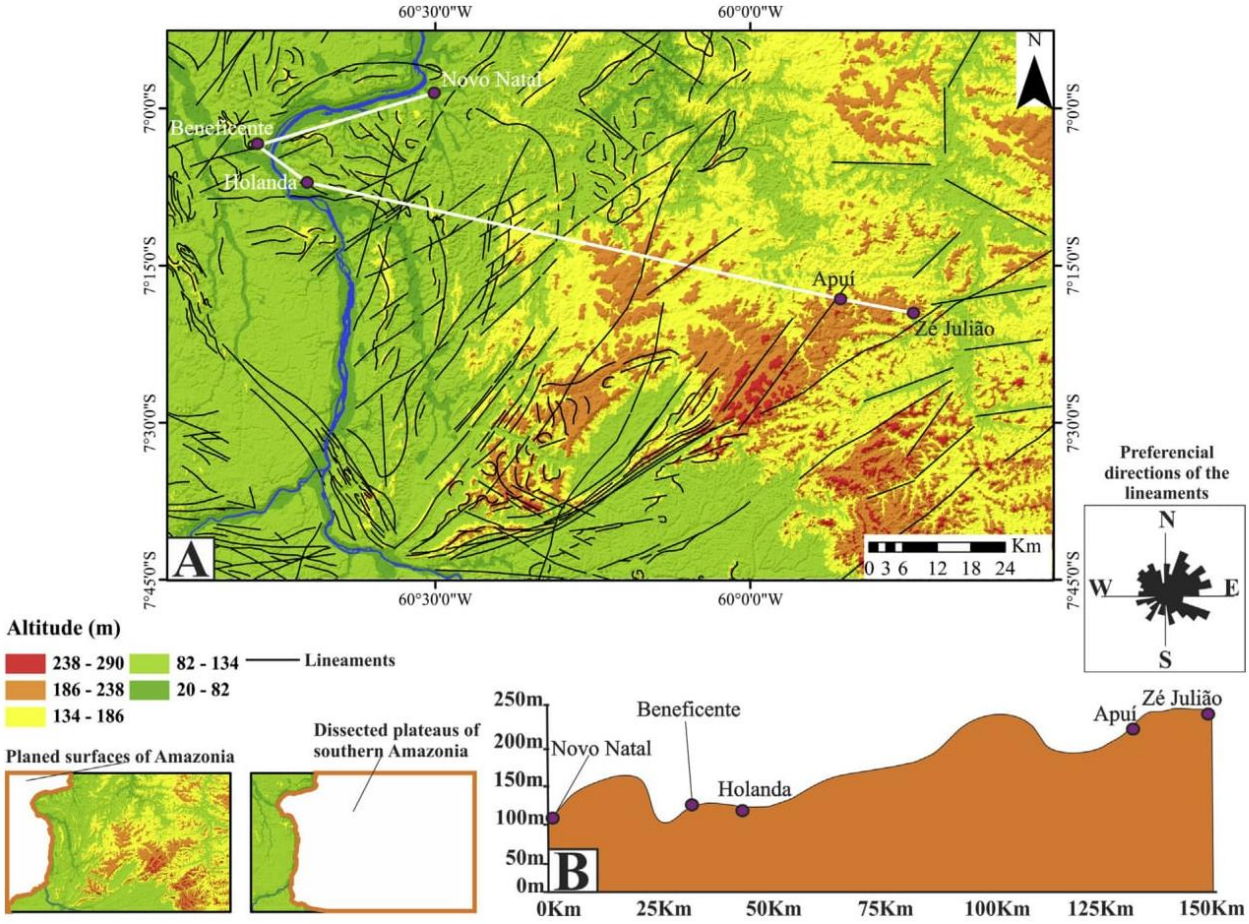

Fig. 2. (A) Planialtimetric map and main tectonic structures. (B) Planialtimetric profile between Novo Natal and Zé Julião deposits.

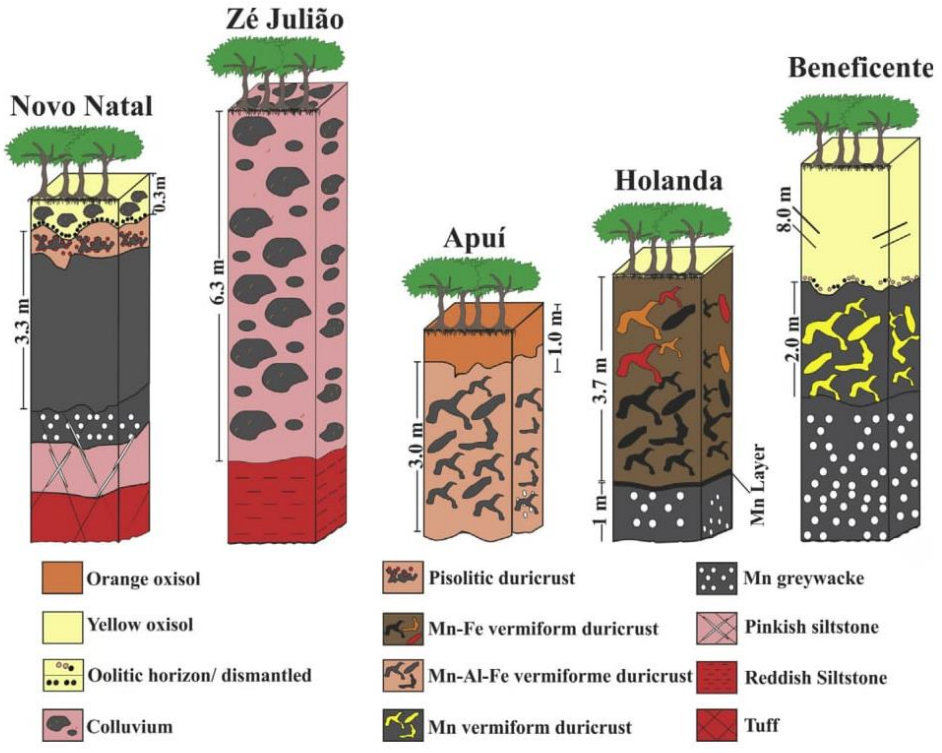

Fig. 3. Schematic profiles of the five studied Mn deposits.

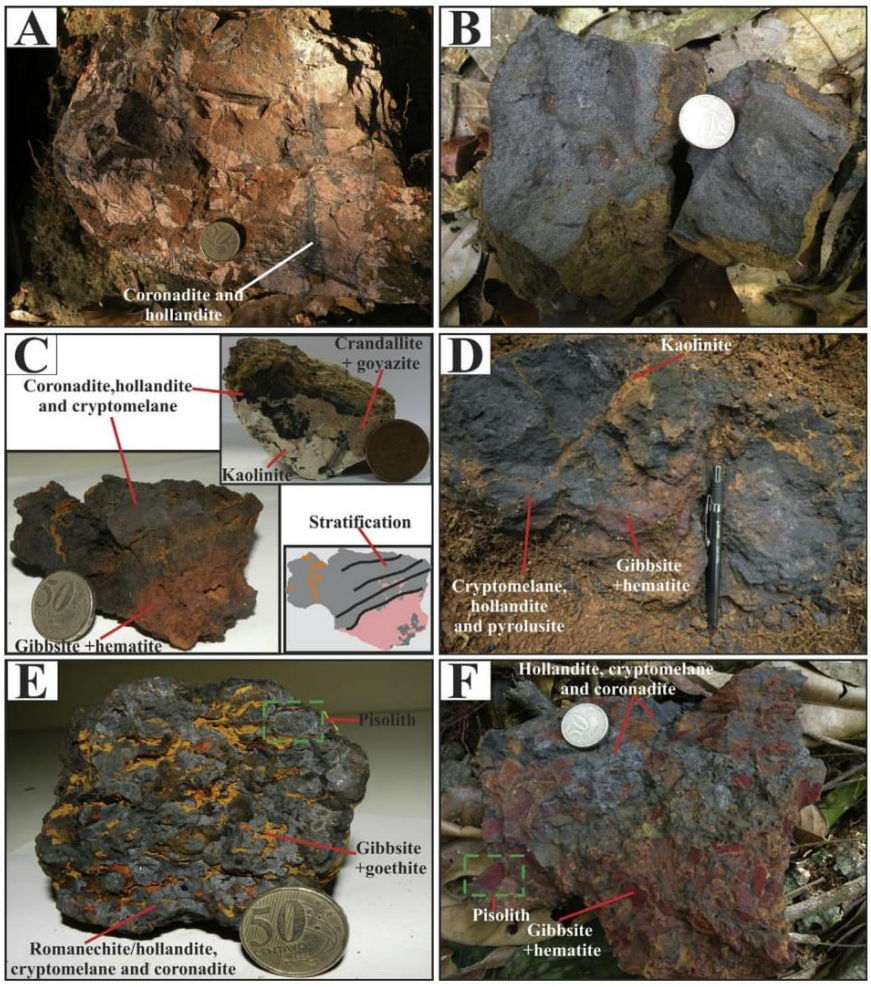

Fig. 4. Macroscopic features of the Novo Natal deposit. (A) Pinkish siltstone (PS) with manganese filling fractures. (B) Tabular Mn-greywacke (A3). (C) Remnant stratification in Mn-duricrusts and phosphorous manganese duricrust of crandallite, goyazite, hollandite, cryptomelane and coronadite. (D) Massive duricrust (M1) with framework composed by cryptomelane, hollandite and pyrolusite and fractures filled by gibbsite, goethite and hematite. (E) Protopisolitic duricrust (Pp1 and Pp2) with romanechite and pyrolusite and cavities filled by goethite and hematite. (F) Pisolitic duricrust (Pi1) showing gibbsitic and hematitic pisoliths enveloped by hollandite, coronadite and cryptomelane plasma.

gibbsite, goethite and hematite. The protopisolitic duricrust is bluish-grey, hard and has submetallic brightness (Fig. 4E). The framework (comprising 60 to 80% of these duricrusts) is composed of cryptomelane (6–14%) and coronadite (1–2%) (Table 1); however, in sample Pp1, the main mineral is hollandite (93%), whereas the main mineral in Pp2 is romanechite (76%) (Fig. 7D, Table 1). The few pisoliths (<1.5 cm in diameter) have tinny cores and frosted cortexes composed of the same minerals as the framework. The cavities (comprising 20–40% of the duricrust) are filled with gibbsite, quartz, kaolinite, goethite and hematite.

The pisolitic duricrust (sample Pi1) has reddish hematite and gibbsite pisoliths (comprising 15–54% of the duricrust) surrounded by pinkish gibbsite (30–40%) and kaolinite (6–15%) plasma (Figs. 3 and 4F, Table 1). Hollandite (29%), cryptomelane (9%) and coronadite (1%) fill voids and fractures (Table 1). In this Mn-plasma, there are tiny and scarce crystals of galena (<10 μm long; Fig. 8B). The upper portion of the pisolitic duricrust (sample Pi2) contains more goethite (27%) and hematite (27%) (Table 1). Close to the surface, the Mn duricrust is dismantled, showing angular rounded fragments and pisoliths in abrupt contact with oxisol. The yellowish sandy clay oxisol (sample S7), which is 0.5 m thick (Fig. 3), is composed of gibbsite, kaolinite, and quartz with subordinate hematite and anatase. Similar material also covers the slopes.

4.2. Zé Julião deposit

4.2.1. Mn colluvium

Colluvium that is up to 6 m thick was developed from the reddish siltstone (Fig. 3). It is formed by angular fragments (up to 0.4 m in diameter) of hollandite (2–32%) and/or romanechite (12–84%), coronadite (2–4%) and cryptomelane (1–5%) (Table 1, Fig. 7E). It has a grayish-blue, dense and hard framework with metallic brightness (Fig. 5A) or a grayish, sandy clay, friable, porous and pulverulent framework with earthy brightness and moderate density (Fig. 5B). As in Novo Natal, tiny and scarce galena crystals occur. Cavities, fractures and fissures that are similar to those of the Mn vermiform duricrust are filled by kaolinite, quartz, gibbsite, goethite and hematite.

4.3. Apuí deposit

4.3.1. Mn duricrusts

In this deposit, only vermiform duricrust (3 m) and oxisol (1 m) outcrop (Fig. 3). At the bottom, the vermiform duricrust (sample VB) has a bluish-brown skeleton, encompasses 54% of the bulk crust, and is composed of cryptomelane, hollandite and coronadite (27%), with minor amounts of goethite and hematite. Filling the

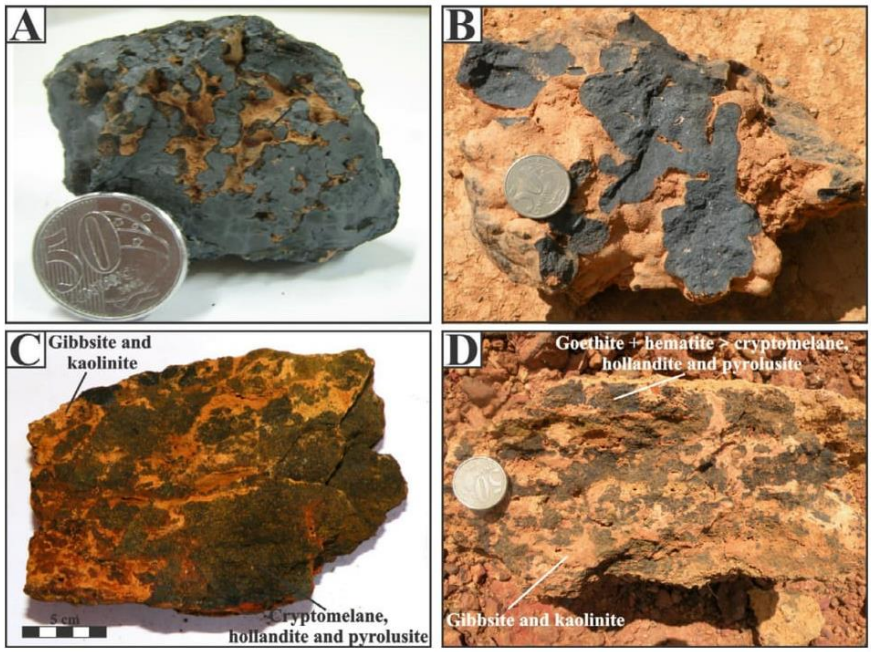

Fig. 5. (A and B) Colluvium fragment of Zé Julião showing metallic brightness and, in detail, the contact among kaolinite and hollandite, coronadite and cryptomelane. (C) Vermiform duricrust of Apuí (VB) with higher content of manganese minerals than gibbsite and kaolinite. (D) Upper part of the vermiform duricrust (VT) showing more goethite and hematite than Mn-minerals (cryptomelane, hollandite and pyrolusite).

skeleton is a pinkish plasma (comprising 46% of the crust) of gibbsite (32%), kaolinite (13%) and rutile (1%) (Table 1). At the top (sample VT), the vermiform duricrust contains more hematite (38%) and goethite (12%) than Mn-minerals (19%) (Fig. 5C and D, Table 1). The orange sandy oxisol (sample S5) is composed of quartz (43%), gibbsite (33%) and kaolinite (8%), as well as loose hematite pisoliths with brown goethite coatings. Tiny crystals of cerianite (CeO_2) and galena that are 3–10 μm long are intergrown with acicular hollandite and gibbsite (Fig. 8C).

4.4. Holanda and Beneficente deposits

4.4.1. Mn-greywackes

These deposits (Fig. 6A and B) are complementary and feature a bedrock of grayish-blue, porous, medium- to coarse-grained Mn-greywacke (samples A1–A2) that is up to 2.5 m thick in outcrops (Figs. 3, 6C, D). The Holanda Mn-greywackes contain several Mn-layers (up to 8 cm thick) of romanechite (77%), pyrolusite (16%) and cryptomelane (3%) that are associated with kaolinite, hematite and goethite (<2%) (Table 1). In both deposits, quartz grains (23% and 33%, respectively) are moderately well- to well-sorted, subrounded to subspherical and often fractured, with evidence of dissolution. The Mn-matrix in both deposits (64–75% of the bulk rock) is composed of romanechite (63–74%) in both its acicular and botryoidal forms (Fig. 7F). Cryptomelane, hematite, goethite and barite (<20 μm long, Fig. 8D) are subordinate minerals (≤2%). In the Mn-greywackes of the Beneficente Group, there is also whitish kaolinite and hollandite and cryptomelane lenses that are up to 6 cm long. Underlying the Mn-greywacke of the Beneficente Group is goethitic sandstone.

4.4.2. Mn duricrusts

From Mn-greywackes were developed lateritic vermiform duricrusts (samples H1 to H4 in Holanda and B1 to B4 in Beneficente) with thicknesses ranging from 2 to 3.7 m (Figs. 3, 6E and F). The skeletons of H1 and H4 are porous, have earthy brightness and are composed of romanechite (35–60% of the bulk rock), cryptomelane (1–2%), kaolinite (15–28%), quartz (6–20%), goethite (8–12%) and hematite (6–7%) (Table 1). The Beneficente duricrust is bluish, hard, has metallic brightness and is composed of romanechite (64–80% of the bulk rock), quartz (12–16%) and occasionally pyrolusite (9–19%), as well as minor amounts of goethite (2–5%) and hematite (1–2%). Toward the top occurs a layer (Pi6) that is 10 cm thick and contains red and orange pisoliths of hematite (34%) and goethite (11%) that are sustained by gibbsite (17%), kaolinite (12%) and traces of pyrolusite (<1%) (Fig. 3; Table 1). Cavities (20%) are filled by kaolinite, goethite and hematite.

Oxisol is thin at Holanda and reaches a thickness of 8 m at Beneficente (sample S6). It is yellowish, rich in quartz and kaolinite, and contains vertical reddish spots that are hard and hematitic (Fig. 3).

5. Geochemistry

5.1. Major and minor elements

Overall, in all samples, the contents of MgO and Na_2O are <0.01% (Table 2). The MnO content in the Mn-rocks ranges between 12.96% and 46.93%, whereas in the Mn-layer of Holanda, it reaches up to 68.95% (Table 2). In most of the duricrusts and colluvium fragments, MnO and Fe_2O_3 are the main elements, although their concentrations are highly variable (13.13–62.66% MnO and 2.17–50.02% Fe_2O_3) due to the diversity in textures (i.e., massive, protopisolitic and pisolitic) that control the mineral content. Near the surface, the contents of Al_2O_3, TiO_2 and LOI increase due to the amounts of gibbsite, kaolinite and anatase/rutile that are present in the duricrusts and oxisols. The contents of P_2O_5 up to 0.81% may be related to the solid solution of crandallite/goyazite (Table 2).

5.2. Trace elements

The Mn-rocks and duricrusts record the highest concentrations of Ba and Co (<205,541 and 2696 ppm, respectively) as well as Pb,

Fig. 6. Macroscopic features of the manganiferous deposits. (A) Galery mine of Beneficente showing Mn-greywaCke, duricrust and oxisol. (B) Holanda outcrop showing the lateral extension of Mn-greywacke and duricrust. (C and D) Mn-greywackes of Holanda (A1) and Beneficente (A2), respectively. (E) Vermiform duricrust overlying the Mn greywacke of Beneficente (B1–B4). (F) Vermiform duricrust (H1–H4) overlying the Mn greywacke of Holanda.

especially in the Mn-rocks of Novo Natal (17,200–43,638 ppm) (Table 3). The concentrations of other elements, such Sr, Cu and Zr, must also be highlighted; Sr and Cu record concentrations of up to 999 and 3579 ppm, respectively, and are more concentrated in the duricrusts and colluvium fragments of Novo Natal and Zé Julião. In contrast, Zr is more concentrated in the upper part of the Beneficente oxisol (1065 ppm) (Table 3).

Relative to the bulk continental crust of Taylor and McLennan (1985), all of the Mn-rocks and duricrusts are enriched in Ag, As, Ba, Co, Mo, Pb and Tl (Fig. 9). However, the Novo Natal deposit is most enriched in Ag, Cu, Pb and Tl (in the duricrust), while Apuí is less enriched in Co (Fig. 9A and C).

The Apuí duricrusts and the Novo Natal oxisol (sample S7) record the highest REE concentrations (491–1402 ppm); the Mn-greywacke (sample A3) records the lowest REE concentrations (Table 4). Relative to chondritic values (Taylor and McLennan, 1985), all samples are enriched in REE and record the depletion of HREE relative to LREE (with La_N/Yb_N ratios of 1-75.81) (Fig. 10). The pinkish siltstones of Novo Natal record negative Eu anomalies ($Eu/Eu^* = 0.38$), while the Zé Julião ($Eu/Eu^* = 1.28–2.08$) and Beneficente duricrusts record positive Eu anomalies ($Eu/Eu^* = 2.5–3.09$). The Beneficente duricrusts also record negative Tb anomalies ($Tb/Tb^* = 0.21–0.79$), the vermiform duricrusts of Apuí record positive Ce anomalies ($Ce/Ce^* = 10.96–26.35$), and the Apuí ($Gd/Gd^* = 1.86–2.15$) and Novo Natal ($Gd/Gd^* = 1.13–1.84$) duricrusts record positive Gd anomalies (Table 4).

5.3. Geochemical associations

Within the entire data set, principal component analysis (PCA) was applied to selected elements with loads of >0.2 (except for K_2O, MgO, Na_2O, Ag and V) and were loaded together with the mineral amounts shown in Table 1. The dataset was better described using factors 1 and 2, which expressed 37.12% and 19.26% of the observed variance, respectively. The previous analysis of chemical features, in addition to their mineralogic distribution, allowed five main groups of samples and their geochemical associations to be recognized: Group 1- pisolitic and vermiform duricrusts of Novo Natal and Apuí (samples Pi1, Pi2, VB and VT), together with most samples of the Zé Julião colluvium (Z4-Z7), contain goethite, hematite, and gibbsite, which are associated with Al_2O_3, Fe_2O_3, LOI, Th, Sc, Rb, Y, U, Ce, Pr, Nd, Ho, Er, Tm and Yb; Group 2- Mn-greywackes and duricrusts of Beneficente and Holanda (except H2) and samples Z1 to Z3 of the Zé Julião colluvium are associated with romanechite, MnO, CaO, Ba, Ni, Be, Co, Zn and Mo; Group 3- Mn-rocks of Novo Natal (samples PS and M3) feature an association defined by quartz, coronadite, SiO_2, P_2O_5 and Pb; Group 4- Mn-layer of Holanda and the massive and protopisolitic

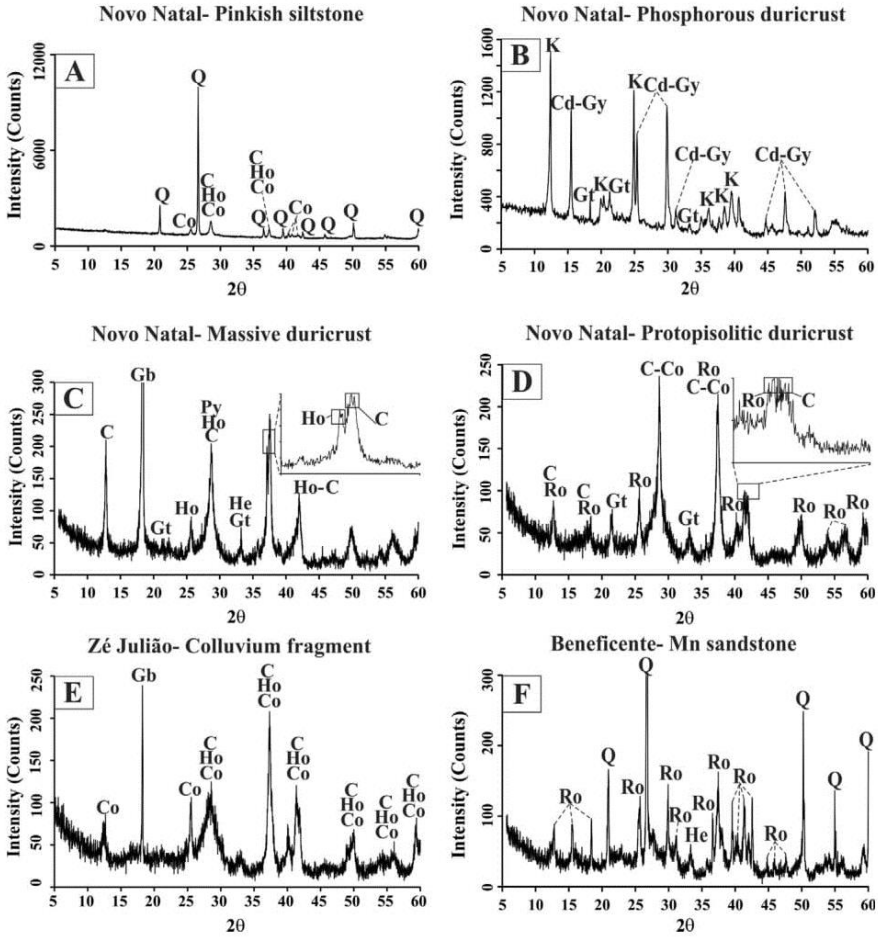

Fig. 7. Mineral most common at the Mn-rocks and related duricrust. C- cryptomelane, Co- coronadite, Cd- crandallite, He- hematite, Ho- hollandite, Gb- gibbsite, Gt- goethite, Gy- goyazite, Py- pyrolusite, Q- quartz and Ro- romanechite.

Table 1
Mineral content in weight%. Q- quartz, C-cryptomelane, Co- coronadite, Ho- hollandite, Ro- romanechie, Py- pyrolusite, Gt- goethite, He- hematite, K- kaolinite, An/Ru- anatase or rutile and Il- illite. – not identified.

Lithotype	Sample	Q	C	Co	Ho	Ro	Py	Gt	He	K	Gb	An/Ru	Il	Sum
Novo Natal														
Oxisol	S7	24	–	–	–	–	–	2	8	26	38	2	–	100
Duricrust	Pi2	–	–	–	–	–	–	27	27	15	30	1	–	100
Duricrust	Pi1	–	9	1	29	–	–	10	5	6	40	<1	–	100
Duricrust	Pp2	–	14	2	–	76	–	5	1	–	2	–	–	100
Duricrust	Pp1	–	6	1	93	–	–	–	–	<1	–	–	–	100
Duricrust	M1	1	34	–	25	–	24	2	<1	–	14	–	–	100
Mn greywacke	A3	48	1	1	23	26	–	<1	1	–	–	–	–	100
Pinkish siltstone	PS	78	2	12	6	–	–	<1	1	–	–	–	–	100
Zé Julião														
Colluvium fragment	Z8	39	1	2	17	–	–	11	13	3	14	<1	–	100
Colluvium fragment	Z7	10	2	3	32	–	–	21	10	<1	22	1	–	100
Colluvium fragment	Z6	14	1	–	–	12	–	16	25	3	28	1	–	100
Colluvium fragment	Z5	–	2	–	–	49	–	11	10	21	6	<1	–	100
Colluvium fragment	Z4	5	3	–	–	52	–	13	9	9	9	<1	–	100
Colluvium fragment	Z3	5	5	4	2	84	–	<1	<1	–	–	<1	–	100
Colluvium fragment	Z2	5	2	–	5	58	–	15	7	–	8	<1	–	100
Colluvium fragment	Z1	5	3	2	19	49	–	12	3	–	7	<1	–	100
Apuí														
Oxisol	S5	43	–	–	–	–	–	<1	14	8	33	1	–	100
Duricrust	VT	–	2	1	15	–	–	12	38	3	28	<1	–	100
Duricrust	VB	–	8	1	18	–	–	11	16	13	32	1	–	100
Holanda														
Duricrust	H4	6	1	–	–	60	–	12	6	15	–	<1	–	100

(*continued on next page*)

Table 1 (*continued*)

Lithotype	Sample	Q	C	Co	Ho	Ro	Py	Gt	He	K	Gb	An/Ru	Il	Sum
Duricrust	H3	10	2	–	–	54	–	8	6	20	–	<1	–	100
Duricrust	H2	20	1	–	–	35	–	9	7	28	–	1	–	100
Duricrust	H1	12	1	–	–	51	–	10	7	19	–	<1	–	100
Mn layer	ML	–	3	–	–	77	16	1	1	2	–	<1	–	100
Mn greywacke	A1	23	1	–	–	74	–	1	1	–	–	<1	–	100
Beneficente														
Oxisol	S6	28	–	–	–	–	–	10	14	47	–	1	–	100
Oxisol	S6	32	–	–	–	–	–	17	12	38	–	1	–	100
Duricrust	Pi6	25	–	–	–	–	<1	11	34	12	17	1	–	100
Duricrust	B4	12	–	–	–	72	9	5	2	–	–	–	–	100
Duricrust	B3	14	–	–	–	64	19	2	1	–	–	–	–	100
Duricrust	B2	12	1	–	–	84	–	2	1	–	–	–	–	100
Duricrust	B1	16	–	–	–	80	–	3	1	–	–	–	–	100
Mn greywacke	A2	33	1	–	–	63	–	2	1	–	–	–	–	100

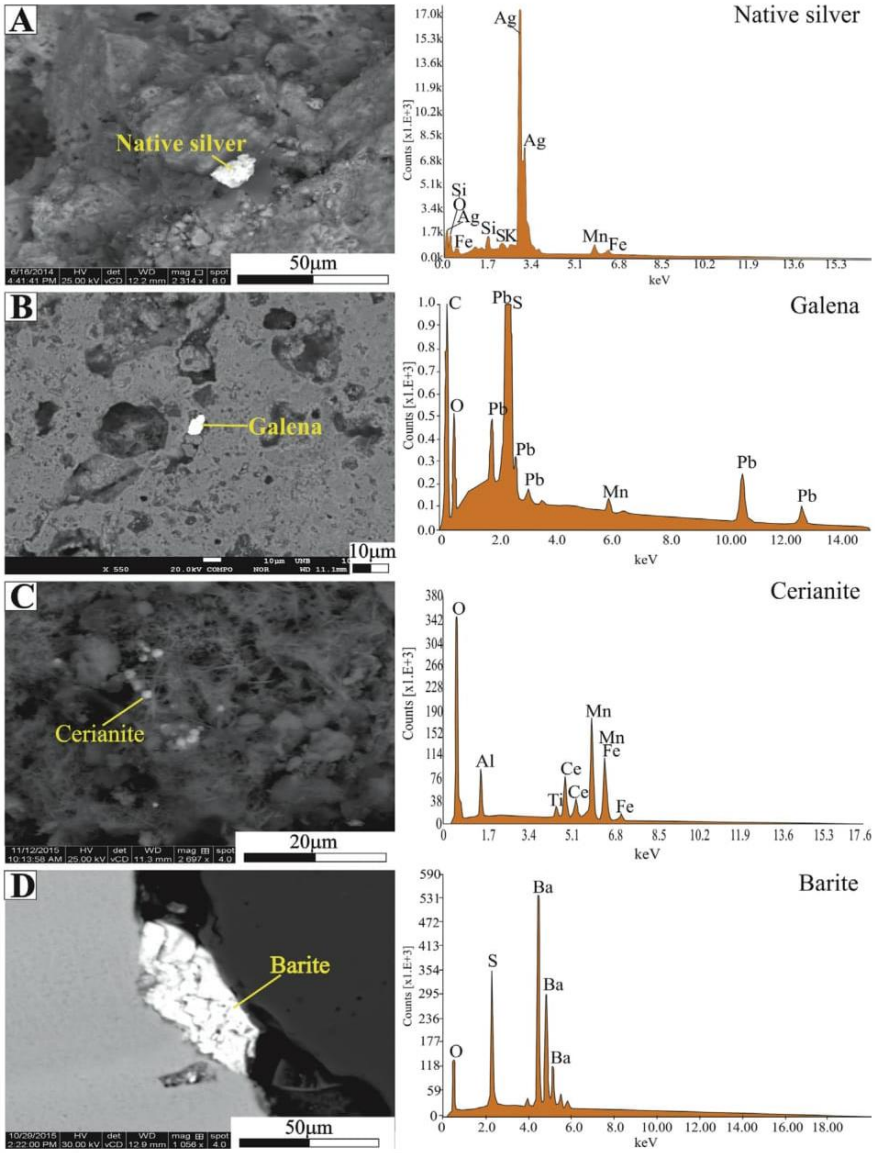

Fig. 8. (A) Native silver found in the Mn-greywacke (A3) of Novo Natal and respective EDS. (B) Tiny crystal of galena in the pisolitic duricrust (Pi1) of the Novo Natal and respective. (C) Tiny crystals of cerianite in vermiform duricrust of Apuí and respective EDS. (D) Tiny crystal of barite found in Mn-greywacke (A2) of Beneficente and respective EDS.

Table 2
Chemical composition (wt%). *Sum not closer to 100% is due to high contents of Ba and Pb.

Lithotype	Sample	SiO_2	Al_2O_3	Fe_2O_3	K_2O	CaO	MgO	MnO	Na_2O	P_2O_5	TiO_2	LOI	Sum
Novo Natal													
Oxisol	S7	34.59	33.83	9.94	0.05	0.01	0.01	0.57	<0.01	0.26	1.51	18.6	99.37
Duricrust	Pi2	6.06	22.54	48.37	0.01	0.02	<0.01	4.83	<0.01	0.10	0.88	16.7	99.51
Duricrust	Pi1	2.40	27.87	15.68	0.52	0.09	<0.01	25.82	0.02	0.32	0.47	19.8	92.99
Duricrust	Pp2	0.23	1.00	5.33	0.73	0.14	<0.01	54.1	0.02	0.31	0.09	11.7	73.65
Duricrust	Pp1	0.68	1.10	5.95	0.34	0.11	<0.01	53.11	0.01	0.35	0.06	11.4	73.11
Duricrust	M1	0.72	8.42	5.28	2.13	0.03	<0.01	62.66	0.07	0.13	0.04	14.9	94.38
Mn greywacke	A3	46.70	0.70	3.30	0.07	0.06	<0.01	32.82	<0.01	0.24	0.02	6.1	90.01
Pinkish siltstone	PS	73.39	1.91	2.00	0.15	0.02	<0.01	12.96	<0.01	0.34	0.05	3.2	94.02
Zé Julião													
Colluvium	Z8	39.43	10.00	25.03	0.06	0.02	<0.01	11.27	<0.01	0.31	0.43	10.5	97.05
Colluvium	Z7	10.12	14.23	33.88	0.11	0.03	<0.01	20.69	<0.01	0.41	0.49	15.1	95.06
Colluvium	Z6	14.88	18.80	40.28	0.07	0.02	<0.01	8.32	<0.01	0.16	0.72	14.7	97.95
Colluvium	Z5	10.58	12.66	20.63	0.16	0.05	<0.01	32.95	<0.01	0.33	0.50	13.2	91.06
Colluvium	Z4	9.33	10.88	21.30	0.22	0.07	<0.01	34.86	0.01	0.37	0.47	13.2	90.71
Colluvium	Z3	5.14	3.80	9.76	0.25	0.09	<0.01	47.9	0.01	0.43	0.18	11.5	79.06
Colluvium	Z2	5.28	4.33	18.74	0.14	0.06	<0.01	45.8	<0.01	0.55	0.29	12.0	87.19
Colluvium	Z1	4.95	4.21	14.46	0.18	0.05	<0.01	49.58	<0.01	0.55	0.35	12.7	87.03
Apuí													
Oxisol	S5	46.66	24.93	13.80	0.12	0.01	0.04	0.10	<0.01	0.03	1.14	12.9	99.73
Duricrust	VT	1.64	19.35	50.02	0.14	0.03	<0.01	13.13	0.01	0.15	0.28	12.7	97.45
Duricrust	VB	5.81	25.20	28.34	0.54	0.10	<0.01	20.70	0.03	0.16	0.55	17.0	98.43
Holanda													
Duricrust	H4	14.22	5.99	18.21	0.07	0.2	<0.01	38.88	<0.01	0.42	0.28	11.9	90.17
Duricrust	H3	19.56	7.80	14.33	0.13	0.06	<0.01	35.86	<0.01	0.34	0.36	11.5	89.94
Duricrust	H2	33.19	10.93	15.58	0.08	0.02	<0.01	22.51	<0.01	0.35	0.56	10.7	93.92
Duricrust	H1	21.38	7.68	17.52	0.04	0.05	<0.01	32.38	<0.01	0.44	0.46	11.5	91.45
Mn layer	ML	0.75	0.77	1.54	0.17	0.11	<0.01	68.95	0.01	0.41	0.03	11.2	83.94
Mn greywacke	A1	23.59	5.81	1.37	0.07	0.06	<0.01	46.93	<0.01	0.27	0.22	10.6	88.92
Beneficente													
Oxisol	S6	46.42	18.27	22.66	0.01	0.02	<0.01	0.05	<0.01	0.75	1.04	10.6	99.82
Oxisol	S6	46.54	14.07	26.42	<0.01	0.02	<0.01	0.05	<0.01	0.81	0.78	11.2	99.89
Duricrust	Pi6	33.10	13.97	40.92	0.02	0.01	<0.01	0.53	<0.01	0.54	0.73	9.1	98.92
Duricrust	B4	10.88	2.80	6.09	0.07	0.07	<0.01	54.49	<0.01	0.77	0.19	10.7	86.06
Duricrust	B3	12.73	1.73	2.83	0.07	0.06	<0.01	58.99	<0.01	0.43	0.15	9.9	86.89
Duricrust	B2	10.48	1.18	2.17	0.05	0.05	<0.01	55.55	<0.01	0.35	0.09	9.3	79.22
Duricrust	B1	14.60	1.62	3.41	0.04	0.05	<0.01	55.95	<0.01	0.40	0.11	9.8	85.98
Mn greywacke	A2	25.33	1.35	2.28	0.06	0.09	<0.01	39.55	<0.01	0.71	0.08	9.1	78.55

Table 3
Trace elements concentrations (ppm).

Lithotype	Sample	Ag	As	Ba	Be	Co	Cu	Ga	Hf	Mo	Nb	Ni	Pb	Rb	Sc	Sr	Tl	Th	U	V	Y	Zr	Zn
Novo Natal																							
Oxisol	S7	1	51	1713	<1	46	166	48	29	4	45	8	401	2	23	61	1	39	10	61	104	1065	10
Duricrust	Pi2	1	95	612	3	259	261	70	15	19	21	17	495	7	28	45	8	51	5	535	28	545	23
Duricrust	Pi1	19	142	44690	9	878	2702	63	11	27	5	48	14100	11	11	610	62	15	5	119	22	452	246
Duricrust	Pp2	25	80	99500	21	1786	3579	117	4	66	3	57	4391	7	5	990	97	20	11	90	66	119	248
Duricrust	Pp1	20	64	120300	21	1918	3412	122	2	90	2	52	292	5	4	507	58	5	10	107	54	52	224
Duricrust	M1	84	76	44794	7	1036	1643	96	1	24	<0.1	27	5001	21	5	168	45	2	5	65	26	47	148
Mn greywacke	A3	5	75	71100	2	522	2016	63	1	57	2	13	17200	2	3	51	7	2	5	80	5	32	117
Pinkish siltstone	PS	2	40	14055	6	359	1446	14	2	27	1	10	43638	4	2	19	2	1	2	<8	5	16	38
Zé Julião																							
Colluvium	Z8	1	79	20413	8	453	386	38	12	10	10	57	529	2	16	51	5	39	6	284	18	389	88
Colluvium	Z7	2	137	33348	10	782	566	51	14	11	12	72	238	2	40	103	10	40	12	467	26	490	130
Colluvium	Z6	1	30	14632	4	318	330	71	10	6	18	26	169	1	38	59	5	39	8	668	20	357	66
Colluvium	Z5	2	27	85230	12	1203	743	60	11	11	8	43	197	2	34	328	17	31	9	508	27	412	165
Colluvium	Z4	2	43	88741	15	1236	713	62	10	12	8	63	185	3	30	390	15	27	11	479	27	354	185
Colluvium	Z3	2	41	204315	21	1941	1333	72	4	20	3	71	109	4	24	580	25	10	13	260	18	130	228
Colluvium	Z2	2	53	122954	19	1713	754	89	7	23	7	82	368	5	26	999	19	16	12	249	25	254	199
Colluvium	Z1	2	37	125533	20	1603	855	87	10	21	7	81	244	6	23	131	16	16	13	215	25	332	196
Apuí																							
Oxisol	S5	<0.1	3	105	<1	4.6	2	36	17.2	0.8	27	5.3	10	7	13	51	<0.1	30	4	131	42	594	5
Duricrust	VT	1	23	9541	4	254	11	66	6.0	3.0	12	56	2180	14	19	95	8	22	6	144	20	223	81
Duricrust	VB	1	21	19954	11	389	80	40	3.5	3.3	7	90	1141	13	11	39	5	13	5	149	11	125	165
Holanda																							
Duricrust	H4	0.8	44	96627	14	446	24	64	7	4	6	47	23	3	16	95	9	10	4	229	15	242	153
Duricrust	H3	0.6	34	97619	14	1047	20	63	8	9	7	64	50	6	15	102	19	17	7	674	21	296	213
Duricrust	H2	0.4	32	47531	7	669	16	40	12	5	12	42	40	5	18	31	15	16	6	608	18	416	208

(*continued on next page*)

Table 3 (*continued*)

Lithotype	Sample	Ag	As	Ba	Be	Co	Cu	Ga	Hf	Mo	Nb	Ni	Pb	Rb	Sc	Sr	Tl	Th	U	V	Y	Zr	Zn
Duricrust	H1	0.6	30	82187	17	1290	21	62	9	6	11	39	28	2	19	47	10	12	5	749	19	344	270
Mn layer	ML	0.3	12	155748	21	2696	53	69	1	17	1	188	12	4	3	125	23	1	4	522	39	18	712
Mn greywacke	A1	0.4	10	107479	22	1756	28	63	5	9	3	60	10	3	12	67	11	7	5	427	20	169	274
Beneficente																							
Oxisol	S6	<0.1	41	768	1	2	9	45	16	4	19	6	7	0.3	19	42	<0.1	16	11	328	20	584	5
Oxisol	S6	<0.1	29	1038	1	2	8	37	20	2	25	3	10	0.2	19	57	<0.1	21	11	233	26	733	4
Duricrust	Pi6	1	26	1536	1	15	9	46	15	4	17	12	39	1	22	82	0.2	29	9	445	22	547	9
Duricrust	B4	2	86	136475	12	1266	51	61	7	26	4	62	43	1	9	74	13	5	5	478	24	240	258
Duricrust	B3	2	115	128400	13	1310	31	57	4	30	3	112	27	1	5	47	25	4	5	363	10	158	320
Duricrust	B2	2	84	205341	10	1356	32	66	3	25	2	84	16	1	4	32	19	2	2	268	9	95	296
Duricrust	B1	2	102	137727	12	1331	35	61	3	26	3	106	15	1	5	37	16	3	3	242	10	102	298
Mn greywacke	A2	5	102	111200	14	842	78	105	3	28	2	110	67	2	6	64	21	3	4	119	18	104	320
C. Crust	C.C	0.1	2	550	3	17	25	17	5.8	1.5	12	44	17	112	13.6	350	1	11	3	107	22	190	71

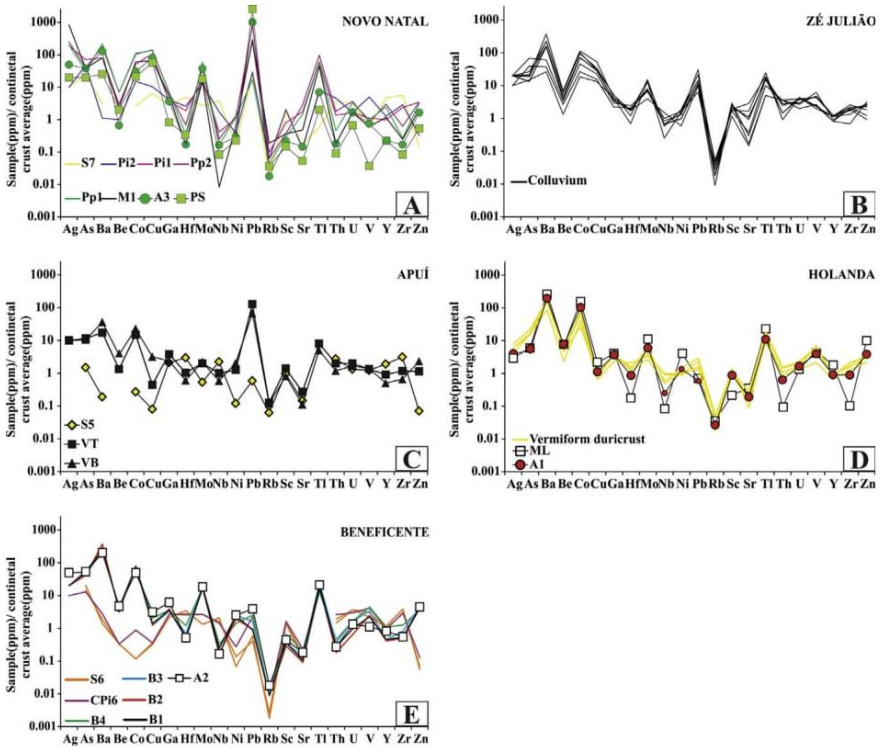

Fig. 9. Trace elements in ppm normalized by the average crustal of Taylor and McLennan (1985).

Table 4
Rare earth elements concentrations (ppm). $Eu/Eu^* = (Eu/0.087)/[(Sm/0.231)\times(Gd/0.306)]^{1/2}$; $Ce/Ce^* = (Ce/0.957)/[(La/0.367)\times(Pr/0.137)]^{1/2}$; $Tb/Tb^* = (Tb/0.06)/[(Gd/0.31)\times(Dy/0.38)]^{1/2}$; $Gd/Gd^* = (Gd/0.31)/[(Eu/0.087)\times(Tb/0.06)]^{1/2}$.

Lithotype	Sample	La	Ce	Pr	Nd	Sm	Eu	Gd	Tb	Dy	Ho	Er	Tm	Yb	Lu	REE	Eu/Eu^*	Ce/Ce^*	Tb/Tb^*	Gd/Gd^*	$(La/Yb)_N$
Novo Natal																					
Oxisol	S7	99.3	207.2	19.46	75.3	15.99	3.1	17.0	3.06	19.07	3.79	11.55	1.85	11.96	1.97	491	0.58	1.10	0.97	1.30	5.61
Duricrust	Pi2	79.4	147.7	14.80	49.2	7.10	1.3	6.0	1.00	5.20	1.00	3.30	0.50	3.40	0.60	321	0.61	1.01	1.02	1.25	15.78
Duricrust	Pi1	61.0	120.5	14.80	55.6	7.50	1.7	6.4	0.80	4.00	0.80	2.20	0.40	2.40	0.40	279	0.75	0.94	0.90	1.30	17.17
Duricrust	Pp2	20.1	65.1	11.80	69.2	25.40	5.9	26.0	4.00	19.50	3.00	8.00	1.10	6.90	1.00	267	0.70	0.99	1.02	1.27	1.97
Duricrust	Pp1	9.3	19.3	3.70	21.9	10.00	2.8	17.4	2.90	15.10	2.80	6.50	1.00	6.00	0.80	120	0.65	0.77	1.02	1.45	1.05
Duricrust	M1	20.8	141.5	13.60	69.8	26.70	5.5	20.3	3.30	14.00	2.20	5.20	0.80	5.00	0.70	329	0.72	1.97	1.12	1.13	2.81
Mn greywacke	A3	7.7	14.0	1.40	6.1	1.30	0.9	8.2	1.20	5.50	1.00	2.70	0.40	2.40	0.30	53	0.84	1.00	1.02	1.87	2.17
Pinkish siltstone	PS	46.0	69.8	9.31	28.1	3.51	0.4	2.2	0.23	1.08	0.17	0.47	0.06	0.41	0.05	162	0.38	0.79	0.85	1.84	75.81
Zé Julião																					
Colluvium	Z8	47.5	121.5	11.43	39.9	7.10	1.31	5.09	0.78	4.11	0.70	2.06	0.36	2.26	0.36	244	0.67	1.22	0.98	1.19	14.20
Colluvium	Z7	33.9	203.9	8.43	29.7	6.05	1.25	5.30	1.00	5.85	1.13	3.34	0.55	3.56	0.54	305	0.67	2.83	1.03	1.12	6.43

Table 4 (*continued*)

Lithotype	Sample	La	Ce	Pr	Nd	Sm	Eu	Gd	Tb	Dy	Ho	Er	Tm	Yb	Lu	REE	Eu/Eu*	Ce/Ce*	Tb/Tb*	Gd/Gd*	$(La/Yb)_N$
Colluvium	Z6	34.8	100.5	7.34	26.0	4.84	1.12	4.26	0.75	4.68	0.88	2.76	0.45	2.99	0.48	192	0.75	1.47	0.96	1.10	7.86
Colluvium	Z5	31.1	227.6	7.71	27.1	5.56	1.35	5.31	1.04	6.49	1.11	3.38	0.54	3.45	0.53	322	0.76	3.44	1.01	1.06	6.09
Colluvium	Z4	40.3	172.7	10.60	37.1	7.47	1.15	6.28	1.13	6.73	1.14	3.38	0.55	3.36	0.50	292	0.51	1.96	0.99	1.31	8.10
Colluvium	Z3	18.8	110.9	5.37	20.8	4.54	3.24	4.98	0.74	5.31	0.68	1.91	0.31	1.83	0.26	180	2.08	2.59	0.82	0.76	6.94
Colluvium	Z2	31.0	128.3	7.95	29.0	6.27	3.15	5.87	0.99	6.90	0.99	2.93	0.46	3.01	0.42	227	1.59	1.91	0.89	0.79	6.96
Colluvium	Z1	34.8	122.8	8.75	32.7	6.58	2.63	5.99	0.95	7.10	0.94	2.90	0.44	2.93	0.42	230	1.28	1.65	0.83	0.90	8.03
Apuí																					
Oxisol	S5	57.6	86	8.23	20.9	4.16	0.86	5.04	1.03	7.18	1.52	4.49	0.73	5.1	0.74	204	0.57	0.92	0.97	1.27	7.63
Duricrust	VT	21.6	451	4.30	16.4	2.9	0.60	4.30	0.50	2.70	0.60	1.60	0.30	1.9	0.30	509	0.52	10.96	0.84	1.86	7.68
Duricrust	VB	25.8	1328	5.40	19.2	3.6	0.80	6.80	0.70	4.50	1.00	2.80	0.50	3.0	0.50	1402	0.49	26.35	0.72	2.15	5.81
Holanda																					
Duricrust	H4	25.1	246.1	6.84	23.0	4.89	1.52	4.03	0.73	4.92	0.75	2.55	0.40	2.59	0.40	324	1.05	4.40	0.94	0.91	6.55
Duricrust	H3	30.5	104.3	7.29	23.7	4.40	0.77	3.40	0.61	4.12	0.71	2.14	0.38	2.45	0.39	185	0.61	1.64	0.93	1.18	8.41
Duricrust	H2	40.9	173.5	11.43	41.5	7.70	1.70	5.76	0.93	6.42	0.90	2.83	0.44	2.84	0.43	297	0.78	1.88	0.87	1.09	9.73
Duricrust	H1	20.1	148.6	7.06	24.5	5.20	1.47	3.71	0.62	4.59	0.59	1.85	0.29	1.94	0.28	221	1.02	2.92	0.86	0.92	7.00
Mn layer	ML	32.8	126.0	18.95	82.7	18.19	4.92	16.09	2.12	14.70	2.15	5.78	0.86	5.25	0.70	331	0.88	1.18	0.79	1.18	4.22
Mn greywacke	A1	36.9	247.5	10.74	38.2	7.74	2.05	5.88	0.89	5.90	0.80	2.33	0.37	2.23	0.33	362	0.93	2.91	0.86	1.03	11.18
Beneficente																					
Oxisol	S6	49.7	101.4	11.87	42.4	7.32	1.35	5.80	0.93	4.97	1.00	2.97	0.53	3.73	0.60	235	0.63	0.98	0.99	1.23	9.00
Oxisol	S6	37.7	76.8	8.95	31.9	5.50	1.04	4.54	0.73	3.96	0.75	2.20	0.41	2.76	0.46	178	0.64	0.98	0.98	1.24	9.23
Duricrust	Pi6	52.9	110.4	12.90	45.9	7.09	1.31	5.13	0.80	4.28	0.87	2.58	0.45	3.20	0.52	248	0.66	0.99	0.98	1.19	11.17
Duricrust	B4	10.0	20.5	3.25	15.0	3.34	2.88	2.43	0.11	2.81	0.30	1.15	0.21	1.09	0.19	63	3.09	0.84	0.24	1.02	6.20
Duricrust	B3	8.1	18.3	2.94	13.8	2.77	1.97	2.05	0.09	2.89	0.30	1.02	0.18	0.94	0.16	56	2.53	0.88	0.21	1.15	5.82
Duricrust	B2	10.8	23.0	2.69	10.9	2.34	2.00	2.19	0.17	4.02	0.53	1.60	0.27	1.62	0.22	62	2.70	1.00	0.33	0.89	4.50
Duricrust	B1	23.4	76.5	10.53	48.2	9.83	3.69	10.29	1.28	8.33	0.96	2.60	0.45	2.91	0.54	200	1.12	1.14	0.79	1.12	5.43
Mn greywacke	A2	15.8	45.2	4.30	17.0	3.40	0.90	2.80	0.40	1.40	0.20	0.60	0.10	0.50	0.10	93	0.89	1.28	1.16	1.11	21.35
Chondrite	CH	0.37	0.96	0.14	0.71	0.23	0.09	0.31	0.06	0.38	0.09	0.25	0.04	0.25	0.04	4	1	1.03	0.99	1	1

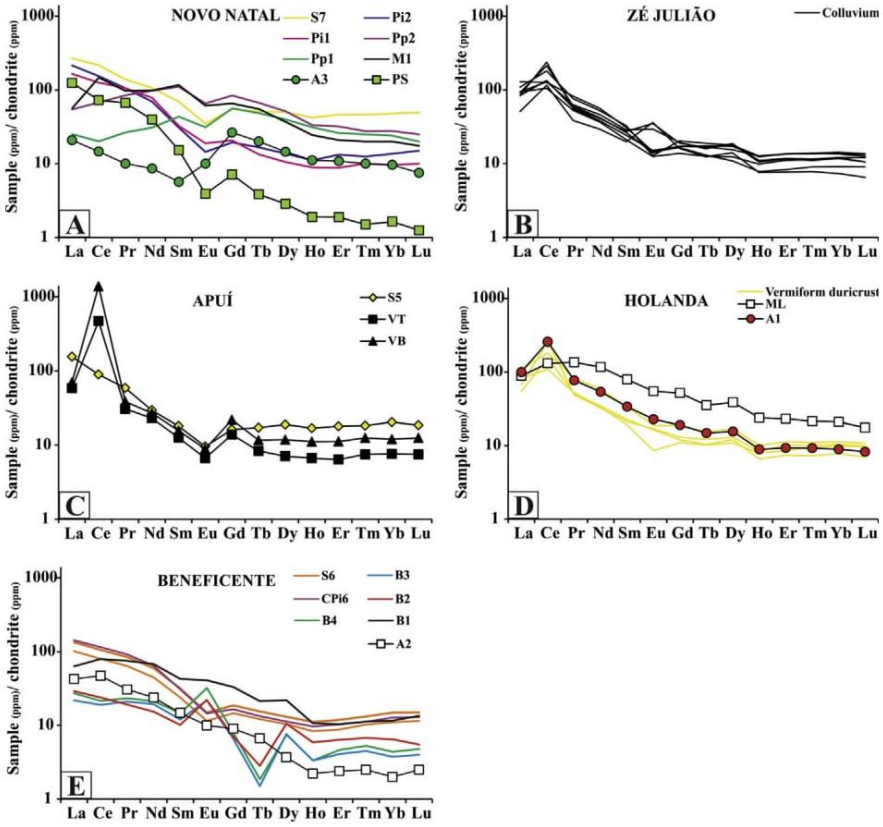

Fig. 10. Rare earth elements in ppm normalized by the chondrite of Taylor and McLennan (1985).

duricrusts of Novo Natal comprise an association of hollandite, cryptomelane, pyrolusite, Ag, As, Cu, Ga, Sr, Tl, Sm, Eu, Gd, Tb and Dy; Group 5- the pisolitic duricrust of Beneficente (sample Pi6), oxisols, the upper portion of the Zé Julião colluvium (sample Z8) and one sample of the vermiform duricrust of Holanda (sample H2) are characterized by the association of kaolinite, anatase/rutile, TiO_2, Zr, Hf, La and Nb (Fig. 11).

6. SEM and EMPA: petrographic and microchemical analysis

6.1. Novo Natal- coronadite and hollandite of Mn-rocks

Coronadite and hollandite fill fractures and veins and display zoned acicular structures. Coronadite generally occupies the inner regions of veins and hollandite occupies the edges of veins; these comprise at least three generations, according to the arrangement of these fractures (Fig. 12A). Coronadite also occurs as rod cells around the quartzose framework of the pinkish siltstone. In the Mn-greywackes, hollandite composes the matrix, while coronadite occurs as veinlets or crystals or is disseminated in the matrix and frequently occurs as crowns around hollandite (Fig. 12B and C). Hollandite also fills fractures or exhibits acicular textures in these Mn-rocks (PS and M3).

6.1.1. Novo Natal, Zé Julião and Apuí lateritic duricrusts and colluvium- hollandite

In the duricrusts of Novo Natal and Apui, hollandite is zoned and shows staghorn and boxwork habits or forms angular fragments. The protopisolitic duricrusts of Novo Natal (Pp1 and Pp2) contain two generations of hollandite: the first one, which is widespread throughout the framework, forms angular fragments (~600 μm in diameter) that encompass less than 2% of the duricrust (Fig. 12D). The second and main generation comprises up to 90% of the duricrust and is zoned, includes angular fragments and is intersected by three generations of hollandite veinlets (Fig. 12D), some of which are Pb-hollandite (that are not related to the hierarchy of the generations of the veinlets), as in the duricrusts and colluvium fragments of Novo Natal and Zé Julião. The angular fragments of hollandite intergrown with gibbsite with staghorn and boxwork habits (Fig. 12E, F and G) are characteristic of the massive and vermiform duricrusts of Novo Natal (M1) and Apuí (VB and VT). Voids are filled by acicular hollandite.

6.2. Mineral geochemistry: coronadite and hollandite: sedimentary rock and duricrust

Coronadite records PbO contents ranging between 16.57 and 28.88% and small amounts of BaO (0.30–8.09%) (Table A4; Fig. 13A). The coronadite in the vermiform duricrusts of Apuí (samples VB and VT) has higher contents of CoO (1.28–1.54%) and lower contents of MnO_2 (60.07–60.48%) compared to those of the Mn-rocks of Novo Natal (samples PS and A3; Table A4). According to formula units based on 16 oxygens and Mn^{4+}/Mn^{2+} calculated assuming full site occupancy, the coronadite in the studied Mn-rocks has the following formula: $Pb_{(0.77-1.24)}Ba_{(0.02-0.37)}Mn^{4+}_{(6.85-6.92)}Mn^{2+}_{(0.59-0.72)}Fe^{3+}_{(0.01-0.02)}Al^{3+}_{(0.11-0.21)}Cu_{(0.06-0.11)}Co_{(0.01-0.03)}V_{(0-0.02)}O_{16}$ (Table A5). In contrast, the coronadite found in the Apuí duricrusts has the following formula: $Pb_{(0.93-1.11)}Ba_{(0.14-0.19)}Mn^{4+}_{(6.40-6.43)}Mn^{2+}_{(0.59-0.65)}Fe^{3+}_{(0.47-0.50)}Al^{3+}_{(0.19-0.27)}Cu_{(0.06-0.1)}Co_{(0.17-0.20)}V_{(0-0.01)}O_{16}$ (Table A5).

In Mn-rocks and duricrusts, hollandite has higher contents of BaO (6.17–17.61%) and MnO_2 (63.71–82.12%) and lower contents of SiO_2, K_2O, CaO, Na_2O, P_2O_5 and V_2O_5 (<1%). Nevertheless, in the protopisolitic (sample Pp2) and phosphatic (Pd) duricrusts of Novo Natal, the K_2O content of the hollandite is higher (<2.1%) (Table A6). Two types of hollandite were identified: the most common contains PbO (0.84–9.42%), whereas the hollandite without PbO only occurs in the protopisolitic duricrust (sample Pp2; Fig. 13A). The hollandite of the vermiform duricrusts (samples VB and VT) of Apui and that of the phosphatic portions (sample Pd) of Novo Natal contain more Al_2O_3 and Fe_2O_3 than the Mn-rocks, although in the Mn-greywacke (sample A3), Fe_2O_3 is higher (<9%). Furthermore, the hollandite from the phosphatic portions (sample Pd) is enriched in P_2O_5, CuO and CoO (Table A6) relative to those in the Mn-rocks. The hollandite of the fragments of Zé Julião colluvium records the highest contents of PbO (5.99–9.42%). According to all of these chemical characteristics and the formula units based on 16 oxygens and Mn^{4+}/Mn^{2+} calculated assuming full site occupancy, the hollandite of the studied Mn-rocks has the following formula: $Ba_{(0.72-0.98)}K_{(0-0.12)}Pb_{(0.05-0.23)}Na_{(0.01)}Mn^{4+}_{(6.64-7.15)}Mn^{3+}_{(0.37-0.40)}Fe^{3+}_{(0.01-0.68)}Cu_{(0.04-0.08)}Co_{(0.01-0.04)}Al^{3+}_{(0.04-0.13)}Si_{(0.01-0.07)}O_{16}$. In contrast, the hollandite in the duricrust has the following formula: $Ba_{(0.34-0.92)}K_{(0-0.37)}Pb_{(0-0.4)}Na_{(0-0.04)}Mn^{4+}_{(6.26-7.32)}Mn^{3+}_{(0.35-0.41)}Fe^{3+}_{(0.01-0.49)}Cu_{(0.06-0.17)}Co_{(0.01-\ 0.10)}Al^{3+}_{(0.04-0.96)}\ Si_{(0.01-0.17)}O_{16}$ (Table A7).

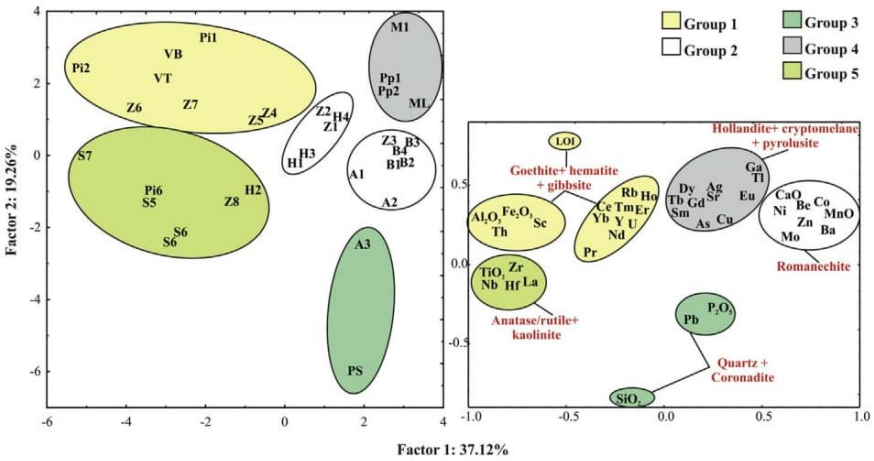

Fig. 11. The main mineral and geochemical associations that identify the studied lithotypes. A1, A2 and A3: Mn-greywackes of Holanda, Beneficente and Novo Natal. H1–H4: vermiform duricrusts of Holanda. Z1–Z8: colluvium fragments of Zé Julião. B1–B4: vermiform duricrusts of Beneficente. VT and VB: vermiform duricrusts of Apuí. Pi1 and Pi2: pisolitic duricrusts of Novo Natal. Pi6: pisolitic duricrust of Beneficente. M1: massive duricrust of Novo Natal. Pp1 and Pp2: protopisolitic duricrust of Novo Natal. PS: pinkish siltstone. ML: manganiferous layer of Holanda. S6, S7 and S5: oxisols of Beneficente, Novo Natal and Apuí, respectively.

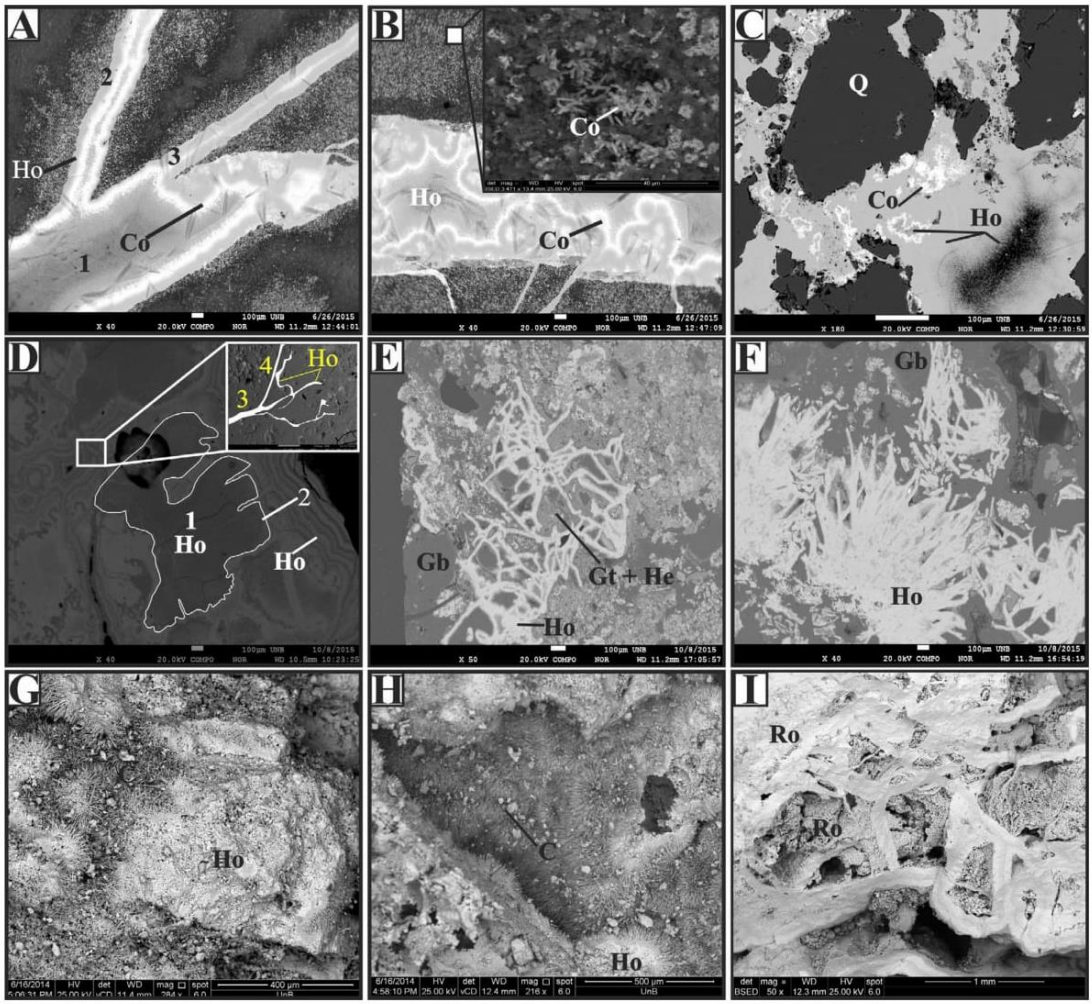

Fig. 12. The main features of the Mn-minerals observed by SEM and EMPA. (A) Fractures of the pinkish siltstone (PS) filled by coronadite (Co) and hollandite (Ho); note the formation of at least three generations of coronadite (1, 2 and 3) and hollandite. (B) Zoned structure displayed by coronadite and hollandite in the pinkish siltstone; into detail the rod cells of coronadite in quartz matrix. (C) Hollandite matrixing quartz (Q) grains of the Mn greywacke (A3), locally it occurs as needles and surrounded by coronadite. (D) Framework of the protopisolitic duricrust (Pp1) composed by at least four generations of hollandite as angular fragments, zoned and veinlets. (E) Relicts of hollandite in the vermiform duricrust of Apuí (VT); note the replamatrix of hollandite for goethite (Gt), hematite (He) and gibbsite (Gb). (F) Staghorn of hollandite involved by gibbsite in the vermiform duricrust of Apuí (VT). (G and H) Contact between acicular cryptomelane (C) and fragments of hollandite in the massive duricrust Novo Natal (M1). (I) Romanechite (Ro) as boxwork constituting the framework of the protopisolitic duricrust (Pp2) of Novo Natal and filled cavities as botryoidal romanechite.

6.3. Cryptomelane of the massive duricrust of Novo Natal

Cryptomelane, which is most common in the massive duricrust of Novo Natal (CM1), forms needles or heterogeneous mass intergrowths with gibbsite and often coexists with hollandite or botryoidal pyrolusite (Fig. 12H). It contains up to 79% MnO_2, between 4 and 4.5% K_2O (Fig. 13A) up to 5% Al_2O_3 and less than 4% other elements (i.e., SiO_2, Fe_2O_3, Mn_2O_3 PbO, CuO, Na_2O, Co and BaO) (Table A8). According to the formula units based on 16 oxygens and Mn^{4+}/Mn^{3+} calculated assuming full site occupancy, the formula of this cryptomelane is $K_{0.69-0.77}Mn^{3+}_{0.33-0.40}Mn^{4+}_{6.76-6.87}O_{16}$ (Table A9).

6.4. Romanechite of the Beneficente, Holanda and Zé Julião deposits

In the Mn-greywackes of the Beneficente, Holanda and Zé Julião deposits, the romanechite in the matrix is zoned, exhibits boxwork habit (Fig. 12I) and is botryoidal when filling voids. In the duricrusts and colluvial fragments, it is massive and sometimes zoned. It is composed of only Mn_2O_3 (65.58–71.16%) and BaO (16.20–18.47%) (Table A10, Fig. 13A); according to the formula units based on 10 oxygens and Mn^{4+}/Mn^{3+} calculated assuming full site occupancy, its formula is $Ba_{0.63-0.72}Mn^{3+}_{0.64-0.72}Mn^{3+}_{4.04-4.11}O_{10}$ (Table A11).

6.5. Goethite and hematite

These minerals display botryoidal and acicular habits in voids or are massive when they are associated with gibbsite pisoliths and quartz grains. In Apuí and Novo Natal, they record 1.61–6.19% MnO and 1.27–13.31% Al_2O_3, which decreases the amount of recorded Fe_2O_3 (58.11–89.4%) (Table A12) and causes the displacement of the main X-ray reflection (110) in the XR diffractogram. Their SiO_2 contents ($\leq$13.5%) are most likely related to the presence of quartz inclusions.

7. Discussion

7.1. Geochemical features

Different environments (i.e., sedimentary, hydrothermal and lateritic) produce a wide and complex variety of structures, textures, minerals and geochemical features that are assigned to

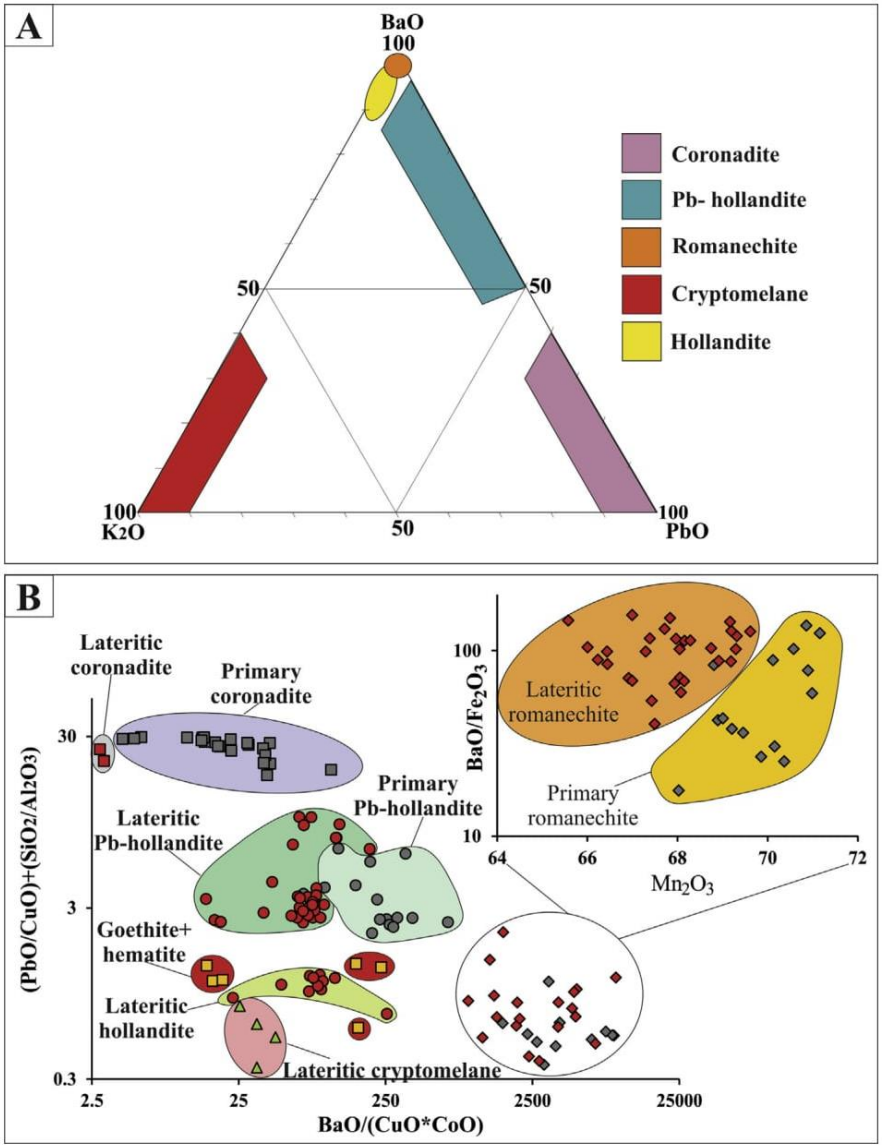

Fig. 13. (A) Ternary diagram K2O-BaO-PbO plot the main Mn-minerals according mineral-geochemistry. (B) A plot that differenciates the primary Mn-minerals from lateritic minerals.

two types of ore: one is related to Novo Natal, Zé Julião and Apui, which record higher concentrations of trace elements and were deposited in a rift basin, and the second one is more pure, is related to Beneficente and Holanda, and was deposited in a post-rift basin. Moving from the sedimentary rock to the lateritic duricrust, the main Mn-minerals of coronadite, hollandite and romanechite changed their chemical compositions and textures. The more mobile elements (MgO, CaO, Na_2O and K_2O) were removed, while the contents of SiO_2, Al_2O_3, Fe_2O_3, MnO, Pb and Co increased. This geochemical change is better shown in Fig. 13B, where the values of BaO/(CuO*CoO) versus (PbO/CuO) + (SiO_2/Al_2O_3) differ between primary coronadite and hollandite and those formed in lateritic conditions. Primary romanechite was distinguished from lateritic romanechite based on their different contents of Mn_2O_3 and BaO/Fe_2O_3 (Fig. 13B). Phosphatic portions (i.e., the solid solution of crandallite-goyazite, sample Pd, Fig 14A) caused P_2O_5 to become trapped in hollandite (Table A6), as well as to form intergrowths with gibbsite, whereas Mn-minerals (Fig. 14B) helped some Al and Mn become trapped in goethite and hematite (1.27–13.31% Al_2O_3 and 1.61–6.19% MnO). The abundance, occurrence and paragenesis of these minerals are shown in Fig. 14C.

The oxidizing environment and the processes of coprecipitation, adsorption, complexation and ion exchange trapped REE within Fe- and Mn-oxides (Braun et al., 1990; Ohta and Kawabe, 2001). In this environment, the reduction of MnO_2 (Mn^{4+} to Mn^{3+} or Mn^{2+}) acted as a catalyst for Ce^{3+} oxidation, forming cerianite and explaining the low contents of Mn^{4+} present in the chemical formulas of hollandite and coronadite (approximately 0.15 and 0.31%, respectively) in studied Mn duricrust relative to Mn-rocks. The reduction of Mn^{4+} to Mn^{3+} also allowed goethite and hematite to trap Mn. Goethite and hematite can also retain Th and Sc; these elements, together with Y, may also be residually concentrated in minerals such as zircon (Middelburg et al., 1988; Kotschoubey et al., 2005; Calagari and Abedini, 2007). These processes explain the association of group 1 (goethite, hematite, gibbsite, Al_2O_3, Fe_2O_3, Sc, Th, Y, U, LOI, Rb, Ce, Pr, Nd, Ho, Er, Tm and Yb) that reg-

ulates most samples of Zé Julião and some samples of the Apuí and Novo Natal duricrusts, which contain more goethite (10–27%), hematite (5–38%) and gibbsite (6–40%) (Fig. 11).

The Ba^{2+} and SO_4^{2-} released in solution from barite, in addition to the availability of MnO_8^{-6} and H_2O, formed romanechite and hollandite as a matrix in the Mn-greywacke (M2), following the equations below:

$$BaSO_4 \rightarrow Ba^{2+}_{(aq)} + SO^{2-}_{4(aq)} \quad (I)$$

$$4H_2O + MnO_8^{-6} \rightarrow Mn^{3+} + 8H^{+} + 6O_2 \quad (II)$$

$$2Ba^{2+}_{(aq)} + 5Mn^{3+} + 4H^{+} + 6O_2 \rightarrow Ba_2Mn_5O_{10}.2H_2O \quad (III)$$

The repetition of this process created the zoned structures displayed by the romanechite in Mn-greywacke (A2). Although romanechite has a low capacity to scavenge trace elements (Post, 1999; Pracejus and Bolton, 1992), trace elements may become trapped on the surface of romanechite (Ohta and Kawabe, 2001) or within its mineral structure, where Ni^{3+} (0.57 Å), Co^{3+} (0.61 Å) and Mo^{4+} (0.65 Å) can replace Mn^{3+} (0.643 Å) or Mn^{4+} (0.60 Å). These features explain the geochemical association of group 2 (MnO, Ba, Co, Ni, Be, Zn and Mo), which governs the vermiform duricrust of Beneficente and some of the Mn-greywackes and duricrusts of Holanda, Novo Natal and Zé Julião.

Associations 3 and 4 (quartz, coronadite, SiO_2, P_2O_5 and Pb; and Pb-hollandite, cryptomelane, pyrolusite, Ag, As, Cu, Ga, Sr, Tl, Sm, Eu, Gd, Tb and Dy, respectively), mirror most of the Mn-rocks and the lateritic duricrusts of Novo Natal and the Mn layer of Holanda (ML), which is explained by their mineral compositions. Coronadite and hollandite containing PbO and CuO and cryptomelane containing CuO (Tab. A4, A6 and A8) are produced by the remobilization and ability of Pb and Cu to form complexes with Mn, thus creating the several generations of Mn-minerals in the Mn-rocks of Novo Natal (Fig. 12A, B and D). During this process, other elements with geochemical affinities, such as Dy, Tb, Sm, Eu, As, Ag, Cu, Sr and Tl, are also trapped in these minerals, as well as pyrolusite

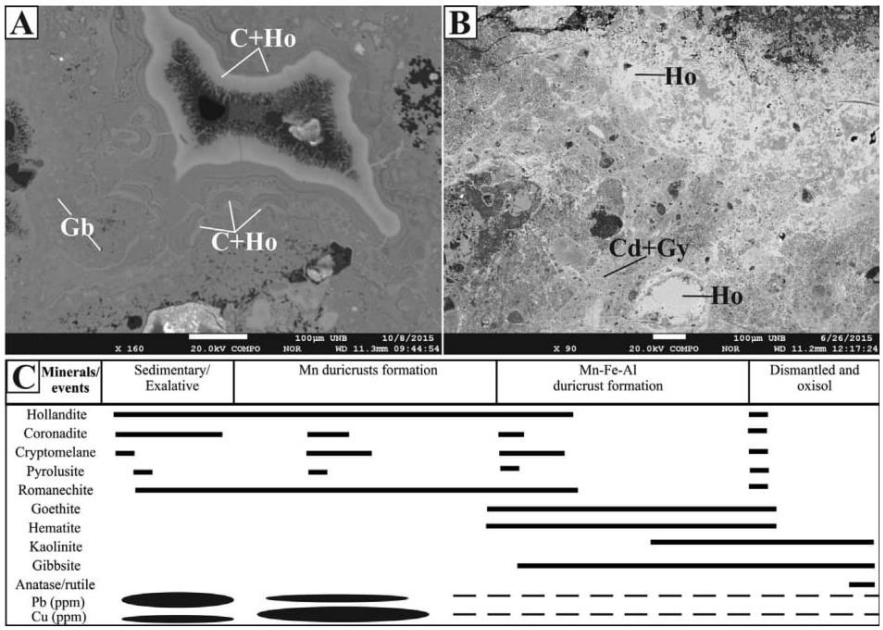

Fig. 14. (A) Detail of the massive duricrust (M1) where gibbsite (Gb- massive dark grey) coexist with relicts of cryptomelane (C) and hollandite (Ho) (light grey and zoned dark grey). (B) Detail of pale grey phosphatic portions (Pd) of the Novo Natal duricrust, where crandallite (Cd) and goyazite (Gy) involving hollandite (light grey). (C) Abundance, mode of occurrence and mineral paragenesis of southwestern Amazonia small Mn deposits.

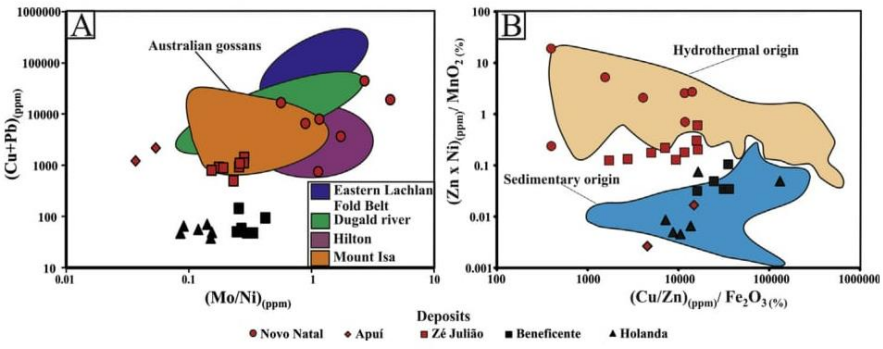

Fig. 15. (A) $(Mo/Ni)_{(ppm)}$ vs $(Cu + Pb)_{ppm}$ comparing the studied deposit with Australian gossans of Taylor and Scott (1982) and Scott et al. (2001). (B) $(Cu/Zn)_{ppm}/Fe_2O_{3(\%)}$ vs $(Zn/Ni)_{ppm}/MnO_{2(\%)}$ comparing the studied deposit with hydrothermal and sedimentary environment of Zantop (1978), Moorby et al. (1984), Bernat et al. (1989), Costa et al. (2005) and Choque Fernandez et al. (2005).

(Pracejus and Bolton, 1992). Gallium in group 4 is related to its immobility or its association with Al-phosphates. Hollandite and coronadite also trap P_2O_5, especially in the Mn-greywacke (A3), where the phosphorous content of both minerals reaches up to 0.37% (Supplementary data files). In the hollandite of the phosphorous portions (sample Pd), the phosphorus content reaches up to 1.05%.

Group 5 (TiO_2, Zr, Hf, La and Nb) mostly identified soils, due to the resistance of rutile and zircon, along with the neoformation of anatase, under the harsher weathering conditions of Amazonia.

7.2. Sedimentary, hydrothermal and geochemical environments

Galena, native silver, coronadite, Pb-hollandite, anomalous Cu and high contents of Tl in the Mn-duricrusts of Novo Natal (45–97 ppm Tl) are similar to those of the gossans described by Calderoni et al. (1985) (which record an average value of 74 ppm). Also, the positive Gd anomalies in Novo Natal and Apuí ($Gd/Gd^* = 1.25–2.15$) are higher, similar to those recorded by the massive sulfides and Mn-deposits with hydrothermal sources ($Gd/Gd^* = 1.3–2.8$, Barrett et al., 1991, Zhao and Jiang, 2007 and Del Rio-Salas et al., 2013). Moreover, the sulfide source of the Novo Natal, Zé Julião and Apuí deposits is also supported by their correlations to the Cu, Pb and Zn concentrations of Australian gossans (Taylor and Scott, 1982; Scott et al., 2001) (Fig. 15A), while evidence of a hydrothermal influence is indicated by their (Zn/Ni)/MnO_2 ratios (Fig. 15B), although Apuí data plot in the sedimentary field. Hence, the Mn of Novo Natal, Zé Julião and Apuí are assigned to the Vila do Carmo Group, which is the Proterozoic volcano-sedimentary sequence of the Apuí region that was deposited in an intracontinental rift basin (Reis et al., 2013) under the influence of sulfide hydrothermal activity. The sulfide hydrothermal activity, which is correlated to the VMS deposits of Cu, Zn, Pb, Ag and Au and gossans (1.78–1.75 Ga) found in this region (i.e., the Juma, Sucunduri and Aripuanã Rivers) (Carvalho and Figueiredo, 1982; Leite et al., 2005 and Brito et al., 2010) are the most likely sources of Mn. This link between Mn and sulfide activity allows us to classify the Mn-deposits of Apuí, Zé Julião and Novo Natal as dubhite (Nicholson, 1992). On the other hand, the Mn-minerals of Beneficente and Holanda, which are more pure, have only a sedimentary source and could thus have been produced by supergene marine/fresh water related to the Beneficente Group, which represents a post-rifting sedimentary sequence (Fig. 15B).

7.3. Provenance of the Mn in the southwestern region of Amazonia

The rocks of the Sunsás, Rondônia Juruena and Tapajós Parima provinces were selected according to the provenance of the sedimentary rocks of the Sumaúma Supergroup postulated by Reis et al. (2013).

The REE/(Zr/Hf) vs $TiO_2 \times 1000/(Co/Ni)$ ratios of the Apuí, Zé Julião and Novo Natal deposits indicate that the felsic volcanic rocks of the Colíder Group and the granitic bodies of the Igarapé das Lontras and Teodósia suites of the Rondônia Juruena and Tapajós Parima provinces were the sources of the Mn of the Vila do Carmo Group (Fig. 16A). The Beneficente and Holanda deposits also record evidence of a felsic source, but are mainly assigned to the Serra da Providência intrusive suite, which records the contribution of the granitic suites of the Sunsás Province (1.45–1.10 Ga) of Santos et al. (2006). The Beneficente deposit also records the mafic rock sources of the Mata-Matá diabase, Serra da Providência, Trincheira Complex and the Nova Brasilândia Group (Fig. 16B). This mafic provenance is also indicated by the observed high contents of Co and Ni and the negative Tb anomalies recorded in the vermiform duricrusts (B2 to B4: $Tb/Tb^* = 0.21–0.33$), which are similar to those recorded in the Mata-Matá diabase ($Tb/Tb^* = 0.21–0.34$; CPRM, 2014).

8. Evolution of manganese and paleoenvironmental implications

The volcanic basement and intrusive granitic bodies (i.e., the Colíder Group and the Teodósia and Igarapé das Lontras intrusive suites), are structured within an intracontinental cratonic Paleoproterozoic rift basin (Reis et al., 2013), which served as a shelter for the rhythmites of the Vila do Carmo Group (Fig. 17A). The Teodósia intrusive suite, which records an average Mn concentration of 1064 ppm (CPRM, 2014) is the most likely source for the Mn of the Mn-greywackes of the Vila do Carmo Group. The downward circulation of warm waters heated by mantle convection (Fig. 17B) brought up Mn, Fe, Ba, Pb, Cu, Ag and Au leached from the VMS orebodies of the volcano-sedimentary rocks. Along fractures and veinlets, coronadite and hollandite formed in the pinkish siltstone (sample PS) of Novo Natal. Meanwhile, the Mn-greywackes (sample A3) overlapped the pinkish siltstone; their primary mineralogy was modified by hydrothermal activity, which formed hollandite in the matrix and coronadite and Pb-hollandite along fractures. This environment is similar to those found in Mn

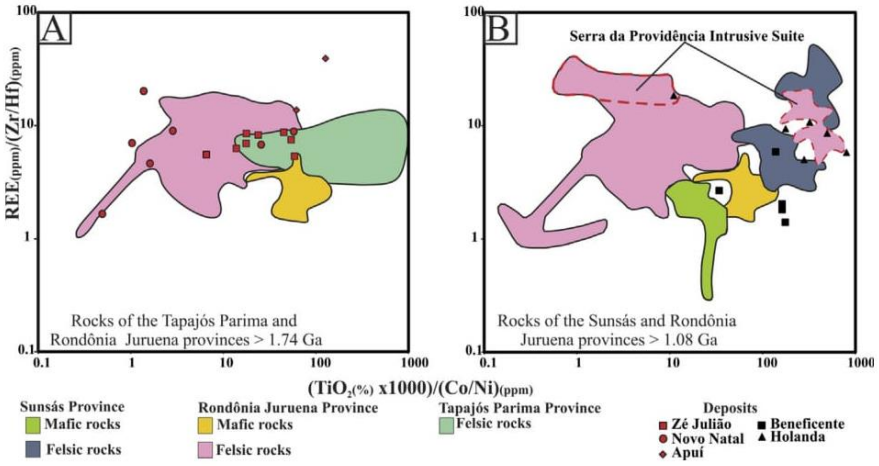

Fig. 16. (A and B) Provenance of the Mn Vila do Carmo and Beneficente Group, respectively, using ($TiO_2 \times 1000$)/(Co/Ni) vs REE/(Zr/Hf) data. The lithostratigraphic units are from Payolla (1994), Rizzotto (1999), Barros (2007), Valério et al. (2009), Brito et al. (2010), Rizzotto and Hartmann (2012), Scandolara et al. (2013), Barreto et al. (2014), CPRM (2014) and Da Silva et al. (2014).

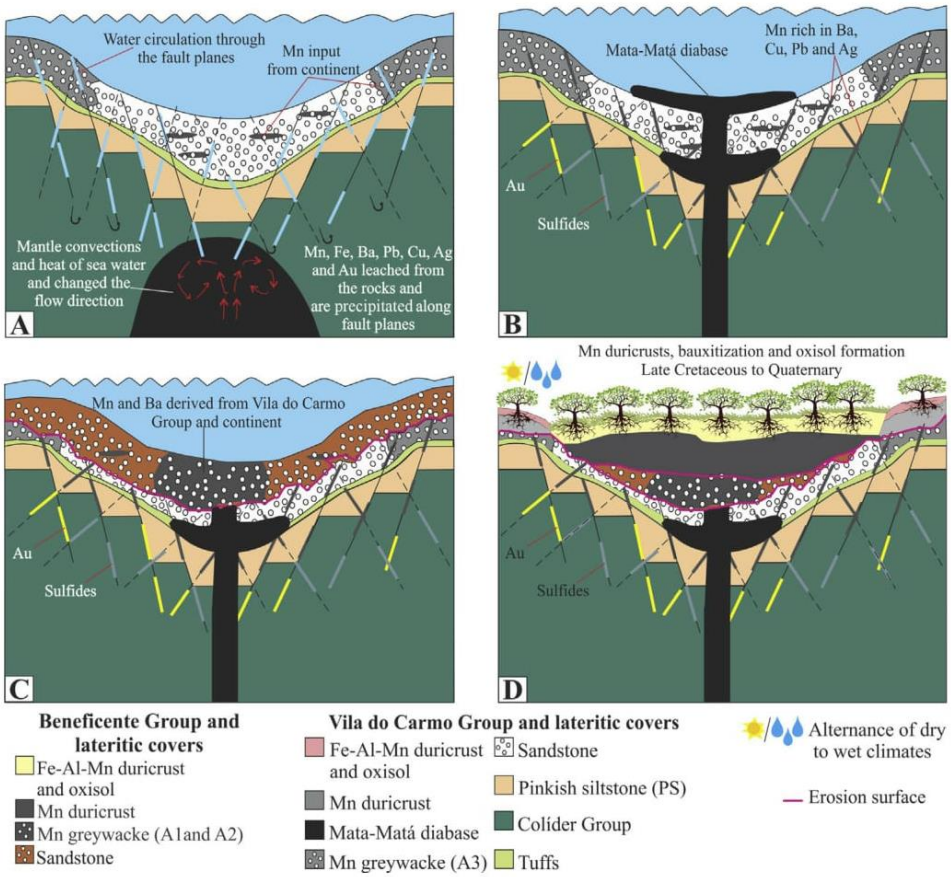

Fig. 17. Schematic evolution of the Mn ore in southwestern of Amazonia. (A) deposition of the volcano-sedimentary rocks of Vila do Carmo Group sediments in a paleoproterozoic rifte basin. Mantelic convection heat the sea water leaching Mn, Fe, Ba, Pb, Cu, Ag and Au from the volcano-sedimentary stacking. (B) Along the fault Mn, Cu and Pb as well as Au and sulfides were precipited. After that, mafic sills and dykes of Mata-Matá diabase (1576 Ga) intersected the volcano-sedimentary stacking. (C) Erosion followed by deposition of Beneficente Group during the Mesoproterozoic where Vila do Carmo Group and Mata-Matá diabase are the main source of Mn for the sediments. (D) Aggressive weathering with formation of lateritic crust during the Cenozoic.

deposits in Mexico (Freiberg, 1983), Greece (Liakopoulos et al., 2001) and India (Ghosh et al., 2015).

After the intrusion of sills and dykes of the Mata-Matá diabase into the Vila do Carmo Group, which was linked to mantle convection, erosional events occurred (as is indicated by the presence of angular discordance) (Reis et al., 2013) (Fig. 17C), and the Beneficente Group was deposited in a coastal Mesoproterozoic environment under the influence of fluvial channels (during the post-rift phase) (Fig. 17C). The erosion of the surrounding rocks, which were mostly granitic suites (i.e., the Sunsás Province and Serra da Providência intrusive suites) and the Vila do Carmo Group, with some contributions of the Mata-Matá diabase and mafic rocks from the Sunsás Province, represented the sources for the Mn of the Beneficente and Holanda deposits.

The presence of Paleozoic and Cenozoic sediments helped to partially protect the Proterozoic sedimentary rocks from erosion. However, when exposed to a drier climate following the Late Cretaceous, lateritic duricrusts with a large diversity of textures (i.e., massive, pisolitic, protopisolitic and vermiform) were formed (Fig. 17D). The most mobile elements were released, and new phases of coronadite, hollandite, cryptomelane and romanechite, which maintained the hydrothermal signature of the Vila do Carmo Group (i.e., the Novo Natal, Apuí and Zé Julião deposits) and the sedimentary signature of the Beneficente Group (i.e., the Holanda and Beneficente deposits), were formed. Concomitant to the transformations of the Mn-minerals and the accumulation of Mn, gibbsite was neoformed in the upper portion of the duricrust, as were goethite, hematite and kaolinite, based on the weathering of clastic minerals, which increased the present amounts of Fe_2O_3 and Al_2O_3 in accordance with the bauxitization process that affected all rocks within the region (Albuquerque and Horbe, 2015). The reactivation of normal faults and the incision of large rivers (i.e., Aripuanã, Sucunduri and Jatuarana) dissected the relief, degraded the duricrust and formed the Mn duricrust colluvium in Zé Julião and the Mn gravels spread throughout the region.

9. Conclusions

The Mn deposits of Novo Natal, Apuí and Zé Julião, which contain unusual amounts of Pb, Cu, Tl and Ag, were produced in the Proterozoic during a rift stage in a sedimentary environment belonging to the Vila do Carmo Group, which was supplied by volcanic and granitic rocks under the influence of hydrothermal activity. Additionally, the post-rift basin, which was supplied only by mafic and felsic rocks, experienced a second Mn deposition event, which produced the Beneficente and Holanda deposits. Lateritization formed duricrusts, and new generations of coronadite, hollandite, cryptomelane and romanechite inherited the geochemical signatures of the Mn-rocks. The preservation of duricrust in Apuí and Zé Julião as plateaus and in Holanda, Beneficente and Novo Natal as lower dissected relief occurred due to the erosion

promoted by the incision of large rivers and neotectonic activity during the Cenozoic.

Although this study was performed to identify the two geological environments of these Mn deposits, the Beneficente Group is the best target for future Mn geological surveys, due to the fact that it covers the largest area and records the most local hydrothermal processes. However, the influences of hydrothermal and sulfide activity identified in Novo Natal, Zé Julião and Apuí, based on the presence of high concentrations of Pb and its Gd and Tl anomalies, indicate that these areas represent good targets for VMS deposits.

Acknowledgments

The authors thank to the Postgraduate Program in Geology from the University of Brasilia, to CAPES for granting a PhD scholarship to the first author and CNPq for financial support (process n ° 471971/2010-3 and 473359/2012) and research grants of the second and third authors. We also thank the anonymous referees that provided helpful suggestions for improving the manuscript.

Appendix A. Supplementary data

Supplementary data associated with this article can be found, in the online version, at http://dx.doi.org/10.1016/j.oregeorev.2017.06.012.

References

Albuquerque, M.F.S., Horbe, A.M.C., 2015. Mineralogia, geoquímica e evolução da lateritização em Apuí, sudeste do Amazonas. Braz. J. Geol. 45, 569–590.

Barreto, C.J.S., Lafon, J.M., Costa, L.T.R., Lima, E.F., 2014. Paleoproterozoic (~1.89 Ga) felsic volcanism of the Iricoumé Group, Guyana Shield, South America: geochemical and Sm-Nd isotopic constraints on sources and tectonic environment. Int. Geol. Rev. 56, 1332–1356.

Barrett, T.J., Cattalani, S., Maclea, W.H., 1991. Massive sulfide deposits of the Noranda area, Quebec. I. The Horne mine. Can. J. Earth Sci. 28, 465–488.

Barros, A.J.P., 2007. Granitos da região de Peixoto de Azevedo – Novo Mundo e mineralizações auríferas relacionadas – Província Aurífera Alta Floresta (MT). PhD thesis, Campinas, Brazil, Universidade Estadual de Campinas, p. 154.

Bernat, M., Causse, C., Perseil, E.A., Feraud, G., 1989. Variations of element distribution in ferromanganese nodules and its bearing on growth rates. Miner. Deposita 24, 258–269.

Betiollo, L.M., Reis N.J., Almeida, M.E., Bahia, R.C., Splendor, F., Costa, U.P., Luzardo, R., 2009. Magmatismo Máfico, Calimiano (Sill Mata-Matá), rio Aripuanã, Amazonas- Implicações Geológicas. In: XI Simpósio de Geologia da Amazônia, Resumos Expandidos.

Braun, J., Pagel, M., Muller, J., Bilong, P., Michard, A., Guillet, B., 1990. Cerium anomalies in lateric profiles. Geochim. Cosmochim. Acta 54, 781–795.

Brito R.S., Silveira F.V., Larizzati J.H., 2010. Metalogenia do distrito aurífero do rio Juma- Nova Aripuanã-AM. Informe recursos minerais. Série Ouro, Brasília, CPRM.

Calagari, A.A., Abedini, A., 2007. Geochemical investigation on Permo-Triassic bauxite horizon at Kanisheeteh, east of Bukan, west-Azarbaidjan, Iran. J. Geochem. Explor. 94, 1–18.

Calderoni, G., Ferrini, V., Masi, U., 1985. Distribution and significance of Pb and Tl in the sulfides and host rocks from hydrothermal mineralization of the Tolfa Mountains (Latium, Central Italy). Chem. Geol. 51, 29–39.

Carvalho, M.S., Figueiredo, A.J., 1982. Caracterização Litoestratigráfica da Bacia de Sedimentação do Grupo Beneficente no Alto Rio Sucundurí-AM. 1st Amazon Geology Symposium, Belém, Brazil, Extended Abstracts, pp. 26–44.

Chisonga, B.C., Gutzmer, J., Beukes, N.J., Huizenga, J.M., 2012. Nature and origin of the protolith succession to the Paleoproterozoic Serra do Navio manganese deposit, Amapa Province, Brazil. Ore Geol. Rev. 47, 59–76.

Choque Fernandez, O.J., Costa, M.L., Pollmann, H., Ribeiro, P.A., Silva, N.C., 2005. Contribuições mineralógicas e geoquímicas sobre a origem do minério de manganês do Morro do Urucum (Corumbá, Brasil): 1st Brazilian Symposium of Metallogeny, Gramado, Brazil, Extended Abstracts, pp. 1–4.

Conly, A.G., Scott, S.D., Bellon, H., 2011. Metalliferous manganese oxide mineralization associated with the Boleo Cu-Co-Zn district, Mexico. Econ. Geol. 106, 1173–1196.

Cornell, D.H., Schutte, S.S., 1995. A volcanic-exhalative origin for the world's largest (Kalahari) manganese field. Miner. Deposita 30, 146–151.

Costa, M.L., Choque Fernandez, O.J., Requelme, M.E.R., 2005. Depósito de manganês do Azul, Carajás: estratigrafia, mineralogia, geoquímica e evolução geológica, In: Marini, O.J., Queiroz, E.T., Ramos, B.V., (Eds.). Caracterização de depósitos minerais em distritos mineiros da Amazônia. Departamento Nacional de Producao Mineral, Fundo Setorial de Recursos Minerais-Agencia para Desenvolvimento Tecnico da Industria Mineral Brasileira (ADIMB), Brasilia, pp. 227–333.

CPRM, 2013. Folha Sumaúma (SB.20-Z-D). Programa Geologia do Brasil. Carta geológica ao milionésimo-Escala 1:250.000. CPRM, Serviço Geológico do Brasil, Manaus.

CPRM, 2014. Geologia e recursos minerais da Folha Sumaúma – SB.20-Z-D, Estado do Amazonas, escala 1:250.000. CPRM, Serviço Geológico do Brasil, Manaus. Programa Geologia do Brasil – PGB. Levantamentos Geológicos Básicos do Brasil.

Da Silva, F.R., Barros, M.A.S., Pierosan, R., Pinho, F.E.C., Rocha, M.L.B., Vasconcelos, B. R., Dezula, S.E.M., Tavares, C., Rocha, J., 2014. Geoquímica e geocronologia U-Pb (SHRIMP) de granitos da região de Peixoto de Azevedo: Província Aurífera Alta Floresta, Mato Grosso. Braz. J. Geol. 44, 433–455.

Del Rio-Salas, R., Ochoa-Landín, L., Eastoe, C.J., Ruiz, J., Meza-Figueroa, D., Valencia-Moreno, M., Zúñiga-Hernández, H., Zúñiga-Hernández, L., Moreno-Rodríguez, V., Mendívil-Quijada, H., 2013. Genesis of manganese oxide mineralization in the Boleo region and Concepción Peninsula, Baja California Sur: constraints from Pb-Sr isotopes and REE geochemistry. Ver. Mex. Cienc. Geol. 30, 482–499.

Force, E.R., Paradis, S., Simandl, G.J., 1999. Sedimentary manganese, in selected British Columbia mineral deposit profiles. In: Simandl, G.J, Hora, Z.D., Lefebure, D.V. (Eds.), Industrial Minerals, London, British Columbia Geological Survey Open-file, pp. 47–50.

Frakes, L., Bolton, B., 1992. Effects of ocean chemistry, sea level, and climate on the formation of primary sedimentary manganese ore deposits. Econ. Geol. 87, 1207–1217.

Freiberg, D.A., 1983. Geologic setting and origin of the Lucifer manganese deposit, Baja California Sur, Mexico. Econ. Geol. 78, 931–943.

Ghosh, R., Chakraborty, D., Halder, M., Baidya, T.K., 2015. Manganese mineralization in Archean greenstone belt, Joda-Noamundi sector, Noamundi basin, East Indian Shield. Ore Geol. Rev. 70, 96–109.

Glasby, G.P., Papavassiliou, C.T., Liakopoulos, A., Galanopoulos, V., 2001. Past mining of the Vani manganese deposit, Milos Island, Greece. 5th International Mining History Congress, Milos, pp. 93–105.

Gonçalves, E., Serfaty, A., 1976. Perfil analítico do manganês. Departamento Nacional da Produção Mineral/DNPM, Brasília.

Gutzmer, J., Beukes, N.J., 1996. Mineral paragenesis of the Kalahari manganese field, South Africa. Ore Geol. Rev. 11, 405–428.

Kotschoubey, B., Truckenbrodt, W., Calaf, J.M.C., 2005. Evolução Geológica da Porção Meridional da Província Bauxitífera de Paragominas durante o Neógeno/Pleistoceno (Noroeste da Bacia do Grajaú, Nordeste do Pará e Extremo oeste do Maranhão). Braz. J. Geol. 35, 263–272.

Leal, P.R., Correa, M.J., Ametrano, S.J., Etcheverry, R.O., De Brodtkorb, M.K., 2008. The manganese deposits of the Pampean Ranges, Argentina. Can. Mineral 46, 1215–1233.

Leite, J.A.D., Sousa, M.Z.A., Saes, G.S., Macambira, M.J.B., Xavier, R.P., Siqueira, A.J., Batata, M.E.F., Oliveira, F.A., Silva Jr, J.G., Quadros, A.P., 2005. Caracterização do Depósito Polimetálico (Zn, Pb, Ag, Cu-Au) de Aripuanã, Mato Grosso. In: Marini, O. J., Queiroz, E. T., and Ramos, B.V. (Eds.), Caracterização de depósitos minerais em distritos mineiros da Amazônia, Brasilia, Departamento Nacional de Producao Mineral, Fundo Setorial de Recursos Minerais-Agencia para Desenvolvimento Técnico da Industria Mineral Brasileira (ADIMB), pp. 601–686.

Liakopoulos, A., Glasby, G.P., Boulegue, J., 2001. Nature and origin of the Vani manganese deposit, Milos, Greece: an overview. Ore Geol. Ver. 18, 181–209.

Liberatore, G., Alecrim, J.D., Medeiros, J.B., Malouf, R.F., Pinheiro, S.S., Achão, S.M., Santos, J.O.S., 1972. Projeto Aripuanã – Sucundurí, DNPM/CPRM, Manaus.

Maynard, J.B., 2014. Manganiferous Sediments, Rocks, and Ores. In: Holland, H.D., Turekian, K.K. (Eds.), Treatise on Geochemistry, Second Edition. Elsevier, pp. 327–349.

Maynard, J.B., 2010. The chemistry of manganese ores through time: a signal ofincreasing diversity of earth – surface environment. Econ. Geol. 105, 535–552.

Middelburg, J.J., Van Der Weijden, C.H., Woittiez, J.R.M., 1988. Chemical processes affecting the mobility of major, minor and trace elements during weathering of granitic rocks. Chem. Geol. 68, 253–273.

Moorby, S.A., Cronan, D.S., Galsby, G.P., 1984. Geochemistry of hydrothermal Mn-oxide deposits from the S.W. Pacific island arc. Geochim. Cosmochim. Acta 48, 433–441.

Nicholson, K., 1992. Contrasting mineralogical-geochemical signatures of manganese oxides: guides to metallogenesis. Econ. Geol. 87, 1253–1264.

Nicholson, K., Nayak, V.K., Nanda, J.K., 1997. Manganese ores of the Ghoriajhor Monmunda area, Sundergarh District, Orissa, India: geochemical evidence for a mixed Mn source. In: Nicholson, K., Hein, J.R., Buhn, B., Dasgupta, S. (Eds.), Manganese Mineralization: Geochemistry and Mineralogy of Terrestrial and Marine Deposits. Geological Society, London, pp. 117–121. Special Publication.

Ohta, A., Kawabe, I., 2001. REE (III) adsorption onto Mn dioxide (d-MnO_2) and Fe oxyhydroxide: Ce (III) oxidation by d-MnO_2. Geochim. Cosmochim. Acta 65, 695–703.

Okita, P.M., 1992. Manganese carbonate mineralization in the Molango District, Mexico. Econ. Geol. 87, 1345–1366.

O'Reilly, G.A., 1992. Petrographic and Geochemical Evidence for a Hypogene Origen of Granite- Hosted, Vein Type Mn Mineralization at the New Ross Mn Deposits, Lunenburg County, Nova Scotia. Can. Econ. Geol. 87, 1275–1300.

Payolla, B.L., 1994. As rochas graníticas e sieníticas das cachoeiras Teotônio e Santo Antônio, rio Madeira, Porto Velho, Rondônia: geologia, petrografia e geoquímica. Msc thesis, Brasília, Brazil, Universidade de Brasília, p. 145.

Post, J.E., 1999. Manganese oxide minerals crystals structures and economic and environmental significance. Proc. Natl. Acad. Sci. U.S.A. 96, 3447–3454.

Pracejus, B., 1989. Nature and formation supergene manganese deposits on Groote Eylandt, N.T., Australia, Unpublished. Ph.D thesis, Adelaide University, p. 231.
Pracejus, B., Bolton, B.R., 1992. Geochemistry of supergene manganese oxide deposits, Groote Eylandt. Aust. Econ. Geol. 87, 1310–1335.
Reis, N.J., Bahia, R.B.C., Almeida, M.E., Costa, U.A.P., Betiollo, L.M., de Oliveira, A.C., Splendor, F., 2013. O supergrupo Sumaúma no contexto geológico da Folha SB.20-Z-D (SUMAÚMA), sudeste do Amazonas: modo de ocorrência, discussão de idades em zircões detríticos e correlações no SW do Cráton do Amazonas. In: Wankler, F.L., Holanda, E.C., Vasques, M.L. (Eds.), Contribuições à Geologia da Amazônia, Belém, pp. 199–222.
Rizzotto, G.J., 1999. Petrologia e geotectônica do Grupo Nova Brasilândia, Rondônia. Msc thesis. Porto Alegre, Brazil, Federal University of Rio Grande do Sul, p. 131.
Rizzotto, G.J., Hartmann, L.A., 2012. Geological and geochemical evolution of the Trincheira Complex, a mesoproterozoic ophiolite in the southwestern Amazon Craton, Brazil. Lithos. 148, 277–295.
Rodrigues, O.B., Kosuki, R., Coelho Filho, A., 1986. Distrito manganesífero de Serra do Navio, Amapá. In: Schobbenhaus, C., Coelho, C.E.S. (Eds). Principais Depósitos Minerais do Brasil, DNPM/CVRD, pp. 167–175.
Roy, S., 1992. Enviroments and process of manganese deposition. Econ. Geol. 87, 1218–1236.
Roy, S., 1997. Genetic diversity of manganese deposition in the terrestrial geological record, In: Nicholson, K., Hein, J., Bühn, B., Dasgupta, S. (Eds.). Manganese Mineralisation: Geochemistry and Mineralogy of Terrestrial and Marine Deposits, Special Publication—Geological Society of London, London, pp. 5–27.
Roy, S., 2006. Sedimentary manganese metallogenesis in response to the evolution of the Earth system. Earth-Sci. Rev. 77, 273–305.
Roy, S., Purkait, P.K., 1968. Mineralogy and genesis of the metamorphosed manganese silicate rocks (gondite) of Gowari Wadhona, Madhya Pradesh, India. Contrib. Mineral. Petr. 20, 86–114.
Santos, J.O.S., 2003. Geotectônica dos Escudos das Guianas e Brasil Central. In: Bizzi, L.A., Schobbenhaus, C., Vidotti, R.M., Gonçalves, J.H. (Eds.). Geologia, Tectônica e Recursos Minerais Minerais do Brasil: texto, mapas e SIG. CPRM- Serviço Geológico do Brasil, pp. 169–226.
Santos, J.O.S., Hartmann, L.A., Faria, M.S.G. de, Riker, S.R.L., Souza, M.M. de, Almeida, M.E., McNaughton, N.J., 2006. A compartimentação do Cráton Amazonas em Províncias: Avanços ocorridos no período 2000–2006. In: SBG- Núcleo Norte, Simp. Geol. Amaz., 9, Belém, PA, Resumos Expandidos.CD-Rom.
Scandolara, J.E., Fuck, R.A., Dall'Agnol, R., Dantas, E.L., 2013. Geochemistry and origin of the early Mesoproterozoic mangerite-charnockite-rapakivi granite association of the Serra da Providência suite and associated gabbros, central-eastern Rondônia, SW Amazonian Craton, Brasil. J. South Am. Earth Sci. 45, 166–193.
Scott, K.M., Ashley, P.M., Lawie, D.C., 2001. The geochemistry, mineralogy and maturity of gossans derived from volcanogenic Zn-Pb-Cu deposits in the eastern Lachlan Fold Belt, NSW. Aust. J. Geochem. Explor. 72, 169–191.
Silva, P.J.M., Horbe, A.M.C., Horbe, M.A., 2012. Mineralogia e geoquímica de ocorrências manganesíferas da bacia Alto Tapajós, sudeste do Amazonas, Brasil. Bol. Mus. Para. Emílio Goeldi. Cienc. Nat. 7, 11–28.
Taylor, G.F., Scott, K.M., 1982. Evaluation of mineralisation Queensland gossans in relation to lead-zinc in the Mount Isa Inlier, Queensland. J. Aust. Geol. Geophys. 7, 159–180.
Taylor, S.R., McLennan, S.M., 1985. The continental crust: its composition and evolution. An Examination of the Geochemical Record Preserved in Rocks. Blackwell Scientific Publications, Oxford.
Valério, C.S., Souza, V.S., Macambira, M.J.B., 2009. The 1.90–1.88 Ga magmatism in the southernmost Guyana Shield, Amazonas, Brazil: geology, geochemistry, zircon geochronology, and tectonic implications. J. South Am. Earth Sci. 28, 304–320.
Zantop, H., 1978. Geologic setting and genesis of iron oxides and manganese oxides in the San Francisco manganese deposit, Jalisco, Mexico. Econ. Geol. 73, 1137–1149.
Zhao, K., Jiang, S., 2007. Rare earth element and yttrium analyses of sulfides from the Dachang Sn-polymetallic ore field, Guangxi Province, China: implication for ore genesis. Geochem. J. 41, 121–134.

APPENDIXS

For mineral quantification obeying the following criteria, was obtained by stoichiometric calculations with the aid of XRD patterns and chemical composition and the centesimal mineral composition of "webmineral.com" (Table A1):

1. Convert MnO of the bulk-rock geochemistry, of the sample into MnO_2, as well as, Ba into BaO, Pb into PbO and V into V_2O_5.

2. Whenever the mineral assemblage includes cryptomelane (C), romanechite (Ro) and hollandite (Ho), some rules must be followed to mineral quantification. For being the only mineral to have potassium, cryptomelane is the first mineral to be calculated according Equation 1.

Equation 1: $C= [K_2O_{(sample)} \times MnO_{2(centesimal\ composition)}] / K_2O_{(centesimal\ composition)}$.

All K_2O of the sample is used to calculate cryptomelane. Then, the content of cryptomelane (C) must be subtracted from the content of MnO_2 of bulk-rock geochemistry sample. To calculate romanechite (Ro) and hollandite (Ho), is used a math system involving BaO and MnO_2 content's related to romanechiteand hollandite, respectively, according Equation 2:

Equation 2: $$\begin{cases} 14.38Ho+19.72Ro=BaO_{(sample)} \\ 65.57Ho+76.65Ro=MnO_{2(sample)}\text{- (C)} \end{cases}$$

Where 14.38% and 19.72% are the content of $BaO_{(centesimal)}$ in hollandite and romanechite, respectively, and 67.27% and 76.65% are the content of MnO_2 in these minerals. The next step is substitute the Ho and Ro values on equation to obtain MnO_2. These MnO_2 values represent the centesimal content of romanechite and hollandite in the sample.

3. Whenever the mineral assemblage includes cryptomelane (C), coronadite (Co), hollandite (Ho) and/or romanechite (Ro) and pyrolusite (Py), see Table A2.

4. Some cautions should be considered, when:

- Samples without quartz (Q), but with kaolinite (K) and gibbsite (Gb), all content of SiO_2 is assigned to kaolinite. For the other minerals following Table A3.
- When quartz, kaolinite and gibbsite coexist, the content of quartz is estimate based at the main reflection of x-ray diffractogram. Then, the calculation of kaolinite and gibbsite must be calculated according Table A3.
- Samples with high amounts of Pb (4.7% of PbO) and low contents of V (< 4 ppm) inhibited the quantification of coronadite from vanadium. Thus, a math system is

used in order to determinate the contents of coronadite (Co) and hollandite (Ho) using Equation 3

$$\text{Equation 3: } \begin{cases} 1.64Co+14.38Ho=BaO_{(sample)} \\ 26.3Co+5.23Ho= PbO_{(sample)} \end{cases}$$

- After calculate the values of coronadite (Co) and hollandite (Ho) and substitute in equation 3 to know the content of BaO and PbO consumed by coronadite and hollandite. The next step is calculate the real content of coronadite and hollandite according to Equation 4.
- Equation 4: Co= 71.71% x $BaO_{(Co)}$ / 1.64% or 71.71% x $PbO_{(Co)}$ 26.3%; / Ho= 67.27% x $BaO_{(Ho)}$/ 14.38% or 67.27% x $PbO_{(Ho)}$/ 5.23%; Note: 71.71% and 67.27% refer to the percentage of MnO + MnO_2 of coronadite and hollandite, as well as, 26.3% and 5.23% and 1.64% and 14.38% to the percentage centesimal composition of PbO and BaO at coronadite and hollandite, respectively.

Table A1: Centesimal composition of the minerals (webmineral.com)

Mineral	Centesimal composition
Hollandite (Ho)	SiO_2= 0.70 %; Fe_2O_3= 12.17 %; Al_2O_3=1.20%; BaO = 14.38 %; Na_2O= 0.36 %; 4.16 % MnO / 62.17 % MnO_2; PbO= 5.23%
Romanechite (Ro)	SiO_2= 1.10 %; BaO = 19.72 %; MnO_2= 76.65%; H_2O= 3.97 %
Cryptomelane (C)	K_2O= 6.41 %; MnO_2 = 94.66%
Coronadite (Co)	Al_2O_3= 0.55%; BaO = 1.64 %; PbO= 26.3; 3.80 % MnO / 67.05 % MnO_2; V_2O_5= 1.95%
Pyrolusite (Py)	100% MnO_2
Quartz (Q)	100% SiO_2
Kaolinite (K)	Al_2O_3 = 39.5 %; SiO_2 = 46.49 %; H_2O =14.01 %
Gibbsite	Al_2O_3= 65.37 %; H_2O = 34.63 %
Hematite (He)	100% Fe_2O_3
Goethite (Gt)	Fe_2O_3= 89.86 %; H_2O = 10.14 %
Anatase/ rutile (An/Ru)	100% TiO_2

Table A1: Mineral and sequence of calculations of mineral composition (* content of the element to form the mineral; S- element amount in whole rock).

Sequence	Mineral	How to calculate
1°	Cryptomelane (C)	C= [$K_2O_{(S)}$ x $MnO_{2(C)}$] / $K_2O_{(C)}$
2°	Coronadite (Co)	Co=[$V_2O_{5(S)}$ x $MnO_{2(Co)}$] / $V_2O_{5(Co)}$ $BaO^*_{(Co)}$= [Co x $BaO_{(Co)}$]/100 $Al_2O_3{}^*_{(Co)}$= [Co x $Al_2O_{3(Co)}$]/100 Sample without hollandite: Co=[$PbO_{(S)}$ x $MnO_{2(Co)}$] / $PbO_{(Co)}$
3°	Romanechite (Ro)	Ro= [$MnO_{2(S)}$ - Co - C] x 100 / $MnO_{2(Ro)}$ $SiO_2{}^*_{(Ro)}$= [Rox $SiO_{2(Ro)}$] /100 $H_2O^*_{(Ro)}$= [Ro x $H_2O_{(Ro)}$] /100 Samples with pyrolusite: Ro= [$BaO_{(S)}$- $BaO^*_{(Co)}$] x $MnO_{2(Ro)}$ / $BaO_{(Ro)}$
3°	Hollandite (Ho)	Ho= [$MnO_{2(S)}$ - Co - C] x 100 / $MnO_{2(Ho)}$ $SiO_2{}^*_{(Ho)}$= [Ho x $SiO_{2(Ho)}$] /100 $Al_2O_3{}^*_{(Ho)}$= [Ho x $Al_2O_{3(Ho)}$] /100 $Fe_2O_3{}^*_{(Ho)}$= [Ho x $Fe_2O_{3(Ho)}$] /100 Samples with pyrolusite: Ho= [$BaO_{(S)}$- $BaO_{(Co)}$] x $MnO_{2(Ho)}$ / $BaO_{(Ho)}$
4°	Quartz (Q)	Q= $SiO_{2(S)}$ - ($SiO_{2(Ro)}$ and/or $SiO_{2(Ho)}$)
5°	Gibbsite (Gb)	Gb= ($Al_2O_{3(S)}$ -$Al_2O_{3(Ho)}$ and/or $Al_2O_{3(Co)}$) x 100 / $Al_2O_{3(Gb)}$ $H_2O_{(Gb)}$= [Gb x $H_2O_{(Gb)}$]/100
6°	Hematite (He) Goethite (Gt)	% of $Fe_2O_{3(Gt)}$ ={[$Fe_2O_{3(Gt)}$ x ($H_2O_{(S)}$ - $H_2O^*_{(Gb)}$ - and/or $H_2O^*_{(Ro)}$)] / $H_2O_{(Gt)}$}/100 Gt= ($Fe_2O_{3(S)}$ - $Fe_2O_3{}^*_{(Ho)}$) x % of $Fe_2O_{3(Gt)}$ He= $Fe_2O_{3(S)}$ – Gt
7°	Anatase/ rutile (An/Ru)	All content of TiO_2
8°	Pyrolusite (Py)	Py= $MnO_{2(S)}$- Co – Ho or Ro

Table A3: Sequence of calculation whenever the mineral assemblage is composed by quartz, kaolinite, hematite, goethite and anatase (* content of the element to form the mineral; S-element amount in whole rock).

Sequence	Mineral	How to calculate
1°	Quartz (Q)	$Q = \text{value estimated}/SiO_{2\,(ws)}$
2°	Kaolinite (K)	$K = (SiO_{2\,(ws)} - Q) \times 100/SiO_{2(cc)}$ $Al_2O_3{}^*_{(K)} = K \times Al_2O_{3\,(cc)}/100$ $H_2O^*_{(K)} = K \times H_2O_{(cc)}/100$
3°	Gibbsite (Gb)	$Gb = (Al_2O_{3\,(ws)} - Al_2O_{3(K)}) \times 100/Al_2O_{3\,(cc)}$ $H_2O^*_{(Gb)} = K \times H_2O_{(cc)}/100$
4°	Hematite (He) Goethite (Gt)	$\%\ \text{of Fe}_{(Gt)} = \{[Fe_2O_{3(Gt)} \times (H_2O_{(ws)} - H_2O^*_{(K)})]/H_2O_{(Gt)}\}/100$ $Gt = (Fe_2O_{3(S)} \times \%\ \text{of Fe}_{(Gt)}$ $He = Fe_2O_{3(S)} - Gt$
5°	Anatase/ rutile	All content of TiO_2

Table A4: Microprobe analysis of coronadite in Mn rocks and related duricrusts.

		Coronadite													
Lithotype	Sample	SiO_2	Al_2O_3	Fe_2O_3	K_2O	CaO	P_2O_5	MnO_2	Na_2O	CuO	CoO	BaO	PbO	V_2O_3	∑(%)
Mn greywacke	A3	0.38	0.91	4.49	0.00	0.03	0.33	61.63	0.04	0.58	0.11	2.60	26.42	0.05	97.56
Mn greywacke	A3	0.42	0.93	7.49	0.00	0.05	0.19	59.25	0.04	0.65	0.18	2.17	25.14	0.02	96.49
Mn greywacke	A3	0.37	0.97	5.35	0.00	0.05	0.35	60.99	0.00	0.56	0.19	1.84	26.78	0.06	97.51
Mn greywacke	A3	0.42	1.25	6.14	0.00	0.01	0.37	60.41	0.05	0.62	0.19	1.73	26.91	0.16	98.26
Mn greywacke	A3	0.45	0.93	2.53	0.00	0.04	0.21	67.83	0.00	0.74	0.28	8.09	16.57	0.00	97.68
Mn greywacke	A3	0.40	0.87	3.24	0.00	0.02	0.28	63.92	0.05	0.55	0.14	2.25	25.82	0.15	97.69
Pinksih siltstone	PS	0.26	1.02	3.62	0.00	0.04	0.28	64.19	0.02	0.69	0.21	5.94	19.86	0.20	96.32
Pinksih siltstone	PS	0.08	0.83	0.11	0.00	0.00	0.00	67.12	0.01	0.80	0.08	1.83	26.63	0.00	97.48
Pinksih siltstone	PS	0.07	0.57	0.13	0.00	0.01	0.00	67.99	0.00	0.79	0.07	0.30	28.84	0.00	98.76
Pinksih siltstone	PS	0.04	0.66	0.13	0.00	0.00	0.00	67.68	0.00	0.70	0.09	0.89	28.68	0.17	99.06
Pinksih siltstone	PS	0.08	0.56	0.11	0.00	0.00	0.00	67.17	0.01	0.62	0.05	0.45	28.81	0.00	97.85
Pinksih siltstone	PS	0.09	1.17	0.16	0.00	0.03	0.00	71.07	0.04	0.64	0.09	6.13	18.44	0.00	97.85
Pinksih siltstone	PS	0.04	0.92	0.29	0.00	0.04	0.02	68.73	0.03	0.70	0.16	2.02	25.67	0.24	98.85
Pinksih siltstone	PS	0.06	0.57	0.10	0.00	0.03	0.00	69.08	0.03	0.68	0.10	0.95	27.69	0.03	99.32
Pinksih siltstone	PS	0.09	0.56	0.12	0.00	0.00	0.01	67.99	0.00	0.94	0.09	0.41	28.11	0.00	98.32
Pinksih siltstone	PS	0.04	0.86	0.31	0.00	0.00	0.00	69.07	0.00	0.62	0.11	0.76	28.88	0.03	100.69
Pinksih siltstone	PS	0.06	0.90	0.18	0.00	0.02	0.00	70.23	0.03	0.53	0.14	2.72	24.97	0.00	99.78
Pinksih siltstone	PS	0.11	0.85	0.17	0.01	0.02	0.00	69.40	0.00	0.59	0.17	3.80	22.63	0.04	97.79
Pinksih siltstone	PS	0.08	0.67	0.26	0.00	0.00	0.06	68.67	0.00	0.67	0.14	0.38	28.27	0.00	99.20
Pinksih siltstone	PS	0.05	0.69	0.14	0.00	0.01	0.00	69.22	0.04	0.47	0.08	0.83	28.31	0.26	100.10
Pinksih siltstone	PS	0.10	0.99	0.27	0.00	0.00	0.00	71.20	0.04	0.62	0.22	5.06	20.27	0.02	98.79
Pinksih siltstone	PS	0.16	0.80	0.17	0.00	0.04	0.00	68.12	0.07	0.63	0.18	2.52	23.90	0.06	96.65
Duricrust	VB/VT	0.32	0.97	5.90	0.03	0.03	0.00	60.07	0.06	0.48	1.54	2.10	24.42	0.00	95.91
Duricrust	VB/VT	0.33	1.37	5.58	0.20	0.04	0.00	60.48	0.12	0.75	1.28	2.90	20.57	0.07	93.69

Table A5: Chemical composition and formula units based on 16 oxygens and $Mn^{4+/}Mn^{2+}$ of the coronadite calculated assuming full site occupancy

Coronadite																					
Lithotype	Pinkish Siltstone													Mn sandstone							Duricrust	
Sample	PS	PS	PS	PS	PS	PS	OS	PS	PS	PS	PS	PS	PS	A3	A3	A3	A3	A3	A3	A3	VB/VT	VB/VT
Al_2O_3	1.17	0.92	0.57	0.56	0.86	0.90	0.85	0.67	0.69	0.99	0.80	0.57	0.66	0.91	0.93	0.97	1.25	0.89	0.93	0.87	0.97	1.37
P_2O_5	0.00	0.00	0.00	0.00	0.00	0.00	0.00	0.00	0.00	0.00	0.00	0.00	0.00	0.33	0.19	0.35	0.37	0.20	0.21	0.28	0.00	0.00
Fe_2O_3	0.16	0.29	0.10	0.12	0.31	0.18	0.17	0.26	0.14	0.27	0.17	0.13	0.13	4.49	7.49	5.35	6.14	14.31	2.53	3.24	5.90	5.58
MnO_2	64.39	62.79	63.14	62.44	63.53	64.02	63.14	62.81	63.13	64.45	61.97	62.50	62.34	56.99	54.40	56.14	55.66	49.82	61.68	58.45	55.02	54.88
MnO	5.45	4.84	4.85	4.53	4.52	5.06	5.11	4.78	4.97	5.51	5.02	4.48	4.36	3.78	3.95	3.96	3.87	5.00	5.02	4.46	4.12	4.57
PbO	18.44	25.67	27.69	28.11	28.88	24.97	22.63	28.27	28.31	20.27	23.90	28.84	28.68	26.42	25.14	26.78	26.91	21.74	16.57	25.82	24.42	20.57
CuO	0.64	0.70	0.68	0.94	0.62	0.53	0.59	0.67	0.47	0.62	0.63	0.79	0.70	0.58	0.65	0.56	0.62	0.49	0.74	0.55	0.48	0.75
CoO	0.09	0.16	0.10	0.09	0.11	0.14	0.17	0.14	0.08	0.22	0.18	0.07	0.09	0.11	0.18	0.19	0.19	0.20	0.28	0.14	1.54	1.28
BaO	6.13	2.02	0.95	0.41	0.76	2.72	3.80	0.38	0.83	5.06	2.52	0.30	0.89	2.60	2.17	1.84	1.73	2.61	8.09	2.25	2.10	2.90
V_2O_5	0.00	0.20	0.03	0.00	0.03	0.00	0.04	0.00	0.21	0.02	0.05	0.00	0.15	0.06	0.02	0.07	0.19	0.14	0.00	0.18	0.00	0.09
∑ (%)	96.22	97.15	97.90	96.99	99.20	98.21	96.15	97.58	98.62	96.91	94.89	97.68	98.00	96.27	95.10	96.21	96.94	95.39	96.05	96.24	94.54	91.98
Formula units based on 16 oxygens and Mn^{4+}/Mn^{2+} calculated assuming full site occupancy																						
Al^{3+}	0.21	0.17	0.11	0.11	0.16	0.16	0.16	0.13	0.13	0.18	0.15	0.11	0.12	0.18	0.18	0.19	0.24	0.18	0.17	0.17	0.19	0.27
P	0.00	0.00	0.00	0.00	0.00	0.00	0.00	0.00	0.00	0.00	0.00	0.00	0.00	0.05	0.03	0.05	0.05	0.03	0.03	0.04	0.00	0.00
Fe^{3+}	0.01	0.02	0.01	0.01	0.02	0.01	0.01	0.02	0.01	0.02	0.01	0.01	0.01	0.37	0.64	0.45	0.51	1.23	0.20	0.27	0.50	0.47
Mn^{4+}	6.86	6.85	6.92	6.92	6.88	6.89	6.88	6.90	6.88	6.86	6.88	6.92	6.89	6.54	6.37	6.46	6.37	5.89	6.69	6.61	6.43	6.40
Mn^{2+}	0.71	0.65	0.65	0.62	0.60	0.67	0.68	0.64	0.66	0.72	0.68	0.61	0.59	0.53	0.57	0.56	0.54	0.72	0.67	0.62	0.59	0.65
Pb	0.77	1.09	1.18	1.21	1.22	1.05	0.96	1.21	1.20	0.84	1.03	1.24	1.23	1.18	1.15	1.20	1.20	1.00	0.70	1.14	1.11	0.93
Cu	0.07	0.08	0.08	0.11	0.07	0.06	0.07	0.08	0.06	0.07	0.08	0.10	0.08	0.07	0.08	0.07	0.08	0.06	0.09	0.07	0.06	0.10
Co	0.01	0.02	0.01	0.01	0.01	0.02	0.02	0.02	0.01	0.03	0.02	0.01	0.01	0.01	0.02	0.03	0.03	0.03	0.04	0.02	0.21	0.17
Ba	0.37	0.12	0.06	0.03	0.05	0.17	0.23	0.02	0.05	0.31	0.16	0.02	0.06	0.17	0.14	0.12	0.11	0.17	0.50	0.14	0.14	0.19
V	0.00	0.02	0.00	0.00	0.00	0.00	0.00	0.00	0.02	0.00	0.01	0.00	0.02	0.01	0.00	0.01	0.02	0.02	0.00	0.02	0.00	0.01
∑ (%)	9.02	9.03	9.02	9.02	9.02	9.02	9.03	9.02	9.02	9.03	9.03	9.02	9.02	9.11	9.18	9.13	9.15	9.34	9.08	9.09	9.23	9.21

Table A6: Microprobe analysis of hollandite in Mn rocks and related duricrusts.

Hollandite															
Lithotype	Sample	SiO_2	Al_2O_3	Fe_2O_3	K_2O	CaO	P_2O_5	MnO_2	Na_2O	CuO	CoO	BaO	PbO	V_2O_3	∑(%)
Pinkish siltstone	PS	0.15	0.66	0.23	0.00	0.02	0.01	74.83	0.03	0.72	0.34	16.90	2.67	0.00	96.56
Pinkish siltstone	PS	0.11	0.34	0.10	0.02	0.03	0.00	68.60	0.07	0.43	0.12	15.50	1.87	0.00	87.18
Pinkish siltstone	PS	0.33	0.31	0.23	0.00	0.07	0.01	74.86	0.05	0.63	0.29	17.59	2.25	0.00	96.61
Pinkish siltstone	PS	0.34	0.22	0.23	0.00	0.07	0.00	74.97	0.05	0.49	0.23	17.61	2.03	0.11	96.35
Pinkish siltstone	PS	0.09	0.35	0.14	0.02	0.04	0.00	71.66	0.08	0.46	0.05	15.30	1.76	0.04	89.97
Pinkish siltstone	PS	0.09	0.60	0.16	0.01	0.03	0.00	72.57	0.05	0.40	0.10	13.69	5.67	0.07	93.44
Mn greywacke	A3	0.20	0.60	1.54	0.05	0.10	0.35	71.31	0.07	0.64	0.11	13.83	4.60	0.00	93.39
Mn greywacke	A3	0.27	0.73	5.31	0.01	0.09	0.28	70.36	0.01	0.66	0.16	12.62	5.62	0.01	96.12
Mn greywacke	A3	0.19	0.39	9.27	0.07	0.09	0.27	68.51	0.07	0.48	0.08	14.62	1.65	0.00	95.68
Mn greywacke	A3	0.13	0.32	0.15	0.03	0.06	0.30	75.13	0.05	0.59	0.14	16.73	1.14	0.15	94.92
Mn greywacke	A3	0.10	0.33	0.14	0.63	0.15	0.12	77.53	0.05	0.62	0.09	14.20	1.65	0.00	95.62
Mn greywacke	A3	0.11	0.35	0.15	0.64	0.13	0.12	76.24	0.04	0.58	0.09	13.92	1.50	0.08	93.94
Mn greywacke	A3	0.27	0.45	0.19	0.03	0.09	0.15	75.12	0.04	0.57	0.12	15.66	1.40	0.00	94.08
Mn greywacke	A3	0.15	0.40	0.30	0.04	0.06	0.08	75.12	0.03	0.59	0.10	16.63	1.36	0.10	94.96
Mn greywacke	A3	0.48	0.40	0.17	0.04	0.10	0.17	74.26	0.07	0.53	0.14	16.26	1.63	0.00	94.24
P duricrust	Pd	0.56	3.81	2.14	0.67	0.04	1.05	69.38	0.01	1.56	0.51	13.63	0.84	0.00	94.19
P duricrust	Pd	0.38	3.96	1.49	0.63	0.04	0.82	70.57	0.03	1.45	0.48	13.15	0.94	0.00	93.92
P duricrust	Pd	0.45	3.98	1.55	0.31	0.01	0.31	69.71	0.04	0.99	0.39	14.25	1.71	0.00	93.68
P duricrust	Pd	0.39	4.62	1.23	0.50	0.03	0.75	69.69	0.02	1.71	0.55	14.08	1.59	0.00	95.16
P duricrust	Pd	1.19	4.29	7.02	2.09	0.02	0.68	69.11	0.01	0.54	0.27	6.17	3.43	0.23	95.06
P duricrust	Pd	0.51	4.34	3.22	0.31	0.00	0.35	63.86	0.08	0.57	0.30	12.64	2.79	0.06	89.02
Duricrust	Z7-8	0.11	0.64	0.14	0.03	0.05	0.27	66.26	0.06	0.56	0.29	12.68	9.42	0.28	90.77
Duricrust	Z7-8	0.12	0.60	0.15	0.01	0.05	0.36	66.31	0.02	0.56	0.34	12.31	9.42	0.29	90.54
Duricrust	Z7-8	0.11	0.60	0.17	0.01	0.05	0.32	68.39	0.02	0.50	0.24	13.90	7.02	0.13	91.44
Duricrust	Z7-8	0.15	0.56	0.15	0.03	0.05	0.39	66.48	0.02	0.67	0.28	13.04	8.18	0.07	90.05
Duricrust	Z7-8	0.12	0.63	0.15	0.01	0.06	0.40	69.17	0.01	0.45	0.16	14.04	5.99	0.16	91.35
Duricrust	Z7-8	0.13	0.59	0.16	0.02	0.09	0.44	67.82	0.05	0.65	0.37	14.06	6.15	0.12	90.67
Duricrust	Z7-8	0.14	0.70	0.13	0.00	0.06	0.31	67.44	0.05	0.50	0.21	12.75	8.52	0.39	91.19
Duricrust	Z7-8	0.12	0.61	0.15	0.00	0.06	0.46	68.74	0.02	0.45	0.26	13.43	7.04	0.12	91.44
Duricrust	M1	0.19	1.56	1.69	1.07	0.06	0.00	72.89	0.03	0.32	0.17	13.88	0.28	0.06	92.19
Duricrust	Pp2	0.26	0.56	0.16	0.58	0.09	0.00	82.12	0.05	0.69	0.13	7.37	0.00	0.00	92.00
Duricrust	Pp2	0.09	0.22	0.18	0.38	0.15	0.00	73.79	0.00	0.66	0.50	16.09	0.00	0.06	92.14
Duricrust	Pp2	0.19	0.30	0.17	0.68	0.19	0.00	75.32	0.06	0.53	0.36	14.58	0.04	0.00	92.42
Duricrust	Pp2	0.16	0.24	0.15	0.36	0.11	0.00	74.83	0.09	0.55	0.32	15.68	0.00	0.00	92.48
Duricrust	Pp2	0.12	1.13	0.24	1.14	0.15	0.00	74.07	0.07	0.65	0.87	12.92	0.14	0.06	91.56
Duricrust	Pp2	0.14	0.29	0.15	0.38	0.09	0.00	74.44	0.06	0.52	0.33	15.64	0.00	0.14	92.18
Duricrust	Pp2	0.16	0.32	0.13	0.46	0.13	0.00	75.45	0.02	0.57	0.30	15.98	0.05	0.00	93.56
Duricrust	Pp2	0.11	0.36	0.14	0.59	0.18	0.07	74.96	0.05	0.67	0.30	15.14	0.00	0.00	92.55
Duricrust	Pp2	0.21	0.43	0.11	0.56	0.08	0.00	80.62	0.03	0.68	0.13	10.00	0.00	0.00	92.85
Duricrust	Pp2	0.15	0.30	0.16	0.57	0.14	0.00	75.17	0.04	0.55	0.33	15.72	0.00	0.05	93.17
Duricrust	Pp2	0.19	0.25	0.17	0.37	0.19	0.00	73.89	0.06	0.71	0.25	13.99	1.67	0.10	91.85
Duricrust	Pp2	0.12	0.29	0.11	0.45	0.22	0.00	74.80	0.05	0.68	0.21	13.62	2.04	0.00	92.58
Duricrust	Pp2	0.20	0.45	0.13	0.62	0.08	0.00	79.11	0.04	0.71	0.17	9.74	0.02	0.00	91.26
Duricrust	Pp2	0.13	0.36	0.14	0.40	0.18	0.00	73.84	0.05	0.76	0.29	14.33	1.90	0.07	92.44
Duricrust	Pp2	0.12	0.23	0.14	0.55	0.25	0.00	75.13	0.08	0.51	0.37	11.91	2.47	0.14	91.90
Duricrust	VB/VT	0.32	3.18	1.32	0.22	0.06	0.00	69.27	0.06	0.65	0.27	13.31	2.29	0.00	90.95
Duricrust	VB/VT	0.28	2.83	1.03	0.24	0.07	0.00	71.99	0.12	0.73	0.23	13.74	2.37	0.04	93.65
Duricrust	VB/VT	0.27	2.88	0.72	0.18	0.06	0.00	69.68	0.07	0.74	0.27	14.72	1.85	0.00	91.45
Duricrust	VB/VT	0.21	2.59	0.62	0.17	0.08	0.00	70.13	0.06	0.68	0.32	14.94	1.70	0.00	91.49
Duricrust	VB/VT	0.33	3.71	2.01	0.17	0.07	0.05	67.90	0.05	0.73	0.27	12.88	2.60	0.23	91.01
Duricrust	VB/VT	0.46	5.19	4.81	0.22	0.02	0.03	63.71	0.10	0.58	0.23	11.29	3.24	0.00	89.86
Duricrust	VB/VT	0.21	2.61	0.54	0.21	0.07	0.00	69.92	0.08	0.67	0.27	14.51	1.88	0.00	90.97
Duricrust	VB/VT	0.23	2.00	0.58	0.19	0.09	0.00	69.75	0.09	0.76	0.21	14.38	1.76	0.00	90.04
Duricrust	VB/VT	0.25	2.64	0.54	0.18	0.06	0.00	73.25	0.02	0.80	0.29	14.48	1.74	0.00	94.25
Duricrust	VB/VT	0.47	2.10	1.15	0.19	0.06	0.00	68.81	0.05	0.73	0.23	13.79	1.95	0.99	90.52
Duricrust	VB/VT	0.30	2.97	2.85	0.31	0.08	0.00	65.72	0.12	0.71	0.20	11.97	2.74	0.00	87.97
Duricrust	VB/VT	0.21	1.94	1.38	0.17	0.09	0.00	71.48	0.03	0.76	0.25	14.12	1.85	0.16	92.42
Duricrust	VB/VT	0.32	3.56	1.99	0.23	0.05	0.00	69.64	0.12	0.72	0.31	12.76	1.89	0.11	91.68
Duricrust	VB/VT	0.47	5.61	2.15	0.31	0.02	0.16	66.49	0.11	0.61	0.26	12.62	2.56	0.00	91.37
Duricrust	VB/VT	0.27	1.76	1.22	0.22	0.11	0.00	71.17	0.11	0.86	0.20	13.65	2.11	0.00	91.68
Duricrust	VB/VT	0.19	1.53	1.04	0.19	0.12	0.00	71.66	0.10	0.89	0.23	14.06	1.86	0.00	91.88

Table A7: Chemical composition and formula units based on 16 oxygens and $Mn^{4+/}Mn^{3+}$of the hollandite calculated assuming full site occupancy

Hollandite													
Lithotype	Sample	Al_2O_3	SiO_2	Fe_2O_3	MnO_2	Mn_2O_3	PbO	CuO	CoO	BaO	K_2O	Na_2O	∑ (%)
Mn greywacke	A3	0.60	0.20	1.54	67.87	3.44	4.60	0.64	0.11	13.83	0.05	0.07	92.95
Mn greywacke	A3	0.73	0.27	5.31	66.97	3.39	5.62	0.66	0.16	12.62	0.01	0.01	95.75
Mn greywacke	A3	0.39	0.19	9.27	65.21	3.30	1.65	0.48	0.08	14.62	0.07	0.07	95.33
Mn greywacke	A3	0.32	0.13	0.15	71.51	3.62	1.14	0.59	0.14	16.73	0.03	0.05	94.41
Mn greywacke	A3	0.33	0.10	0.14	73.79	3.74	1.65	0.62	0.09	14.20	0.63	0.05	95.34
Mn greywacke	A3	0.35	0.11	0.15	72.57	3.67	1.50	0.58	0.09	13.92	0.64	0.04	93.62
Mn greywacke	A3	0.45	0.27	0.19	71.50	3.62	1.40	0.57	0.12	15.66	0.03	0.04	93.85
Mn greywacke	A3	0.40	0.15	0.30	71.50	3.62	1.36	0.59	0.10	16.63	0.04	0.03	94.72
Mn greywacke	A3	0.40	0.48	0.17	70.68	3.58	1.63	0.53	0.14	16.26	0.04	0.07	93.98
Pinkish siltstone	PS	0.66	0.15	0.23	71.22	3.61	2.67	0.72	0.34	16.90	0.00	0.03	96.53
Pinkish siltstone	PS	0.34	0.11	0.10	65.29	3.31	1.87	0.43	0.12	15.50	0.02	0.07	87.16
Pinkish siltstone	PS	0.31	0.33	0.23	71.25	3.61	2.25	0.63	0.29	17.59	0.00	0.05	96.54
Pinkish siltstone	PS	0.22	0.34	0.23	71.36	3.61	2.03	0.49	0.23	17.61	0.00	0.05	96.17
Pinkish siltstone	PS	0.35	0.09	0.14	68.21	3.45	1.76	0.46	0.05	15.30	0.02	0.08	89.91
Pinkish siltstone	PS	0.60	0.09	0.16	69.07	3.50	5.67	0.40	0.10	13.69	0.01	0.05	93.34
Duricrust	Pd	3.81	0.56	2.14	66.04	3.34	0.84	1.56	0.51	13.63	0.67	0.01	93.11
Duricrust	Pd	3.96	0.38	1.49	67.17	3.40	0.94	1.45	0.48	13.15	0.63	0.03	93.08
Duricrust	Pd	3.98	0.45	1.55	66.35	3.36	1.71	0.99	0.39	14.25	0.31	0.04	93.38
Duricrust	Pd	4.62	0.39	1.23	66.33	3.36	1.59	1.71	0.55	14.08	0.50	0.02	94.38
Duricrust	Pd	4.29	1.19	7.02	65.78	3.33	3.43	0.54	0.27	6.17	2.09	0.01	94.12
Duricrust	Pd	4.34	0.51	3.22	60.78	3.08	2.79	0.57	0.30	12.64	0.31	0.08	88.62
Duricrust	Z7-8	0.64	0.11	0.14	63.07	3.19	9.42	0.56	0.29	12.68	0.03	0.06	90.19
Duricrust	Z7-8	0.60	0.12	0.15	63.11	3.20	9.42	0.56	0.34	12.31	0.01	0.02	89.84
Duricrust	Z7-8	0.60	0.11	0.17	65.09	3.30	7.02	0.50	0.24	13.90	0.01	0.02	90.96
Duricrust	Z7-8	0.56	0.15	0.15	63.28	3.20	8.18	0.67	0.28	13.04	0.03	0.02	89.56
Duricrust	Z7-8	0.63	0.12	0.15	65.84	3.33	5.99	0.45	0.16	14.04	0.01	0.01	90.73
Duricrust	Z7-8	0.59	0.13	0.16	64.55	3.27	6.15	0.65	0.37	14.06	0.02	0.05	90.00
Duricrust	Z7-8	0.70	0.14	0.13	64.19	3.25	8.52	0.50	0.21	12.75	0.00	0.05	90.44
Duricrust	Z7-8	0.61	0.12	0.15	65.43	3.31	7.04	0.45	0.26	13.43	0.00	0.02	90.82
Duricrust	M1	1.56	0.19	1.69	69.38	3.51	0.28	0.32	0.17	13.88	1.07	0.03	92.08
Duricrust	Pp2	0.56	0.26	0.16	78.16	3.96	0.00	0.69	0.13	7.37	0.58	0.05	91.92
Duricrust	Pp2	0.22	0.09	0.18	70.23	3.56	0.00	0.66	0.50	16.09	0.38	0.00	91.91
Duricrust	Pp2	0.30	0.19	0.17	71.69	3.63	0.04	0.53	0.36	14.58	0.68	0.06	92.23
Duricrust	Pp2	0.24	0.16	0.15	71.22	3.61	0.00	0.55	0.32	15.68	0.36	0.09	92.38
Duricrust	Pp2	1.13	0.12	0.24	70.50	3.57	0.14	0.65	0.87	12.92	1.14	0.07	91.35
Duricrust	Pp2	0.29	0.14	0.15	70.85	3.59	0.00	0.52	0.33	15.64	0.38	0.06	91.95
Duricrust	Pp2	0.32	0.16	0.13	71.81	3.64	0.05	0.57	0.30	15.98	0.46	0.02	93.44
Duricrust	Pp2	0.36	0.11	0.14	71.35	3.61	0.00	0.67	0.30	15.14	0.59	0.05	92.32
Duricrust	Pp2	0.43	0.21	0.11	76.73	3.89	0.00	0.68	0.13	10.00	0.56	0.03	92.77
Duricrust	Pp2	0.30	0.15	0.16	71.55	3.62	0.00	0.55	0.33	15.72	0.57	0.04	92.99
Duricrust	Pp2	0.25	0.19	0.17	70.33	3.56	1.67	0.71	0.25	13.99	0.37	0.06	91.55
Duricrust	Pp2	0.29	0.12	0.11	71.19	3.61	2.04	0.68	0.21	13.62	0.45	0.05	92.37
Duricrust	Pp2	0.45	0.20	0.13	75.30	3.81	0.02	0.71	0.17	9.74	0.62	0.04	91.19
Duricrust	Pp2	0.36	0.13	0.14	70.28	3.56	1.90	0.76	0.29	14.33	0.40	0.05	92.20
Duricrust	Pp2	0.23	0.12	0.14	71.51	3.62	2.47	0.51	0.37	11.91	0.55	0.08	91.51
Duricrust	VB/VT	3.18	0.32	1.32	65.93	3.34	2.29	0.65	0.27	13.31	0.22	0.06	90.89
Duricrust	VB/VT	2.83	0.28	1.03	68.52	3.47	2.37	0.73	0.23	13.74	0.24	0.12	93.56
Duricrust	VB/VT	2.88	0.27	0.72	66.32	3.36	1.85	0.74	0.27	14.72	0.18	0.07	91.38
Duricrust	VB/VT	2.59	0.21	0.62	66.75	3.38	1.70	0.68	0.32	14.94	0.17	0.06	91.42
Duricrust	VB/VT	3.71	0.33	2.01	64.63	3.27	2.60	0.73	0.27	12.88	0.17	0.05	90.65
Duricrust	VB/VT	5.19	0.46	4.81	60.64	3.07	3.24	0.58	0.23	11.29	0.22	0.10	89.83
Duricrust	VB/VT	2.61	0.21	0.54	66.55	3.37	1.88	0.67	0.27	14.51	0.21	0.08	90.90
Duricrust	VB/VT	2.00	0.23	0.58	66.39	3.36	1.76	0.76	0.21	14.38	0.19	0.09	89.95
Duricrust	VB/VT	2.64	0.25	0.54	69.72	3.53	1.74	0.80	0.29	14.48	0.18	0.02	94.19
Duricrust	VB/VT	2.10	0.47	1.15	65.49	3.32	1.95	0.73	0.23	13.79	0.19	0.05	89.47
Duricrust	VB/VT	2.97	0.30	2.85	62.55	3.17	2.74	0.71	0.20	11.97	0.31	0.12	87.89
Duricrust	VB/VT	1.94	0.21	1.38	68.03	3.45	1.85	0.76	0.25	14.12	0.17	0.03	92.19
Duricrust	VB/VT	3.56	0.32	1.99	66.28	3.36	1.89	0.72	0.31	12.76	0.23	0.12	91.54
Duricrust	VB/VT	5.61	0.47	2.15	63.29	3.20	2.56	0.61	0.26	12.62	0.31	0.11	91.19
Duricrust	VB/VT	1.76	0.27	1.22	67.74	3.43	2.11	0.86	0.20	13.65	0.22	0.11	91.57
Duricrust	VB/VT	1.53	0.19	1.04	68.21	3.45	1.86	0.89	0.23	14.06	0.19	0.10	91.75
Formula units based on 16 oxygens and Mn^{4+}/Mn^{3+} calculated assuming full site occupancy													
LIthotype	Sample	Al^{3+}	Si	Fe^{3+}	Mn^{4+}	Mn^{3+}	Pb	Cu	Co	Ba	K	Na	∑ (%)
Mn greywacke	A3	0.10	0.03	0.17	6.93	0.39	0.18	0.07	0.01	0.80	0.01	0.02	8.72
Mn greywacke	A3	0.13	0.04	0.39	6.77	0.38	0.22	0.07	0.02	0.72	0.00	0.00	8.75
Mn greywacke	A3	0.07	0.03	0.68	6.64	0.37	0.07	0.05	0.01	0.84	0.01	0.02	8.79
Mn greywacke	A3	0.05	0.02	0.01	7.10	0.40	0.04	0.06	0.02	0.94	0.01	0.01	8.66
Mn greywacke	A3	0.05	0.01	0.01	7.15	0.40	0.06	0.07	0.01	0.78	0.11	0.01	8.67
Mn greywacke	A3	0.06	0.02	0.01	7.15	0.40	0.06	0.06	0.01	0.78	0.12	0.01	8.67
Mn greywacke	A3	0.08	0.04	0.01	7.09	0.40	0.05	0.06	0.01	0.88	0.01	0.01	8.64
Mn greywacke	A3	0.07	0.02	0.02	7.08	0.39	0.05	0.06	0.01	0.93	0.01	0.01	8.66
Mn greywacke	A3	0.07	0.07	0.01	7.04	0.39	0.06	0.06	0.02	0.92	0.01	0.02	8.67
Pinkish siltstone	PS	0.11	0.02	0.02	7.01	0.39	0.10	0.08	0.04	0.94	0.00	0.01	8.72
Pinkish siltstone	PS	0.06	0.02	0.01	7.08	0.39	0.08	0.05	0.02	0.95	0.00	0.02	8.68
Pinkish siltstone	PS	0.05	0.05	0.02	7.02	0.39	0.09	0.07	0.03	0.98	0.00	0.01	8.71
Pinkish siltstone	PS	0.04	0.05	0.02	7.04	0.39	0.08	0.05	0.03	0.98	0.00	0.01	8.69
Pinkish siltstone	PS	0.06	0.01	0.01	7.11	0.40	0.07	0.05	0.01	0.90	0.00	0.02	8.65
Pinkish siltstone	PS	0.10	0.01	0.01	7.06	0.39	0.23	0.04	0.01	0.79	0.00	0.01	8.68
Duricrust	Pd	0.64	0.08	0.15	6.51	0.36	0.03	0.17	0.06	0.76	0.12	0.00	8.89
Duricrust	Pd	0.66	0.05	0.11	6.58	0.37	0.04	0.16	0.05	0.73	0.11	0.01	8.86
Duricrust	Pd	0.67	0.06	0.11	6.55	0.37	0.07	0.11	0.04	0.80	0.06	0.01	8.84
Duricrust	Pd	0.77	0.06	0.09	6.47	0.36	0.06	0.18	0.06	0.78	0.09	0.01	8.92
Duricrust	Pd	0.70	0.17	0.49	6.31	0.35	0.13	0.06	0.03	0.34	0.37	0.00	8.94
Duricrust	Pd	0.78	0.08	0.25	6.38	0.36	0.11	0.07	0.04	0.75	0.06	0.02	8.89

Duricrust	Z7-8	0.12	0.02	0.01	6.94	0.39	0.40	0.07	0.04	0.79	0.01	0.02	8.80
Duricrust	Z7-8	0.11	0.02	0.01	6.95	0.39	0.40	0.07	0.04	0.77	0.00	0.01	8.78
Duricrust	Z7-8	0.11	0.02	0.01	6.98	0.39	0.29	0.06	0.03	0.85	0.00	0.01	8.75
Duricrust	Z7-8	0.10	0.02	0.02	6.95	0.39	0.35	0.08	0.04	0.81	0.01	0.01	8.78
Duricrust	Z7-8	0.11	0.02	0.01	7.01	0.39	0.25	0.05	0.02	0.85	0.00	0.00	8.72
Duricrust	Z7-8	0.11	0.02	0.01	6.97	0.39	0.26	0.08	0.05	0.86	0.00	0.02	8.76
Duricrust	Z7-8	0.13	0.02	0.01	6.96	0.39	0.36	0.06	0.03	0.78	0.00	0.02	8.76
Duricrust	Z7-8	0.11	0.02	0.01	7.00	0.39	0.29	0.05	0.03	0.81	0.00	0.01	8.73
Duricrust	CM1	0.27	0.03	0.12	6.92	0.39	0.01	0.03	0.02	0.78	0.20	0.01	8.77
Duricrust	Pp2	0.09	0.04	0.01	7.32	0.41	0.00	0.07	0.01	0.39	0.10	0.01	8.45
Duricrust	Pp2	0.04	0.01	0.01	7.11	0.40	0.00	0.07	0.06	0.92	0.07	0.00	8.69
Duricrust	Pp2	0.05	0.03	0.01	7.13	0.40	0.00	0.06	0.04	0.82	0.12	0.02	8.68
Duricrust	Pp2	0.04	0.02	0.01	7.12	0.40	0.00	0.06	0.04	0.89	0.07	0.03	8.67
Duricrust	Pp2	0.19	0.02	0.02	7.02	0.39	0.01	0.07	0.10	0.73	0.21	0.02	8.78
Duricrust	Pp2	0.05	0.02	0.01	7.12	0.40	0.00	0.06	0.04	0.89	0.07	0.02	8.67
Duricrust	Pp2	0.05	0.02	0.01	7.11	0.40	0.00	0.06	0.03	0.90	0.08	0.01	8.68
Duricrust	Pp2	0.06	0.02	0.01	7.12	0.40	0.00	0.07	0.03	0.86	0.11	0.01	8.69
Duricrust	Pp2	0.07	0.03	0.01	7.27	0.41	0.00	0.07	0.01	0.54	0.10	0.01	8.51
Duricrust	Pp2	0.05	0.02	0.01	7.11	0.40	0.00	0.06	0.04	0.89	0.10	0.01	8.69
Duricrust	Pp2	0.04	0.03	0.01	7.12	0.40	0.07	0.08	0.03	0.80	0.07	0.02	8.67
Duricrust	Pp2	0.05	0.02	0.01	7.14	0.40	0.08	0.07	0.02	0.77	0.08	0.01	8.66
Duricrust	Pp2	0.07	0.03	0.01	7.26	0.41	0.00	0.07	0.02	0.53	0.11	0.01	8.53
Duricrust	Pp2	0.06	0.02	0.01	7.10	0.40	0.07	0.08	0.03	0.82	0.07	0.01	8.69
Duricrust	Pp2	0.04	0.02	0.02	7.17	0.40	0.10	0.06	0.04	0.68	0.10	0.02	8.64
Duricrust	VB/VT	0.55	0.05	0.10	6.69	0.37	0.09	0.07	0.03	0.77	0.04	0.02	8.78
Duricrust	VB/VT	0.48	0.04	0.07	6.76	0.38	0.09	0.08	0.03	0.77	0.04	0.03	8.77
Duricrust	VB/VT	0.50	0.04	0.05	6.73	0.38	0.07	0.08	0.03	0.85	0.03	0.02	8.79
Duricrust	VB/VT	0.45	0.03	0.05	6.78	0.38	0.07	0.08	0.04	0.86	0.03	0.02	8.78
Duricrust	VB/VT	0.64	0.05	0.15	6.59	0.37	0.10	0.08	0.03	0.74	0.03	0.01	8.81
Duricrust	VB/VT	0.91	0.07	0.36	6.26	0.35	0.13	0.07	0.03	0.66	0.04	0.03	8.90
Duricrust	VB/VT	0.45	0.03	0.04	6.79	0.38	0.07	0.07	0.03	0.84	0.04	0.02	8.78
Duricrust	VB/VT	0.35	0.03	0.04	6.85	0.38	0.07	0.09	0.03	0.84	0.04	0.03	8.75
Duricrust	VB/VT	0.44	0.04	0.04	6.82	0.38	0.07	0.09	0.03	0.80	0.03	0.01	8.74
Duricrust	VB/VT	0.37	0.07	0.09	6.79	0.38	0.08	0.08	0.03	0.81	0.04	0.01	8.75
Duricrust	VB/VT	0.54	0.05	0.22	6.62	0.37	0.11	0.08	0.02	0.72	0.06	0.04	8.82
Duricrust	VB/VT	0.33	0.03	0.10	6.85	0.38	0.07	0.08	0.03	0.81	0.03	0.01	8.73
Duricrust	VB/VT	0.61	0.05	0.14	6.64	0.37	0.07	0.08	0.04	0.72	0.04	0.03	8.79
Duricrust	VB/VT	0.96	0.07	0.16	6.35	0.35	0.10	0.07	0.03	0.72	0.06	0.03	8.89
Duricrust	VB/VT	0.30	0.04	0.09	6.87	0.38	0.08	0.10	0.02	0.78	0.04	0.03	8.74
Duricrust	VB/VT	0.26	0.03	0.08	6.91	0.39	0.07	0.10	0.03	0.81	0.04	0.03	8.73

Table A8: Microprobe analysis of cryptomelane in Mn rocks and related duricrusts

Cryptomelane														
Lithotype	Sample	SiO_2	Al_2O_3	Fe_2O_3	K_2O	CaO	P_2O_5	MnO_2	Na_2O	CuO	CoO	BaO	PbO	V_2O_3	∑(%)
Duricrust	M1	0.42	5.07	0.61	4.03	0.05	0.00	76.15	0.23	0.40	0.18	1.83	0.32	0.00	89.30
Duricrust	M1	0.32	4.52	0.37	4.47	0.01	0.00	79.15	0.16	0.25	0.10	0.83	0.03	0.05	90.26
Duricrust	M1	0.40	5.05	0.46	4.10	0.00	0.00	77.08	0.11	0.32	0.16	1.70	0.23	0.06	89.67
Duricrust	M1	0.37	4.79	0.29	4.52	0.02	0.00	78.07	0.20	0.34	0.08	1.21	0.11	0.00	89.98

Table A9: Chemical composition and formula units based on 16 oxygens and $Mn^{4+/}Mn^{3+}$of the cryptomelane calculated assuming full site occupancy

Cryptomelane				
Lithotype	Duricrust	Duricrust	Duricrust	Duricrust
Sample	M1	M1	M1	M1
Al_2O_3	5.07	4.52	5.05	4.79
SiO_2	0.42	0.32	0.40	0.37
Fe_2O_3	0.61	0.37	0.46	0.29
MnO_2	72.48	74.84	73.02	74.51
Mn_2O_3	3.33	3.92	3.69	3.23
PbO	0.32	0.03	0.23	0.11
CuO	0.40	0.25	0.32	0.34
CoO	0.18	0.10	0.16	0.08
BaO	1.83	0.83	1.70	1.21
K_2O	4.03	4.47	4.10	4.52
Na_2O	0.23	0.16	0.11	0.20
∑ (%)	88.90	89.80	89.23	89.63
Formula units based on 16 oxygens and Mn^{4+}/ Mn^{3+} calculated assuming full site occupancy				
Al^{3+}	0.81	0.71	0.80	0.75
Si	0.06	0.04	0.05	0.05
Fe^{3+}	0.06	0.02	0.03	0.02
Mn^{4+}	6.76	6.87	6.78	6.87
Mn^{3+}	0.34	0.40	0.38	0.33
Pb	0.01	0.00	0.01	0.00
Cu	0.04	0.02	0.03	0.03
Co	0.02	0.01	0.02	0.01
Ba	0.10	0.04	0.09	0.06
K	0.69	0.76	0.70	0.77
Na	0.06	0.04	0.03	0.05
∑ (%)	8.95	8.92	8.93	8.94

Table A10: Microprobe analysis of romanechite in Mn rocks and related duricrusts

Lithotype	Sample	SiO_2	Al_2O_3	Fe_2O_3	K_2O	CaO	P_2O_5	Mn_2O_3	Na_2O	CuO	CoO	BaO	PbO	V_2O_3	∑ (%)
Romanechite															
Mn greywacke	A2	0.18	0.34	0.29	0.04	0.13	0.03	70.99	0.03	0.01	0.19	17.04	0.00	0.11	89.37
Mn greywacke	A2	0.21	0.48	0.46	0.04	0.11	0.17	69.46	0.00	0.02	0.23	16.55	0.01	0.00	87.74
Mn greywacke	A2	0.21	0.42	0.14	0.04	0.10	0.23	71.16	0.05	0.05	0.15	17.38	0.00	0.00	89.93
Mn greywacke	A2	0.17	0.36	0.13	0.03	0.04	0.00	70.86	0.03	0.02	0.14	17.75	0.02	0.06	89.60
Mn greywacke	A2	0.20	0.52	0.22	0.04	0.07	0.10	70.90	0.06	0.04	0.16	17.17	0.07	0.13	89.67
Mn greywacke	A2	0.17	0.32	0.21	0.04	0.10	0.00	68.81	0.07	0.01	0.20	17.53	0.00	0.00	87.44
Mn greywacke	A2	0.14	0.26	0.17	0.04	0.05	0.06	70.58	0.03	0.01	0.22	17.36	0.02	0.00	88.94
Mn greywacke	A2	0.13	0.29	0.20	0.04	0.08	0.00	70.12	0.03	0.00	0.17	17.76	0.09	0.05	88.96
Mn greywacke	A2	0.18	0.35	0.56	0.06	0.12	0.07	70.16	0.02	0.00	0.15	17.03	0.00	0.00	88.69
Mn greywacke	A2	0.18	0.36	0.61	0.04	0.12	0.16	69.86	0.09	0.00	0.18	16.33	0.00	0.00	87.93
Mn greywacke	A2	0.22	0.31	0.46	0.05	0.10	0.07	69.21	0.08	0.00	0.16	17.41	0.00	0.00	88.06
Mn greywacke	A2	0.17	0.30	0.67	0.05	0.14	0.09	70.37	0.02	0.06	0.18	16.91	0.01	0.00	88.95
Mn greywacke	A2	0.17	0.56	0.92	0.06	0.16	0.13	68.03	0.08	0.06	0.09	16.20	0.00	0.00	86.45
Mn greywacke	A2	0.22	0.36	0.41	0.05	0.10	0.03	68.90	0.03	0.03	0.15	17.27	0.00	0.10	87.63
Mn greywacke	A2	0.42	0.41	0.39	0.05	0.11	0.18	69.01	0.07	0.04	0.13	16.80	0.05	0.02	87.66
Duricrust	B1-B4	0.15	0.42	0.21	0.06	0.10	0.00	66.45	0.08	0.05	0.15	17.76	0.00	0.06	85.47
Duricrust	B1-B4	0.13	0.23	0.26	0.03	0.06	0.00	66.92	0.00	0.05	0.19	18.44	0.00	0.14	86.45
Duricrust	B1-B4	0.24	0.32	0.17	0.03	0.08	0.01	68.05	0.06	0.09	0.21	17.29	0.02	0.00	86.57
Duricrust	B1-B4	0.18	0.38	0.15	0.04	0.08	0.00	67.39	0.05	0.01	0.26	17.42	0.00	0.06	86.01
Duricrust	B1-B4	0.34	0.44	0.26	0.04	0.11	0.08	67.94	0.06	0.02	0.23	17.27	0.05	0.10	86.92
Duricrust	B1-B4	0.18	0.40	0.12	0.05	0.08	0.14	65.58	0.06	0.00	0.30	17.42	0.01	0.00	84.33
Duricrust	B1-B4	0.12	0.24	0.26	0.03	0.05	0.00	67.00	0.08	0.00	0.15	17.87	0.00	0.00	85.81
Duricrust	B1-B4	0.22	0.28	0.18	0.02	0.10	0.01	66.44	0.09	0.00	0.18	17.80	0.00	0.05	85.36
Duricrust	B1-B4	0.19	0.40	0.17	0.05	0.11	0.21	66.01	0.09	0.05	0.31	17.72	0.00	0.07	85.38
Colluvium	Z1- Z6	0.17	0.32	0.20	0.04	0.05	0.00	69.19	0.00	0.00	0.11	17.47	0.00	0.00	87.54
Colluvium	Z1- Z6	0.27	0.36	0.17	0.05	0.09	0.00	68.75	0.08	0.00	0.15	17.52	0.00	0.07	87.51
Colluvium	Z1- Z6	0.25	0.33	0.14	0.06	0.09	0.00	69.32	0.02	0.02	0.18	16.76	0.00	0.00	87.16
Colluvium	Z1- Z6	0.17	0.29	0.14	0.03	0.08	0.07	69.20	0.05	0.00	0.24	17.85	0.00	0.19	88.31
Colluvium	Z1- Z6	0.25	0.36	0.17	0.04	0.07	0.07	69.30	0.03	0.00	0.17	17.29	0.01	0.00	87.77
Colluvium	Z1- Z6	0.29	0.31	0.13	0.05	0.10	0.04	67.72	0.00	0.02	0.17	17.02	0.05	0.03	85.92
Colluvium	Z1- Z6	0.19	0.22	0.16	0.01	0.06	0.00	68.16	0.07	0.06	0.22	18.06	0.00	0.00	87.21
Colluvium	Z1- Z6	0.25	0.44	0.15	0.07	0.10	0.08	67.97	0.09	0.00	0.21	17.34	0.03	0.07	86.80
Colluvium	Z1- Z6	0.25	0.43	0.24	0.03	0.07	0.01	68.06	0.06	0.06	0.20	17.16	0.05	0.00	86.62
Colluvium	Z1- Z6	0.19	0.33	0.12	0.04	0.08	0.00	67.84	0.01	0.03	0.16	17.95	0.00	0.00	86.73
Colluvium	Z1- Z6	0.49	0.37	0.19	0.05	0.08	0.00	66.24	0.04	0.06	0.22	16.93	0.11	0.00	84.78
Colluvium	Z1- Z6	0.27	0.30	0.15	0.06	0.09	0.02	68.29	0.06	0.00	0.12	16.98	0.04	0.00	86.38
Colluvium	Z1- Z6	0.24	0.39	0.12	0.06	0.07	0.13	69.17	0.07	0.06	0.14	17.17	0.00	0.07	87.69
Colluvium	Z1- Z6	0.18	0.24	0.14	0.04	0.07	0.00	69.62	0.08	0.05	0.18	17.72	0.04	0.06	88.43
Colluvium	Z1- Z6	0.82	0.39	0.11	0.05	0.10	0.08	67.00	0.02	0.06	0.18	17.08	0.00	0.07	85.96
Colluvium	Z1- Z6	0.21	0.19	0.21	0.03	0.07	0.00	68.92	0.09	0.01	0.20	18.47	0.06	0.09	88.55
Colluvium	Z1- Z6	0.16	0.24	0.33	0.05	0.06	0.00	67.43	0.03	0.03	0.12	17.69	0.00	0.06	86.19
Colluvium	Z1- Z6	0.19	0.20	0.29	0.02	0.06	0.01	68.08	0.05	0.02	0.18	17.27	0.00	0.17	86.51
Colluvium	Z1- Z6	0.25	0.28	0.44	0.05	0.07	0.00	67.50	0.02	0.00	0.15	17.69	0.00	0.00	86.44
Colluvium	Z1- Z6	0.16	0.26	0.26	0.03	0.08	0.00	68.15	0.06	0.00	0.14	17.80	0.08	0.00	87.01
Colluvium	Z1- Z6	0.12	0.35	0.18	0.05	0.05	0.00	67.30	0.05	0.04	0.16	17.79	0.00	0.24	86.32

Table A11: Chemical composition and formula units based on 10 oxygens and $Mn^{4+/}Mn^{3+}$ of the romanechite calculated assuming full site occupancy

Romanechite																														
Lithotype	Mn greywacke															Duricrust				Colluvium fragment										
Sample	A2	A2	A2	A2	A2	A2	A2	A2	A2	A2	A2	A2	A2	A2	A2	B1	B1	B1	B1	Z1	Z6	Z1	Z6	Z1	Z6	Z1	Z6	Z1	Z6	Z1	Z6
Al_2O_3	0.34	0.48	0.42	0.36	0.52	0.32	0.26	0.29	0.35	0.36	0.31	0.30	0.56	0.36	0.41	0.23	0.32	0.38	0.44	0.32	0.36	0.33	0.29	0.36	0.31	0.22	0.44	0.39	0.24	0.39	0.19
P_2O_5	0.03	0.17	0.23	0.00	0.10	0.00	0.06	0.00	0.07	0.16	0.07	0.09	0.13	0.03	0.18	0.00	0.01	0.00	0.08	0.00	0.00	0.00	0.07	0.07	0.04	0.00	0.08	0.13	0.00	0.08	0.00
Fe_2O_3	0.29	0.46	0.14	0.13	0.22	0.21	0.17	0.20	0.56	0.61	0.46	0.67	0.92	0.41	0.39	0.26	0.17	0.15	0.26	0.20	0.17	0.14	0.14	0.17	0.13	0.16	0.15	0.12	0.14	0.11	0.21
MnO_2	60.57	59.22	60.70	60.80	60.63	59.22	60.32	60.29	60.05	59.38	59.48	60.17	58.32	59.26	58.99	58.25	58.57	58.13	58.47	59.46	59.20	59.25	59.52	59.38	58.15	58.91	58.54	59.26	59.90	57.68	59.69
Mn_2O_3	9.60	9.44	9.64	9.27	9.46	8.84	9.45	9.06	9.32	9.64	8.98	9.40	8.95	8.89	9.23	8.00	8.74	8.54	8.73	8.97	8.80	9.28	8.92	9.14	8.82	8.53	8.70	9.13	8.96	8.59	8.51
SiO_2	0.18	0.21	0.21	0.17	0.20	0.17	0.14	0.13	0.18	0.18	0.22	0.17	0.17	0.22	0.42	0.13	0.24	0.18	0.34	0.17	0.27	0.25	0.17	0.25	0.29	0.19	0.25	0.24	0.18	0.82	0.21
CuO	0.01	0.02	0.05	0.02	0.04	0.01	0.01	0.00	0.00	0.00	0.00	0.06	0.06	0.03	0.04	0.05	0.09	0.01	0.02	0.00	0.00	0.02	0.00	0.00	0.02	0.06	0.00	0.06	0.05	0.06	0.01
CoO	0.19	0.23	0.15	0.14	0.16	0.20	0.22	0.17	0.15	0.18	0.16	0.18	0.09	0.15	0.13	0.19	0.21	0.26	0.23	0.11	0.15	0.18	0.24	0.17	0.17	0.22	0.21	0.14	0.18	0.18	0.20
BaO	17.04	16.55	17.38	17.75	17.17	17.53	17.36	17.76	17.03	16.33	17.41	16.91	16.20	17.27	16.80	18.44	17.29	17.42	17.27	17.47	17.52	16.76	17.85	17.29	17.02	18.06	17.34	17.17	17.72	17.08	18.47
K_2O	0.04	0.04	0.04	0.03	0.04	0.04	0.04	0.04	0.06	0.04	0.05	0.05	0.06	0.05	0.05	0.03	0.03	0.04	0.04	0.04	0.05	0.06	0.03	0.04	0.05	0.01	0.07	0.06	0.04	0.05	0.03
∑ (%)	88.28	86.81	88.95	88.66	88.53	86.53	88.03	87.94	87.75	86.89	87.12	87.98	85.45	86.66	86.63	85.58	85.66	85.10	85.87	86.73	86.53	86.26	87.24	86.88	84.99	86.37	85.76	86.70	87.42	85.05	87.53
Formula units based on 10 oxygens and Mn^{4+}/Mn^{3+} calculated assuming full site occupancy																															
Al^{3+}	0.04	0.06	0.05	0.04	0.06	0.04	0.03	0.03	0.04	0.04	0.04	0.03	0.07	0.04	0.05	0.03	0.04	0.05	0.05	0.04	0.04	0.04	0.03	0.04	0.04	0.03	0.05	0.05	0.03	0.05	0.02
P	0.00	0.01	0.02	0.00	0.01	0.00	0.01	0.00	0.01	0.01	0.01	0.01	0.01	0.00	0.02	0.00	0.00	0.00	0.01	0.00	0.00	0.00	0.01	0.01	0.00	0.00	0.01	0.01	0.00	0.01	0.00
Fe^{3+}	0.02	0.03	0.01	0.01	0.02	0.02	0.01	0.02	0.04	0.05	0.03	0.05	0.07	0.03	0.03	0.02	0.01	0.01	0.02	0.01	0.01	0.01	0.01	0.01	0.01	0.01	0.01	0.01	0.01	0.01	0.02
Mn^{4+}	4.08	4.04	4.05	4.09	4.06	4.09	4.08	4.10	4.07	4.04	4.08	4.06	4.04	4.08	4.04	4.11	4.09	4.09	4.07	4.10	4.09	4.09	4.09	4.08	4.09	4.10	4.08	4.07	4.10	4.06	4.11
Mn^{3+}	0.71	0.71	0.71	0.69	0.70	0.67	0.70	0.68	0.70	0.72	0.68	0.70	0.68	0.67	0.70	0.62	0.67	0.66	0.67	0.68	0.67	0.70	0.67	0.69	0.68	0.65	0.67	0.69	0.68	0.67	0.64
Si	0.01	0.01	0.01	0.01	0.01	0.01	0.01	0.01	0.01	0.01	0.01	0.01	0.01	0.01	0.02	0.01	0.01	0.01	0.02	0.01	0.01	0.01	0.01	0.01	0.01	0.01	0.01	0.01	0.01	0.04	0.01
Cu	0.00	0.00	0.00	0.00	0.00	0.00	0.00	0.00	0.00	0.00	0.00	0.00	0.00	0.00	0.00	0.00	0.01	0.00	0.00	0.00	0.00	0.00	0.00	0.00	0.00	0.00	0.00	0.00	0.00	0.00	0.00
Co	0.02	0.02	0.01	0.01	0.01	0.02	0.02	0.01	0.01	0.01	0.01	0.01	0.01	0.01	0.01	0.02	0.02	0.02	0.02	0.01	0.01	0.01	0.02	0.01	0.01	0.02	0.02	0.01	0.01	0.01	0.02
Ba	0.65	0.64	0.66	0.68	0.65	0.69	0.67	0.68	0.65	0.63	0.68	0.65	0.64	0.67	0.65	0.74	0.68	0.70	0.68	0.68	0.69	0.66	0.69	0.67	0.68	0.71	0.68	0.67	0.69	0.68	0.72
K	0.01	0.01	0.00	0.00	0.01	0.01	0.00	0.00	0.01	0.01	0.01	0.01	0.01	0.01	0.01	0.00	0.00	0.00	0.01	0.01	0.01	0.01	0.00	0.00	0.01	0.00	0.01	0.01	0.01	0.01	0.00
∑ (%)	5.53	5.53	5.53	5.53	5.53	5.54	5.53	5.53	5.53	5.53	5.53	5.53	5.53	5.54	5.53	5.55	5.54	5.54	5.54	5.53	5.54	5.53	5.54	5.53	5.53	5.54	5.54	5.53	5.54	5.53	5.54

Table A12: Microprobe analysis of goethite and hematite in Mn rocks and related duricrusts

Lithotype	Sample	SiO_2	Al_2O_3	Fe_2O_3	K_2O	CaO	P_2O_5	MnO_2	Na_2O	CuO	CoO	BaO	PbO	V_2O_3	∑ (%)
Goethite and hematite															
Duricrust	Pi1	3.15	3.49	83.89	0.01	0.04	0.19	2.94	0.00	0.15	0.10	0.00	0.38	0.20	94.54
Duricrust	Pi1	10.74	10.75	61.18	0.00	0.01	0.00	4.89	0.01	0.01	0.07	0.11	0.41	0.14	88.31
Duricrust	Pi1	10.76	10.51	68.76	0.04	0.03	0.06	3.66	0.03	0.11	0.03	0.05	0.25	0.33	94.61
Duricrust	Pi1	2.18	4.73	82.10	0.00	0.02	0.17	1.61	0.03	0.06	0.03	0.00	0.13	0.11	91.19
Duricrust	Pi1	0.79	6.63	83.27	0.00	0.00	0.22	3.46	0.02	0.00	0.14	0.08	0.03	0.29	94.94
Duricrust	Pi1	1.30	2.55	84.72	0.00	0.02	0.01	6.19	0.05	0.01	0.08	0.13	0.08	0.00	95.15
Duricrust	Pi1	2.79	3.31	82.95	0.00	0.01	0.07	4.32	0.02	0.02	0.09	0.03	0.26	2.14	96.00
Duricrust	Pi1	1.54	1.71	89.08	0.05	0.02	0.02	3.58	0.04	0.00	0.09	0.00	0.05	0.01	96.18
Duricrust	Pi1	1.60	1.27	89.40	0.00	0.00	0.09	2.01	0.08	0.07	0.08	0.00	0.03	0.17	94.80
Duricrust	Pi1	2.00	1.81	89.09	0.03	0.01	0.02	2.67	0.00	0.00	0.09	0.04	0.00	0.20	95.95
Duricrust	Pi1	5.84	2.41	79.44	0.00	0.03	0.01	4.06	0.00	0.00	0.11	0.04	0.08	0.28	92.31
Duricrust	Pi1	2.10	2.36	83.50	0.05	0.06	0.00	4.57	0.08	0.09	0.08	0.14	0.16	0.27	93.45
Duricrust	Pi1	1.49	1.78	88.52	0.03	0.05	0.01	3.48	0.05	0.02	0.05	0.00	0.05	0.21	95.75
Duricrust	Pi1	1.40	1.67	88.95	0.03	0.03	0.01	3.20	0.09	0.06	0.03	0.00	0.01	0.26	95.72
Duricrust	Pi2	4.44	5.17	71.69	0.01	0.04	0.08	4.85	0.03	0.01	0.09	0.21	0.48	0.00	87.07
Duricrust	Pi2	13.50	13.31	58.11	0.03	0.01	0.01	5.50	0.03	0.00	0.04	0.06	0.33	0.00	90.93

CAPÍTULO V: ARTIGO 2- NEODYMIUM, STRONTIUM AND LEAD ISOTOPES: AN INSIGHT OF PROVENANCE AND BEHAVIOR UNDER EXTREME WEATHERING CONDITIONS

(Submetido à Chemical Geology no dia 09/02/2018)

Elsevier Editorial System(tm) for Chemical Geology

Manuscript Draft

Manuscript Number:

Title: NEODYMIUM, STRONTIUM AND LEAD ISOTOPES: AN INSIGHT OF PROVENANCE AND BEHAVIOR UNDER EXTREME WEATHERING CONDITIONS

Article Type: Research paper

Keywords:
Keywords: duricrusts, redistribution, provenance, behavior

Corresponding Author: Mr. Márcio Fernando dos Santos Albuquerque, M.D

Corresponding Author's Institution: Universidade de Brasília

First Author: Márcio Fernando dos Santos Albuquerque, M.D

Order of Authors: Márcio Fernando dos Santos Albuquerque, M.D; Adriana Horbe, PhD; Elton Dantas, PhD

Este manuscrito, submetido junto ao periódico Chemical Geology, reúne o conjunto de dados químicos e isotópicos (isótopos de Nd e Sr) das rochas sedimentares do Supergrupo Sumaúma (grupos Vila do Carmo e Beneficente). É também discutido o comportamento dos isótopos de Nd, Sr e Pb em perfis lateríticos desenvolvidos sobre as rochas supracitadas.

NEODYMIUM, STRONTIUM AND LEAD ISOTOPES: AN INSIGHT OF PROVENANCE AND BEHAVIOR UNDER EXTREME WEATHERING CONDITIONS

Márcio Fernando dos Santos Albuquerque[1], Adriana Maria Coimbra Horbe[2], Elton Luiz Dantas[2]

1-Graduate Program in Geology, Brasilia University, Geoscience Institute, Darcy Riberio University Campus, 70910-900, Brasília, Federal District, Brazil, albuquerqueIII@hotmail.com; 2- Brasilia University, Geoscience Institute, Darcy Riberio University Campus, 70910-900, Brasília, Federal District, Brazil

ABSTRACT

Chemical and isotopic analysis have been carried out in southwestern Amazonia, Brazil, with the goal to establishing the source of sedimentary rocks in two Proterozoic and Paleozoic basins and the behavior of Sr, Nd and Pb isotopes during lateritization. The surrounding intrusive suites (Colíder Group, Teodósia, Igarapé das Lontras and Serra da Providência) were the main source areas to the Vila do Carmo and Beneficente Group. The Vila do Carmo Group also received supply from Tapajós Parima Province and Beneficente Group was supplied also by Sunsás and Carajás Provinces. While the Alto Tapajós basin is product of erosion of Sumaúma basin conditioned after Cachimbo graben intrusion. The extreme tropical weathering conditions since the early Cenozoic, probable ages of the lateritic duricrusts, do not affect the geochemical and Nd and Pb isotopes of the parent rocks. The variations of Nd isotopes along the lateritic profiles depend of leaching and redistribution of radiogenic mineral, while the variations of Pb isotopes are assigned to U and Th decay throughout the geological time. By the other hand, the behavior of Sr isotopes show contributions of extraneous Sr input, most probably related to interaction with rainwater and groundwater. Moreover, the set of mineralogical, geochemical and isotopic features of tuffs, sedimentary rocks, lateritic duricrusts and oxisols together with gammaspectometry airborne allowed improve the geological knowledge of southwestern Amazonia.

Keywords: duricrusts, redistribution, provenance, behavior

1. INTRODUCTION

Several tools employed to identify the source of sediments and sedimentary rocks, such as heavy minerals, major and trace elements, allow classify the sedimentary rocks, the weathering degree in the source area, as well the type of rocks that supplied the sediments and the tectonic setting (Nesbit and Young, 1982; Herron, 1988; Roser and Korsh, 1988; McLennan, 1990; Henrique-Pinto et al., 2015). The Rb-Sr and Sm-Nd isotopic systems, tracers of mantellic and crustal signatures, also evoke the source areas of the sediments, the geotectonic setting and sedimentary environment (Bhatia and Crook, 1986; Floyd and Leveridge, 1987; McLennan et al., 1990; Rollinson, 1993; Cullers and Podkovyrov, 2002).

Moreover, these isotopes are commonly employed to measure the rate of material eroded from the continents to rivers and oceans and how the source influences the chemical composition of waters (Tripathy et al., 2011). However, there are some provisos related to Sr isotopes during diagenesis or extreme weathering (Nelson and DePaolo, 1988) since they are easily fractionated and removed due to mineral

weathering (Negrel, 2006; Ma et al., 2010). Kurtz et al. (2001) and Dia et al. (2006) reported that the extraneous Sr input (aeolian sediments) modifies the $^{87}Sr/^{86}Sr$ ratios in regolith horizons, whereas Ma et al. (2010) do not recommend the use of Sr isotopes for provenance of soils formed under extreme weathering.

The redistribution of heavy minerals throughout the weathering profile (Nesbitt, 1979; Morey and Setterholm, 1997; Ma et al., 2007; McQueen and Scott, 2008; Laveuf and Cornu, 2009), Nd released and trapped into Fe, Mn and P oxy-hydroxides and the extraneous Nd input from aeolian source are the main reasons of Nd isotopic ratios changes in the weathering profiles (MacFarlane et al., 1994; Ohlander et al., 2000; Viers and Wasseburg, 2004, Babechuk et al., 2015). On the other hand, according to Ma et al. (2010) the aeolian Nd input is negligible and the slight changes in the Nd isotopic ratios are assigned to Nd removal from bedrock to saprolite. The authors also concluded that ^{143}Nd under lateritization conditions is more easily removed than ^{144}Nd, despite that recommends the use of Nd isotopes as tracers of provenance of sedimentary rocks and soils.

The few studies concerning Pb isotopes behavior at weathering profiles have been carried out in gossans which recognized several facies in Australia and Burkina Faso and ratified the Pb isotopes immobility during extreme weathering (Gulson and Mizon, 1979; Kribek et al., 2016). Also, the combination of Pb, Nd and Sr isotopic ratios have been useful in the discrimination of the source of the hydrothermal and sedimentary Mn around the world (Clauer et al., 1984; Romer et al., 2011; Conly et al., 2011; Del-Rio Salas et al., 2013; Yang et al., 2015).

The southwestern Amazonia (Brazil) with two sedimentary basins and bauxites, ferruginous and manganiferous duricrusts and thick oxisols developed from them (Reis et al., 2013; Albuquerque and Horbe, 2015; CPRM, 2015; Albuquerque et al. 2017), it becomes an excellent place to employ the Nd, Sr and Pb isotopic systems concerning sedimentary provenance studies and improve the understanding the behavior of these isotopes under extreme weathering. Thus, the goal of this study is to recognize the source of sediments of these sedimentary basins and to evaluate the weathering effect over Nd, Pb and Sr isotopes along the regolith. Besides that, the region is under geological mapping refinement, so the combination of isotopic analysis, mineralogical and geochemical (both in rocks and regolith horizons) together with airborne gamma spectrometry also aiming improve the geological knowledge.

2. ENVIRONMENTAL AND GEOLOGICAL SETTING

The study area is located in the southwestern Amazonia, Brazil, between 6-13°S and 59-62°W (Fig. 1). The geological mapping of the region is under review by Brazilian Geological Survey (CPRM), and there is no integration between of the eastern and western portions of the geological maps (Fig. 1). Nevertheless, available data indicates that the basement is composed by rhyolites, dacites and rhyodacites, with some subvolcanic rocks (Colíder Group with 1.78-1.80 Ga; Santos, 2003; Fig.1). Intrusive into volcanic basement there are granitic suites (Teodosia- 1.758 to 1.757 Ga; and Igarapé das Lontras- 1.754 Ga), which are intersected by monzogranite batholiths (Serra da Providência intrusive suite, 1.57-1.53 Ga) (CPRM, 2015).

Over the volcanic basement and granitic bodies was developed a Proterozoic intracratonic basin in rift called Sumaúma basin, divide in Vila do Carmo and Beneficente Groups (Reis et al., 2013). The volcano-sedimentary sequence (Vila do Carmo Group, 1.76-1.74 Ga) comprise quartz sandstones, volcanoclastic and pyroclastic rocks cut by diabase (Mata-Matá, 1.576 Ga) (Betiollo et al., 2009; Reis et al., 2013). These rocks are overlapped by orthoconglomerates and massive quartz-sandstones with

rare mudstones of alluvial fans and floodplain; pinkish to purplish silicified quartz-sandstones deposited at tidal plains and river channels; and sublitharenites and quartz sandstones intercalated with siltstones and mudstones of aeolian and washover environment (Beneficente Group, 1.01-1.43 Ga; CPRM, 2013; Reis et al. 2013).

The Paleozoic new rift process allowed the developed of a new sedimentary basin (AltoTapajós Group, Silurian-Devonian). It gathers fine to medium grained sandstones with conglomeratic lenses and siltstones interspersed with fine sandstones deposited in coastal and lagoon environment (CPRM, 2013; CPRM, 2015). From the Sumaúma and Alto Tapajós basins were developed an extensive lateritic covers (Silva et al., 2012; Albuquerque and Horbe, 2015; CPRM, 2015; Albuquerque et al., 2017) composed by ferruginous and manganiferous duricrusts, bauxites, colluviums and thick oxisols.

In the Neogene conglomerates, conglomeratic sandstones and mottled mudstones (Salva Terra Formation) were deposited into preterit alluvial plains, and gravel, sand, silt and clay into the modern alluvial plains (CPRM, 2006).

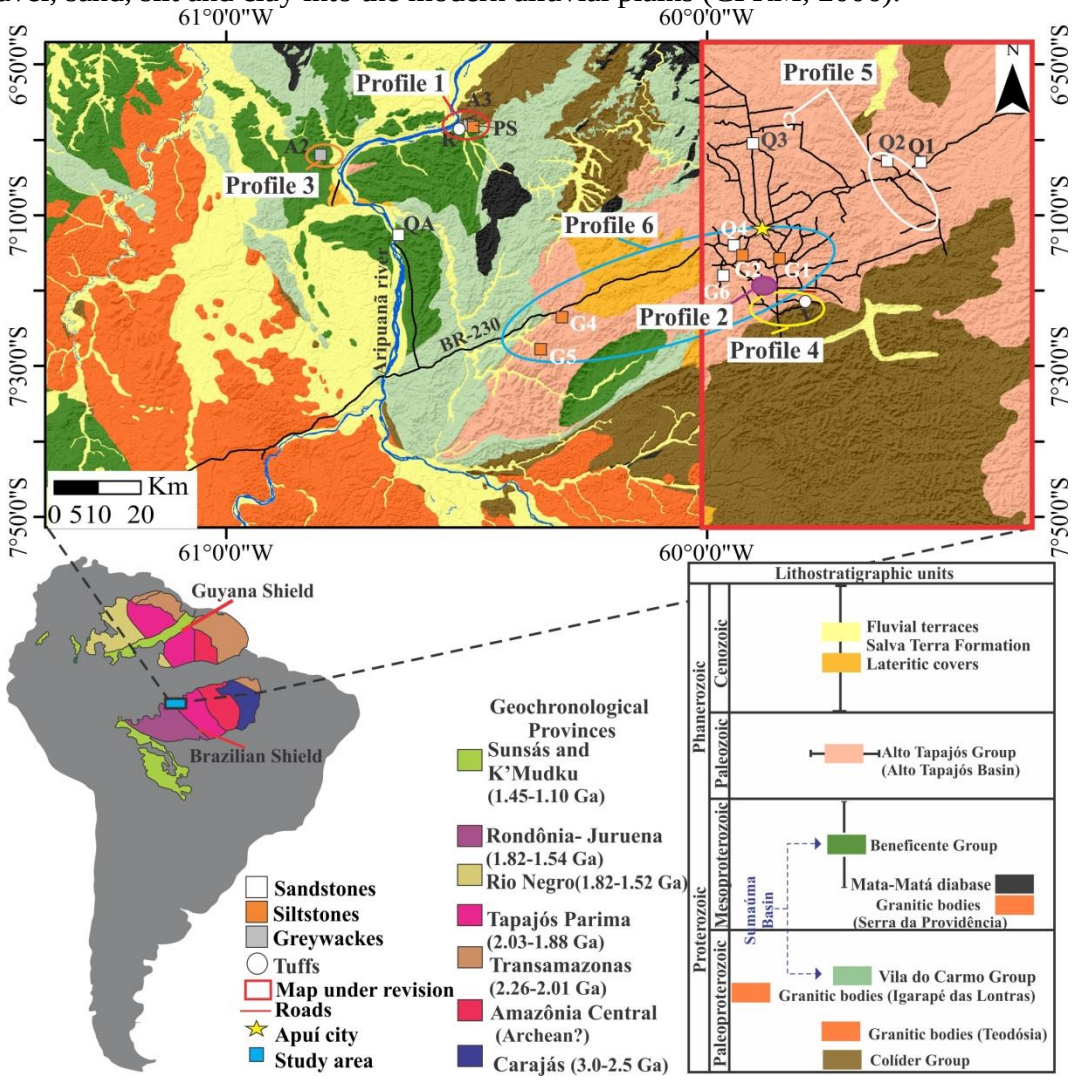

Figure 1: Localization of study area and geological setting with samples collected and the lateritic profiles. Geological map carried out for Geological Survey of Brazil, CPRM (2006, 2013, 2014 and 2015). The eastern portion (red square) is under revision

3. SAMPLING MATERIALS AND ANALYTICAL METHODS

Thirty eight samples from six profiles including rocks, bauxites, manganese, ferruginous and iron-aluminum duricrusts and soils have been collected. The samples were dried at room temperature, pulverized and submitted to mineral identification by optical microscopy (10 thin sections), XRD (Shimadzu XRD – 6000) equipped with copper tube and scanning electron microscopy (SEM, Quanta 250 FEI) after Au-Pd metallization. All the samples were analyzed for major (SiO_2, Al_2O_3, Fe_2O_3, MgO, CaO, Na_2O, K_2O, TiO_2, P_2O_5 e MnO) and trace elements (Ag, As, Au, Ba, Bi, Be, Cd, Co, Cr, Cs, Cu, Ga, Hf, Hg, Mo, Nb, Ni, Pb, Rb, Sb, Sc, Se, Sn, Sr, Ta, Tl, Th, U, V, W,Y, Zn, Zr and REE) by fusing an aliquot using Li metaborate or tetraborate followed by dissolution in a triacid solution. The elemental determinations have been performed by inductively coupled plasma mass spectrometry, whereas the loss of ignition (LOI) was analyzed by gravimetry. All of the samples were carried out at Acme Analytical Laboratories LTD, Canada.

The Nd and Sr isotopes were performed in 38 samples, of which 10 were selected for Pb isotopic analysis. For isotopic analysis were separated 20- 40 mg aliquots of rocks, crusts and soils, to be digested under clean laboratory conditions in two stages using concentrated HF/ HNO_3 and 6N HCl on a hot plate. The Sm, Nd and Sr isotopes were loaded onto Thermo Ionization Mass Spectrometry (Geochronology Laboratory of the University of Brasilia), according to the procedures of Gioia and Pimentel (2000). REE and Sr isotopes were separated using chromatographic columns with AG50W-X8 cation-exchange resin. After that, Nd was isolated from the others REE using AG50-X2 resin. Sr, Nd and Sm were loaded separately on tungsten filament with TaF solution. Neodymium was reprocessed on double rhenium filament with H_3PO_4 (0.1 M) and measured as metal Nd^+. The $^{143}Nd/^{144}Nd$ ratios are presented in parts per 104 units from $^{143}Nd/^{144}Nd_{CHUR}$ as present day measured: $\varepsilon Nd_{(0)}=[(^{143}Nd/^{144}Nd)_{amostra}/I_{CHUR(0)}-1]*10^4$, thus, $^{143}Nd/^{144}Nd_{sample}$ is the present day ratio measured in the sample, and $I_{CHUR(0)}$ (0.512638) represents the $^{143}Nd/^{144}Nd$ ratio in the CHUR reference reservoir at the present (Jacobsen and Wasserburg, 1980). The analytical uncertainty is of 0.0004% e 0.05% for $^{143}Nd/^{144}Nd$ and $^{147}Sm/^{144}Nd$, respectively.

Pb was loaded onto standard Re filaments with a mixture of silica gel and phosphoric acid. All of these analyses were performed on a Thermal Ionization Mass Spectrometer (Finnigan MAT 262) in Geochronological Research Center- São Paulo University. Based on multiple analyses of a common Pb standard (NBS-981), the samples were corrected by 0.13%/a.m.u for instrumental mass fractionation. The NBS-981 standard deviation (1s) for $^{206}Pb/^{204}Pb$ = 16.898 ± 0.008; $^{207}Pb/^{204}Pb$ = 15.439 ± 0.010 and $^{208}Pb/^{204}Pb$ = 36.535 ± 0.032.

Mass balance was performed in five of the six profiles (P1, P2, P4, P5 and P6), those that are better developed. It was calculate the P_2O_5 and REE mass balance using Zr as immobile element. The enrichment factor is based on the following formula $EF=[Ce_{(hz)}* Zr_{(pt)}]/[Ce_{(pt)}* Zr_{(hz)}]$, where EF= enrichment factor; $Ce_{(hz)}$= element amount in horizon, $Ce_{(pt)}$= element amount in protolith; $Zr_{(hz)}$= Zr concentration in horizon and; $Zr_{(pt)}$= Zr concentration in protolith. Thus, enriched elements display EF values > 1.1, depleted elements in comparison to protolith show EF< 0.9, while immobile elements show values between 0.9 and 1.1. It is worth mentioning that the profile 2 is correlated with the profile 1, so for the mass balance analysis and behavior of Nd, Sr and Pb isotopes during weathering, the Mn-greywacke (A3) was used as protolith.

Geological and relief maps were performed using ArcGis 10 and Global Mapper 13.

The airborne gamma-ray spectrometric images were obtained and processed from the Prospectors Airborne System LTDA, Rio de Janeiro, Brazil, as part of two aero geophysical projects (Aripuanã and Sucunduri) of the CPRM/Geological Survey of Brazil in the 2010. On Oasis Montagi 6.3 the K, Th and U channels of airborne gamma-ray spectrometric images were normalized and made a unique mosaic.

4. PETROGRAPHY OF THE SEDIMENTARY ROCKS

The quartz-sandstones, Mn-greywackes and tuffs were gather together and described according the similarities and fieldwork observations due to the eastern part of study area is still in mapping refinement. Also, the term Mn-rocks is used when Mn-siltstones and Mn-greywackes are discussed together.

4.1 Vila do Carmo Group: Quartz-sandstones (samples Q1 and Q3), tuffs (samples V and R) and Mn-rocks (samples PS and A3)

The quartz sandstones are greyish, super mature, laminated with low porosity and closed framework (Fig. 2A). The well rounded and sorted quartz grains have silica overgrowth (3% of bulk rock), display concave convex contacts with few contacts sutured and polygonal (Fig. 2B). There is pseudo-matrix with opaque inclusions and altered microclines to illite. The tuffaceous rocks (samples V and R), interbedded with the quartz-sandstones, are composed by angular quartz (≤ 6 cm diameter; 45% of bulk rock), sericitized feldspar porphyries (25%), volcanic fragments (3%) and sphene, rutile, Ti-magnetite, zircon and epidote (≤ 2.5%) (Fig. 2C and D). They are sustained by quartz-feldspar matrix or volcanic glass (25%).

Interbedded with tuffaceous rocks, there are Mn-siltstone (sample PS) and Mn-greywacke (sample A3) framed into Vila do Carmo Group (Albuquerque et al., 2017). The Mn-siltstone is pinkish, has quartz framework (78% of bulk rock) and displays fractures filled by coronadite and hollandite (22% of bulk rock) (Fig. 2E). The Mn-greywacke (A3) has quartz grains (48%) supported by matrix, which is composed by hollandite and cryptomelane with widespread coronadite (Fig. 2F). The quartz grains are poorly sorted, moderately to well rounded, fractured with silica overgrowth.

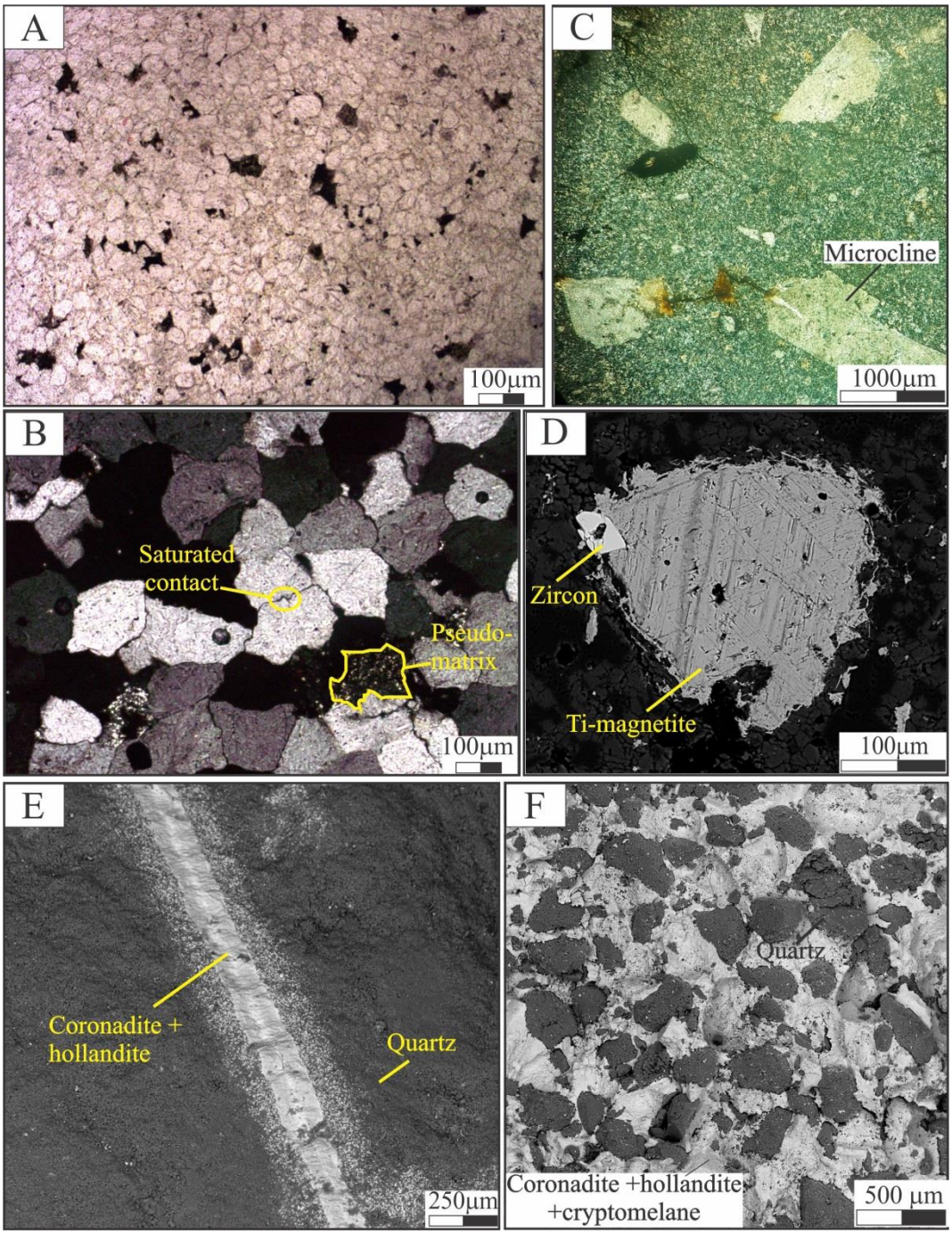

Figure 2: Main features of quartz-sandstones, tuffs and Mn-rocks of study area. A- Framework of quartz-sandstones (Q1 and Q3). B- Detail of satured contact between quartz grains and pesudomatrix. C- Overview of tuff fragment showing microclines sustained by quartz-feldspar matrix. D- Ti-magnetite of the tuffs with zircon inclusion involved by quartz-feldspar matrix. E- Pinkish siltstone showing fine quartz matrix crossed by coronadite and hollandite veins. F- Quartz grains sustained by hollandite, cryptomelane and coronadite matrix in Mn-greywackes.

4.2 Beneficente Group: Quartz-sandstones (QA and Q2) and Mn-greywacke (A2)

The quartz-sandstones (QA and Q2) are whitish to pinkish, sub-mature to mature, fractured with closed framework composed by quartz grains with sorting moderate to well. The quartz grains (90% of the rock) are imbricated with convex concave contacts, silica overgrowth (up to 3% of the bulk rock) and secondary ferruginous cement overlay. Among the quartz grains there are pseudo-matrix (3%) and

lithic fragments (2%) (Fig. 3A and B). Anatase, Ti-magnetite, ilmenite and zircon comprises up to 2% of the rocks (Fig. 3C, D, E and F).

The Mn-greywacke (A2) has quartz grains (33%) supported by matrix of romanechite (67%).

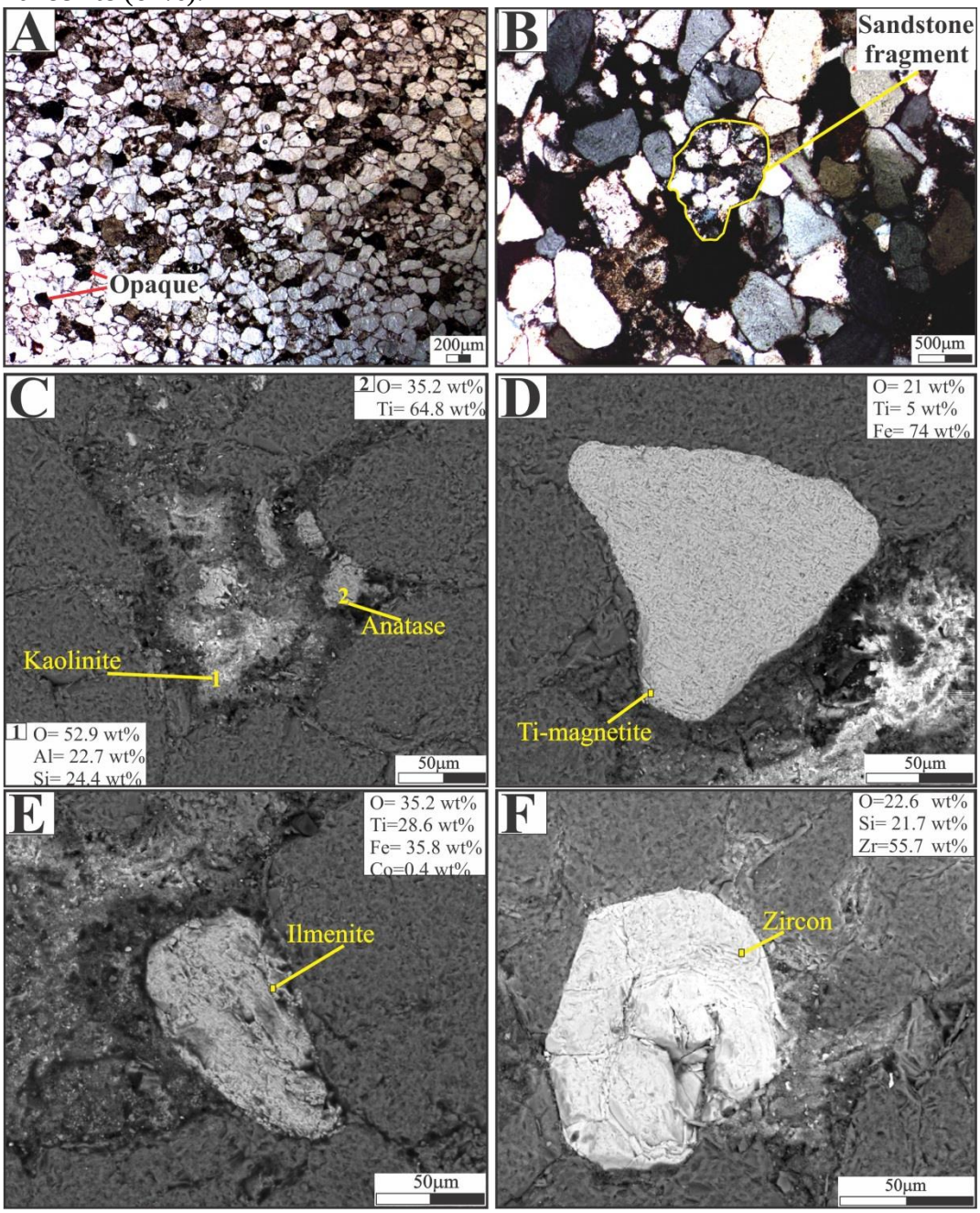

Figure 3: Main features and mineral composition of quartz-sandstones (QA and Q2). A- Framework of quartz-sandstones highlighting the opaque minerals and quartz. B- Sandstone fragment. C- Anatase derived from weathering of Ti-magnetite. D and E- Ti-magnetite and ilmenite at quartz framework. F- Euhedral zircon grain widespread in framework.

4.3 Alto Tapajós Group: quartz-sandstone (Q4) and feldspathic greywackes (G1, G2, G4, G5 and G6)

The quartz-sandstone (Q4, 90% of quartz) is whitish to greyish, mature and silicified. The quartz grains are poor to moderate sorted, rounded to sub-rounded with silica overgrowth (up to 7% of bulk rock (Fig. 4A). Also, there are magnetite and Ti-magnetite (1%), sandstones and volcanic fragments (2%) and minor amount of

fragments of siltstones (Fig. 4B and C). The sandstone fragments show angular to sub-rounded quartz grains cemented by silica, while the volcanic fragments have a fine grained silica matrix replete of slatted muscovite and opaque. The siltstones fragments in sutured contact with quartz grains are composed by kaolinite mass impregnated by iron oxides (Fig. 4D).

The feldspathic greywackes are greyish, laminate, composed mainly by angular microcline grains (25% of bulk rock) with 50 to 80 μm diameter (Fig. 4E and F), supported by very fine quartz-illite matrix (80% of bulk rock) with thin veinlets of illite, heterogeneous mass of fluorapatite, rounded to subhedral zircon and rutile grains (Fig. 5A). In the sample G5 there is no illite (Fig. 4G and H).

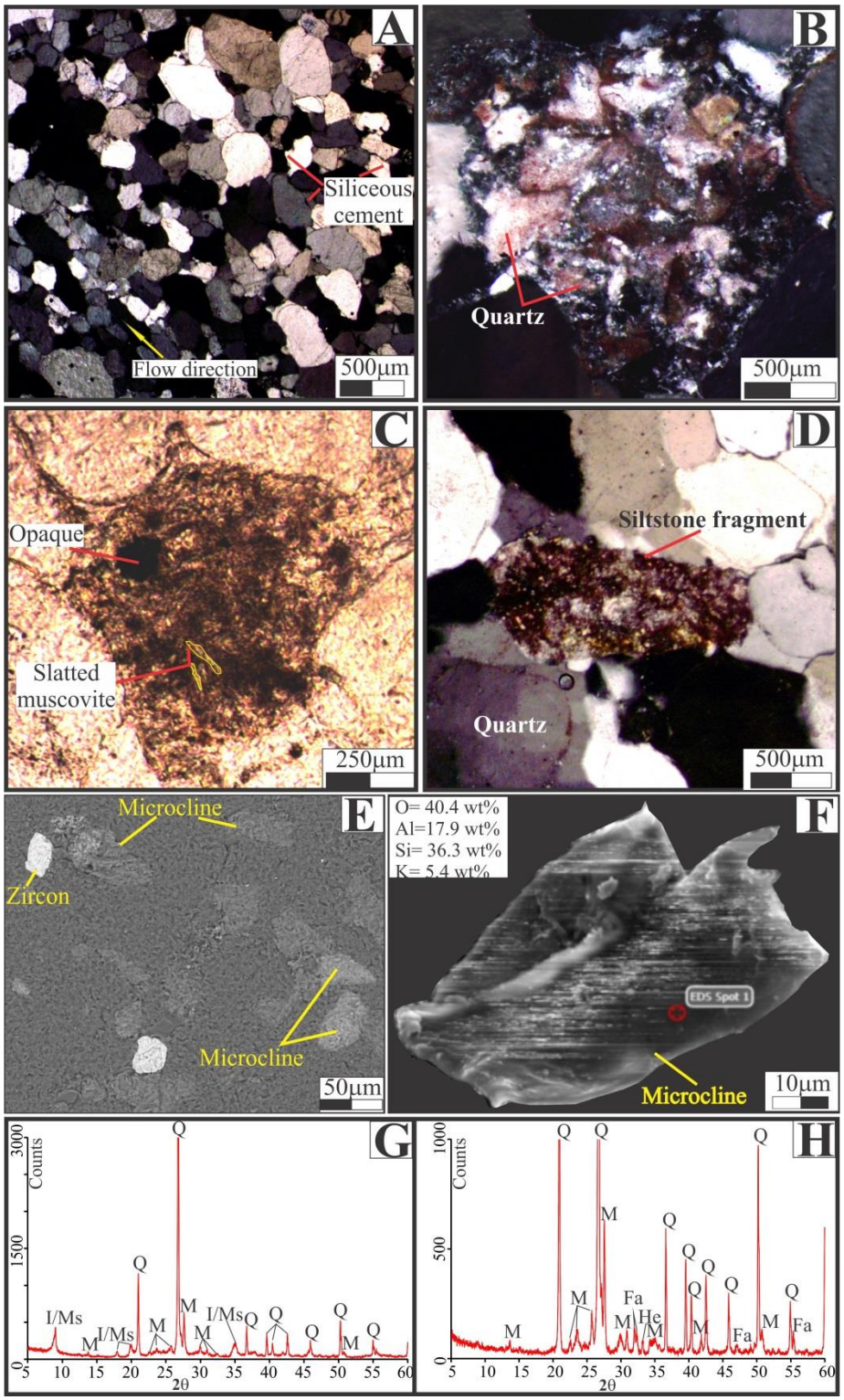

Figure 4: Main features of quartz-sandstones and feldspar greywackes. A- Framework showing flow direction and siliceous cement surrounding quartz grains of quartz-sandstone Q4. B- Sandstone fragment in sample Q4 showing angular quartz grains and siliceous cement. C- Volcanic fragment in sample Q4 with opaque and slatted muscovite. D- Siltstone fragment in sample Q4 composed by Kaolinite and quartz. D- Fragments of microcline and zircon grains involved by quartz-illite matrix of the greywackes. E- In detail microcline fragments. F and G- XRD of two types of greywackes depending of the illite and fluorapatite amounts of the greywackes. I-illite, Ms- muscovite, Q-quartz, M-microcline, He- hematite, Fa-fluorapatite.

5. GEOCHEMISTRY SEDIMENTARY ROCKS

The greywackes of the Alto Tapajós Group constituted mainly by microcline, illite, muscovite, fluorapatite and traces of rutile/anatase have more Al_2O_3, K_2O, P_2O_5, MgO and TiO_2, (Tab. 1). The greywackes G5 and G6 show the highest CaO contents (2.4 and 0.63%, respectively; Tab. 1). The quartz sandstones have high SiO_2/Al_2O_3 ratios and LOI $\leq$ 2, while the Mn-greywackes with 32.82 to 39.95% of MnO also displays higher Fe_2O_3 content (Tab. 1).

The CIA index in which the oxide units are given in moles (Nesbitt and Young, 1982; Nesbitt and Young, 1989) (Tab. 1), although must be take carefully, especially for K_2O, Na_2O and CaO more susceptible to be removed during weathering conditions, allowed to identify four set of rocks: 1) quartz-sandstones and Mn-rocks of the Sumaúma basin with high CIA (> 84) closer to kaolinite and gibbsite index; 2) quartz-sandstones of Sumaúma (Vila do Carmo Group) and Alto Tapajós basins with intermediary CIA values (70-83) associated to illite and muscovite; 3) greywackes of Alto Tapajós basin with low CIA (70 and 50) associated to high microcline content; 4) greywacke of Alto Tapajós basin (G5) with the lowest CIA (< 50) and similar amounts of K_2O and CaO due to the presence of fluorapatite and microcline.

Among all samples, the Mn-rocks (PS, A2 and A3) have the highest trace elements content, especially Ba (14055-111200 ppm). Some of the Mn-rocks (PS and A3) have also high contents of Cu (1146-2016 ppm) and Pb (17200-43638 ppm) (Tab. 1).

Concerning to the bulk continental crustal average (BCC, Taylor and McLennan, 1985), all the quartz sandstones and the greywacke G6 are depleted in almost all trace elements. Only the quartz sandstone Q2 is enriched in Ba and Cu (Fig.5A and B)

The greywackes framed into the Paleozoic Alto Tapajós Group display enrichment in As, Hf (except G2), Y, U and Zr relative the bulk continental crust (BCC). There are other slight differences, depletion in Th and Rb and enrichment in Pb and Zn is the character of the greywacke G5, while the enrichment in Cu is peculiar of greywacke G4. By the other hand, the greywackes G2 and G4 also have enrichment in Ta, Nb and Ga (Fig. 5A).

The Mn-rocks (PS and A3) are featured by depletion in Hf, Nb, Zr, Th, Sr, Sc and Rb and enrichment in Cu and Pb relative the BCC (Fig. 5C). However, the sample A2 of the Beneficente Group is enriched in Ta, Ni and Zn.

The Paleozoic greywackes (samples G2 and G4) of Alto Tapajós Group have similar and the higher contents of REE (225 ppm), by the other hand the minor contents (39-53 ppm) are assigned to Mn-greywacke (A3) and quartz-sandstones, except the sample QA of the Proterozoic Beneficente Group (Tab.1).

Relative the chondrite average of Taylor and McLennan (1985), all samples displays LREE>HREE (La_n/Yb_n 6.21-75.81) and negative Eu anomaly (0.38-0.89)(Fig.5 D, E and F). Positive Ce anomalies are incipient, except in quartz-sandstone (sample Q2) and Mn-greywacke (sample A2) of the older Beneficente Group rocks with Ce/Ce* ratios between 1.14 and 1.28, respectively.

Table 2: Major oxides in wt.% and trace element concentrations in ppm of the sedimentary rocks of the southwestern of Amazonia

Lithotype	Greywakes					Quartz-sandstones					Mn-rocks		
Sample	G1	G2	G4	G5	G6	Q4	QA	Q2	Q1	Q3	A3	PS	A2
SiO_2	75.12	66.9	65.27	81.94	81.8	98.24	91.95	97.46	98.73	98.03	46.7	73.39	25.33
Al_2O_3	11.85	16.43	16.2	6.45	8.1	0.78	3.71	0.57	0.35	0.37	0.7	1.91	1.35
Fe_2O_3	0.75	1.04	1.35	0.42	0.54	0.65	1.7	0.75	0.11	0.97	3.3	2	2.28
K_2O	6.1	8.46	4.74	3.89	5.07	0.2	0.22	0.05	0.06	0.05	0.07	0.15	0.06
CaO	0.3	0.02	0.05	2.4	0.63	<0.01	0.01	0.01	0.01	0.01	0.06	0.02	0.09
MgO	0.42	0.68	1.01	0.09	0.13	0.04	0.01	0.01	0.01	0.01	0.01	0.01	0.01
MnO	<0.01	<0.01	<0.01	<0.01	<0.01	<0.01	0.2	<0.01	<0.01	0.03	32.82	12.96	39.55
Na_2O	0.07	0.06	0.07	0.04	0.06	<0.01	0.01	0.01	0.01	0.01	0.01	0.01	0.01
P_2O_5	0.7	0.44	1.12	2.26	0.89	0.01	0.01	0.17	0.04	0.03	0.24	0.34	0.71
TiO_2	0.41	0.62	0.66	0.21	0.22	0.05	0.22	0.04	0.05	0.04	0.02	0.05	0.08
LOI	4.1	5.2	9.3	2.1	2.4	<0.1	2	0.02	0.6	0.3	6.1	3.2	9.1
SiO_2/Al_2O_3	6	4	4	13	10	126	25	171	282	265	67	38	19
CIA	61.9	63.8	75.2	42.7	54.6	78.3	93.1	86.5	77.8	80.6	77.6	89.9	84.6
As	3.6	8.9	4.8	3.5	1.4	<0.5	<0.5	1.1	<0.5	0.7	74.9	39.6	101.7
Ba	499	545	550	277	432	30	115	722	23	125	71100	14055	111200
Cu	15.6	22.9	38.8	3.6	9.5	1.2	2	37.3	1.3	2.9	2016	1446	78
Ga	15.3	21.8	20.9	7.1	8.6	1.4	3.3	1.7	3.7	<0.5	63.4	14.3	104.5
Hf	9.5	5.1	8.3	7.5	6.2	1.4	2.9	2.7	2.2	1.3	1	2.2	3.3
Nb	10.2	13.7	15.8	7.5	5.1	1.7	5.8	1.6	4.2	1.5	1.7	1	2.2
Ni	7.7	4.1	5.7	2.1	7.2	8.2	8.1	3.9	0.2	13.6	13	9.5	110.4
Pb	20.1	18	16.8	23.2	6.2	2.1	5	4.6	0.5	0.7	17200	43638	67
Rb	132	184	192	74	98	5.3	7	2.5	1.3	1.2	1.6	4.1	2.2
Sc	6	9	10	5	3	0.5	3	1	0.5	0.5	3	2	6
Sr	61.6	104	83.9	59.6	53.9	6.8	25	31.4	18.7	14.5	51	18.8	64
Ta	0.9	1.1	1.2	0.7	0.5	0.2	<0.2	0.4	0.4	0.1	6.7	1.6	21.2
Th	13.4	19.5	19.4	7.1	7.1	2.7	5.1	2.9	<0.1	2.6	1.7	1.4	2.8
U	3.8	3.1	4.5	2.9	2.2	0.6	1	1.6	0.6	0.7	4.6	2.3	3.7
V	34	61	56	17	19	15	25	25	5	13	80	4	119
Y	25	27.9	61.2	26	16	8.6	13	13.6	5.7	6.4	5	4.8	18
Zn	19	6	42	92	7	1	3	0.5	0.5	2	117	38	320
Zr	382	218	295	302	217	41	108	122	104	50	32	15.6	104
La	33.6	50.3	53	22.2	12.5	11	25.1	10.7	12.1	7.6	7.7	46	15.8
Ce	70	98	104	48	30	23	49	25	24	15	14	70	45
Pr	8.5	11	12.2	5.3	4.2	2.6	7	2.4	2.3	2	1.4	9.3	4.3
Nd	31.2	39.3	45.1	20.2	17.5	9.2	24.8	9.8	9	8.3	6.1	28.1	17
Sm	6.1	6.8	8.1	4	4.3	1.6	4.3	2.6	1.8	1.4	1.3	3.5	3.4
Eu	1.2	1.3	1.5	0.8	0.9	0.3	0.8	0.6	0.3	0.3	0.9	0.4	0.9
Gd	5.3	6.1	8.4	3.8	3.6	1.6	3.1	2.8	1.5	1.3	8.2	2.2	2.8
Tb	0.8	0.9	1.4	0.6	0.6	0.3	0.5	0.4	0.2	0.2	1.2	0.2	0.4
Dy	4.3	4.8	8.4	3.4	3.2	1.6	2.7	2.1	1.1	1.2	5.5	1.1	1.4
Ho	0.9	1	2	0.8	0.6	0.3	0.5	0.4	0.2	0.2	1	0.2	0.2
Er	2.5	3	5.6	2.3	1.7	0.9	1.5	1.2	0.6	0.6	2.7	0.5	0.6
Tm	0.4	0.4	0.8	0.3	0.2	0.1	0.2	0.2	0.1	0.1	0.4	0.1	0.1
Yb	2.3	2.8	4.4	2.2	1.4	1	1.5	0.9	0.6	0.7	2.4	0.4	0.5
Lu	0.4	0.4	0.7	0.3	0.2	0.1	0.2	0.1	0.1	0.1	0.3	0.1	0.1
LREE	150	206	224	100	69	48	111	51	49	35	31	157	87
HREE	17	19	32	14	12	6	10	8	4	4	22	5	6
ΣREE	167	226	256	114	81	54	121	59	54	40	53	162	93
Eu/Eu*	0.63	0.61	0.57	0.64	0.66	0.56	0.67	0.63	0.61	0.61	0.84	0.38	0.89
Ce/Ce*	0.97	0.97	0.96	1.03	0.97	1.02	0.87	1.14	1.06	0.91	1.00	0.79	1.28
$(La/Yb)_N$	9.8	12.1	8.1	6.8	6.2	7.2	11.3	7.7	14.1	7.9	2.2	75.8	21.3

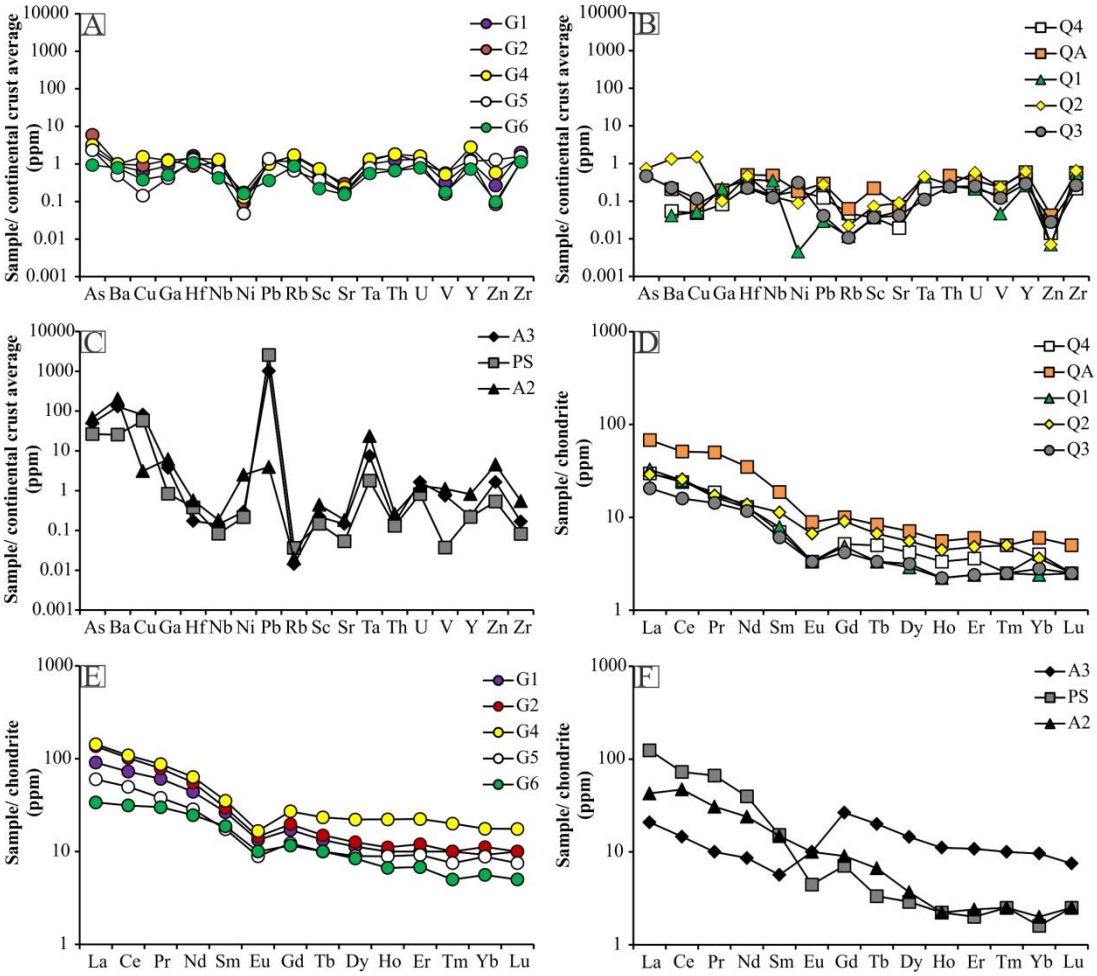

Figure 5: Trace and rare earth elements normalized by continental crust average and chondrite (Taylor and McLennan, 1985), respectively.

6. MINERALOGICAL FEATURES OF THE LATERITIC PROFILES

The location together with the main physical features and mineral composition of the six studied lateritic profiles widespread in an area of about 19,000 km^2, are shown at figures 1, 6 and 7 and at Table 2. The chemical and mineralogical features of these profiles are better detailed in Albuquerque and Horbe (2015) and Albuquerque et al. (2017). The profile P1 has as parent rock a volcano-sedimentary sequence which gathers in the bottom a tuff (R), a pinkish siltstone (PS) and a Mn-greywacke (A3) framed into Vila do Carmo Group (Fig. 6). From these rocks were developed a thick lateritic duricrust (~3 m thick) with massive (M1), protopisolitic (Pp1 and Pp2) and pisolitic (Pi1 and Pi2) facies (Fig.6; Tab. 2). Covering the lateritic duricrust, there is a yellowish sandy clay oxisol (S7) 0.5 m thick, which has gibbsite and kaolinite as main minerals and hematite, goethite and anatase subordinated. The profile P2, which is correlated to profile 1 and have the same protolith is composed by Mn-Al-Fe vermiform duricrust (VB and VT) pinkish to greyish, 3.0 m thick (Fig.6; Tab. 2). The reddish sandy clay oxisol (S5) differ from those of profile 1 because it has more quartz.

The bottom of the profile P3 is a Mn-greywacke (A2) framed into Beneficente Group (Fig.6), overlapped by a vermiform Mn-duricrust with 2.0 m of thick (B1-B4). Covering the duricrust there is yellowish oxisol (S6) with up 8.0 m thick composed of quartz, kaolinite, hematite, goethite and anatase.

The tuff (V) of Vila do Carmo Group is the protolith of the profile P4. From this rock was developed a thick lateritic duricrust with facies massive bauxite (Bx- 2.5 m thick) and massive and fragmental ferruginous duricrust (C7 and C3- 1.5 m thick), covered by oxisol (S4) with about 0.3 m of thick is formed by kaolinite and gibbsite (Fig. 7).

The profile P5 is composed from bottom to top by quartz-sandstone (Q2), pisolitic bauxites (B1A and B1C) with 2.0 m thick, Fe-Al vermiform duricrust (C2; Tab. 2; Fig. 7) with up 1.0 m thick and a thin yellowish oxisol (~30cm) composed by gibbsite, kaolinite, hematite and anatase.

The profile P6 has as parent rock the greywackes and sandstone (G1 to G5 and Q4) of Alto Tapajós Group from where was developed a fragmental and laminated Fe and Fe-Al duricrusts (C1, C4 and C6) blocks with up 2.0 m of diameter (Tab. 2, Fig.7).

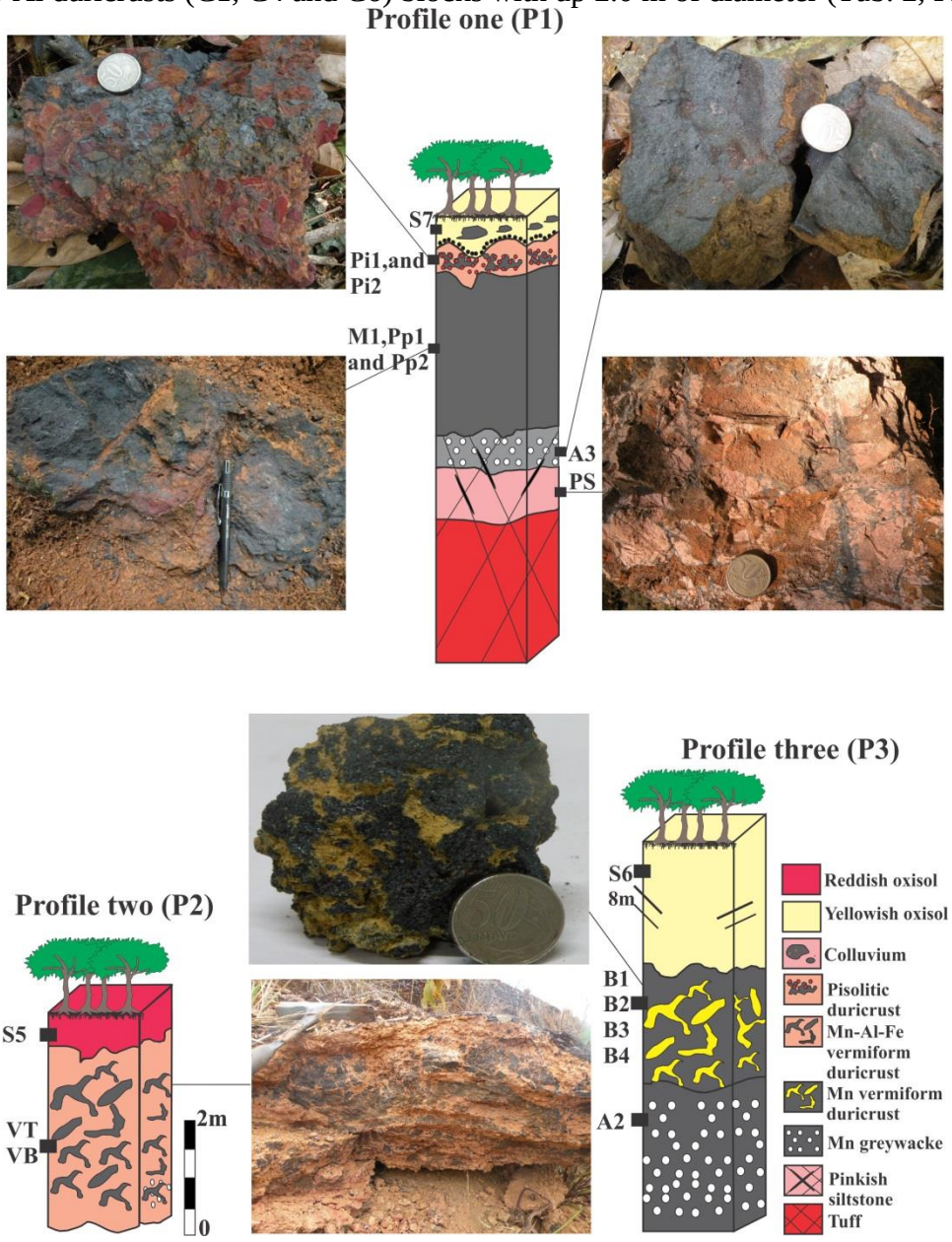

Figure 6: Mn lateritic profiles developed from Mn-rocks in study area

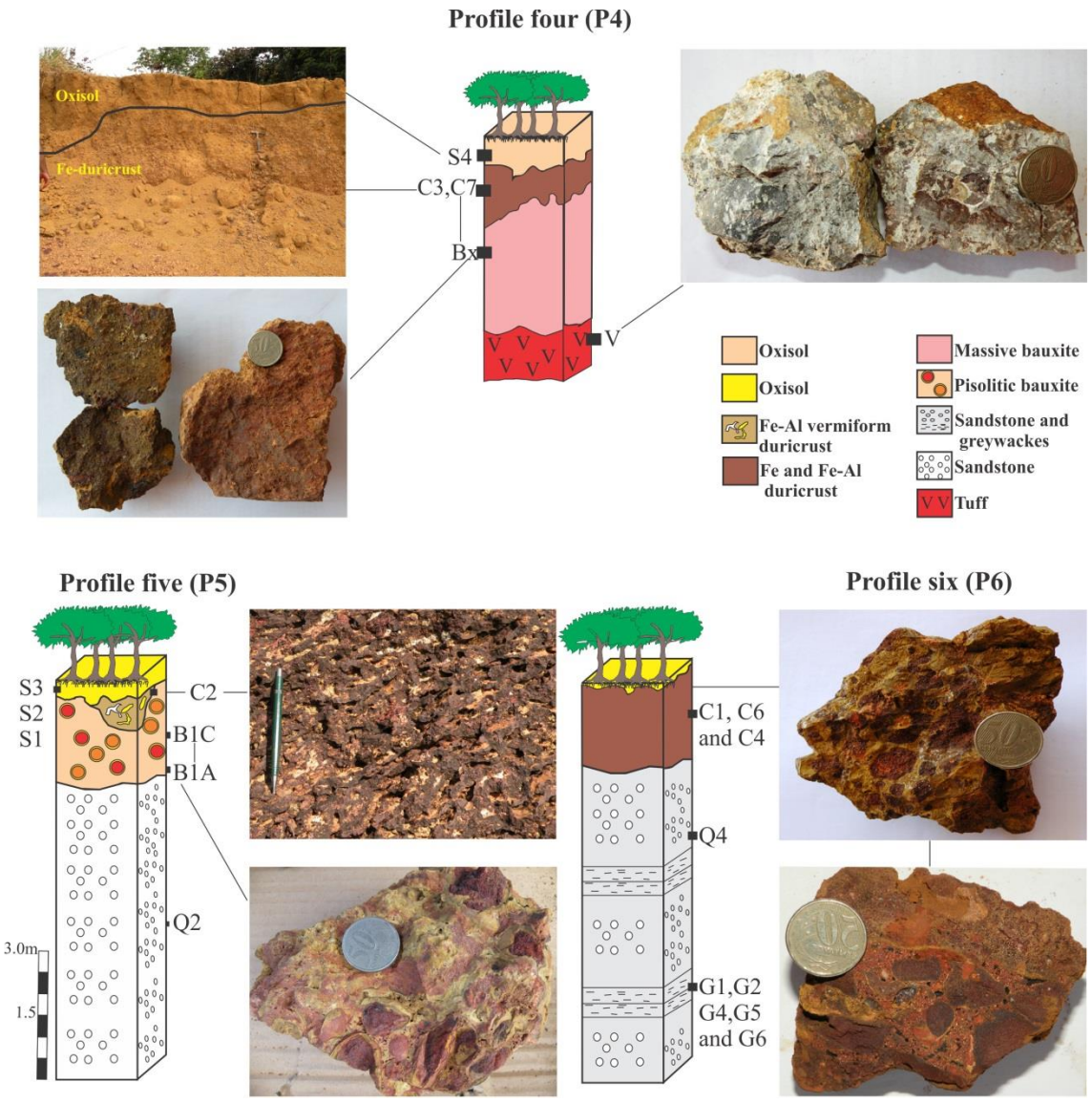

Figure 7: Ferruginous duricrusts and bauxites developed from tuffs, sandstones and sedimentary rocks of Vila do Carmo, Beneficente and Alto Tapapós Group.

Table 3: Main features and mineral composition of the duricrusts of each profile. N.I- not identified

Duricrust	Sample	Framework/skeleton	Pisoliths/Angular fragments	Cavities/ fractures
Mn-Al-Fe Pisolitic	Pi1 and Pi2	Pinkish framework, composed by gibbsite, hematite and kaolinite. Secondary frosted to metallic plasma of hollandite, cryptomelane and goethite involves the framework Coronadite veinlets are widespread in framework	Red pisoliths of hematite and gibbsite with up to 2 cm diameter are sustained by framework	Filled by kaolinite and quartz
Mn-Al-Fe Vermiform	VT (top) and VB (bottom)	Skeleton composed by dendritic hollandite, crypetomelane and pyrolusite. Involving the skeleton there is a plasma of gibbsite, hematite, goethite and kaolinite, with cerianite subordinated. Increase of hematite and gibbsite toward to top. Coronadite veinlets are widespread in skeleton	N.I	Filled by kaolinite and quartz
Mn Protopisolitic	Pp1 and Pp2	Bluish grey, hard, dense, with metallic luster, rich in romanechite/hollandite, cryptomelane and pyrolusite	Pisoliths (1.5 cm ϕ) involved by cortex are widespread in the framework. Both are composed by the same minerals of framework.	Filled by quartz, kaolinite, gibbsite, goethite and hematite
Mn Massive	M1	Greyish, pulverulent and porous rich in cryptomelane, hollandite and pyrolysite with intergrown of gibbsite and hematite	N.I	Filled by kaolinite and goethite
Fe massive duricrust	C7	The framework is brownish, porous and composed by hematite, goethite and gibbsite as major phases, and quartz, kaolinite and anatase as trace minerals. Widespread on the framework is common the presence of quartz pebbles of up to 2 cm of diameter. They are fractured, corroded and show indications of dissolution	N.I	The cavities constitute pipes with 3cm diameter and are filled with yellow kaolinite
Massive bauxite	Bx	The framework comprises about 97% of the duricrust, it is compact, brown to pink reddish, little porous with gibbsite and hematite as major minerals	N.I	The cavities are filled by small gibbsite geodes (($\leq$ 3 cm of ϕ) and, sometimes, for whitish clayey material of illite and kaolinite
Fe-Al vermiform	C2	The skeleton is friable (80% of bulk duricrust) composed by goethite, hematite and gibbisite as main minerals and by kaolinite and quartz subordinated	N.I	Filled by whitish kaolinite and quartz
Pisolitic bauxite	B1A and B1C	Pinkish plasma (55% of bulk duricrust), sometimes, whitish to reddish composed mainly by gibbsite and hematite	Hematitic and Al-goethitic ($\leq$ 2.5 cm ϕ) comprise about 40% of the duricrust and are involved by brownish to orange goethitic cortex.	Filled by kaolinite, quartz and anatase.
Mn-vermiform	B1 to B4	Hard, dense and porous bluish grey skeleton (80% of bulk duricrust) with submetallic to earthy brightness composed mainly romanechite and quartz	N.I	Filled by kaolinite, goethite and hematite in a total of 20% of the bulk duricrust
Fe and Fe-Al Fragmental	C1, C3, C6	The sandy clay framework comprises between 45 to 60% of bulk duricrust. It is orange when composed by goethite, hematite and quartz, or it is reddish pink when is formed by ooliths of gibbsite and kaolinite surrounded by hematite and goethite.	The framgments (till 35% of bulk duricrust) are reddish to violet with till 3.5 cm diameter. They are of gibbisite and hematite or composed mainly by hematite with quartz inclusions	Comprises until 25% of bulk duricrust, they are filled by gibbisite, hematite and kaolinite or goethite, quartz and rutile and have coloring whitish pink and whitish yellow.
Fe Laminated	C4	Intercalation of thin blades of goethite with quartz, kaolinite and hematite subordinated	N.I	Filled by hematite botryoidal

7. NEODYMIUM ISOTOPES

According to Nd isotopes, the Sumaúma Supergroup is divided into three mains groups which gathers: 1- Pinkish siltstone (PS) and quartz-sandstone (Q1) of the Vila do Carmo Group and quartz-sandstones (A2 and Q2) of the Beneficente Group, featured by the highest TDM (2.29-3.4 Ga), $^{147}Sm/^{144}Nd$ (0.1232-0.1653), f(Sm/Nd) (-0.37 to -0.16) and Sm/Nd (0.204-0.274) values; 2- Tuffs (R and V), quartz-sandstone (Q3) and Mn-greywacke (A3) of the Vila do Carmo Group, which have intermediate values of TDM (1.81-2.19 Ga), $^{147}Sm/^{144}Nd$ (0.1055-0.1131), f(Sm/Nd) (-0.46 to -0.41) and Sm/Nd ratio (0.175-0.193); 3- Quartz-sandstone QA of the Beneficente Group with the lowest values of TDM (1.64 Ga), $^{147}Sm/^{144}Nd$ (0.1050), f(Sm/Nd) (-0.47) and Sm/Nd ratio (0.1) (Tab. 3). Despite that classification, the $\varepsilon Nd_{(0)}$ values are some random and vary from -21.43 to -11.07 in all samples (Tab.3).

The Nd isotopes also divided the Paleozoic sedimentary sequence of Alto Tapajós Group into two main set of rocks: i) the greywacke G5 and the quartz-sandstone Q4 with $\varepsilon Nd_{(0)}$ between -18 and -16, $f_{(Sm/Nd)}$ between -0.72 and -0.69 and Sm/Nd between 0.092-0.1 and the lowest TDM (1.25-1.28Ga); ii) G1, G2, G4 and G6 with the lowest $\varepsilon Nd_{(0)}$ values, highest TDM and $f_{(Sm/Nd)}$ (Tab. 3).

Among the lateritic profiles, the lateritic duricrusts of the profile P1, together with the ferruginous duricrusts (C2, C3 and C7) of the profiles P4 and P5 developed from Sumaúma Supergroup (Vila do Carmo and Beneficente groups) have the highest values of εNd(0). By the other hand the Mn-Al-Fe vermiform (VT, VB), Mn protopisolitic (Pp2, Pp1), Mn massive (M1) and Fe-massive (C7) duricrusts developed from Vila do Carmo display the highest ratios values of $^{147}Sm/^{144}Nd$, Sm/Nd (except in the sample VB) and f(Sm/Nd).

Table 3: Isotopic composition of sedimentary rocks, duricrusts and oxisols

Lithotype	Sample	Sm (ppm)	Nd (ppm)	$^{147}Sm/^{144}Nd$	$^{143}Nd/^{144}Nd$	$\varepsilon_{Nd\ (0)}$	TDM	$^{87}Sr/^{86}Sr$	Rb/Sr	Sm/Nd	f(Sm/Nd)
Profile 1 (P1)											
Oxisol	S7	15.683	71.234	0.1331	0.511852	-15.33	2.24	0.77931	0.034	0.220	-0.32
Pisolitic duricrust	Pi2	6.589	43.759	0.091	0.511753	-17.26	1.59	0.76443	0.162	0.151	-0.54
Pisolitic duricrust	Pi1	7.615	50.737	0.0907	0.511814	-16.07	1.51	0.73172	0.018	0.150	-0.54
Protopisolitic duricrust	Pp2	22.669	69.177	0.1981	0.511790	-16.54	-	0.73077	0.007	0.330	0.01
Protopisolitic duricrust	Pp1	10.118	22.659	0.2699	0.511873	-14.93	-	0.73013	0.009	0.447	0.37
Massive duricrust	M1	26.613	70.094	0.2295	0.511787	-16.61	-	0.73441	0.123	0.380	0.17
Mn-greywacke	A3	3.015	16.113	0.1131	0.511840	-15.56	1.81	-	0.031	0.187	-0.43
Pinkish siltstone	PS	6.253	29.193	0.1295	0.511677	-18.75	2.47	-	0.218	0.214	-0.34
Profile 2 (P2)											
Oxisol	S5	4.122	25.327	0.0984	0.511686	-18.56	1.78	0.72889	0.145	0.163	-0.50
V. duricrust	VT	2.704	7.774	0.2102	0.511404	-24.08	-	0.74137	0.147	0.348	0.07
V. duricrust	VB	1.859	24.526	0.4580	0.511523	-20.77	1.33	0.74060	0.323	0.076	1.33
Profile 3 (P3)											
Oxisol	S6	-	-	-	-	-	-	0.75151	0.004	-	-
Mn-duricrust	B2	2.868	14.544	0.119	0.511702	-18.25	2.15	-	0.031	0.197	-0.39
Mn-greywacke	A2	1.490	6.0070	0.150	0.511646	-19.35	3.40	0.74667	0.034	0.248	-0.24
Profile 4 (P4)											
Fragmental duricrust	C3	3.827	17.518	0.1320	0.511930	-13.81	2.06	1.00090	2.918	0.218	-0.33
Massive duricrust	C7	2.858	7.475	0.2311	0.511769	-16.94	2.12	-	8.962	0.382	0.18
Massive bauxite	Bx	9.088	64.469	0.0852	0.511426	-23.63	1.91	-	0.260	0.141	-0.57
Tuff	V	6.343	36.337	0.1055	0.511685	-18.58	1.90	0.85185	1.743	0.175	-0.46
Profile 5 (P5)											
Oxisol	S3	4.310	23.813	0.1094	0.511800	-16.36	1.80	0.72045	0.003	0.181	-0.44
Vermiform duricrust	C2	13.08	89.254	0.0886	0.511856	-15.25	1.44	0.72805	0.234	0.147	-0.55
Pisolitic bauxite	B1C	6.170	28.265	0.1320	0.511683	-18.63	2.53	0.71642	0.009	0.218	-0.33
Pisolitic bauxite	B1A	8.007	51.286	0.0944	0.511517	-21.87	1.94	0.71990	0.005	0.156	-0.52
Sandstone	Q2	2.740	10.018	0.1653	0.512071	-11.07	3.12	0.83148	0.080	0.274	-0.16
Profile 6 (P6)											
Fragmental duricrust	C1	3.747	22.441	0.1009	0.511690	-18.50	1.82	0.89175	1.526	0.167	-0.49
Fragmental duricrust	C6	5.055	21.629	0.1413	0.511740	-17.52	2.75	0.86870	2.438	0.234	-0.28
Laminated duricrust	C4	2.862	16.447	0.1052	0.511736	-17.60	1.82	0.90847	1.425	0.174	-0.47
Greywacke	G1	6.418	33.498	0.1158	0.511448	-23.21	2.48	0.88267	2.138	0.192	-0.41
Greywacke	G2	2.870	9.355	0.1855	0.511474	-22.70	-	0.89680	1.769	0.307	-0.06
Greywacke	G4	3.899	16.860	0.1398	0.511654	-19.19	2.88	0.86399	1.824	0.231	-0.29
Greywacke	G5	3.913	42.603	0.0555	0.511707	-18.17	1.28	0.92178	2.290	0.092	-0.72
Greywacke	G6	4.442	21.896	0.1226	0.511493	-22.33	2.59	0.80935	1.237	0.203	-0.38
Sandstone	Q4	0.969	9.650	0.0607	0.511780	-16.74	1.25	0.78401	0.779	0.100	-0.69
Mean rocks	ME	3.752	22.310	0.1133	0.511593	-20.39	2.10	0.85977	1.673	0.188	-0.43
Sandstone from Beneficente Group											
Sandstone	QA	3.966	22.829	0.105	0.511867	-15.03	1.64	0.74807	0.280	0.100	-0.47
Sandstones and Tuff of Vila do Carmo Group											
Sandstone	Q1	1.944	9.542	0.1232	0.511675	-18.78	2.29	0.72000	0.070	0.204	-0.37
Sandstone	Q3	1.389	7.646	0.1098	0.511539	-21.43	2.19	0.75292	0.083	0.182	-0.44
Tuff	R	9.652	50.082	0.1165	0.511728	-17.75	2.05	1.11019	10.528	0.193	-0.41

8. STRONTIUM ISOTOPES

The tuff (R) of the Vila do Carmo Group has the highest $^{87}Sr/^{86}Sr$ (1.11019) and Rb/Sr (10.528) ratios. However, among the sedimentary rocks, the greywackes and the quartz-sandstone from Alto Tapajós Group (samples Q4, G1, G2, G4, G5 and G6) together with the quartz-sandstone Q2 of the Beneficente Group display the highest $^{87}Sr/^{86}Sr$ (0.78401-0.92178) ratio (Tab. 3).

The ferruginous duricrusts from profile 4 (samples C7 and C3) developed from Vila do Carmo Group has the highest $^{87}Sr/^{86}Sr$ and Rb/Sr (1.0009 and 2.918-8.962) something correlated to the tuff (R). By the other hand, as well as the rocks, the lateritic duricrusts from Alto Tapajós Group also kept the high $^{87}Sr/^{86}Sr$ (0.8687-1.0009) and Rb/Sr ratios (1.425 to 2.438).

Among the oxisols, the one developed from the Mn-rocks of the Vila do Carmo Group (S7) have the highest $^{87}Sr/^{86}Sr$ ratios, while the one overlying Mn-greywackes of the Beneficente Group (S6) show the lowest Rb/Sr ratio (Tab. 3).

9. LEAD ISOTOPES

Lead isotopic analyzed only in the profiles over Mn-rocks of Vila do Carmo Group with coronadite and Pb-hollandite (Tab. 4), indicate that the vermiform duricrusts and the oxisol from profile 2 have the highest $^{206}Pb/^{204}Pb$, $^{207}Pb/^{204}Pb$, $^{208}Pb/^{204}Pb$ and $^{206}Pb/^{207}Pb$ ratios (Tab. 4). Overall, the $^{206}Pb/^{207}Pb$ ratio tends to increase from the Mn-rocks (samples PS and A3) to the oxisols (1.045-1.300) (Tab. 4), while $^{208}Pb/^{206}Pb$ ratios decrease (2.2 to 2.1). Pb/Th and Pb/U ratios are extremely higher in Mn-rocks (8600-43638 and 3440-21819, respectively) and it decreases up to the oxisol (Tab. 4).

Table 4: Pb isotopic compositions of Mn-rocks, lateritic duricrusts and oxisols from profiles from Vila do Carmo Group

Lithotype	Sample	$^{206}Pb/^{204}Pb$	$^{207}Pb/^{204}Pb$	$^{208}Pb/^{204}Pb$	$^{206}Pb/^{207}Pb$	$^{208}Pb/^{206}Pb$	Pb/Th	Pb/U
Mn-duricrusts and oxisol developed from Vila do Carmo Group (Profile 1-P1)								
Oxisol	S7	16.518	15.525	36.212	1.064	2.192	10	40.1
Duricrust	Pi2	17.073	15.663	37.001	1.090	2.167	9.7	99.0
Duricrust	Pi1	16.455	15.532	36.192	1.059	2.200	940	2820
Duricrust	Pp2	16.472	15.502	36.115	1.063	2.193	219	399
Duricrust	Pp1	16.612	15.535	36.287	1.069	2.184	58	29
Duricrust	M1	16.602	15.557	36.376	1.067	2.191	2500	1000
Mn-greywacke	A3	16.345	15.640	36.394	1.045	2.227	8600	3440
Pinkish siltstone	PS	16.248	15.516	36.000	1.047	2.216	43638	21819
Mn-duricrusts and oxisol developed from Vila do Carmo Group (Profile 2- P2)								
Oxisol	S5	20.708	15.926	40.740	1.300	1.967	0.3	2.5
Duricrust	VT	19.599	15.852	39.840	1.236	2.033	99	363
Duricrust	VB	18.463	15.759	38.480	1.172	2.084	88	228
Mn-greywacke	A3	16.345	15.640	36.394	1.045	2.227	8600	3440

10. GEOPHYSICAL FEATURES

Gamaspectrometry airborne was used for complement the geological map and to aid identify the correlation between protolith and lateritic duricrusts. Five domains were individualized in the eastern portion according to K, Th and U on the RGB channels (Fig. 8 A and B): Domain 1 (D1)- high K, reddish to pinkish color, correlated to the acid volcanic rocks of Colíder Group; Domain 2 (D2)- high Th, mainly greenish color, pinkish when in contrast with proximal domains, sometimes black widespread subdomains rich in Th gather the sandstones Q1 and Q3, Mn duricrusts (VT and VB)

and bauxites (Bx) derived from tuffs are related to Vila do Carmo Group and lateritic cover developed from them; Domain 3 (D3)- extremely high Th, black color and some reddish tones are associated to the Mata-Matá diabase or gabbroic rocks; Domain 4 (D4) with high Th, black with purplish color, where outcrop the sandstone Q2 and the pisolitic bauxites, framed into Beneficente Group; Domain 5 (D5) with intermediate Th and U identified by bluish green color related to the sandstones and greywackes (Q4, G5, G1 and G2) with lateritic cover of Alto Tapajós Group. In Domain 5 was individualized a lateritic cover.

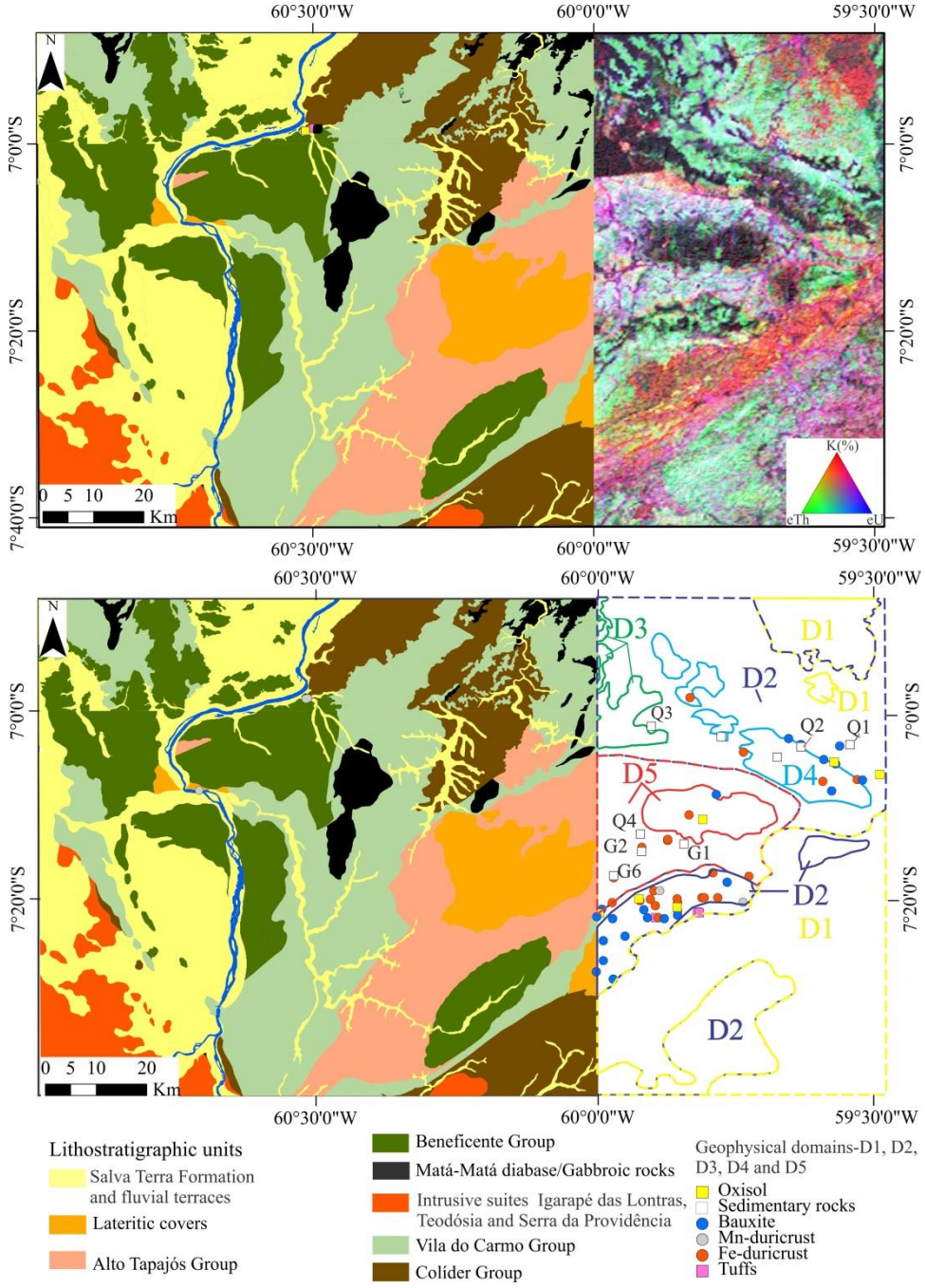

Figure 8: A- Geological map carried out by CPRM (2013, 2014 and 2015) together with a ternary map of K, Th and U on the RGB channels. B- Five geophysical domains extract from ternary map of K, Th and U on the RGB together with samples analyzed and collected in fieldwork.

11. DISCUSSION

11.1 Provenance and geochemical features of sedimentary rocks

The Sumaúma (Vila do Carmo and Beneficente groups) and Alto Tapajós basins received sedimentary supply of several sources that provided the mineral, chemical and physical features. The higher MnO contents in the Sumaúma basin and the higher P_2O_5 content in the Alto Tapajós basin, highlight different sources for both basins. Moreover, the grains of Sumaúma quartz-sandstones more rounded indicate intense transport, while those of the Alto Tapajós sandstones and greywackes mostly sub-rounded allied to the high contents of K_2O related to microcline and illite, suggest proximal source.

The chemical composition and the CIA index indicate change from strong to moderate weathering environment in the source areas related to felsic rocks with some contribution of mafic rocks, especially to the Mn-greywackes and sandstones of Beneficente Group (Fig. 9A). These type of rocks and reworking of old sediments for the Vila do Carmo and Alto Tapajós groups are also indicate by La/Th vs Hf relationship. For the Beneficente Group and the quartz-sandstone Q3 the La/Th vs Hf ratios assigned to intermediary rocks or a mixed of acid and basic rocks (Figure 9B). The $\varepsilon Nd_{(0)}$ and Th/Sc ratios, Eu/Eu* and Gd_N/Yb_N (< 0.85 and 2, respectively) (Fig. 9C and D), as well as Zr/Sc vs Th/Sc, Zr/Y vs Nb/Hf, HREE vs Y and Hf vs Y (Supplementary material- Annex I, Figure A1), also mirror recycling of felsic source from Archean to post-Archean upper continental crust (Taylor and McLennan, 1985; Slack and Stevens, 1994; Mishra and Sen, 2012).

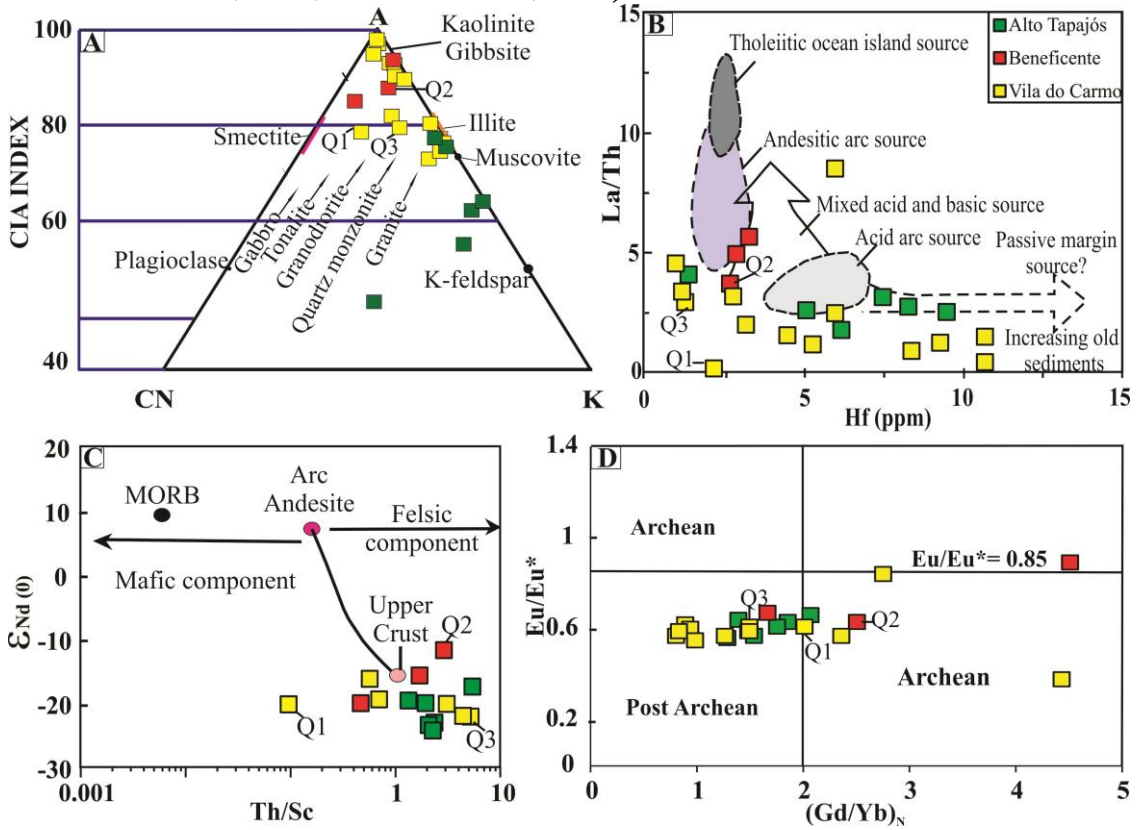

Figure 9: Provenance of sedimentary rocks based on chemical features. A- Chemical composition of sedimentary rocks of southwestern Amazonia in the A-CN-K diagram (Nesbitt and Young, 1982); besides trends plotted according to Nesbitt and Young (1989). B- Characteristics of source area based on Hf vs La/Th ratio (Floyd and Leveridge, 1987). C- Characteristics of source area based in Th/Sc ratio versus $\varepsilon Nd_{(0)}$ (McLennan et al., 1990). *Th values <0.1 ppm was plotted using 0.05 ppm (quartz-sandstone A1). D- Sedimentary rocks plotted in $(Gd/Yb)_N$ versus Eu/Eu* diagram (McLennan et al., 1990) whose provenance

appointed to Post Archean rocks with slight contribution of Archean rocks * Some Chemical and isotopic features of sedimentary rocks of Vila do Carmo Group were reported by Brito et al. (2010).

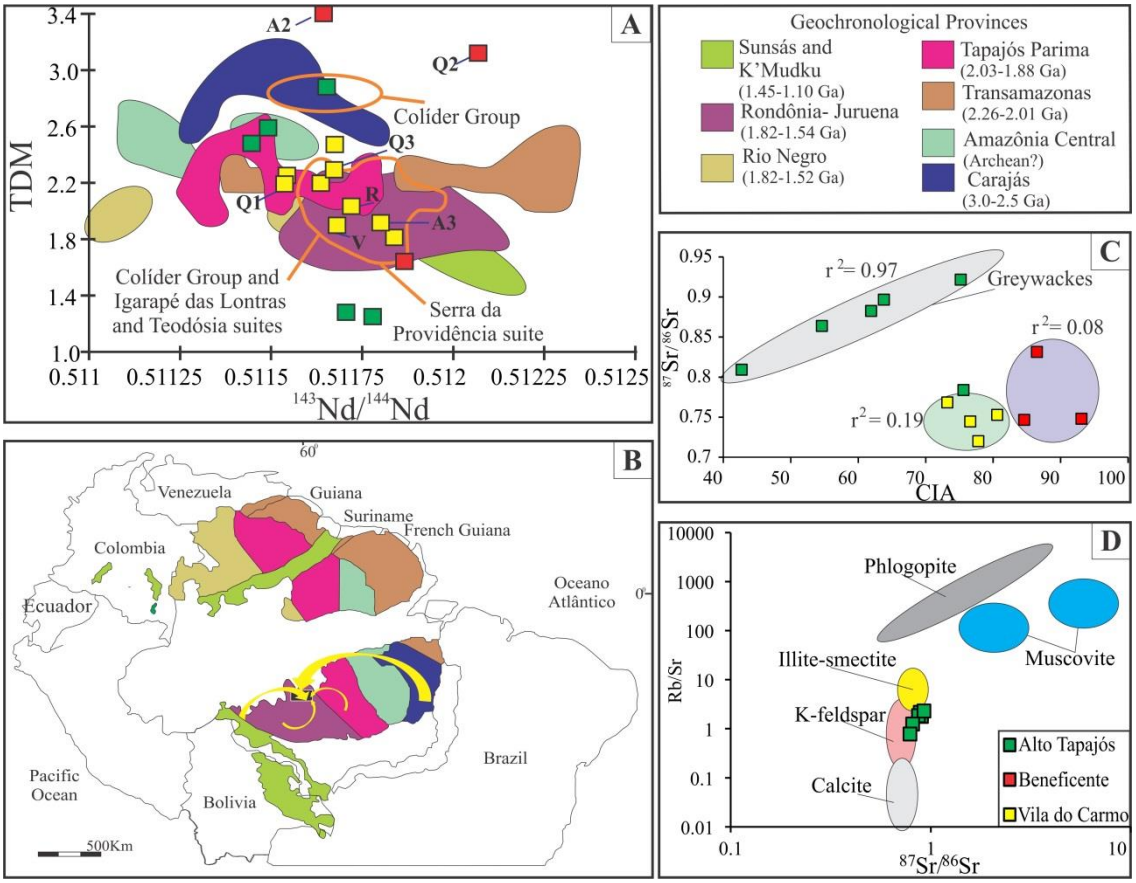

Figure 10: Provenance and relationship with proximity of source area according CIA, trace elements and Nd and Sr isotopes. A and B- Provenance of Vila do Carmo, Beneficente and Alto Tapajós groups plotted in $^{143}Nd/^{144}Nd$ versus TDM and their localization of Geochronological Provinces (Santos et al. 2006) legend in A. Carajás Province- Olszewski et al. (1989) and Sato and Tassinari (1997). Amazônia Central Province- Gaudette et al. (1996) Sato and Tassinari (1997); Norcross et al. (1998) and Santos et al. (2000). Tansamazonas Province- Gruau et al. (1985); McReath and Faraco (1997); Sato and Tassinari (1997) and Voicu et al. (2000). Tapajós Parima Province- Sato and Tassinari (1997); Santos et al. (2000), Barreto et al. (2014) and Marques et al. (2014). Rio Negro Province- Sato and Tassinari (1997). Rondônia Juruena including Colíder Group and Igarapé das Lontras and Teodósia suites- Vignol (1987); Sato and Tassinari (1997); Payolla et al. (2002) and CPRM (2014). Sunsás and K'Mudku- Sato and Tassinari (1997) and Rizzoto (1999). C- Proximal source of the Alto Tapajós Group greywackes in function of the relation $^{87}Sr/^{86}Sr$ versus CIA. D- High values of $^{87}Sr/^{86}Sr$ in greywackes of the Alto Tapajós Group related to K-feldspar and illite. Concentration of Rb/Sr and $^{87}Sr/^{86}Sr$ found at Clow et al. (1997), Kirsimae and Jorgensen (2000), Jenkin et al. (2001), Siebel et al. (2005) and Eberlei et al. (2015).

The TDM and the $^{143}Nd/^{144}Nd$ ratios pointed as main sediment source for the Sumaúma basin (Vila do Carmo and Beneficente groups) rocks with 1.82-1.55 Ga (Rondônia-Juruena Geochronological Province), especially the surrounding rocks (Colíder Group, Teodósia, Igarapé das Lontras and Serra da Providência suites) near Apuí City, (Fig. 10A and B). Older rocks (Tapajós-Parima Province and the Amazonia Central Province) as well as the narrow affinity among Mn-greywacke (A3) of Vila do

Carmo Group with the felsic rocks of Colíder Group, Teodósia and Igarapé das Lontras suites (Fig. 10A) corroborate by Albuquerque et al. (2017), also supplied the Vila do Carmo Group. On the other hand, distal sources of Carajás and Sunsás provinces that are in line with the detrital zircon ages of Brito et al. (2010) and Reis et al. (2013) (Tab. 5), also supplied the Beneficente Group (Fig. 11A and B).

It is worth noting that the Vila do Carmo Group is a potential source of the Beneficente Group, since there is an angular discordance between the units and the sandstone of the Beneficent Group (QA) showed lithic fragments (sandstones), high contents of Fe_2O_3, TiO_2, rutile, Ti-magnetite (as well the tufts of Vila do Carmo- 1.5% of sphene and Ti-magnetite) and zircon population between 1.76 and 1.74 Ga (age inferred from Vila do Carmo) (Reis et al., 2013).

Table 5: U-Pb ages of the main zircon populations of Vila do Carmo and Beneficente groups

Lihostratigraphic Unit	Zircon populations (Ga)	Provenance (Geochronological Province)	Authors
Vila do Carmo Group	1) 2.83-2.65 2) 2.15-1.98	1)Amazônia Central 2)Tapajós Parima- Iriri Xingu Domain	Brito et al. (2010)
Vila do Carmo Group	1.98 to 1.74	Tapajós Parima and Rondônia Juruena (dominant)	Reis et al. (2013)
Beneficente Group	1) 2.98-1.98 2) 1.76-1.74 3) 1.57- 1.54 4) 1.43-1.08	1) Carajás and Tapajós Parima 2 and 3) Rondônia Juruena (Vila do Carmo and Serra da Providência suite) 4) Sunsás	Reis et al. (2013)

The younger sedimentary rocks of Alto Tapajós basin with two main TDM ages (1.28-1.25 Ga and 2.88-2.59 Ga) mirror a wide source contribution of Amazonian Craton (Carajás, Amazonia Central, Tapajós Parima, and Sunsás? provinces due to lower TDM) (Fig. 10 A and B). However, the good correlation between $^{87}Sr/^{86}Sr$ versus CIA (r^2=0.97) and $^{87}Sr/^{86}Sr$ versus Rb/Sr (Fig. 10 C and D) linked to the high amounts of illite and feldspar, implies autochthony or intraformational character conditioned by the Cachimbo graben, which allowed the exposition and erosion of the volcanic basement (Colíder Group) and Sumaúma basin (Reis, 2006; CPRM, 2015). This also explains the fragments of volcanic rocks, siltstones and sandstones in the sandstones.

11.2 Correlation between protolith, lateritic duricrusts and oxisols

The Rb/Sr versus εNd signatures of the Samaúma (Vila do Carmo and Beneficente groups) and Alto Tapajós basin were kept in the respective bauxites, lateritic duricrusts and oxisol (Fig.11A), except the tuff (sample V) with similar Rb/Sr ratio of the sedimentary rocks and the lateritic duricrusts of Alto Tapajós basin. Thus, the mineralogical, chemical and isotopical features allowed distinguish the bauxites from Vila do Carmo and Beneficente Groups. The bauxite from Vila do Carmo Group with well-preserved Ti-magnetites and slight variation in size (Fig. 11B and C) suggest reworking, while the Beneficente sandstones coming from reworking of tuffs of Vila do Carmo Group, have Ti-magnetites with smaller sizes (Fig. 3D). In this context, reworking also explain the anatase in the pisolitic bauxites (B1A and B1C) most probably derived from the weathering of the less preserve Ti-magnetite of Beneficente sandstones.

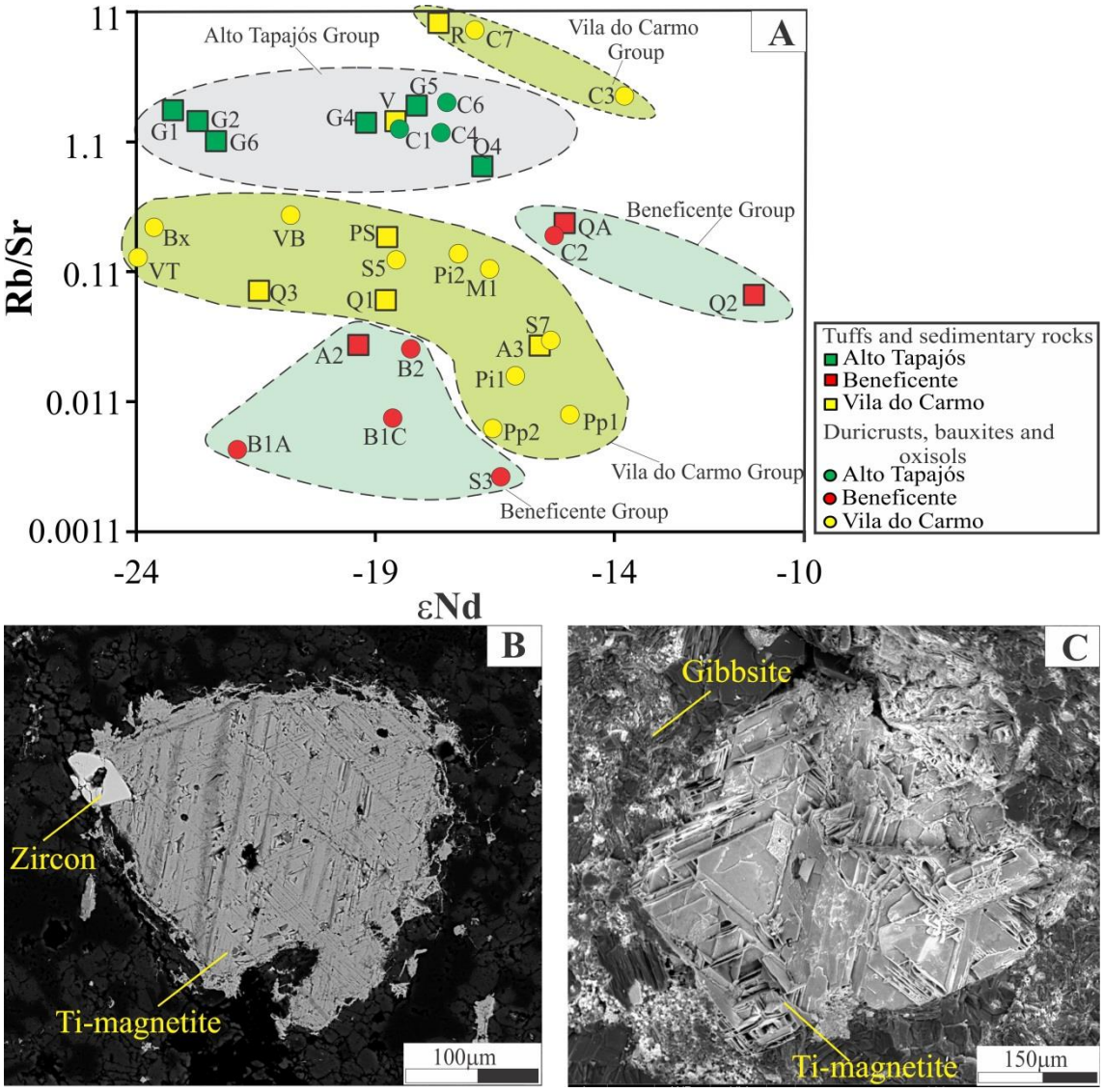

Figure 11: A- εNd(0) vs Rb/Sr gahters sedimentary rocks of each lithostratigraphic unit with lateritic duricrusts and oxisols. B- Detail of Ti-magnetite well preserved in tuffs. C- Ti-magnetite well preserved in bauxites from Vila do Carmo Group.

11.3 Behavior of Nd isotopes under extreme weathering condition

Several authors consider Nd isotopes variations along the lateritic profile result of in situ weathering of minerals from the protolith (e.g. Ohlander et al. 2000, Ma et al. 2010). On the other hand, some of them believe in input of extraneous Nd, generally assigned to current or old aeolic sources (Viers and Wasserburg, 2004; Liu et al., 2013, Babechuk et al., 2015). Besides that, the Pb, Sr and Nd isotopes deconstructed the idea of Sahara dust in Amazonian soils (Belterra Clay) as reported by Abouchami et al. (2013).

In most of the studied samples there is no correlation between Nd isotopes along the profiles. The generally lower $^{147}Sm/^{144}Nd$ and $^{143}Nd/^{144}Nd$ ratios in the bauxites and duricrusts compared to the protoliths, indicate some leach effect (Fig. 12). Also is worthy to be highlighted that there is no relationship between Nd concentrations and $^{143}Nd/^{144}Nd$ isotopic ratios in the mass balance (Tab. 6). This statement indicates no dependence between REE concentration and $^{143}Nd/^{144}Nd$, unlike reported by Viers and Wasserburg (2004). Phosphatic minerals which could be adsorbed by REE in solution

(Aubert et al. 2001); also displayed no relationship with Nd isotopes, except in the massive Fe-duricrust (C7) of the profile P4.

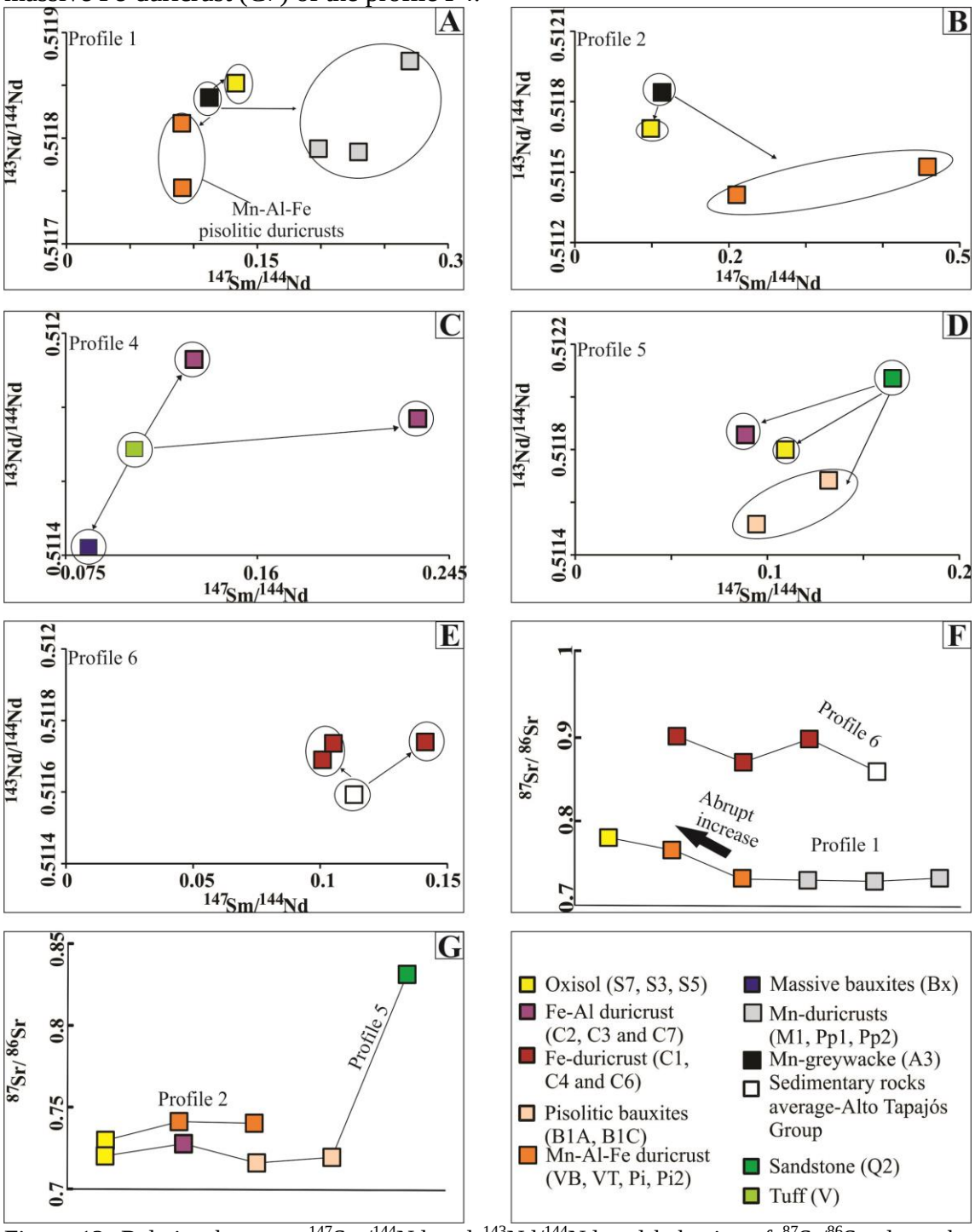

Figure 12: Relation between $^{147}Sm/^{144}Nd$ and $^{143}Nd/^{144}Nd$ and behavior of $^{87}Sr/^{86}Sr$ along the profiles studied

Table 6: Enrichment factor of each sample. Red values: immobile elements or enriched.

	P_2O_5	La	Ce	Pr	Nd	Sm	Eu	Gd	Tb	Dy	Ho	Er	Tm	Yb	Lu	$^{143}Nd/^{144}Nd$	$^{206}Pb/^{207}Pb$	$^{208}Pb/^{206}Pb$
Profile 1																		
S7	0.03	0.39	0.44	0.42	0.37	0.37	0.1	0.06	0.08	0.1	0.11	0.13	0.14	0.15	0.2	0.03	0.03	0.03
Pi2	0.02	0.61	0.62	0.62	0.47	0.32	0.08	0.04	0.05	0.06	0.06	0.07	0.07	0.08	0.12	0.06	0.06	0.06
Pi1	0.09	0.56	0.61	0.75	0.65	0.41	0.13	0.06	0.05	0.05	0.06	0.06	0.07	0.07	0.09	0.07	0.07	0.07
Pp2	0.35	0.7	1.25	2.27	3.05	5.25	1.76	0.85	0.9	0.95	0.81	0.8	0.74	0.77	0.9	0.27	0.27	0.26
Pp1	0.9	0.74	0.85	1.63	2.21	4.73	1.91	1.31	1.49	1.69	1.72	1.48	1.54	1.54	1.64	0.62	0.63	0.60
M1	0.37	1.84	6.88	6.61	7.79	13.98	4.16	1.69	1.87	1.73	1.5	1.31	1.36	1.42	1.59	0.68	0.70	0.67
Profile 2																		
S5	0.01	0.4	0.33	0.32	0.18	0.17	0.05	0.03	0.05	0.07	0.08	0.09	0.1	0.11	0.13	0.05	0.07	0.05
VT	0.09	0.4	4.62	0.44	0.39	0.32	0.1	0.08	0.06	0.07	0.09	0.09	0.11	0.11	0.14	0.14	0.17	0.13
VB	0.17	0.86	24.28	0.99	0.81	0.71	0.23	0.21	0.15	0.21	0.26	0.27	0.32	0.32	0.43	0.26	0.29	0.24
Profile 4																		
C3	<0.1	0.4	0.44	0.7	0.91	1.29	2.02	1.64	1.53	1.63	1.33	1.29	1.26	1.11	0.97	1.87	-	-
C7	1.32	1.37	1.71	1.43	1.34	1.86	1.96	1.97	2.25	2	2.91	2.55	2.67	2.73	2.51	0.96	-	-
Bx	0.95	2.08	1.57	2.13	2.02	2.58	3.1	2.82	3.18	3.19	3.71	3.54	3.33	3.72	2.69	1.88	-	-
Profile 5																		
S3	<1	0.24	0.16	0.19	0.16	0.09	0.09	0.09	0.15	0.18	0.25	0.27	0.36	0.45	0.51	0.06	-	-
C2	0.64	6.74	4.89	5.82	4.76	2.46	2.26	1.38	1.21	0.9	0.65	0.53	0.52	0.56	0.63	0.49	-	-
B1A	0.07	0.58	0.41	0.48	0.4	0.24	0.2	0.17	0.26	0.3	0.35	0.39	0.52	0.58	0.67	0.08	-	-
B1C	0.32	1.12	0.94	1.24	1.06	1	0.95	0.82	0.96	1.24	1.19	1.15	1.38	1.48	1.52	0.42	-	-
Profile 6																		
C1	0.04	1.04	0.9	0.78	0.68	0.62	0.57	0.49	0.57	0.59	0.59	0.66	0.78	0.69	0.79	0.61	-	-
C6	<1	0.56	0.91	0.59	0.61	0.84	0.84	0.73	0.85	0.86	0.92	0.94	1.12	0.97	1.15	0.52	-	-
C4	3.53	0.47	0.61	0.48	0.53	0.52	0.5	0.43	0.44	0.5	0.37	0.43	0.49	0.41	0.53	0.62	-	-

The REE/(Zr+Hf) ratios ≥1 indicates the REE also may be trapped in cerianite and/or in the manganese minerals (Braun et al. 1990 and Ohta and Kawabe 2001), as it happen in the Mn-lateritic profiles developed from the Vila do Carmo Group (P1 and P2) (Fig. 13 A and B). By the other hand, ratio ≤ 1 suggest that the heavy minerals control the REE concentration along the lateritic profile (Horbe and Costa, 1997) and it happen in most of the samples of the studied profiles (Fig. 13 C, D and E). To recognize the real influence of heavy minerals and manganese minerals+cerianite on REE and Nd isotopes of the profiles P1 and P2, was developed a calculation following two equations (Supplementary material-Annex II, Figure A2, A3 and A4):

1. $REE_r/REE_c = \sigma\{[(Ho+C+Co)+Ce_{(ppm)}]_r/[(Ho+C+Co)+Ce_{(ppm)}]_c\} + \beta[(Zr+Hf)r/(Zr+Hf)c]$

2. $(^{147}Sm/^{143}Nd)_{r-c} = (Sm/Nd)_{r-c}.\{[(Ho+C+Co)+Ce_{(ppm)}]_r/[(Ho+C+Co)+Ce_{(ppm)}]_c.\delta + [(Zr+Hf)_r/(Zr+Hf)_c].\omega\}$

The results show that the Mn-minerals and cerianite hold 62.2% and 36.5% of REE, respectively and heavy minerals gather 37.8% and 63.5% of REE in the profiles P1 and P2, respectively (Supplementary material, Annex II, Figure A2, A3 and A4). By the other hand, the ^{143}Nd resulting from ^{147}Sm decay is mainly assigned to heavy minerals (86.34% and 94.76% of $^{147}Sm/^{143}Nd$ in profiles P1 and P2, respectively) (Supplementary material). Thus, the influence of Mn-minerals and cerianite is lesser than the zircon; they hold 5.24% to 13.66% of Nd isotopes (Supplementary material, Annex II, Figure A2, A3 and A4). These results as well the mass balance, ratifies that there is no relationship between the behavior of REE and Nd isotopes under extremeweathering. Also, it appointed that minerals redistribution throughout the lateritic profile with residual concentration of zircon or leaching of Mn minerals (coronadite, hollandite and cryptomelane) and fixation in the new formed cerianite once REE are immobile during weathering (Laveuf and Cornu, 2009; McQueen and Scott, 2008), control the Nd isotopic signature.

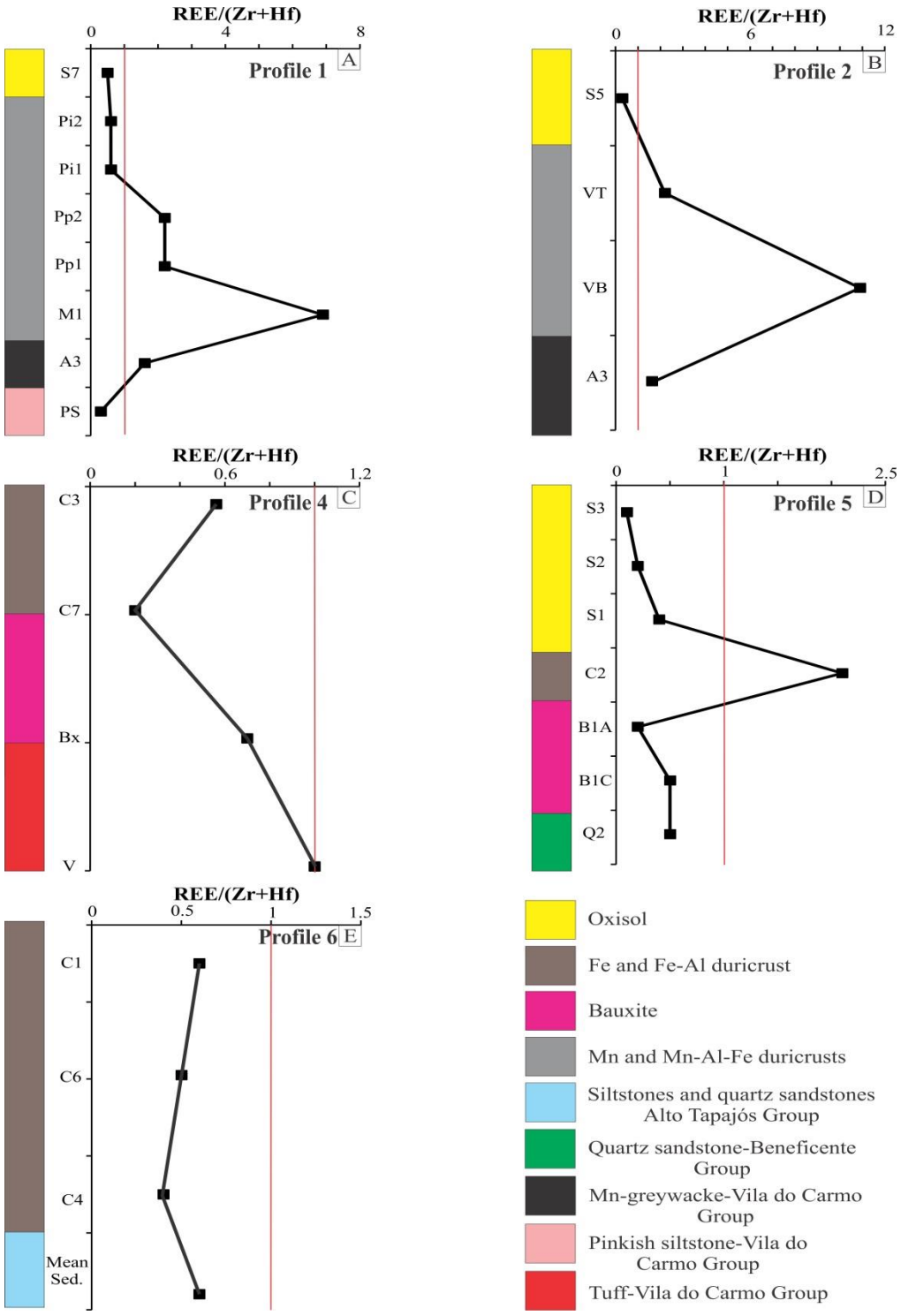

Figure 13: REE/(Zr+Hf) ratios along the profiles studied

11.4 Behavior of Sr isotopes on extreme weathering condition

The Sr isotopic ratios show two contradictory behaviors in the studied profiles. The relatively uniform $^{87}Sr/^{86}Sr$ ratios (0.73013-0.73173) between the massive and protopisolitics duricrusts (M1, Pp1 and Pp2) of profile P1 indicate no weathering effect (Fig. 12F). However, the abrupt increase of Sr isotopes ratios from the pisolitic duricrust (Pi1) to the oxisol (S7) in profile P1 (0.76443-0.77931), and the variability in the duricrusts (C1, C4 and C6) of profile P6 (Fig. 12F), suggests some extraneous Sr

input, most probably related to interaction with rainwater, groundwater, as well as reported by Innocent et al. (1996) and Ma et al. (2010) or some vegetation redistribution. Moreover, the high mobility of Sr and the weatherability of illite and microcline (with high $^{87}Sr/^{86}Sr$ ratios, Fig. 11D) of the siltstones from Alto Tapajós basin could be inhered by ferruginous duricrusts (C1, C4 and C6- profile 6) or adsorbed by hematite, goethite and kaolinite as reported by Cornell and Schwertmann (2006) in soils. By other hand, the extreme leaching, resulting in kaolinite and gibbsite formation (profiles P2 and P5) released Sr from protoliths to solution decreasing the $^{87}Sr/^{86}Sr$ ratios in the oxisols (Fig.12G).

11.5 Insights of Pb isotopes behavior on extreme weathering condition and the nature of Mn-mineralizations

Radiogenic Pb (^{206}Pb, ^{207}Pb and ^{208}Pb) are concentrated into heavy minerals as zircon, xenotime and rutile, whereas the ^{204}Pb (non radiongenic) is related to Pb minerals, such as galena, coronadite, among others. The Pb behavior, as well of Nd isotopes during extreme weathering conditions is lack known, the studies are concerning to gossans (Doe and Stacey, 1974; Gulson and Mizon, 1979; Kribek et al., 2016). These authors identified three main Pb isotopes behaviors in gossans: 1- identical to the primary sulphide; 2- increase of Pb isotopic ratios up profiles; 3- plot on or near the growth curve of Pb along the geological time. Despite that, they concluded that Pb isotopic ratios variations have no relationship with weathering but with decay of U and Th and mixing of Pb sources (Doe and Stacey, 1974; Gulson and Mizon, 1979, Kribek et al., 2016).

Just like in the gossans, the profiles studied displayed variations in $^{206}Pb/^{207}Pb$. The duricrusts and oxisols have higher values than the Mn-rocks, especially in profile P2 ($^{206}Pb/^{207}Pb$ = 1.17-1.3) that may be related to decay of ^{238}U to ^{206}Pb or mixing of sources. This hypothesis is ratified by growth curve of Pb isotopes throughout the geological time ($^{206}Pb/^{204}Pb$ versus $^{207}Pb/^{204}Pb$), where lateritic duricrusts and oxisol from profile P1 are similar of the Mn-rocks and plot near of growth curve, whereas the profile P2 more enriched in $^{206}Pb/^{204}Pb$ (Fig. 14A) is totally different from the protoliths. Other hypothesis is that the Mn-greywacke (A3) could not be the protolith to the profile P2 due to the large differeces of Pb isotopic ratios compared to the lateritic duricrusts and oxisol, unlike occurs in profile P1, where the Pb isotopic ratios are similar.

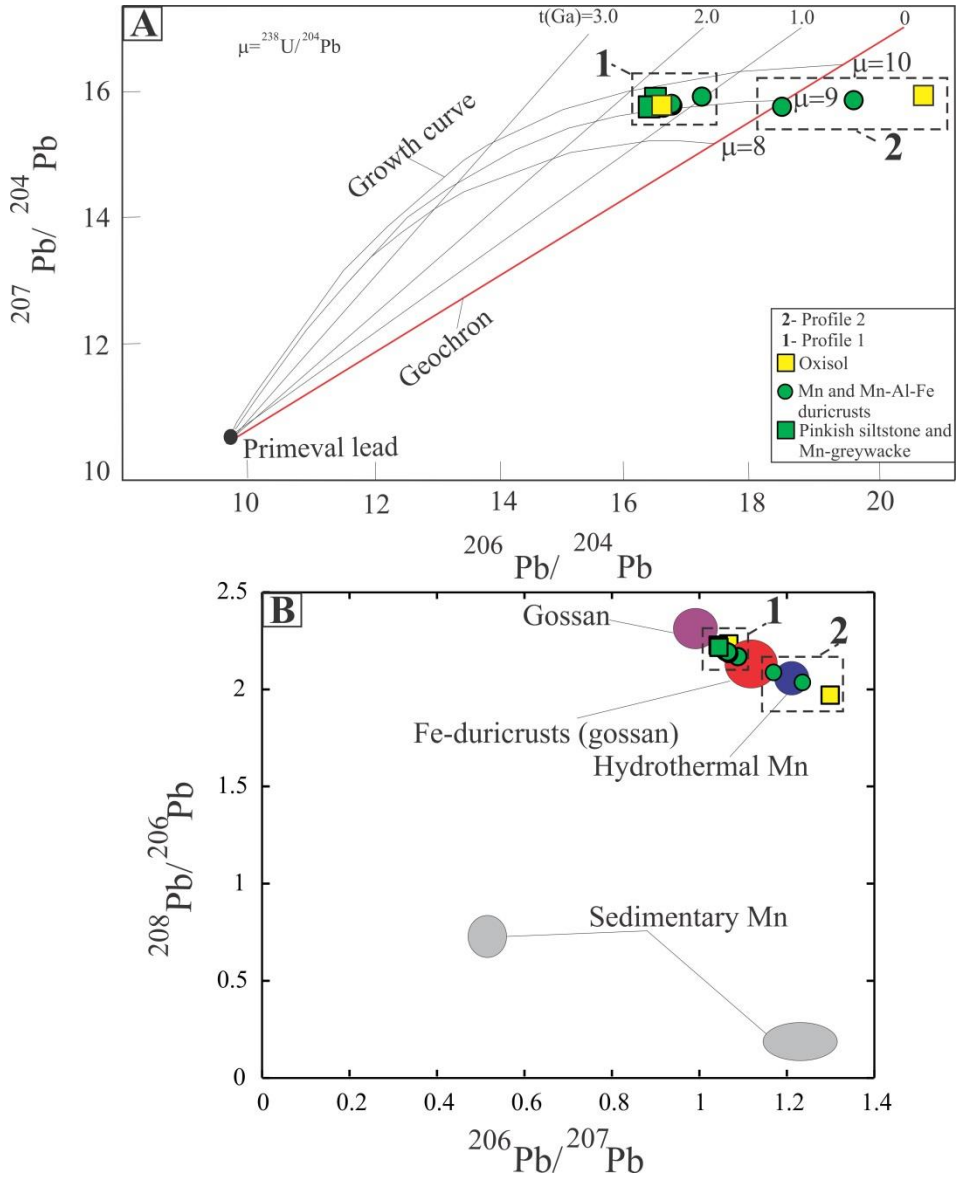

Figure 14: A- Pb growth curve along the geological time (Rollinson, 1993) and correlation with profiles 1 and 2. B- Isotopic signature of profiles 1 and 2. Sedimentary Mn- Doe et al. (1996), Romer et al. (2011), Hydrothermal Mn- Conly et al. (2011) and Yang et al. (2015), Gossan and Fe-duricrusts (gossan)- Kribek et al. (2016)

On the other hand, high Pb/U (3440-21819) and Pb/Th (8600-43638) and low $^{206}Pb/^{207}Pb$ ratios (1.047-1.045) in the Mn-rocks are correlated to those values of primary sulfide in Brooken Hill deposit, Australia (1.03-1.10 of $^{206}Pb/^{207}Pb$), whose Kribek et al. (2016) assigned to Proterozoic age. The Proterozoic age for the Mn-rocks of profiles P1 and P2 is ratified by the Mata-Matá diabase (1.57 Ga- Calymmian). This intrusion heated the marine water and precipitated Mn in the fractures of sedimentary rocks of Vila do Carmo Group (Albuquerque et al., 2017). The hydrothermal origin followed by weathering of the Pb and Cu mineralized sequences (dubhites) is showed by $^{206}Pb/^{207}Pb$ versus $^{208}Pb/^{206}Pb$ diagram (Fig. 14B).

Therefore, the extreme weathering conditions of southwestern Amazonia, Brazil since the ending of Cretaceous/early Cenozoic, probable ages of the lateritic duricrusts in Amazonia (Vasconcelos et al. 1994; Ruffet et al. 1996; Costa et al. 2005; Horbe, 2014) do not affect the Pb and Nd isotopes of the parent rocks. The very good correlation of the $^{143}Nd/^{144}Nd$, $^{206}Pb/^{207}Pb$ and $^{208}Pb/^{206}Pb$ (r^2=+0.99; Tab. 6) in mass

balance results of profiles P1 and P2 ratifies the immobility of Pb during extreme weathering and that heavy minerals control the Nd isotopes.

Finally, the mineralogical, geochemical and isotopic features of the tuffs, sedimentary rocks, lateritic duricrusts and oxisols together with gamma spectometry domains identified allowed improve the geological knowledge of southwestern Amazonia (Fig.15).

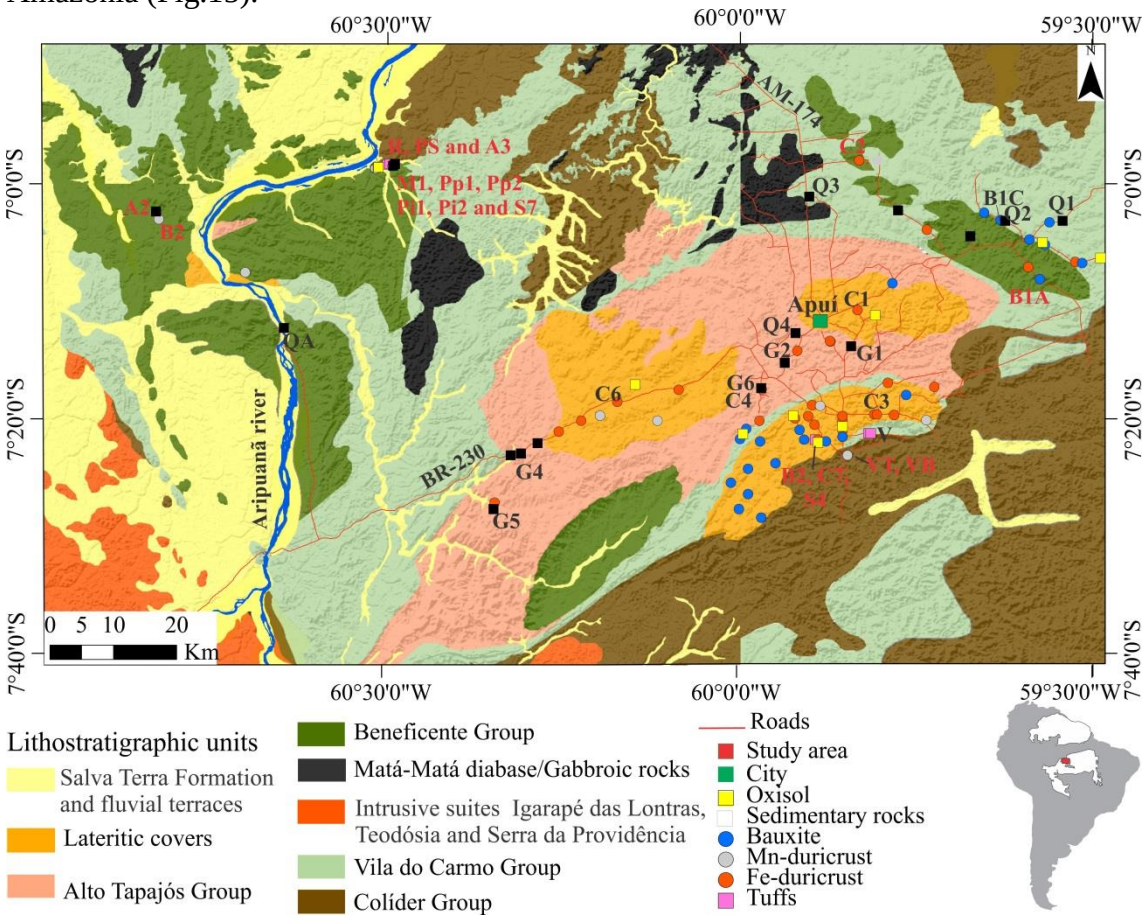

Figure 15: Geological map of study area proposed in this work (Modified from CPRM, 2006).

12. CONCLUSIONS

The geochemistry and Nd and Sr isotopes indicate the Sumaúma basin filled by erosional sediments (Vila do Carmo and Beneficente groups), has complexes sources related to volcanic and granitic rocks (Colíder Group, Igarapé das Lontras, Teodósia and Serra da Providência) associated to Archean to Mesoproterozoic terrains (Tapajós-Parima, Sunsás and Carajás Provinces). The reworking of the older Sumúma basin and Colíder Group was the main sediment supply for the younger Alto Tapajós Basin.

The Nd, Sr and Pb isotopes have different behavior under extreme weathering. The Nd isotopes are mainly related to redistribution throughout the lateritic profile of the minerals with variable radiogenic ratios, while the Sr isotopic variations suggests extraneous Sr input, most probably related to interaction with rainwater and groundwater and longtime of exposure. The Pb isotopes are related to U and Th decay along the geological time and allow recognized the environmental formation of Mn-deposits. The very good correlation of Nd and Pb isotopes ratifies the redistribution of heavy minerals along the profiles is the main reason of the isotopic changes. Finally, the Nd isotopes together with mineral and chemical parameters and gammaspectometry allowed recognized the protoliths of the duricrusts and bauxites.

13. ACKNOWLEDGMENTS

The authors thank to the Postgraduate Program in Geology from the University of Brasilia, to CAPES for granting a PhD scholarship to the first author and CNPq for financial support (process n ° 471971/2010-3 and 473359/2012) and research grants of the second and third authors.

14. REFERENCES

Abouchami, W. .,Näthe, K., Kumar, A., Galer, S.J.G., Jochum, K.P., William, E., Horbe, A.M.C., Rosa, J.C., Balsam,W., Adams, D., Mezger, K., Andreae, M.O., 2013. Geochemical and isotopic characterization of the Bodélé Depression dust source and implications for transatlantic dust transport to the Amazon Basin. Earth and Planetary Science Letters. 380, 112–123

Albuquerque, M.F.S., and Horbe, A.M.C., 2015. Mineralogia, geoquímica e evolução da lateritização em Apuí, sudeste do Amazonas. Braz. J. Geol. 45, 569-590.

Albuquerque, M.F.S., Horbe, A.M.C., Botelho, N.F., 2017. Genesis of manganese deposits in southwestern Amazonia: Mineralogy, geochemistry and paleoenvironment. Ore Geol. Rev. 89, 270-289.

Aubert, D., Stille, P., Probst, A., 2001. REE fractionation during granite weathering and removal by waters and suspended loads: Sr and Nd isotopic evidence. Geochim. Cosmochim. Acta. 65, 387-406.

Babechuk, M.G., Widdowson, M., Murphy, M., Kamber, B.S., 2015. A combined Y/Ho, high field strength element (HFSE) and Nd isotope perspective on basalt weathering, Deccan Traps, India. Chem. Geol. 396, 25-41l

Barreto, C.J.S., Lafon, J.M., Costa, L.T.R., Lima, E.F., 2014. Paleoproterozoic (~1.89 Ga) felsic volcanism of the Iricoumé Group, Guyana Shield, South America: geochemical and Sm-Nd isotopic constraints on sources and tectonic environment. Int. Geol. Rev. 56, 1332-1356

Betiollo, L.M., Reis, N.J., Almeida, M.E., Bahia, R.C., Splendor, F., Costa, U.P., Luzardo, R., 2009. Magmatismo Máfico Calimiano (Sill Mata-Matá), rio Aripuanã, Amazonas- Implicações Geológicos. In: SBG, Núcleo Norte, Simpósio de Geologia da Amazônia, XI, Resumos Expandidos.

Bhatia, M. R., Crook, K. A. W., 1986. Trace element characteristics of graywackes and tectonic setting of sedimentary basins. Contrib. Mineral. Petrol. 92, 181-193.

Braun, J., Pagel, M., Muller, J., Bilong, P., Michard, A., Guillet, B., 1990. Cerium anomalies in lateric profiles. Geochim. Cosmochim. Acta. 54, 781-795.

Brito, R.S., Silveira, F.V., Larizzati, J.H., 2010. Metalogenia do distrito aurífero do rio Juma- Nova Aripuanã-AM. Informe recursos minerais, CPRM, Brasília.

Clauer, N., Stille, P., Bannot-Courtois, C., Moore, W.S., 1984. Nd-Sr isotopic and REE constrainsts on the genesis of hydrothermal manganese crusts in the Galapagos. Nat. 311, 743-745.

Clow, D.W., Mast, M.A., Bullen, T.D., Turk, J.T., 1997. Strontium 87/strontium 86 as a tracer of mineral weathering reactions and calcium sources in an alpine/subalpine watershed, Loch Vale, Colorado. Water. Resour. Res. 33, 1335-1351.

Conly, A.G., Scott, S.D., Bellon, H., 2011. Metalliferous manganese oxide mineralization associated with the Boleo Cu-Co-Zn district, Mexico. Econ. Geol. 106, 1173-1196

Cornell, R.M., Schwertmann, U., 2006. The Iron Oxides: Structure, Properties, Reactions, Occurrences and Uses, 2nd, Wiley-VCH, Weinheim.

Costa, M.L., Choque Fernandez, O.J., Requelm, M.E.R., 2005. Depósito de manganês do Azul, Carajás: estratigrafia, mineralogia, geoquímica e evolução geológica. In: Marini J., Queiroz E.T., Ramos B.W. (eds.). Caracterização de depósitos minerais em distritos mineiros da Amazônia. Brasília, DNPM, FINEP, ADIMB, p. 227-333.

CPRM, 2006. Mapa Geológico do Estado do Amazonas. Geologia e recursos minerais do Estado do Amazonas. Sistemas de Informações Geográficas – SIG, Programa Geologia do Brasil. Escala 1: 1.000.000, Ministério de Minas e Energia. Rio de Janeiro. 1 CD-ROM. Programa Geologia do Brasil.

CPRM, 2013. Folha Sumaúma (SB.20-Z-D). Programa Geologia do Brasil. Carta geológica ao milionésimo-Escala 1:250.000. CPRM, Serviço Geológico do Brasil, Manaus.

CPRM, 2014. Programa de Geologia do Brasil-PGB, Mutum, Folha S B.20-Z-B. Estado do Amaz onas, Carta Geológica. Manaus: CPR M, 2014, 1 mapa colorido, 118,88 x 84,10 cm. Escala 1:250.00

CPRM, 2015. Geologia e recursos minerais da Folha Sumaúma – SB.20-Z-D, Estado do Amazonas, escala 1:250.000. CPRM, Serviço Geológico do Brasil, Manaus. Programa Geologia do Brasil - PGB. Levantamentos Geológicos Básicos do Brasil.

Cullers, R.L., Podkovyrov, N.V., 2002. The source and origin of terrigenous sedimentary rocks in the mesoproterozoic Ui group, southeastern Russia. Precambrian Res. 117, 157-183.

Del Rio-Salas, R., Ochoa-Landín, L., Eastoe, C.J., Ruiz, J., Meza-Figueroa, D., Valencia-Moreno, M., Zúñiga-Hernández, H., Zúñiga-Hernández, L., Moreno-Rodríguez, V., Mendívil-Quijada, H., 2013.Genesis of manganese oxide mineralization in the Boleo region and Concepción Peninsula, Baja California Sur: constraints from Pb-Sr isotopes and REE geochemistry. Rev. Mex. Cienc. Geol. 30, 482-499.

Dia, A., Chauvel, C., Bulourde, M., Gerard, M., 2006. Eolian contribution to soils on Mount Cameroon: isotopic and trace element records. Chem. Geol. 226, 232–252

Doe, B.R., Ayuso, R.A., Futa, K., Peterman, Z.E., 1996. Evaluation of the sedimentary manganese deposits of Mexico and Morocco for determining lead and strontium isotopes in ancient seawater. In: Basu, A., Hart, S. (EDS.), Earth Processes: Reading the Isotopic Code. American Geophysical Union, Washington, pp. 391-408.

Eberlei, T., Habler, G., Wegner, W., Schuster, R., Körner, W., Thöni, M., Abart, R., 2015. Rb/Sr isotopic and compositional retentivity of muscovite during deformation. Lithos, 227,161-178.

Floyd, P. A., Leveridge, B. E., 1987. Tectonic environment of the Devonian Gramscatho basin, south Cornwall: Framework mode and geochemical evidence from turbiditic sandstones. J. Geol. Soc. Lond. 144, 531-542.

Gaudette, H.E., Olszewski, W.J., Santos, J.O.S., 1996. Geochronology of Precambrian rocks from the northern part of the Guiana Shield, State of Roraima, Brazil. J. South Amer. Earth Sci. 9, 183-195.

Gioia, S.M.C.L., Pimentel, M.M., 2000. The Sm-Nd isotopic method in the Geochronology Laboratory of the University of Brasília. An. Acad. Bras. Ciên. 72, 219-245.

Gruau, G., Martin, H., Leveque, B., Capodevilla, R., 1985. Rb-Sr and Sm-Nd geochronology of Lower Proterozoic granite-greenstone terrains in French Guiana, South America. Precambriam Res. 30, 63-80.

Gulson, B.L., Mizon, K.J., 1979. Lead isotopes as a tool for gossan assessment in base metal exploration. J. Geochem. Explor. 11, 299-320.

Henrique-Pinto, R., Janasi, V.A., Tassinari, C.C.G., Carvalho, B.B., Cioffi, C.R., Stríkis, N.M., 2015. Provenance and sedimentary environments of the Proterozoic São Roque Group, SE-Brazil: Contributions from petrography, geochemistry and Sm-Nd isotopic systematics of metasedimentary rocks. J. South Am. Earth Sci. 63, 191-207

Herron, M.M., 1988. Geochemical classification of terrigenous sands and shales from core or log data. J. Sediment. Res. 58 (5), 820-829

Horbe, A.M.C., 2014. Idades paleomagnéticas de crostas lateríticas da Amazônia. Bol. Mus. Para. Emílio Goeldi. Cienc. Nat. 9,93-104.

Horbe, A.M.C., Costa, M. L. 1997. Geoquímica dos ETR no perfil laterítico da Serra do Madeira - Mina Pitinga (Amazonas - Brasil). Geochim. Bras. 11, 309-324.

Innocente, C., Michard, A., Malengreau, N., Loubet, M., Noack, Y., Benedetti, M., Hamelin, B., 1996. Sr isotopic evidence for ion-exchange buffering in tropical laterites from the Paraná, Brazil. Chem. Geol. 136, 219-232.

Jacobsen, S. B., Wasserburg, G.J., 1980. Sm-Nd isotopic evolution of chondrites. Earth Planet. Sci. Lett. 50, 139-155.

Jenkin, G.R.T., Ellam, R.M., Rogers, G., Stuart, F.M., 2001. An investigation of closure temperature of the biotite Rb-Sr system: The importance of cation exchange. Geochim. Cosmochim. Acta. 65, 1141-1160.

Kirsimäe, K., Jorgensen, P., 2000. Mineralogical and Rb-Sr isotope studies of low-temperature diagenesis of Lower Cambrian clays of the Baltic Paleobasin of north Estonia. Clays Clay Miner. 48, 95-105.

Kříbek, B., Zachariáš, J., Knésl, I., Míková, J., Mihaljevič, M., Veselovský, F., Bamba, O., 2016. Geochemistry, mineralogy, and isotope composition of Pb, Zn, and Cu in primary ores, gossan and barren ferruginous crust from the Perkoa base metal deposit, Burkina Faso. J. Geochem. Explor.168, 49–64.

Kurtz, A.C., Derry, L.A., Chadwick, O.A., 2001. Accretion of Asian dust to Hawaiian soils: isotopic, elemental, and mineral mass balances. Geochim. Cosmochim. Acta.65, 1971-1983.

Laveuf, C., Cornu, S., 2009. A review on the potentiality of Rare Earth Elements to trace pedogenetic processes. Geoderma, 154, 1-12

Liu, X-M., Rudnick, R.L., McDonough, W. F., Cummings, M.L., 2013. Influence of chemical weathering on the composition of the continental crust: Insights from Li and Nd isotopes in bauxite profiles developed on Columbia River Basalts. Geochim. Cosmochim. Acta. 115, 73-91

Ma, J., Wei, G., Xu, Yiang., Long, W., 2010. Variations of Sr-Nd-Hf isotopic systematics in basalt during intensive weathering. Chem. Geol. 269, 376-385.

Ma, J.L., Wei, G.J., Xu, Y.G., Long, W.G., Sun, W.D., 2007. Mobilization and re-distribution of major and trace elements during extreme weathering of basalt in Hainan Island, South China. Geochim. Cosmochim. Acta.71, 3223-323.7

Marques, S.N.S., Souza, V.S., Dantas, E. L., Valério, C. S., Nascimento, R.S.C., 2014. Contributions to the petrography, geochemistry and geochronology (U-Pb and Sm-Nd) of the Paleoproterozoic effusive rocks from Iricoumé Group, Amazonian Craton, Brazil. Braz. J. Geol. 44, 121-138

McLennan, S.M., Taylor, S.R., McCulloch, M.T., Maynard, J.B., 1990. Geochemical and Nd-Sr isotopic composition of deep-sea turbidites: crustal evolution and plate tectonic associations. Geochim. Cosmochim. Acta. 54, 2015-2050.

McQueen, K.G., Scott, K.M., 2008. Rock weathering and structure of the regolith. In: Scott, K.M., editors. Regolith Science. CSIRO Publishing, Melbourne, pp 103–124

McReath, I., Faraco, M.T.L., 1997. Sm-Nd and Rb-Sr systems in part of the Vila Nova Metamorphic Suite, Northern Brazil. In: South American Symposium on Isotope Geology –Campos do Jordão, São Paulo, Brazil. Anais, pp. 194-196

Mishra, M., Sen, S., 2012. Provenance, tectonic setting and source-area weathering of Mesoproterozoic Kaimur Group, Vindhyan Supergroup, Central India. Geol. Acta. 10(3), 283-293.

Morey, G.B., Setterholm, D.R., 1997. Rare earth elements in weathering profiles and sediments of Minnesota: Implications for provenance studies. J. Sediment. Res. 67, 105-115.

Negrel, P., 2006. Water–granite interaction: clues from strontium, neodymium and rare earth elements in soil and waters. Appl. Geochem. 21, 1432-1454

Nelson, B. K., DePaolo, D. J., 1988. Comparison of isotopic and petrographic provenance indicators in sediments from Tertiary continental basins of New Mexico. J. Sediment. Petrol. 58, 348- 357.

Nesbitt, H., 1979. Mobility and fractionation of rare earth elements during weathering of granodiorite. Nat. 279, 206-210.

Nesbitt, H.W., 1979. Mobility and fractionation of rare earth elements during weathering of granodiorite. Nat. 279, 206-210.

Nesbitt, H.W., Young, G.M., 1982. Early Proterozoic climates and plate motions inferred from major element chemistry of lutites. Nat. 299, 715-717.

Norcross, C.E., Davies, D.W. and Spooner, E.T.C. 1998. U-Pb geochronology of the Omai intrusion-hosted Au-Quartz vein deposit and host rocks, Guyana, South America. In: 1998 GSA Meeting, Toronto, Ontario, pp. A-127.

Ohlander, B., Ingri, J., Land, M., Schoberg, H., 2000. Change of Sm-Nd isotope composition during weathering of till. Geochim. Cosmochim. Acta. 64, 813-820

Ohta, A., Kawabe, I., 2001. REE (III) adsorption onto Mn dioxide (d-MnO2) and Fe oxyhydroxide: Ce (III) oxidation by d-MnO_2. Geochim. Cosmochim. Acta. 65, 695-703.

Olszewski, W.J., Wirth, K.R., Gibbs, A.K., Gaudette, H.E., 1989. The age, origin and tectonic of the Grão-Pará Group and associated rocks, Serra dos Carajás, Brazil: Archean Continental volcanism and rifting. Precambrian Res. 42, 229-254.

Payolla, B.L., Bettencourt, J.S., Kozuch, M., Leite, W.B., Fetter, A.H., VanSchmus, W.R., 2002. Geological evolution of the basement rocks in the east-central part of the Rondônia Tin Province, SW Amazonian Craton, Brazil: U-Pb and Sm-Nd isotopic constraints. Precambrian Res. 119, 141-169

Reis, N.J., Bahia, R.B.C., Almeida, M.E., Costa, U.A.P., Betiollo, L.M., de Oliveira, A.C., Splendor, F., 2013. O supergrupo Sumaúma no contexto geológico da Folha SB.20-Z-D (SUMAÚMA), sudeste do Amazonas: modo de ocorrência, discussão de idades em zircões detríticos e correlações no SW do Cráton do Amazonas. Contribuições à Geologia da Amazônia 8: 199- 222.

Rizzotto, G.J., 1999. Petrologia e geotectônica do Grupo Nova Brasilândia, Rondônia. Msc thesis. Porto Alegre, Brazil, Federal University of Rio Grande do Sul, 131p.

Rollinson, H. 1993. Using Geochemical Data: evaluation, presentation, interpretation, Longman, London.

Romer, R.L., Kirsch, M., Kroner, U., 2011. Geochemical signature of Ordovician Mn-rich sedimentary rocks on the Avalonian shelf. Can. J. Earth Sci. 48, 703-718.

Roser, B.P., Korsch, R.J., 1988. Provenance signatures of sandstone-mudstone suites determined using discriminant function analysis of major-element data. Chem. Geol. 67, 119-139.

Ruffet, G., Innocent, C., Michard, A., Féraud, G., Beauvais, A., Nahon, D., Hamelin, B., 1996. A geochronological 40Ar/39Ar and 87Rb/87Sr study of K-Mn oxides from the weathering sequence of Azul, Brazil. Geochim. Cosmochim. Acta. 60, 2219-2232.

Santos, J.O.S, Hartmann, L.A., Gaudette, H.E., Groves, D.I., Mc Naughton, N.J., Fletcher, I.R., 2000. A new understanding of the provinces of the Amazon Craton based on integration of field mapping and U-Pb and Sm-Nd geochronology. Gondw. Res. 3,453-488.

Santos, J.O.S. 2003. Geotectônica dos Escudos das Guianas e Brasil Central. In: L.A. Bizzi, C. Schobbenhaus, R.M. Vidotti, J.H. Gonçalves (eds.) Geologia, Tectônica e Recursos Minerais Minerais do Brasil: texto, mapas e SIG. CPRM- Serviço Geológico do Brasil. Cap.4, p 169-226

Santos, J.O.S., Hartmann, L.A., Faria, M.S.G. de, Riker, S.R.L., Souza, M.M. de, Almeida, M.E., McNaughton, N.J., 2006. A compartimentação do Cráton Amazonas em Províncias: Avanços ocorridos no período 2000-2006. In: SBG-Núcleo Norte, Simp. Geol. Amaz., 9, Belém, PA, Resumos Expandidos.CD-Rom

Sato, K., Tassinari, C. C. G., 1997. Principais eventos de acreção continental no Cráton Amazônico baseados em idade-modelo Sm-Nd, calculada em evoluções de estágio único e estágio duplo. In: Costa, M.L.; Angélica, R. S. (coords.). Contribuições à geologia da Amazônia. Belém, SBG. v. 1, p. 91-142.

Siebel, W., Reitter, E., Wenzel, T., Blaha, U., 2005. Sr isotope systematics of K-feldspars in plutonic rocks revealed by the Rb–Sr microdrilling technique. Chem. Geol. 222, 183-199.

Silva, P.J.M., Horbe, A.M.C., Horbe, M.A., 2012. Mineralogia e geoquímica de ocorrências manganesíferas da bacia Alto Tapajós, sudeste do Amazonas, Brasil. Bol. Mus. Para. Emílio Goeldi. Cienc. Nat. 7, 11-28.

Slack, J.F., Stevens, P.J., 1994. Clastic metasediments of the Early Proterozoic Broken Hill Group, New South Wales, Australia: Geochemistry, provenance, and metallogenic significance. Geochim. Cosmochim. Acta. 58, 3633-3652

Taylor, S.R., McLennan, S.M., 1985. The continental Crust: its composition and evolution. An Examination of The Geochemical Record Preserved in rocks, Blackwell Scientific Publications, Oxford

Tripathy, G., Singh, S., Krishnaswami, S., 2012. Sr and Nd Isotopes as tracers of chemical and physical erosion. In: Baskaran, M. (Ed.), Handbook of Environmental Isotope Geochemistry. Advances in Isotope Geochemistry. Springer Berlin Heidelberg, 521-552p

Vasconcelos, P.M., Renne, P.R,. Brimhall, G.H., Becker, T.A., 1994. Direct dating of weathering phenomena by 40Ar/ 39Ar and K-Ar analysis of supergene K-Mn oxides. Geochim. Cosmochim. Acta. 58, 1635-1665.

Viers, J., Wasserburg, G.J. ,2004. Behavoir of Sm and Nd in a lateritic soil profile. Geochim. Cosmochim. Acta. 68, 2043-2054.

Vignol, L.M., 1987. Études geochimiques des granulites du Brésil et la zone d'Ivoire: Les elements (K,Rb, Sr, Sm, Nd) et les isotopes radiogeniques (Sr and Nd). Diplome d'bstudes approfondies de geochimie. Université Paris, VII - Inst. Physique du globe de Paris.

Voicu, G., Bardoux, M., Stevenson, R., Jébrak, M., 2000. Nd and Sr isotope study of hydrothermal scheelite and host rocks at Omai, Guiana Shield: implications for ore fluid source and flow path during the formation of orogenic gold deposits. Miner. Depos. 35, 302-314

Yang, B., Zeng, Z., Wang, X., 2015. Characteristics of Sr, Nd and Pb isotopic compositions of hydrothermal Si-Fe-Mn-oxyhydroxides at the PACMANUS hydrothermal field, Eastern Manus Basin. Acta Oceanol. Sin. 34(8), 27–34.

SUPPLEMENTARY MATERIAL

ANNEX I

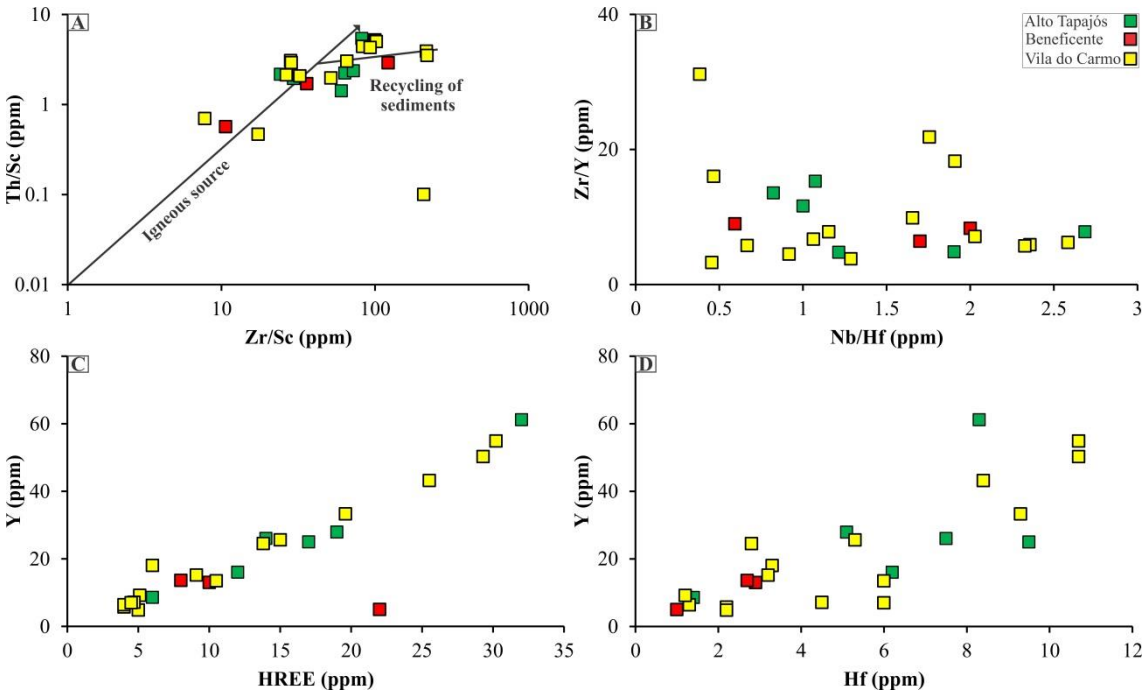

Figure A1- Scatter plot showing (Zr/Sc vs Th/Sc, Zr/Y vs Nb/Hf, HREE vs Y and Hf vs Y) the relationship between the Vila do Carmo, Beneficente and Alto Tapajós groups

ANNEX II

All chemical elements and mineralogical contents mentioned on the text are presented at this present study and at Albuquerque et al. (2017)

Equation 1:

$$\mathbf{REE_r/REE_c = \sigma\{[(Ho+C+Co)+Ce_{(ppm)}]_r/[(Ho+C+Co)+Ce_{(ppm)}]_c\} + \beta[(Zr+Hf)r/(Zr+Hf)c]}$$

- **σ** is a variable that indicates how much REE is related to Mn minerals and cerianite ($Ce_{(ppm)}$ content), whereas **β** is a variable that indicates how much REE is related to heavy minerals, such as zircon, rutile, among others.
- **REE_r** is the content of REE in Mn-greywacke (A3), while **REE_c** is the average of REE in Mn lateritic duricrusts, samples M1, Pp1 and Pp2 in the case of profile 1 and VB and VT in the case of profile 2.
- **$[(Ho+C+Co)+Ce_{(ppm)}]_r$** is the sum of Mn minerals (Ho-hollandite, C-cryptomelane and Co- coronadite) and Ce (ppm) element present in Mn-

greywacke. The hollandite, cryptomelane and coronadite were chosen due to be able to fix trace elements and, as presented by Albuquerque et al. (2017). **$[(Ho+C+Co)+Ce_{(ppm)}]_c$** is the sum of Mn minerals (Ho-hollandite, C-cryptomelane and Co- coronadite) and Ce (ppm) element present in Mn lateritic duricrusts, samples M1, Pp1 and Pp2 in the case of profile 1 and VB and VT in the case of profile 2.

- **(Zr+Hf)r** is the sum of Zr and Hf presente in Mn-greywacke, **(Zr+Hf)c** is the Mn lateritic duricrusts, samples M1, Pp1 and Pp2 in the case of profile 1 and VB and VT in the case of profile 2.

1- Calculate of how much REE is related to heavy minerals and Mn minerals and cerianite

Mn greywacke (A3)→ REE_r= 53 ppm; $[(Ho+C+Co)+Ce_{(ppm)}]_r$= 39 and (Zr+Hf)r= 33

Profile 1- average of the samples M1, Pp1 and Pp2→ REE_c= 238,66ppm; $[(Ho+C+Co)+Ce_{(ppm)}]_c$= 133.63; ppm and (Zr+Hf)c= 75.3 ppm

Profile 2- average of the samples VB and VT→ REE_c= 955.5 ppm; $[(Ho+C+Co)+Ce_{(ppm)}]_c$= 912; ppm and (Zr+Hf)c= 178.75 ppm

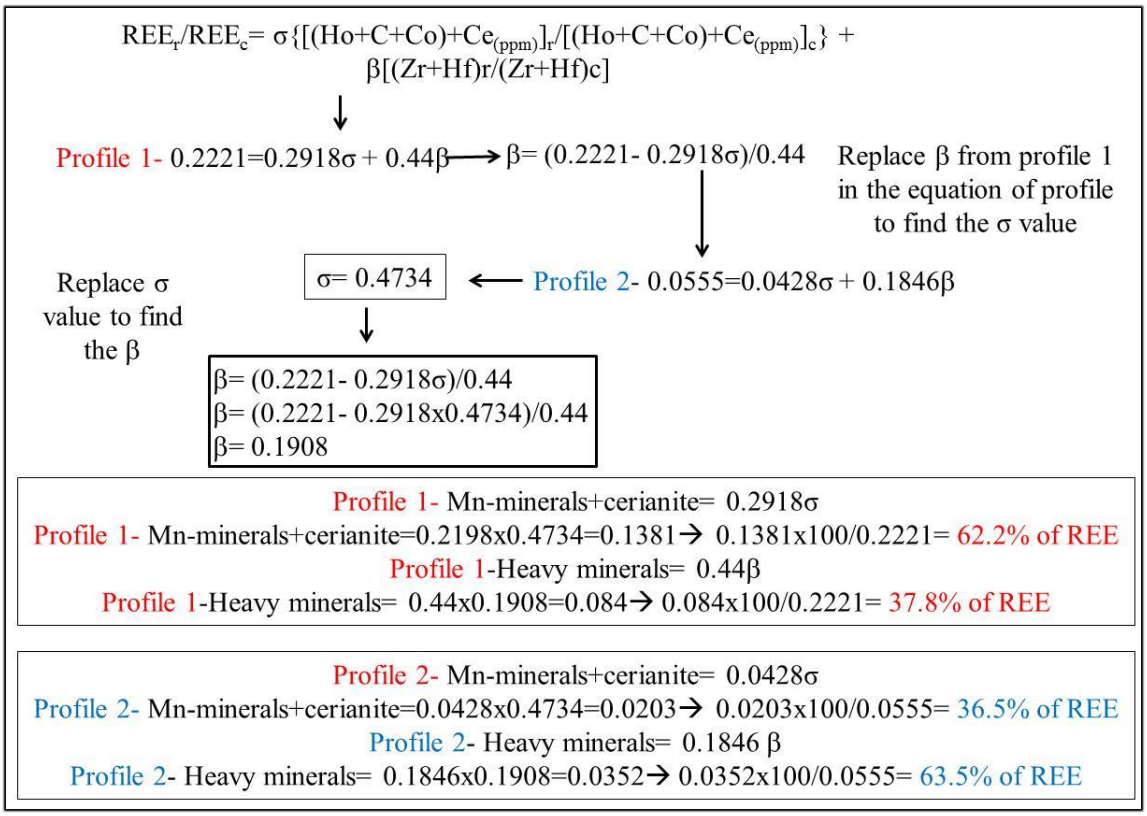

Figure A2- Step by step of to how to calculate the content of REE related to Mn-minerals+cerianite and heavy minerals

Highlights of equation 2:

Mn greywacke (A3)→ $(^{147}Sm/^{144}Nd)_r$= 0.1131; $(^{143}Nd/^{144}Nd)r$= 0.51184; $(Sm/Nd)_r$= 0.187

Profile 1- average of the samples M1, Pp1 and Pp2→ $(^{147}Sm/^{144}Nd)_c$= 0.2325; $(^{143}Nd/^{144}Nd)_c$= 0.511817; $(Sm/Nd)_c$= 0.385667

Profile 2- average of the samples VB and VT→ $(^{147}Sm/^{144}Nd)_c$= 0.3341; $(^{143}Nd/^{144}Nd)_c$= 0.511464; $(Sm/Nd)_c$= 0.212

Variations of $^{147}Sm/^{144}Nd$ through the rock to duricrust in the profile 1-

$(^{147}Sm/^{144}Nd)_{r-c}$→$(^{147}Sm/^{144}Nd)_r/(^{147}Sm/^{144}Nd)_c$= 0.486452;

$(^{143}Nd/^{144}Nd)_{r-c}$→$(^{143}Nd/^{144}Nd)_r/(^{143}Nd/^{144}Nd)_c$ = 1.000046

$(Sm/Nd)_{r-c}$→$(Sm/Nd)_r/(Sm/Nd)_c$= 0.4849

Variations of $^{147}Sm/^{144}Nd$ through the rock to duricrust in the profile 2-

$(^{147}Sm/^{144}Nd)_{r-c}$→$(^{147}Sm/^{144}Nd)_r/(^{147}Sm/^{144}Nd)_c$= 0.338521;

$(^{143}Nd/^{144}Nd)_{r-c}$→$(^{143}Nd/^{144}Nd)_r/(^{143}Nd/^{144}Nd)_c$ = 1.000736

$(Sm/Nd)_{r-c}$→$(Sm/Nd)_r/(Sm/Nd)_c$= 0.8821

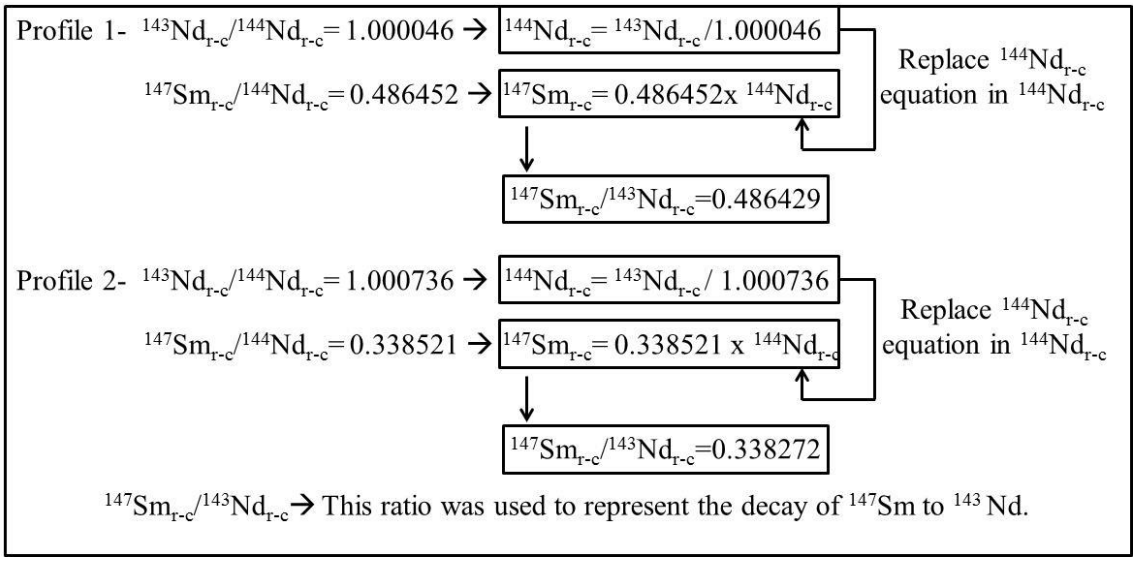

Figure A3- Step by step of to how to calculate the $^{147}Sm/^{143}Nd$ in interface rock to lateritic duricrust

Equation 2:

$$\left(^{147}Sm/^{143}Nd\right)_{r-c} = (Sm/Nd)_{r-c}.\{[(Ho+C+Co)+Ce_{(ppm)}]_r/[(Ho+C+Co)+Ce_{(ppm)}]_c.\delta + [(Zr+Hf)_r/(Zr+Hf)_c].\omega\}$$

- ω is a variable that indicates how much of ^{147}Sm that decay to ^{143}Nd is related to Mn minerals and cerianite ($Ce_{(ppm)}$ content), whereas δ is a variable that indicates how much of ^{147}Sm that decay to ^{143}Nd is related heavy minerals, such as zircon, rutile, among others.
- $\left(^{147}Sm/^{143}Nd\right)_{r-c}$ represent the ratio of $\left(^{147}Sm/^{143}Nd\right)_r/\left(^{147}Sm/^{143}Nd\right)_c$, where $\left(^{147}Sm/^{143}Nd\right)_r$ is the content on Mn-greywacke (A3), while the $\left(^{147}Sm/^{143}Nd\right)_c$ is the average of REE in Mn lateritic duricrusts, samples M1, Pp1 and Pp2 in the case of profile 1 and VB and VT in the case of profile 2.
- $[(Ho+C+Co)+Ce_{(ppm)}]_r$ is the sum of Mn minerals (Ho-hollandite, C-cryptomelane and Co- coronadite) and Ce (ppm) element present in Mn-greywacke. The hollandite, cryptomelane and coronadite were chosen due to be able to fix trace elements and, as presented by Albuquerque et al. (2017). $[(Ho+C+Co)+Ce_{(ppm)}]_c$ is the sum of Mn minerals (Ho-hollandite, C-cryptomelane and Co- coronadite) and Ce (ppm) element present in Mn lateritic duricrusts, samples M1, Pp1 and Pp2 in the case of profile 1 and VB and VT in the case of profile 2.
- $(Zr+Hf)_r$ is the sum of Zr and Hf presente in Mn-greywacke, $(Zr+Hf)_c$ is the Mn lateritic duricrusts, samples M1, Pp1 and Pp2 in the case of profile 1 and VB and VT in the case of profile 2.

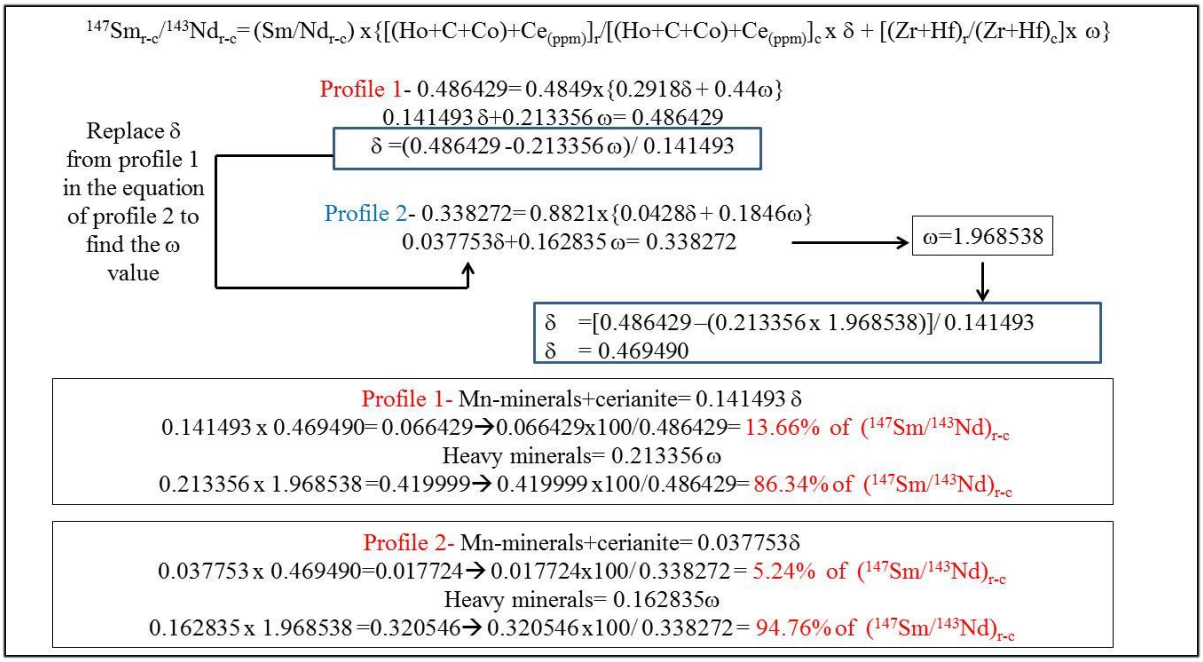

Figure A4- Step by step of to how to calculate the content of Nd isotopes related to Mn-minerals+cerianite and heavy minerals

CAPÍTULO VI: ARTIGO 3- USING AIRBORNE RADIOMETRIC DATA TO IDENTIFY LATERITIC DURICRUST AND SUPERGENE DEPOSITS IN SOUTHWESTEN AMAZONIA

(Artigo em preparação para ser submitido junto à revista Journal of South American Earth Sciences)

Esse artigo reúne dados aerogamespectométricos da região sudeste do estado do Amazonas, e tem por objetivo identificar regiões propícias à ocorrência de crostas lateríticas. Também, com base na geologia, altimetria, mapa de solos e nos modelos estatísticos Booleano e Fuzzy são propostas áreas com interesse exploratório.

USING AIRBORNE RADIOMETRIC DATA TO IDENTIFY LATERITIC DURICRUST AND SUPERGENE DEPOSITS IN SOUTHWESTERN AMAZONIA

Márcio Fernando dos Santos Albuquerque[1]; Túlio Marques Soares[1]; Adriana Maria Coimbra Horbe[2]; Endel Muller Dalat Sousa[1].

1-Graduate Program in Geology, Brasilia University, Geoscience Institute, Darcy Ribeiro University Campus, 70910-900, Brasília, Federal District, Brazil, albuquerqueIII@hotmail.com; 2- Brasilia University, Geoscience Institute, Darcy Ribeiro University Campus, 70910-900, Brasília, Federal District, Brazil.

ABSTRACT

Altimetric data together with gamma spectrometry and magnetometry have been studied in southwestern Amazonia, based on Boolean and Fuzzy statistical logical with the goal to identify favorable areas to lateritic duricruts occurrence. The region is divided into three main surfaces: 1- Surface 1 (SP1: ≤ 134m) composed by lowlands, valleys and dissected hills dominated by volcanic and sedimentary rocks and Mn to Mn-Al-Fe duricrusts; 2- Surface 2 (SP2: 134-186m) with rounded hills with concave top sustained by Fe and Fe-Al duricrusts; 3- Surface 3 (SP3: 186-290 m) with elongated plateaus to rounded hills supported by bauxites, Fe duricrust and rare Mn-Al-Fe duricrusts and colluviums. Lateritic duricrusts are associated to eTh channel what gives it light green colored in the RGB channels. The Boolean and Fuzzy models displayed good correlation with bauxites, Mn and Mn-Al-Fe duricrusts and oxisols, while the Boolean recognized 20% more Fe duricrusts than the Fuzzy models. However, the Fuzzy models were efficient in discarding ironstones located in the western portion of the area, since they does not have relationship with lateritization. Finally, the combination of relief, eTh Fuzzy, stratigraphy and soil map allowed identify favorable areas to the occurrence of Mn, bauxite and phosphatic duricrusts.

Keywords: altimetry, Boolean, Fuzzy, laterite

1. INTRODUCTION

Several studies have been carried out in lateritic terrains due to their great economic value and because their importance to understand the landscape evolution along the geological time since they are the final product of long time rocks exposure to tropical climates (e.g. Costa, 1997; Spier et al. 2006; Beauvais et al. 2008; Anand and Butt, 2010; Bonnet et al. 2014; Monteiro et al. 2014 and Riffel et al. 2015). Despite composing large part of Amazonia landscapes and cover one-third of the continents, there are few studies about the application of airborne gamma ray spectrometry (AGRS). AGRS based on U, Th and K channels has been used with success in Australia, pioneer in this type of study, in the identification of different types of soils and in regolith mapping (Wilford et al. 1997; Dauth, 1997; Taylor et al., 2002; Wilford, 2012 and Moonjun et al. 2017).

The gamma rays emanating from ground surface are classified as primary when reflects the geochemistry and mineralogy of the bedrock, otherwise it is secondary whenever it represent the modification of radioelement redistribution by weathering and pedogenesis (Wilford, 1995; Wilford et al. 1997). Therefore, the weathering products are depleted in K, except when illite and smectite are formed in low weathered soils, saprolites or when manganese duricrusts have K-bearing manganese phases. While the U and Th are assigned to heavy minerals or may be absorbed by goethite and hematite (Dickson and Scott, 1997; Wilford et al. 1997).

Application of AGRS together with GIS, digital elevation model (DEM), magnetometry, multivariate statistical, neural network, Boolean and Fuzzy logic are increasing the mapping efficiency (Behrens et al., 2005; Carrino et al., 2011; Motta and Faria Junior, 2016; Iza et al. 2016, Moonjun et al. 2017). These tools allow recognize different types of soils and lateritic duricrusts derived from different types of rocks (schists, granites, metasedimentary rocks and greenstones belts); high K in soils may be used as parameter of weathering index, however, soils developed from the same bedrock with different characteristics (catenas) and the similar response between soils developed from different bedrocks is still the biggest issues in regolith mapping (Cook et al. 1996; Wilford et al. 1997).

In this context, the purpose of this work is using AGRS to indicate domains with higher probability of occurrence of lateritic duricrust. The large application of these tools will help to developed better and fast tools to improve the regolith mapping techniques, compare the efficiency of the statistical methods such as the Boolean and Fuzzy logic, and identify areas with metallogenic potential based in geophysical and geochemical criteria.

2. GEOLOGICAL SETTING

The study area is located in the southwestern region of Amazonia, Brazil, between 6-8°S and 59-61°W (Fig. 1). The climate is hot and humid and is slightly drier from May to September. The mean annual temperature ranges from 25 to 27°C, the relative humidity is approximately 85%, and the yearly rainfall is 2,336 mm year-1.

This region contains a volcanic basement that is related to Colider Group (1.78-1.80 Ga). Intruding the volcanic basement are granitic bodies of Teodosia (1.758-1.757 Ga) and Igarapé das Lontras (1.754 Ga) suites, all of which are intersected by the monzogranitic batholiths of Serra da Providência suite (1.57-1.53 Ga, Santos, 2003; CPRM, 2015). Two main basins have developed over the volcanic basement and granitic bodies (Reis et al. 2013; CPRM, 2014): the first was infilled by rocks of Sumaúma Supergroup, which comprise Proterozoic volcano-sedimentary sequence, while the second was infilled by rocks of the Alto Tapajós Group, which represent a Paleozoic sedimentary sequence (Fig. 1).

According to Reis et al. (2013), the Sumaúma Supergroup is divided in Vila do Carmo Group and Beneficente Group. The Vila do Carmo Group (1.76-1.74 Ga) comprises the rift phase of the Sumaúma Supergroup and contains volcanoclastic, pyroclastic and clastic units and quartz-sandstones cut by Mata-Matá diabase (1.576 Ga) (Betiollo et al. 2009; Reis et al. 2013). The post-rift phase is related to Beneficente

Group (1.43- 1.08 Ga), which overlaps Vila do Carmo Group. The Beneficente Group contains orthoconglomerates and massive quartz-sandstones with rare mudstones deposited in alluvial fans and floodplains; pinkish to purplish silicified quartz-sandstones that were deposited in tidal plains and river channels and sublitharenites and quartz-sandstones intercalated with siltstones and mudstones that were deposited in aeolian and washover environments (CPRM, 2013; Reis et al. 2013).

Paleozoic basin (Alto Tapajós Group) and Neogene deposits partially cover the older units. The weathering developed manganese, iron and aluminous lateritic duricrusts that sustain a strong dissected landscape formed by plateaus and hills.

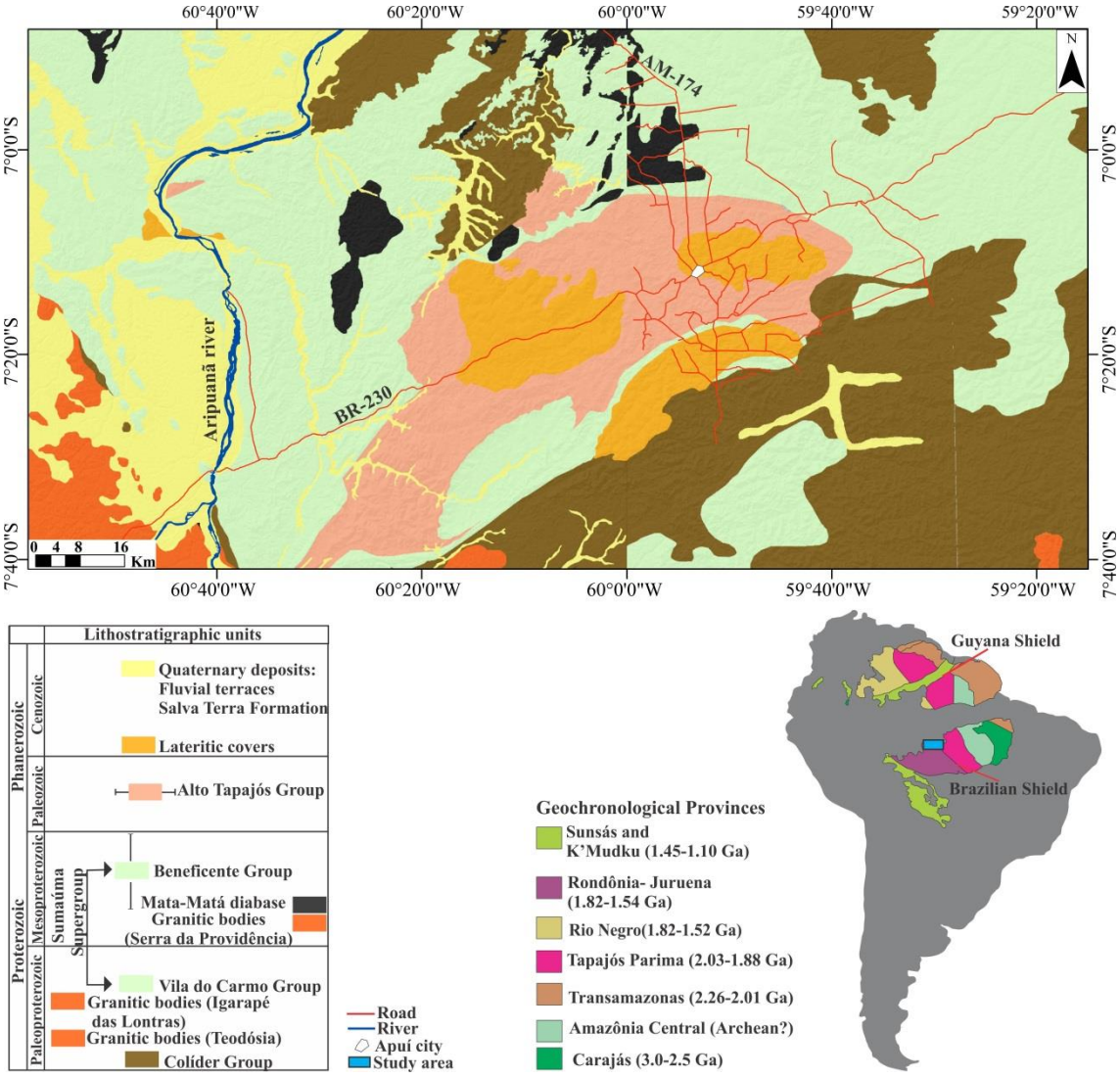

Figure 1: Localization of study area and geological setting. Modified from CPRM (2013, 2014 and 2015) (Geological Survey of Brazil).

3. SAMPLING MATERIALS AND ANALYTICAL METHODS

Along the rivers, roads and vicinal were described and collected 76 lateritic duricrust and oxisols samples (Table 1). Also were cataloged rocks and spodosols. For the relief patterns study was used the Shuttle Radar Topography Mission (SRTM) with a spatial resolution of 30 m performed by the space shuttle Endeavour, in February 2000. From SRTM were generated TIN surfaces (Triangle Irregular Network) using the ArcGIS 10, which allowed distinguishes the control of the lateritic duricrust by the altimetry data.

The airborne gamma-ray spectrometric and magnetometric images were obtained and processed from the Prospectors Airborne System LTDA, Rio de Janeiro, Brazil, as part of two aerogeophysical projects (Aripuanã and Sucunduri) of the CPRM/Geological Survey of Brazil at 2008-2010. The aerogeophysical projects covered about 208,000 km of gamma spectrometric and magnetometric profiles of high resolution with flight lines and control spaced of 0.5 and 10 Km oriented in the N-S and E-W directions, respectively. The flight height was fixed in 100 m above the terrain with slight variations of 15 m. In order to avoid issues related to moisture and by the water retained by dense vegetation that interfere in the gamma spectrometry response reported by Minty (1997), the aerogeophysical projects in the Apuí region were performed in July and August months, the drier months of the region.

On Oasis Montaj 6.3 the K, Th and U channels of airborne gamma-ray spectrometric and magnetometric images were loaded to make a unique mosaic. On Arcgis 10 with the Geosoft extension was made the processing of the airborne geophysical images and the integrated handling of all of the products.

3.1 Boolean Logic

The Boolean logic is a math system that creates rules or logical expressions to select, analyze and process data. It may be defined by the specification of each one of their elements or by specification of ordinary properties to all the elements. The sets are considered as bivalent systems with their states between inclusion and exclusion. Thus, the degree of relevance for the set X is 0 if "y" is not an element of A, by the other hand, the degree of pertinence is 1 if "y" is an element of A (Braghin, 1998). Values of a Boolean set are always completely categorized with no ambiguity or dichotomy about their relevance.

The Boolean logic was first employed in each of the three landscape surfaces (< 134 m; 134 to 186 m and 186 to 290 m) of the studied region, according with (TIN ≥ lower boundary of each surface) Boolean operator “e” “and/&”, loaded into Raster Calculator tool of Arcgis 10.

The Boolean logic was also applied in the $eTh/K_{(\%)}$ and $eU/K_{(\%)}$ ratios. However, the $eU/K_{(\%)}$ was discarded once it not displayed correlation with the fieldwork data. Thus, values of $eTh/K_{(\%)}$ slightly below the mean are the most representative and in Raster Calculator was used the follow equation:

1. ($eTh/K_{(\%)}$ channel ≥ (M-(δ-M)), where M is the mean of $eTh/K_{(\%)}$ channel and δ is the standard deviation

After test all channels, it was noticed that eTh show better correlation with lateritic duricrusts check points. The empirical interval which covers all lateritic duricrusts is slightly below of mean and the maximum value of eTh. The upper and lower boundaries were found by M+2δ and M-(δ/2), respectively (Fig.2).

The Boolean logic applied in eTh channel identified the interval more favorable to occurrence of lateritic duricrust, according with the equation:

2. (eTh ≥ lower boundary) and/& (eTh ≤ upper boundary), where and/& is a Boolean operator

Ultimately, was generated a binary map containing the correlation between the three TIN surfaces and the Boolean products. Each surface was delimitated by follow equations in Raster Calculator tool (Fig. 2):

3. (surface 1∩1) And/& (eTh ∩1)
4. (surface 2∩1) And/& (eTh ∩1)
5. (surface 3∩1) And/& (eTh ∩1)

This binary map provided the regions more favorable to lateritic covers. All results provided a bicolor raster with 0 and 1, where "1" has higher probability of occurrence of lateritic duricrusts, while the lower values were transformed into "0" does not agree with the Boolean model (Fig. 2).

3.2 Fuzzy Logic

Fuzzy logic is an extension of Boolean logic ("partial truth", values between "completely true" and "completely false"). Fuzzy logic can be defined as part of mathematical logic dedicated to the formal principles of uncertain or approximate reasoning, therefore closer to human thought and natural language. The Fuzzy logic may be related to the representation of incomplete or vague state of information. This approach allows imperfect, imprecise or uncertain information, such as natural phenomena, to be stored and expressed in terms of relevance. It also comprises a technique in which input data must be previously rasterized and presented on a continuous scale, with values that belong to a set between true and false, varying between values 1 and 0 - possibility of partial pertinence (Bonham-Carter, 1994).

Initially the fuzzification of the eTh channel was made using the Spatial Data Modeler (SDM) tool together with the categorical reclass which divided it in 10 intervals of possibility of relevance, here denominate "eTh Fuzzy" (Fig. 2).

Imprecise and incomplete information using Fuzzy logic, can be manipulated and processed using the Fuzzy operators (Fuzzy Product, Sum and Gamma operator). The Fuzzy Product is the product between eTh Fuzzy and elevation (TIN- Triangle Irregular Network) (Fig. 2), the final result being less than or equal to the lowest contribution of Fuzzy relevance values of the input maps (Bonham-Carter, 1994). The algebraic sum may also be interpreted as logic "OR", but not only does it assume full compensation, it is also crescent. The membership increases whenever it is combined with a nonzero membership (An et al. 1991). It is represented by the follow equation:

Fuzzy Sum= 1-[(1- eTh Fuzzy) x (1- TIN)] (Fig.2)

Finally, was developed the Fuzzy gamma operator (ɤ) which is the combination of algebraic product and sum (Zimmermann and Zysno, 1980). This operator allows

different degrees of compensation of combining two or more sets of information depending on the choice of ɤ, therefore the choice of an appropriate ɤ value provides compensatory process in the aggregation of subjective information categories (An et al. 1991).The best interval that covers the most of lateritic duricrusts and oxisols was ɤ=0.7, thus the Fuzzy gamma operator (ɤ) obeys the follow equation:

Fuzzy gamma operator (ɤ=0.7)= (Fuzzy sum)$^{0.7}$ x (Fuzzy product)$^{1-0.7}$ (Fig.2)

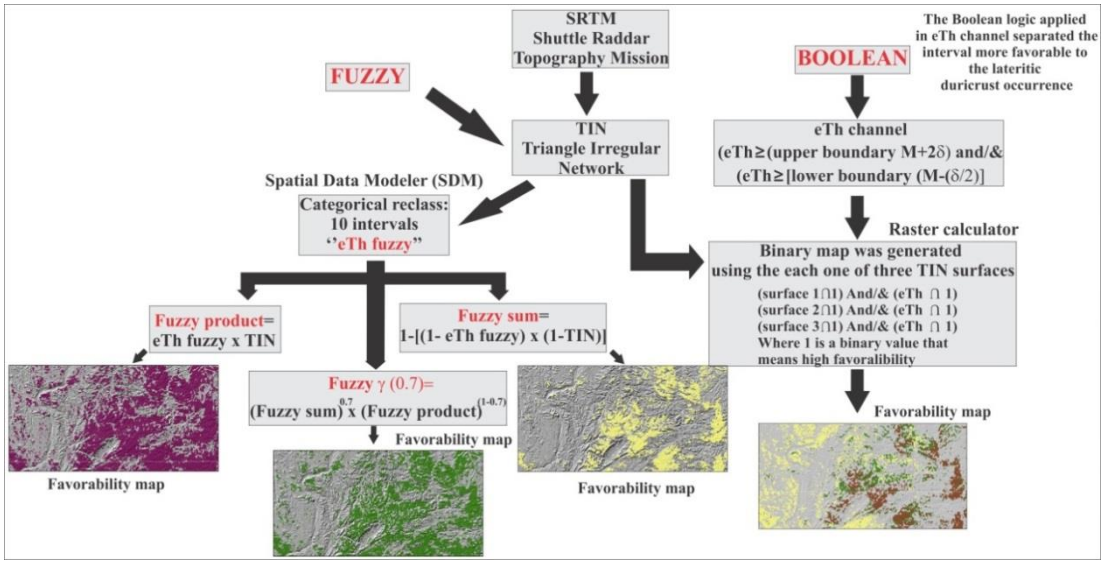

Figure 2: Summary of Boolean and Fuzzy methods in the study area

In order to verify the relevance degree of the models (Boolean and Fuzzy) was calculated the Kappa index which allows judge the favorability degree of this model (Cohen, 1960). Landis and Koch (1977) consider kappa index between 0.81 and 1 have a nearly perfect agreement, between 0.61–0.80 a substantial agreement, and beneath 0.60 moderate agreements, whereas values near zero indicate poor agreement. The Kappa formula is shown below:

- Kp= (β-ω)/(1-ω), where β= (Σ laterites and rocks in agreement with the model)/Σ all samples. It worthy be highlighted that the rocks in agreement with that model are those that not plot in the favorability map elaborate to identify lateritic duricrusts
- ω=[(Σ $_{\text{laterites in agreement and in disagreement}}$/ Σ $_{\text{all samples}}$) x (Σ $_{\text{laterites and rocks in agreement}}$/ Σ $_{\text{all samples}}$)] + [(Σ $_{\text{rocks in agreement and in disagreement}}$/ Σ $_{\text{all samples}}$) x (Σ $_{\text{laterites and rocks in disagreement}}$/ Σ $_{\text{all samples}}$)]

To calculate the kappa index were used 939 checkpoints including rocks, laterites, oxisol and spodossols. The mostly used rock data belongs to CPRM (Brazilian Geological Survey, 2006) and it is available online at http://geowebapp.cprm.gov.br/ViewerWEB/index_lito_250k.html, while the others checkpoints are from Albuquerque and Horbe (2015) and Albuquerque et al. (2017).

Finally, two samples of lateritic duricrusts were chosen for the Scanning Electronic Microscope (SEM, Quanta 250 FEI) analysis following Au-Pd metallization at Amazonas Federal University. The geochemical data were carried out in AcmeLab,

Vancouver, Canada, and are available in Albuquerque and Horbe (2015) and Albuquerque et al. (2017).

4. RESULTS AND DISCUSSION

4.1 Relief and lateritic context in southwestern Amazonia

The southwestern Amazonia gathers two geomorphological domains separated by Aripuanã River, wherein on the right is positioned the Dissecated Plateaus of Southern Amazonia, and on the left, the Planed Surfaces of the Amazonia (Dantas and Maia, 2010; Fig.3A). Three main altimetry surfaces have been recognized in the studied region according the type of lateritic duricrust occurrence. The main mineralogy, macroscopic and microscopic features of the lateritic duricrust is summarized in Table 1.

The surface 1 (SP1) has till 134 m altitude, dominated by strong dissecting valley in "U", lowlands, steep slopes and hills, sedimentary and volcanic rocks and pisolitic, protopisolitic, massive and vermiform Mn to Mn-Al-Fe duricrusts outcrops (Fig 3B and C). The surface 2 (SP2) is composed by rounded hills with concave top, 134 to 186 m altitude and 1 km of extension, where outcrops fragmental, pisolitic and nodular Fe and Fe-Al duricrusts (Fig 3B and D). In surface 3 (SP3) predominate strong dissected elongated plateaus to rounded hills (NE-SW and NW-SE), 186 to 290 m altitude and 4-21 Km of extension and 2-10 Km of width with dendritic to sub dendritic and rectangular drainages linked to large rivers of the region (Aripuanã, Acari and Sucunduri). They are sustained by massive and pisolitic bauxites and massive ferruginous duricrust (Fig 3B, E and F), with rares Mn-Al-Fe duricrusts and Mn colluviums, all of them overlapped by yellowish oxisol developed from tuffs and sandstones from Sumaúma Supergroup.

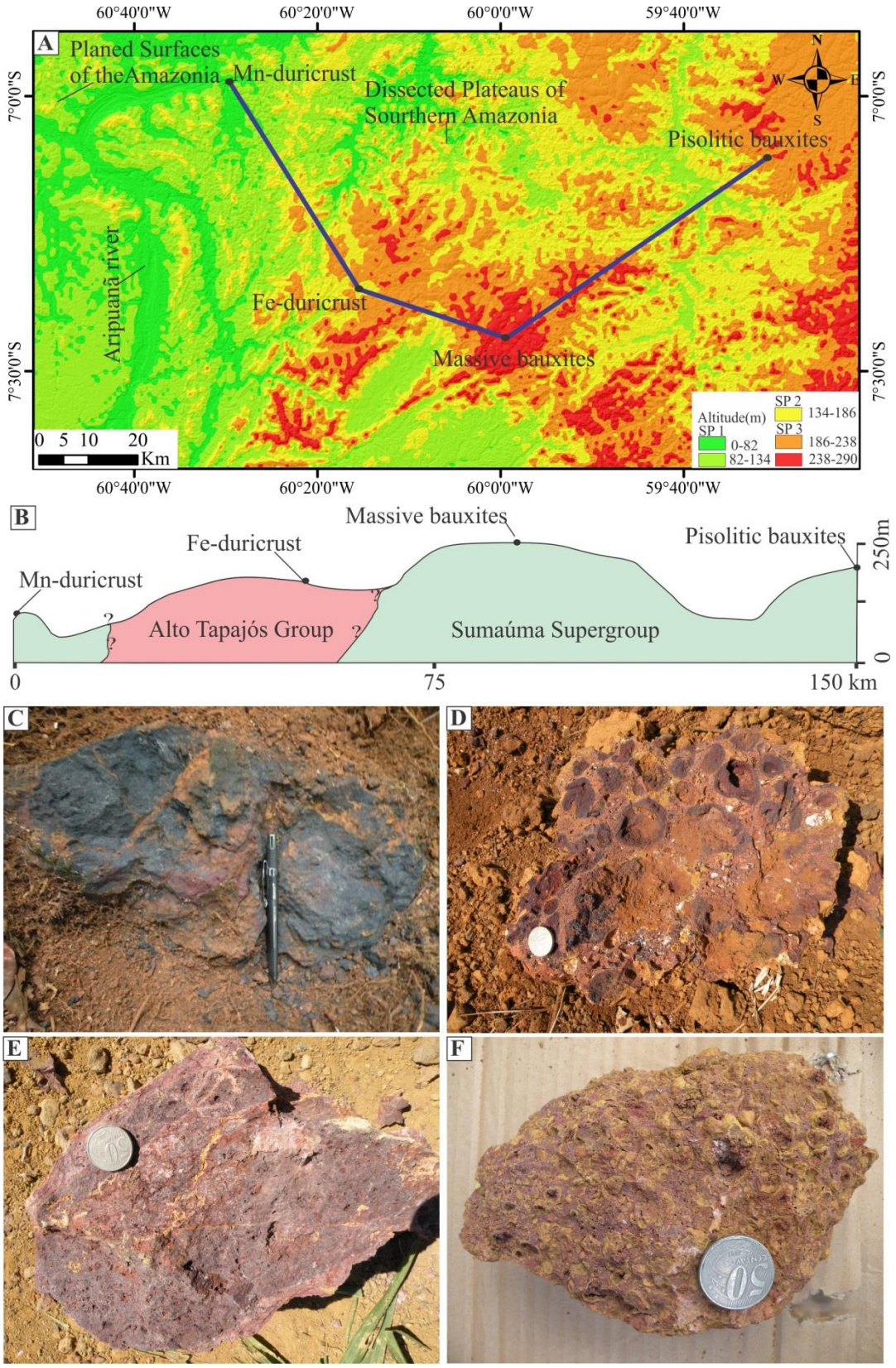

Figure 3: A- Altimetry map subdivided into surfaces. B- Altimetry profile showing the different altitudes of lateritic duricrusts and the lithostratigraphic units. C- Mn massive duricrust duricrust developed from sedimentary rocks of the Sumaúma Supergroup. D- Nodular Fe duricrust developed from sedimentary rocks of the Alto Tapajós Group. E- Massive bauxite volcanic rocks of Sumaúma Supergroup. F- Pisolitic duricrust sandstones of the Sumaúma Supergroup

Table 1: Main characteristics and mineral composition of the duricrusts of each profile. N.I- not identified

Duricrust	Framework/skeleton	Pisoliths/Angular fragments	Cavities/ fractures
Surface 1			
Mn-Al-Fe Pisolitic	Pinkish framework, composed by gibbsite, hematite and kaolinite. Secondary frosted to metallic plasma of hollandite, cryptomelane and goethite involves the framework Coronadite veinlets are widespread in framework	Red pisoliths of hematite and gibbsite with up to 2 cm diameter are sustained by framework	Filled by kaolinite and quartz
Mn Protopisolitic	Bluish grey, hard, dense, with metallic luster, rich in romanechite/hollandite, cryptomelane and pyrolusite	Pisoliths (1.5 cm ϕ) involved by cortex are widespread in the framework. Both are composed by the same minerals of framework.	Filled by quartz, kaolinite, gibbsite, goethite and hematite
Mn Massive	Greyish, pulverulent and porous rich in cryptomelane, hollandite and pyrolysite with intergrown of gibbsite and hematite	N.I	Filled by kaolinite and goethite
Mn-vermiform	Hard, dense and porous bluish grey skeleton (80% of bulk duricrust) with submetallic to earthy brightness composed mainly romanechite and quartz	N.I	Filled by kaolinite, goethite and hematite in a total of 20% of the bulk duricrust
Surface 2			
Fe-Al vermiform	The skeleton is friable (80% of bulk duricrust) composed by goethite, hematite and gibbisite as main minerals and by kaolinite and quartz subordinated	N.I	Filled by whitish kaolinite and quartz
Fe and Fe-Al Fragmental, pisolitic and nodular	The sandy clay framework comprises between 45 to 60% of bulk duricrust. It is orange when composed by goethite, hematite and quartz, or it is reddish pink when is formed by ooliths of gibbsite and kaolinite surrounded by hematite and goethite.	The framgments (till 35% of bulk duricrust) are reddish to violet with till 3.5 cm diameter. They are of gibbisite and hematite or composed mainly by hematite with quartz inclusions	Comprises until 25% of bulk duricrust, they are filled by gibbisite, hematite and kaolinite or goethite, quartz and rutile and have coloring whitish pink and whitish yellow.
Fe Laminated	Intercalation of thin blades of goethite with quartz, kaolinite and hematite subordinated	N.I	Filled by hematite botryoidal
Surface 3			
Massive bauxite	The framework comprises about 97% of the duricrust, it is compact, brown to pink reddish, little porous with gibbsite and hematite as major minerals	N.I	The cavities are filled by small gibbsite geodes (($\leq$ 3 cm of ϕ) and, sometimes, for whitish clayey material of illite and kaolinite
Pisolitic bauxite	Pinkish plasma (55% of bulk duricrust), sometimes, whitish to reddish composed mainly by gibbsite and hematite	Hematitic and Al-goethitic ($\leq$ 2.5 cm ϕ) comprise about 40% of the duricrust and are involved by brownish to orange goethitic cortex.	Filled by kaolinite, quartz and anatase.
Fe Massive duricrust	The framework is brownish, porous and composed by hematite, goethite and gibbsite as major phases, and quartz, kaolinite and anatase as trace minerals. Widespread on the framework is common the presence of quartz pebbles of up to 2 cm of diameter. They are fractured, corroded and show indications of dissolution	N.I	The cavities constitute pipes with 3cm diameter and are filled with yellow kaolinite
Mn-Al-Fe Vermiform	Skeleton composed by dendritic hollandite, crypetomelane and pyrolusite. Involving the skeleton there is plasma of gibbsite, hematite, goethite and kaolinite, with cerianite subordinated. Increase of hematite and gibbsite toward to top. Coronadite veinlets are widespread in skeleton	N.I	Filled by kaolinite and quartz

4.2 AGRS Interpretations

The airborne gamma-ray spectrometric ternary composition, based on eU, eTh and $K_{(\%)}$ RGB channels of the Apuí region, southwestern Amazonia, displayed several gamma spectrometric responses which vary according the type of rock. High K content pinkish colored, especially in the mid part of study area and along the rivers, is related to volcanic rocks and greywackes from Alto Tapajós basin and Colíder Group. High K along the rivers is mainly assigned to volcanic rocks and sediment that accumulate the K leached from the rocks. Granitic bodies which typically have high K, Th and U occur in the southern and southwestern part and displayed a pale to light green color.

The eTh channel displays high to extremely high values (black with red spots colored) assigned to basic rocks. The lateritic duricrust predominantly positioned into eTh channel, are highlighted by the green colors as reported by Dickson and Scott (1997), Carrino et al. (2011), Wilford et al. (1997), Wilford (2012), Iza et al. (2016), Moonjun et al. (2017) among others. However, in mostly cases both the volcano-sedimentary/sedimentary sequences and the lateritic duricrust and oxisols display the same light green colored in eTh channel. This is in disagreement with the data reported by Dickson and Scott (1997) and Isles and Rakin (2000) where the ferruginous duricrusts, pisoliths and bauxites show the highest content of Th in average compared with the bedrocks. Moreover, not every eTh signal identifies lateritic covers, as seen in elevated eTh in the Quaternary deposits (Salva Terra Formation and fluvial terraces) at the left side of Aripuanã river. The Salva Terra Formation brings together ironstones formed by fluctuations of table water in sedimentary rocks (CPRM, 2015), without relationship with lateritic process. Also, the fluvial terraces located mainly around the Aripuaná niver show light green colored in eTh channel in consequence of high Th accumulate after leached from the sediment source, as reported by Gunn et al. (1997).

Sand deposits that is often assigned to weathering and accumulation of quartz from sandstones of Sumaúma Supergroup and Alto Tapajós Group, covers an area of 228.5 Km^2. The areas of these deposits that are correlated to spodossols in soil map, is identified by black with bluish spots in ternary map of K, eTh and eU on the RGB channels (Fig. 4A, Fig. 8A and B). Nevertheless, fluvial terraces close to Aripuanã river, which have the same response in ternary map and are mapped as spodossols, were not considered.

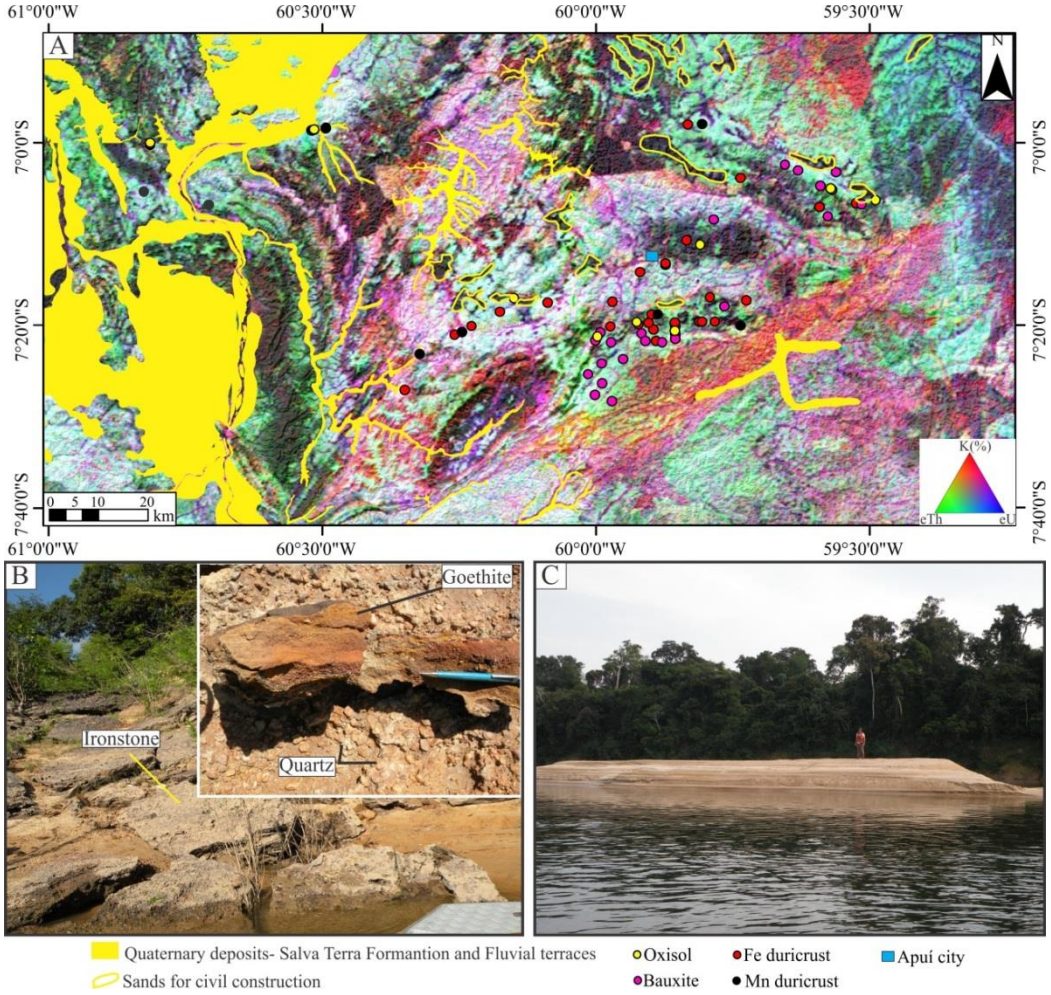

Figure 4: A-Ternary map of K, eTh and eU on the RGB channels highlighting the Quaternary deposits in yellow. B- Ironstones cropping out in the left side of Aripuanã river. C- Fluvial terraces in Aripuanã river.

4.3 Boolean and Fuzzy models

Statistical methods and altimetric data were applied to verify the favorability of duricrust occurrence in the study area. The oxisols which has almost the same chemical composition of the overlapped lateritic duricrusts and are the final product of dismantling and leaching of them (Horbe and Costa, 2005; Costa et al. 2014; Albuquerque and Horbe, 2015), were used to testify the favorability of the Boolean and Fuzzy models.

The eTh channel in the 145.78 (M+2δ) and 8.4 (M-(δ/2)) intervals, covers about 6500 Km^2, 34% of the study area. Whereas the Boolean eTh channel product distributed into the three altimetry surfaces occupy an area of the 5884 Km^2, 31% of the bulk area. Among the three altimetry surfaces favorable to the lateritic duricrust occurrence in the Boolean model, the SP1 covers an area of 2489 Km^2 (13% of bulk area), followed by SP3 (1854 Km^2, 10% of bulk area) and by SP2 (1541 Km^2, 8% of bulk area). The Kappa coefficient (Kp) calculated for all surfaces together is 0.61 what indicate substantial favorability to duricrust occurrence according Landis and Koch (1977) classification.

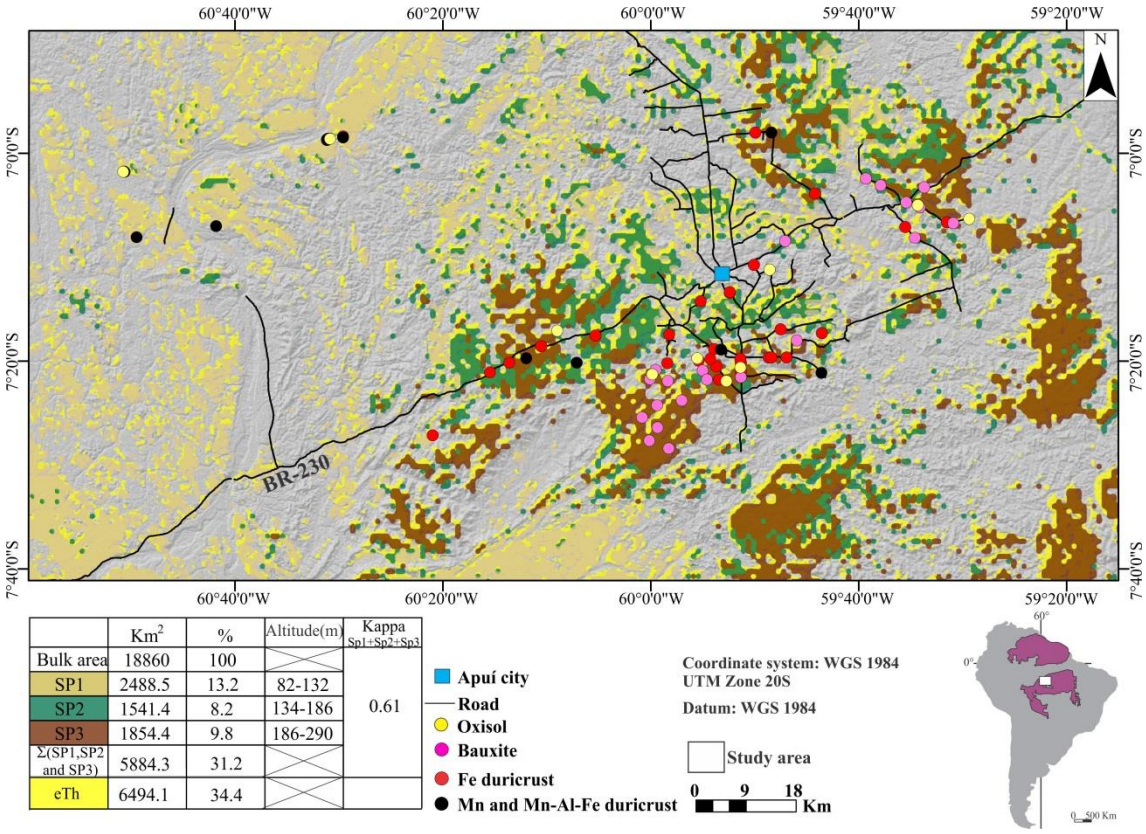

	Km²	%	Altitude(m)	Kappa Sp1+Sp2+Sp3
Bulk area	18860	100		
SP1	2488.5	13.2	82-132	0.61
SP2	1541.4	8.2	134-186	
SP3	1854.4	9.8	186-290	
Σ(SP1,SP2 and SP3)	5884.3	31.2		
eTh	6494.1	34.4		

Figure 5: Predictability map of lateritic crust occurrence based on Boolean logic performed in each surface (SP1, SP2 and SP3) with the lateritic duricrust occurrence reported by Albuquerque and Horbe (2015). Also is showed the eTh channel non Boolean

The Fuzzy technique (eTh Fuzzy, the Fuzzy Sum and product as well as the Fuzzy gamma operator) was applied to improve the accuracy of Boolean products. All generated Fuzzy models show strongly correlation with the mostly site points sampled. In this context, eTh Fuzzy covers 3368 Km^2, 18% of bulk area and has the highest degree of favorability of duricrust occurrence (Kp=0.8), followed by Fuzzy Sum and gamma operator (γ=0.7) which cover 4737 to 4900 Km^2, 25% of bulk area that is classified as substantial favorability (Kp between 0.68 and 0.63) to duricrust occurrence according Landis and Koch (1977) classification. The Fuzzy product comprises about 6049 Km^2, 32% of bulk area and has the lowest kappa index (K=0.56) that mean low favorability.

To identify the main differences between the Boolean and Fuzzy models it is indispensable correlate to the lithostratigraphic and geomorphological settings of the region, once it may discard or attest the regolith/laterite occurrence, as reported by Carrino et al. (2011), Iza et al. (2016), Motta and Faria Junior (2016) and Herrera et al. (2017). Both models show good correlation with bauxites, manganese duricrusts and oxisols (70-100% of agreement, Tab. 2). However, the Boolean recognized 20% more Fe duricrusts (61 of the 79 duricrusts, 67% of agreement) than the eTh Fuzzy, Fuzzy Sum, product and gamma operator (40-47% of agreement, Tab.2). Unlike of Boolean model, the Fuzzy models were efficient in discarding ironstones (without relationship

with lateritization) located in left side of Aripuanã river where predominate lowlands (above 134 m), steep slopes and hills strongly dissecting.

Therefore, the Boolean model overestimates areas with below 134 m and mapping it as duricrust when in fact are ironstones and fluvial terraces, in the mostly cases. For this reason, the Fuzzy models are more confident, especially the eTh Fuzzy with more Kappa index (Kp=0.8), which indicates more reliability. Despite the Fuzzy product overestimates areas above 186 m.

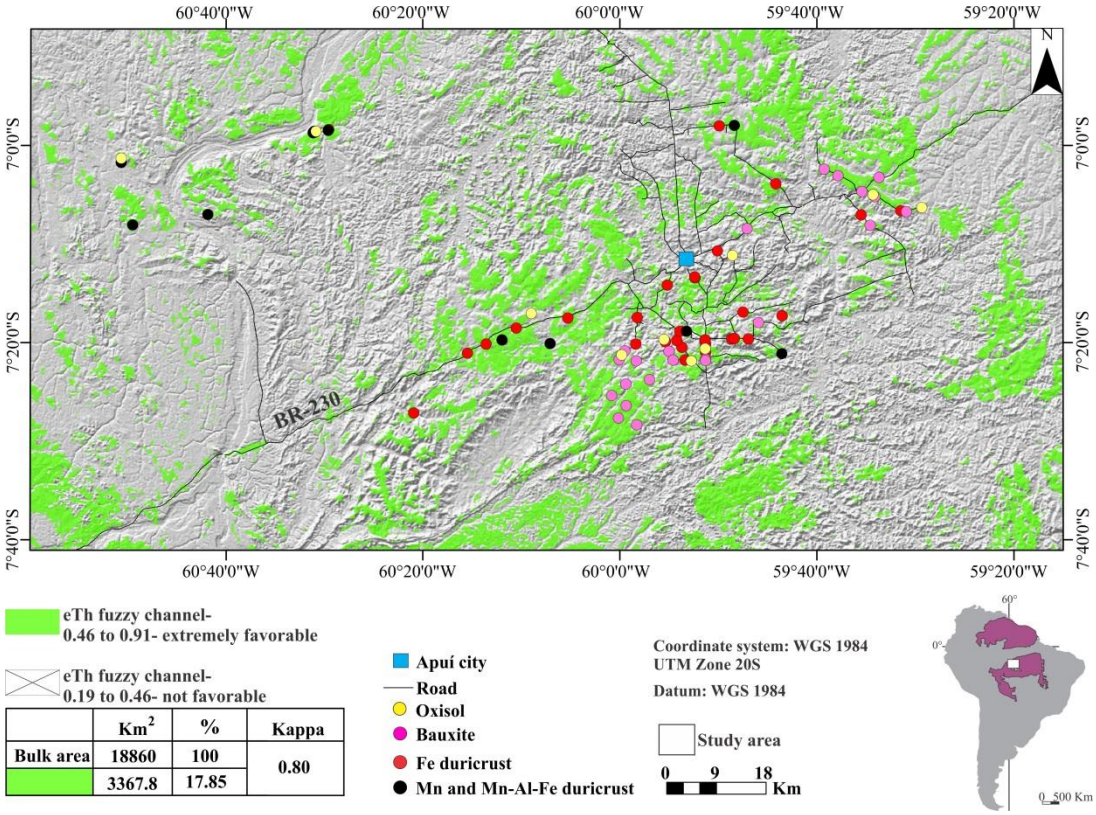

	Km²	%	Kappa
Bulk area	18860	100	0.80
	3367.8	17.85	

Figure 6: Predictability map of lateritic crust occurrence based on eTh Fuzzy divided into 10 classes, of which only the class 0.46 and 0.91 is extremely favorable.

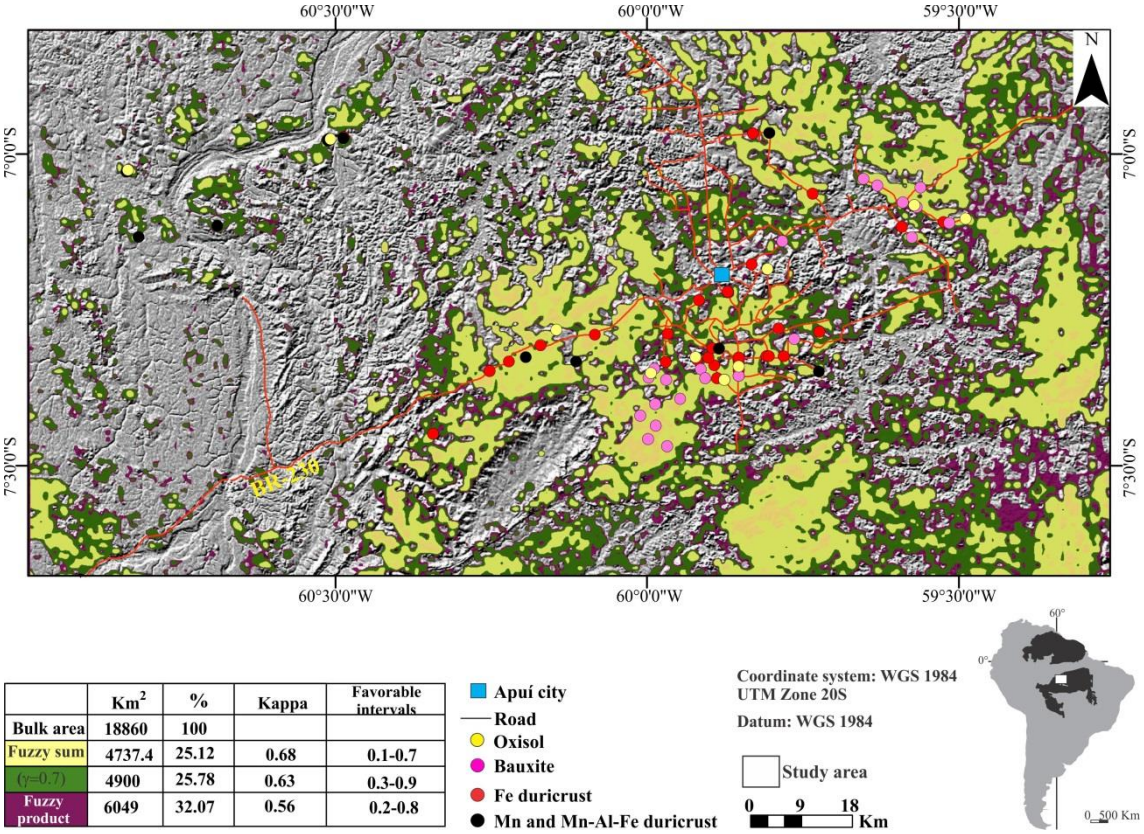

	Km²	%	Kappa	Favorable intervals
Bulk area	18860	100		
Fuzzy sum	4737.4	25.12	0.68	0.1-0.7
(γ=0.7)	4900	25.78	0.63	0.3-0.9
Fuzzy product	6049	32.07	0.56	0.2-0.8

Figure 7: Predictability map of lateritic crust occurrence based on overlap of the Fuzzy product, sum and gamma operator (γ=0.7) in order to compare each one of them.

Table 2: All data presented according the agreement with the Boolean and Fuzzy models.

Rocks + spodosols in agreement CPRM (2006) data + present study	Rocks+ spodosols in disagreement CPRM (2006) data + present study	Laterites and oxisols in agreement	Laterites and Oxisols in disagreement	Kappa index (Kp)
Boolean				
624	236	8 oxisols (80%) 20 bauxites (87%) 13 Mn duricrusts (81.3%) 20 Fe duricrusts (66.7%) Σ= 61	2 oxisols (20%) 3 bauxites (13%) 3 Mn duricrusts (18.7%) 10 Fe duricrusts (33.3%) Σ =18	0.61
eTh Fuzzy				
723	127	8 oxisols (80%) 23 bauxites (100%) 14 Mn duricrusts (87.5%) 14 Fe duricrusts (46.6%) Σ=59	2 oxisols (20%) 0 bauxites 2 Mn duricrusts (12.5%) 16 Fe duricrusts (53.4%) Σ=20	0.80
Fuzzy product				
608	252	7oxisols (70%) 21 bauxites (91.3%) 14 Mn duricrusts (87.5%) 13 Fe duricrusts (43.3%) Σ=55	3 oxisols (30%) 2 bauxites (8.7%) 2 Mn duricrusts (12.5%) 17 Fe duricrusts (56.7%) Σ=24	0.56
Fuzzy Sum				
668	192	7 oxisols (70%) 19 bauxites (82.6%) 13 Mn duricrusts (81.3%) 12 Fe duricrusts (40%) Σ=51	3 oxisols (30%) 4 bauxites (17.4%) 3 Mn duricrusts (18.7%) 18 Fe duricrusts (60%) Σ=28	0.68
Fuzzy gamma (0.7)				
645	215	7 oxisols (70%) 19 bauxites (82.6%) 14 Mn duricrusts (87.5%) 13 Fe duricrusts (43.3%) Σ=53	3 oxisols (30%) 4 bauxites (17.4%) 2 Mn duricrusts (12.5%) 17 Fe duricrusts (46.6%) Σ=26	0.63

5 PERSPECTIVES of AGRS FOR MINERAL TARGETS: MANGANESE, BAUXITE, PHOSPHOROUS AND GOLD+SULPHIDES

The combination between eTh Fuzzy (Kp=0.8), ternary map of K, eTh and eU on the RGB channels, elevation (TIN), stratigraphy, soil map and geochemical data allowed providing some interesting perspectives for regolith mapping and thus for mineral researches in weathering deposits. The most favorable areas indicated by the combination of stratigraphy, eTh Fuzzy and elevation (SP1- 0 to 134m), have provided a 100 Km^2 of lateritic duricrust target areas (light blue colored areas in the Fig.8A) surrounding the Mn deposits (Albuquerque et al. 2017). The altitude over 186 m was discarded for Mn in this model, since the Mn is mostly related to colluviums.

The same combination of parameters used to identify potentially Mn duricrusts, indicate 701 Km^2 favorable for bauxite at surface SP3 (186-290m altitude) (Fig.8A). However, this area may be smaller, once all bauxites checkpoints are related to oxisol type in the soil map (Fig.8B). Moreover, the main Amazonian bauxites (Paragominas, Porto Trombetas, Juruti and Rondon do Pará) deposits are covered by oxisols (Boulangé and Carvalho 1997, Lucas 1997, Kotschoubey et al. 2005, Costa et al. 2014 and Oliveira et al. 2016).

Besides Mn and bauxites, there are other clues that need better investigation for phosphor in duricrust and sandstone, and Au+sulphides. An area of 82.94 Km^2 close to Jatuarana river on phosphatic sandstones framed into Alto Tapajós Group (up 7.44% of P_2O_5 as Liberatore et al., 1972 and Araújo et al., 1976), in altitude of 134-290 m, was

inferred from eTh Fuzzy for the occurrence of duricrust (Fig 8 A and 8B) that is probably phosphatic.

Some duricrusts samples have anomalous contents of Au, Au+Pb+Cu and Pb+Cu and even preserved gold nuggets as seen in the massive bauxite (Bx) and Fe duricrust (C7) (Fig.8A and B, Tab.3, Fig.9). These samples are mainly framed to volcano-sedimentary rocks from Sumaúma Supergroup and related Mn duricrusts, massive bauxites and Fe duricrusts (Tab.3; Fig.8A) where Albuquerque et al. (2017) identified hydrothermal influence. These anomalous Au, Au+Pb+Cu and Pb+Cu values in duricrust may be useful tool for identified VMS deposits like those described by Carvalho and Figueiredo (1982), Leite et al. (2005) and Brito et al. (2010) in the region. The most susceptible area to VMS occurrence is located where crops out massive bauxite and Fe massive duricrust (Bx and C7, respectively) developed of a volcano-sedimentary sequence, such as related by Brito et al. (2010) in Nova Aripuanã gold mine, located 175 Km northern of Apuí city.

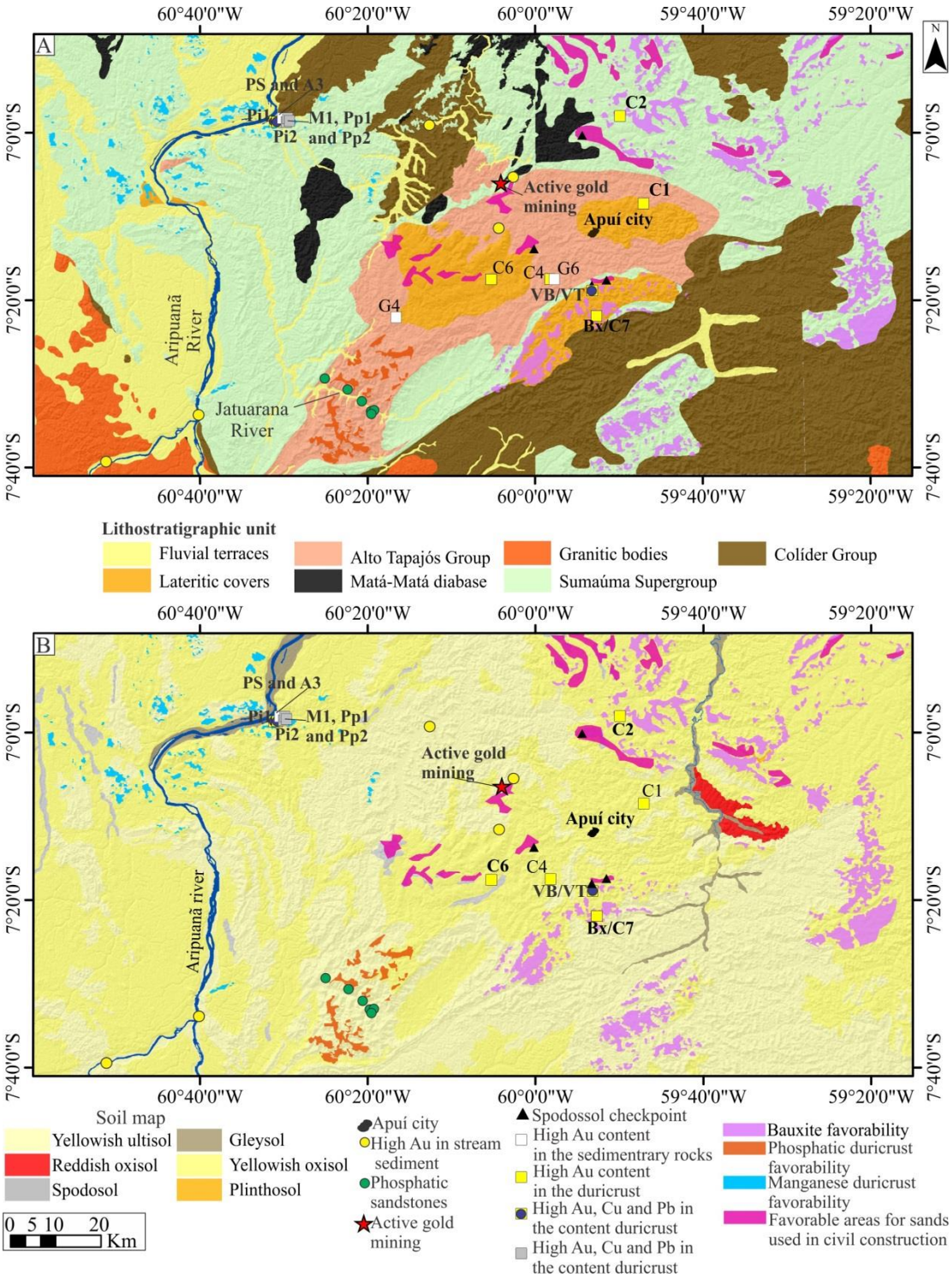

Figure 8: Favorability maps of mineral occurrence. A- Favorable areas to mineral occurrence over geological map (Modified from CPRM, 2013; 2014 and 2015). B- Favorable areas to mineral occurrence over soil map (IBGE- Brazilian Institute of Geography and Statistics, and SIPAM- Amazon Protection System database)

Table 3: Anomalous Au, Cu and Pb content (greyish), together with sulphides occurrences in the sedimentary rocks and duricrusts. *The Au content is presented only in this paper

Type	Sample	Au (ppb)	Cu (ppm)	Pb (ppm)	Sulphides	Author
Sedimentary rocks and lateritic duricrusts related to Alto Tapajós Group						
Fe duricrust	C1	1370	<50	<130	N.I	Albuquerque and Horbe (2015)
Fe duricrust	C6	1290	<50	<130	N.I	Albuquerque and Horbe (2015)
Fe duricrust	C4	2200	<50	<130	N.I	Albuquerque and Horbe (2015)
Greywacke	G6	160	<50	<130	N.I	Albuquerque and Horbe (2015)
Greywacke	G4	230	<50	<130	N.I	Albuquerque and Horbe (2015)
Sedimentary rocks and lateritic duricrusts related to Sumaúma Supergroup						
Fe duricrust	C2	5310	<50	<130	N.I	Albuquerque and Horbe (2015)
Fe duricrust	C7	42990	<50	<130	N.I	Albuquerque and Horbe (2015)
Bauxite	Bx	1320	<50	<130	N.I	Albuquerque and Horbe (2015)
Mn-Al-Fe duricrust	VB	1260	<50	2180	X	Albuquerque et al. (2017)
Mn-Al-Fe duricrust	VT	290	<50	1141	X	Albuquerque et al. (2017)
Mn-Al-Fe duricrust	Pi2	560	261	495	X	Albuquerque et al. (2017)
Mn-Al-Fe duricrust	Pi1	280	2702	14100	X	Albuquerque et al. (2017)
Mn duricrust	Pp2	<100	3579	4391	X	Albuquerque et al. (2017)
Mn duricrust	Pp1	<100	3412	292	X	Albuquerque et al. (2017)
Mn duricrust	M1	<100	1643	5001	X	Albuquerque et al. (2017)
Mn greywacke	A3	<100	2016	17200	X	Albuquerque et al. (2017)
Pinkish siltstone	PS	<100	1446	43638	N.I	Albuquerque et al. (2017)

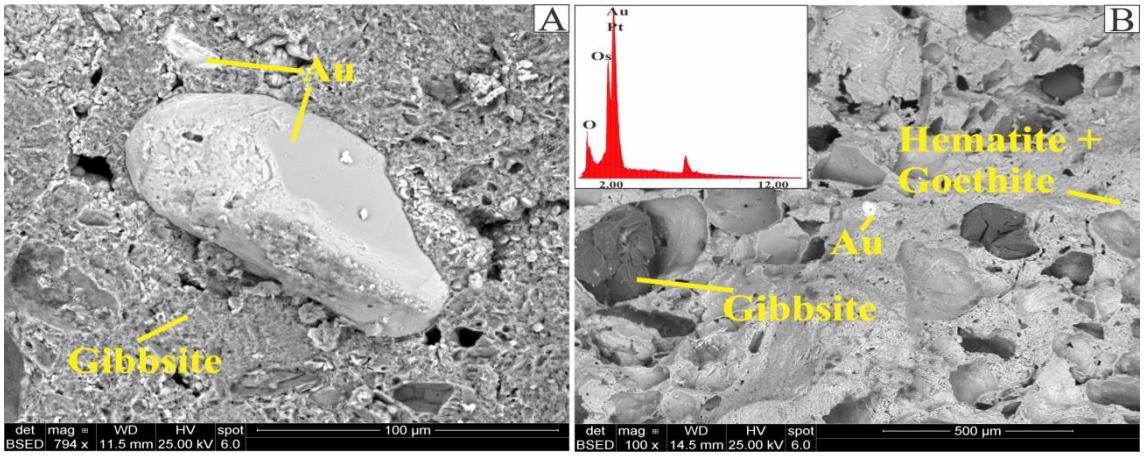

Figure 9: Gold nuggets widespread in lateritic duricrusts. A and B- Small nuggets of found at massive bauxite and Fe-duricrust (Bx and C7), respectively, derived from volcanic rocks of Vila do Carmo Group (Sumaúma Supergroup) and EDS with ratifying the Au occurrence

6 CONCLUSIONS

The application of airborne gamma ray spectrometry using the K, U and Th channels allow identify lateritic duricrust and oxisols, regardless whether it is Mn, Mn-Al-Fe, bauxite, Fe or Fe-Al duricrust types. The Boolean and Fuzzy models displayed good correlation with bauxites, Mn and Mn-Al-Fe duricrusts and oxisols. The main difference between both models is that the Boolean recognized 20% more Fe duricrusts than the Fuzzy models, while the Fuzzy models discarded ironstones located in the western portion of the area, since they does not have relationship with lateritization, therefore they have most useful in geological mapping.

The combination between eTh fuzzy, ternary map of K, eTh and eU on the RGB channels, geological and soil map database and some chemical analysis aid to improve the knowledge of futures researches concerning supergene deposits as bauxites,

manganese and phosphatic duricrusts. Also, anomalous contents of Au, Cu and Pb together with Au nuggets found in lateritic duricrusts, serve as pathfinder for gold and sulphides deposits.

7 ACKNOWLEDGMENTS

The authors thank to the Postgraduate Program in Geology from the University of Brasilia, to CAPES for granting a PhD scholarship to the first author and CNPq for financial support (process n ° 471971/2010-3 and 473359/2012) and research grants of the second and third authors.

8 REFERENCES

Albuquerque, M.F.S., Horbe, A.M.C., 2015. Mineralogia, geoquímica e evolução da lateritização em Apuí, sudeste do Amazonas. Braz. J. Geol. 45, 569–590.

Albuquerque, M.F.S., Horbe, A.M.C., Botelho, N.F., 2017. Genesis of manganese deposits in southwestern Amazonia: Mineralogy, geochemistry and paleoenvironment. Ore Geol. Rev, 89, 270–289

An, P., Moon,W.M., Rencz, A., 1991. Application of Fuzzy set theory to integrated mineral exploration. Can. J. Expl. 27 (1), 1–11.

Anand, R.R., Butt, C.R.M. 2010. A guide for mineral exploration through the regolith in the Yilgarn Craton, Western Australia. Australian Journal of Earth Sciences. 57, 1015–1114.

Araújo J.F.V., Montalvão R.M.G., Lima M.I.C., Fernandes P.E.C.A., Cunha F.M.B., Fernandes C.A.C., Basei M.A.S. 1976. Geologia da Folha SA.21 – Santarém. In: BRASIL, DNPM. Projeto RADAMBRASIL. Cap. I

Beauvais, A., Ruffet, G., Hécnoque, O., Colin, F. 2008. Chemical and physical erosion rhythms of the West African Cenozoic morphogenesis: The 39Ar-40Ar dating of supergene K-Mn oxides. Journal of geophysical research, 113.

Behrens, T., Förster, H., Scholten, T., Steinrücken, U., Spies, E.-D., Goldshmitt, M., 2005. Digital soil mapping using artificial neural networks. Journal of Plant Nutrition and Soil Science 168, 1-13.

Betiollo, L.M., Reis N.J., Almeida, M.E., Bahia, R.C., Splendor, F., Costa, U.P., Luzardo, R., 2009. Magmatismo Máfico, Calimiano (Sill Mata-Matá), rio Aripuanã, Amazonas- Implicações Geológicas. In: XI Simpósio de Geologia da Amazônia, Resumos Expandidos.

Bonham-Carter, G.F., 1994. Geographic Information Systems for Geoscientists: Modelling with GIS. Computer Methods in the Geosciences. 13. Pergamon Publications, Oxford.

Bonnet, N.J., Beauvais, A., Arnaud, N., Chardon, D., Jayananda, M. 2014.First 40Ar/39Ar dating of intense Late Palaeogene lateritic weathering in Peninsular India. Earth and Planetary Science Letters, 386: 126–137

Boulangé B. & Carvalho A.1997. The Bauxite of Porto Trombetas. In: Carvalho A., Boulangé B., Melfi A.J., Lucas Y (eds.) Brazilian bauxites. São Paulo, USP/FAPESP/ORSTOM., p. 55-73.

Braghin, M.A., 1998. Utilização das lógicas Booleanas e Fuzzy para análise metalogenética na Folha Pilar do Sul (SP) via sistemas de informações geográficas. Master degree, Campinas, Brazil. Universidade Estadual de Campinas, p. 148.

Brito, R.S., Silveira, F.V., Larizzati, J. H., 2010. Metalogenia do distrito aurífero do rio Juma- Nova Aripuanã-AM. Informe recursos minerais. Série Ouro, 17, CPRM-Brasília, 35 p.

Carrino, T.A., Silva, A.M., Botelho, N.F., da Silva, A.A.C., 2011. Discriminação de áreas de espesso regolito do leste do Estado do Amazonas usando estatística multivariada, algoritmo hiperespectral e modelagem de dados espaciais. Rev. Bras. Geofis. 29 (1), 155–172.

Carvalho, M.S., Figueiredo, A.J., 1982. Caracterização Litoestratigráfica da Bacia de Sedimentação do Grupo Beneficente no Alto Rio Sucundurí-AM. 1st Amazon Geology Symposium, Belém, Brazil, Extended Abstracts, pp. 26–44.

Cohen, J., 1960. A coefficient of agreement of nominal scales. Educ. Psychol. Meas. 20 (1), 37–46.

Colin, F., Beauvais, A., Ruffet, G., Hécnoque, O. 2005. First 40Ar/39Ar geochronology of lateritic manganiferous pisolites:Implications for the Palaeogene history of a West African landscape. Earth and Planetary Science Letters, 238: 172– 188

Cook, S.E., Corner, R.J., Groves, P.R., Grealish, G.J., 1996. Use of airborne gammaradiometric data for soil mapping. Australian Journal of Soil Research 34, 183–194.

Costa, M.L. 1997. Lateritization as major process of ore deposit formation in the Amazon Region. Exploration Mining Geology 6:79-104.

Costa, M.L., Cruz , G.C., Almeida, H.D.F., Poellmann, H., 2014.On the geology, mineralogy and geochemistry of the bauxite-bearing regolith in the lower Amazon basin: Evidence of genetic relationships. Journal of Geochemical Exploration 146 (2014) 58–74

CPRM, 2013. Folha Sumaúma (SB.20-Z-D). Programa Geologia do Brasil. Carta geológica ao milionésimo-Escala 1:250.000. CPRM, Serviço Geológico do Brasil, Manaus.

CPRM, 2014. Geologia e recursos minerais da Folha Sumaúma – SB.20-Z-D, Estado do Amazonas, escala 1:250.000. CPRM, Serviço Geológico do Brasil, Manaus. Programa Geologia do Brasil – PGB. Levantamentos Geológicos Básicos do Brasil.

CPRM. 2006. Mapa Geológico do Estado do Amazonas. Geologia e recursos minerais do Estado do Amazonas. Sistemas de Informações Geográficas – SIG, Programa Geologia do Brasil. Escala 1: 1.000.000, Ministério de Minas e Energia. Rio de Janeiro. 1 CD-ROM. Programa Geologia do Brasil.

CPRM., 2015. Geologia e recursos minerais da Folha Sumaúma – SB.20-Z-D, Estado do Amazonas, escala 1:250.000. CPRM, Serviço Geológico do Brasil, Manaus. Programa Geologia do Brasil - PGB. Levantamentos Geológicos Básicos do Brasil.

Dantas, M.E., Maia, M.A.M. 2010. Compartimentação Geomorfológica. In: Maia, M.A.M & Marmos, J.L. (orgs). Geodiversidade do Estado do Amazonas. CPRM: Manaus, p. 27-44.

Dauth, C., 1997. Airborne Magnetic, Radiometric and Satellite Imagery for Regolith Mapping in the Yilgarn Craton of Western Australia. Exploration Geophysics. 28, 199-203

Dickson, B.L., Scott, K.M., 1997. Interpretation of aerial gamma-ray surveys - adding the geochemical factors. AGSO J. Aust. Geol. Geophys. 17 (2), 187–200.

Gunn, P.J., Minty, B.R.S., Milligan, P. R. 1997. The Airborne GammaRay Spectrometric Response Over Arid Australian Terranes. In: GUBINS AG (Ed.).

Proceedings of Exploration 97: Fourth Decennial International Conference on Mineral Exploration. Australia, p. 733–740

Herrera, I.L.I.E., Silva Filho, E.P., Iza, E.R.H.F., Horbe, A.M.C., Santos, S.L.M., Cabral, L.N., 2017. Técnica Booleana aplicada à identificação de crostas lateríticas no sudoeste da Amazônia brasileira Rev. Bras. Geomorfol. 18 (2), 411-425

Horbe, A.M.C., Costa, M.L., 2005. Lateritic crusts and related soils in eastern BrazilianAmazonia. Geoderma, 126, 225–239.

http://geowebapp.cprm.gov.br/ViewerWEB/index_lito_250k.html

Isles, D., Rankin, L., 2000. Geological interpretation and exploration targeting from aeromagnetic data. Apostila de Workshop. Brasília, ADIMB, 220 p.

Iza, E.R.H.F., Horbe, A.M.C., Silva, A.M., 2016., Boolean and Fuzzy methods for identifying lateritic regoliths in the Brazilian Amazon using gamma-ray spectrometric and topographic data. Geoderma, 269, 27–38

Landis, J.R., Koch, G.G., 1977. The measurement of observer agreement for categorical data. Biometrics, 33 (1), 159-174.

Leite, J.A.D., Sousa, M.Z.A., Saes, G.S., Macambira, M.J.B., Xavier, R.P., Siqueira, A.J., Batata, M.E.F., Oliveira, F.A., Silva Jr, J.G., Quadros, A.P., 2005. Caracterização do Depósito Polimetálico (Zn, Pb, Ag, Cu-Au) de Aripuanã, Mato Grosso. In: Marini, O. J., Queiroz, E. T., and Ramos, B.V. (Eds.), Caracterização de depósitos minerais em distritos mineiros da Amazônia, Brasilia, Departamento Nacional de Producao Mineral, Fundo Setorial de Recursos Minerais-Agencia para Desenvolvimento Técnico da Industria Mineral Brasileira (ADIMB), pp. 601–686.

Liberatore, G., Alecrim, J.D., Medeiros, J.B., Malouf, R.F., Pinheiro, S.S., Achão, S.M., Santos, J.O.S., 1972. Projeto Aripuanã – Sucundurí, DNPM/CPRM, Manaus.

Lucas Y. 1997. The bauxite of Juriti. In: Carvalho A., Boulangé B., Melfi A. J., Lucas Y (eds.). Brazilian Bauxites. São Paulo, USP/FAPESP/ORSTOM, p.107-133.

Minty, B.R.S., 1997. Fundamental of airborne gamma-ray spectrometry. AGSO J. Aust. Geol. Geophys. 17, 39–50.

Monteiro, H.S., Vasconcelos, P.M., Farley K. A, Spier., C. A., Mello, C.L. 2015. (U–Th)/He geochronology of goethite and the origin and evolution of cangas. Geochimica et Cosmochimica Acta, 131: 267–289.

Moonjun, R., Shrestha, D.P.,Jettena, V. G., Ruitenbeek, F.A.J.V., 2017. Application of airborne gamma-ray imagery to assist soil survey: A case study from Thailand. Geoderma, 289, 196–212

Motta, J.G., Faria Junior, I.R., 2016. A mineral potential mapping approach for supergene nickel deposits in southwestern São Francisco Craton, Brazil. Brazilian Journal of Geology, 46(2): 261-273,

Oliveira, S.B., Costa, M.L., Prazeres Filho, H.J., 2016. The lateritic bauxite deposit of Rondon do Pará: A new giant deposit in the Amazon region, northern Brazil. Economic Geology. 111, 1277–1290

Reis, N.J., Bahia, R.B.C., Almeida, M.E., Costa, U.A.P., Betiollo, L.M., de Oliveira, A.C., Splendor, F., 2013. O supergrupo Sumaúma no contexto geológico da Folha SB.20-Z-D (SUMAÚMA), sudeste do Amazonas: modo de ocorrência, discussão de idades em zircões detríticos e correlações no SW do Cráton do Amazonas. In: Wankler, F.L., Holanda, E.C., Vasques, M.L. (Eds.), Contribuições à Geologia da Amazônia, Belém, pp. 199–222.

Riffel, S.B., Vasconcelos, P.M.,Carmo, I.O., Farley, K.A., 2015. Combined 40Ar/39Ar and (U–Th)/He geochronological constraints on long-term landscape evolution of

the Second Paraná Plateau and its ruiniform surface features, Paraná, Brazil. Geomorphology. 233, 52-63.

Santos, J.O.S., 2003. Geotectônica dos Escudos das Guianas e Brasil Central. In: Bizzi, L.A., Schobbenhaus, C., Vidotti, R.M., Gonçalves, J.H. (Eds.). Geologia, Tectônica e Recursos Minerais Minerais do Brasil: texto, mapas e SIG. CPRM-Serviço Geológico do Brasil, pp. 169–226.

Santos, J.O.S., Hartmann, L.A., Faria, M.S.G. de, Riker, S.R.L., Souza, M.M. de, Almeida, M.E., McNaughton, N.J., 2006. A compartimentação do Cráton Amazonas em Províncias: Avanços ocorridos no período 2000–2006. In: SBG-Núcleo Norte, Simp. Geol. Amaz., 9, Belém, PA, Resumos Expandidos.CD-Rom.

Spier, C.A., Vasconcelos, P.M., Oliveira, S.M.B. 2006. $^{40}Ar/^{39}Ar$ geochronological Constraints on the evolution of lateritic iron deposits in the Quadrilátero Ferrífero, Minas Gerais, Brazil. Chemical Geology, 234: 79–104.

Taylor, M.J., Smettem, K., Pracilio, G., Verboom, W.H., 2002. Investigation of the relationships between soil properties and high resolution radiometrics, central eastern Wheat belt, Western Australia. Exploration Geophysics 33, 95–102.

Wilford, J., 2012. A weathering intensity index for the Australian continent using airborne gamma-ray spectrometry and digital terrain analysis. Geoderma 183–184, 124–142.

Wilford, J.R., 1995. Airborne gamma-ray spectrometry as a tool for assessing relative landscape activity and weathering development of regolith, including soils. AGSO Research Newsletter 22, 12–14.

Wilford, J.R., Bierwirth, P.N., Craig, M.A., 1997. Application of airborne gamma-ray spectrometry in soil/regolithmapping and applied geomorphology. J. Aust. Geol. Geophys. 17 (2), 201–216.

Zimmermann, H. J., Zysno, P., 1980. Latent connectives in human decision making Fuzzy Sets and Systems, 37-51

CAPÍTULO VII: APRESENTAÇÃO DE DADOS E DISCUSSÕES DA GEOCRONOLOGIA (U-Th)/He

8 GEOCRONOLOGIA (U-Th)/He

As amostras selecionadas para datação por (U-Th)/He, bauxita pisolítica (B1A) do perfil P5 e crosta Fe-Al (C6) do perfil P6, ocupam relevo mais elevado (180 a 225 m) e extremamente dissecado, onde predominam platôs e colinas com topo ondulado devido à incisão de grandes rios como Juma e Acari, por exemplo (Figura 9A). Afloram como grandes blocos com até 2 m de espessura e, geralmente, estão recobertos por latossolo amarelo com até 1 m de espessura.

A bauxita pisolítica (B1A), formada a partir das rochas sedimentares do Supergrupo Sumáuma têm gibbsita (43%), goethita+hematita (29%) e caulinita (15%) como principais constituintes mineralógicos, e quartzo (9%) e anatásio+rutilo (4%) como subordinados (Figura 9B). Os pisólitos, que perfazem até 30% da crosta, são marrom avermelhados, friáveis e compostos por hematita e Al-goethita com até 2,5 cm de diâmetro (Figura 10A). Eles são envolvidos por diversas gerações de filmes goethíticos que, por sua vez, são sustentados por plasma gibbsítico (60% da crosta) poroso, rosado, por vezes esbranquiçado com tons avermelhados (Figura 10A e B). Há cavidades preenchidas por caulinita e grãos de quartzo tamanho areia fina.

A crosta Fe-Al (C6) oriunda das rochas sedimentares do Grupo Alto Tapajós é composta por goethita+hematita (57%) e caulinita (27%) como principais fases minerais, com gibbsita (12%), quartzo (4%) e rutilo (<1%) subordinados (Figura 9C). Nos fragmentos avermelhados de hematita com até 2 cm de diâmetro, há grãos angulosos de gibbsita com até 200µm de comprimento recobertos por sutis filmes de hematita (Figura 10C, D e E). O arcabouço argilo-arenoso (45–55%) alaranjado de composição goethíto-caulínitica sustenta os fragmentos avermelhados de hematita, e neles há diversas inclusões de gibbsita, zircão e, por vezes, quartzo (Figura 10F).

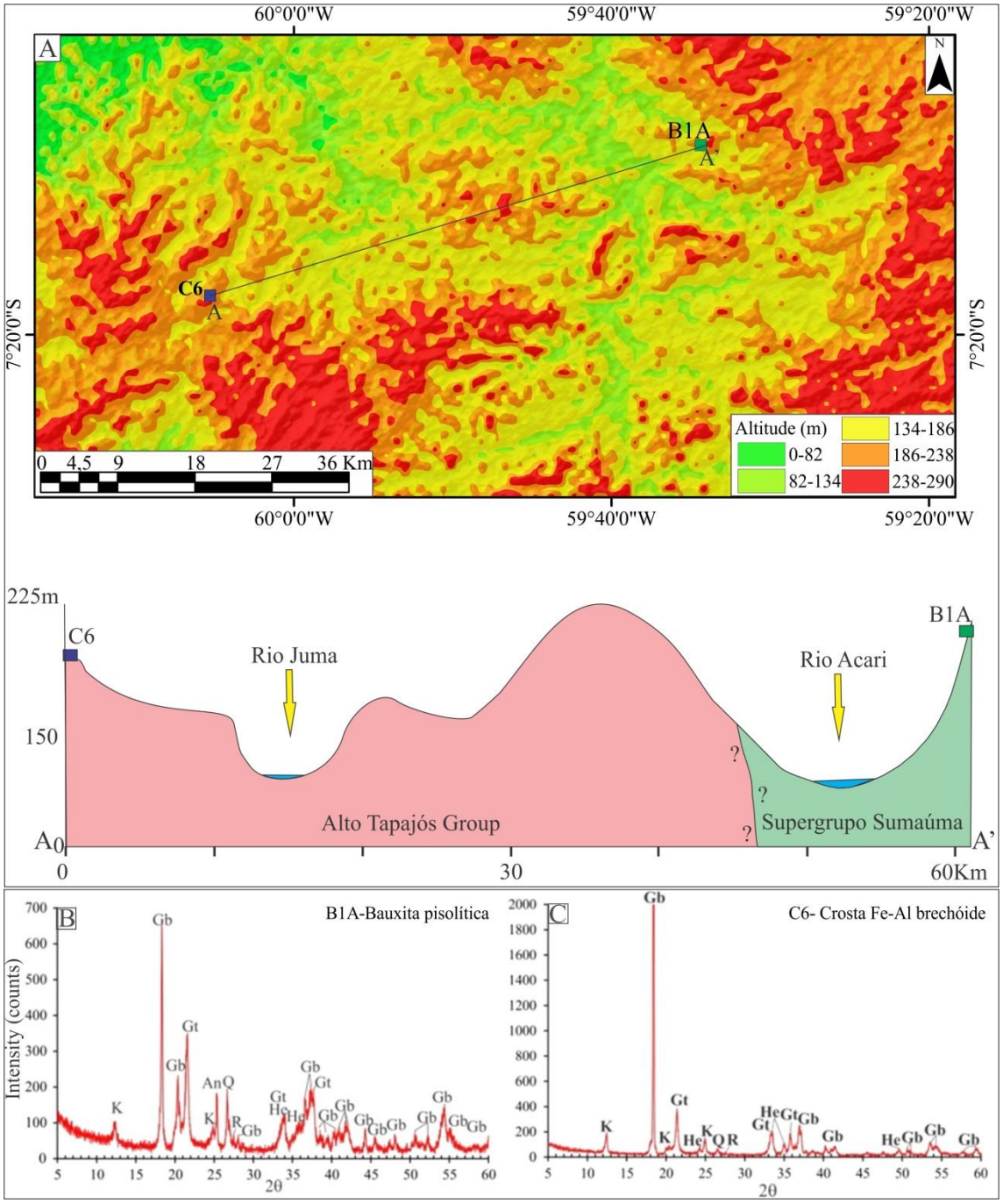

Figura 9: Mapa mostrando a posição altimétrica das amostras datadas por (U-Th)/He, bem como perfil topográfico e substrato rochoso. B e C- Composição mineralógica obtida por meio de difratometria por raios-X. K- caulinita. Gb-gibbsita. Gt-goethita. An- anatásio. R-rutilo. Q-quartzo. He-hematita.

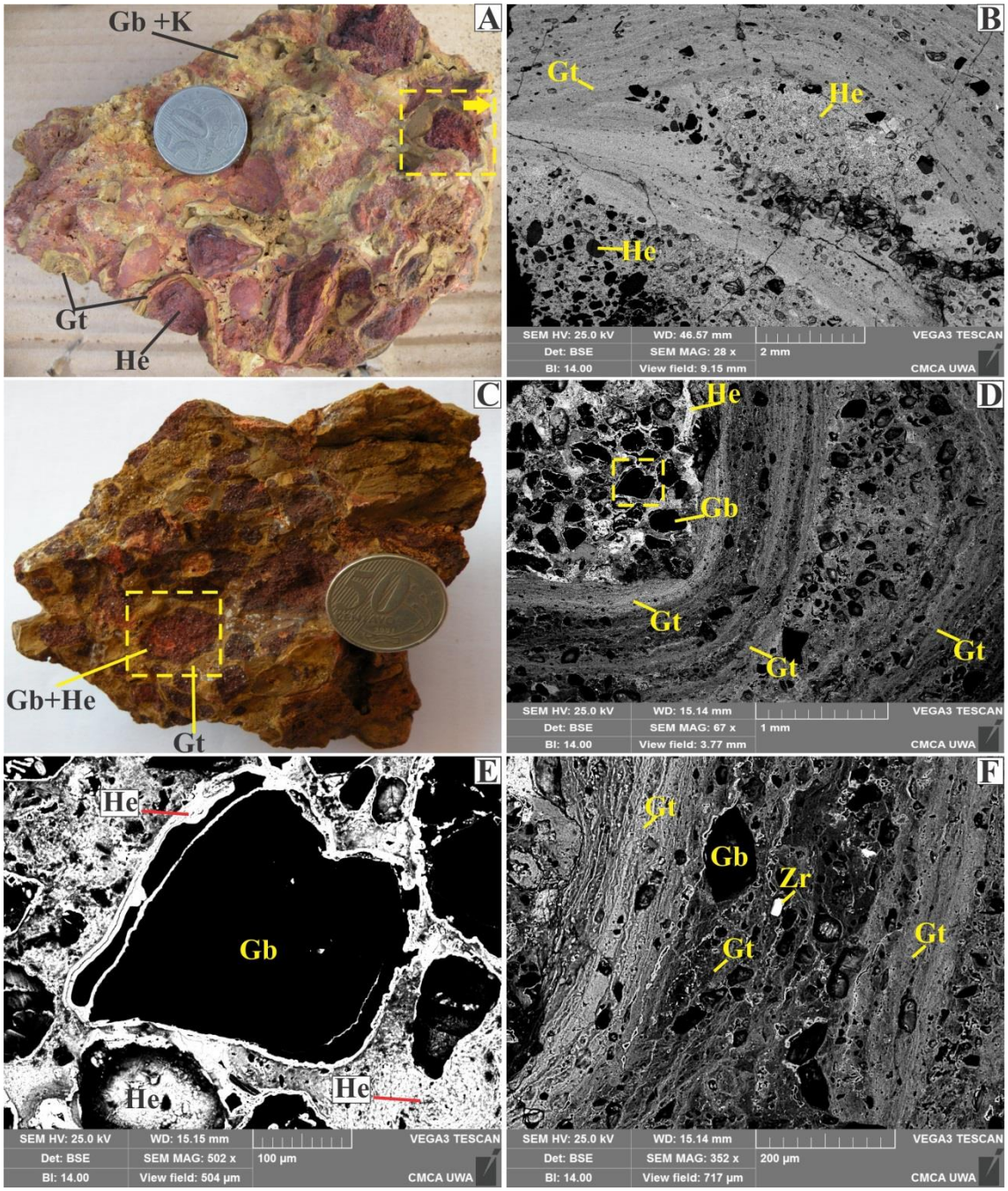

Figura 10: Principais aspectos macroscópicos e microscópicos das amostras analisadas. A- Bauxita pisolítica (B1A) composta por pisólitos de hematita (He), cortéx de goethita (Gt) e plasma de gibbsita (Gb) e caulinita (K). Em amarelo o detalhe da foto B. B- Relação de contato entre o pisólito hematítico e diversas gerações de goethita. C- Crosta Fe-Al (C6) composta por pisólitos de hematita e gibbsita. Em amarelo detalhe da foto D. D- Detalhe do núcleo e borda do pisólito. E- Diminutos gãos angulosos de gibbsita nos núcleos do pisólito. F- Cortéx goethítico com inclusões de gibbsita e zircão (Zr).

Os resultados de (U-Th)/He estão sumarizados na Tabela 5. Como esperado, as hematitas que compõem o núcleo dos pisólitos são mais antigas que as goethitas dos cortéx. No entanto, há diferenças significativas entre os núcleos de hematita e os cortéx de goethita. Enquanto as hematitas da bauxita pisolítica têm intervalos de formação bem demarcados entre 18,7 a 28,4 Ma; aquelas da crosta Fe-Al (C6) são mais antigas e destacam três intervalos de formação de hematita em 144,1 a 292 Ma. Os múltiplos filmes de goethita da bauxita e da crosta Fe-Al apresentam correlação temporal com início de formação em 13.1-14.9 Ma, após isso houve três episódios de precipitação de goethita em 16,2-17,2 Ma; 18.9-20,8 Ma e 22,5 Ma. Em média os erros analíticos das hematitas da bauxita e da crosta Fe-Al são de ± 2,4 e ± 20,4 Ma, respectivamente; enquanto que das goethitas giram em torno de 1,7 e 1,8 Ma.

O conteúdo médio de $He_{(ncc)}$ nas amostras varia de 0,432 a 2,536 ncc nas hematitas e entre 0,542 a 1,015 nas goethitas. A razão média Th/U apresenta grande variação nas hematitas (3,05 a 16,05), enquanto que nas goethitas esta variação é menor (8,21 a 8,85) (Tabela 4). De modo geral o conteúdo de He nas goethitas e hematitas são maiores nas amostras mais antigas como nas hematitas da crosta C6, por outro lado, menores valores de Th/U estão relacionados a hematitas mais antigas. Tal relação, Th/U vs idade, não é perceptível nas goethitas (Figura 11A, B, C e D).

Tabela 5: Resultados da datação (U-Th)/He em goethitas e hematitas.

Componente	Mineral	Amostra	$^{232}Th_{(ng)}$	$\pm_{(\%)}$	$^{238}U_{(ng)}$	$\pm_{(\%)}$	$He_{(ncc)}$	$\pm_{(\%)}$	$TAU_{(\%)}$	Th/U	Idade (Ma)	$\pm1\sigma_{(Ma)}$
Bauxita pisolítica desenvolvida sobre o Supergrupo Sumaúma (Amostra B1A)												
Pisólito	Hematita	B1A	0,335	1,5	0,091	2,0	0,587	0,9	1,6	3,67	28,4	2,9
Pisólito	Hematita	B1A	0,329	2,2	0,047	2,6	0,419	1,1	2,0	6,97	27,7	2,8
Pisólito	Hematita	B1A	0,353	2,2	0,069	2,5	0,458	1,1	2,0	5,09	24,7	2,5
Pisólito	Hematita	B1A	0,606	1,5	0,010	2,3	0,395	1,0	1,8	57,60	21,2	2,2
Pisólito	Hematita	B1A	0,365	1,5	0,045	2,1	0,322	1,1	1,6	8,02	20,2	2,0
Pisólito	Hematita	B1A	0,599	1,5	0,040	2,0	0,411	1,1	1,7	14,97	18,7	1,9
Média	Hematita	B1A	0,431	1,7	0,050	2,3	0,432	1,1	1,8	16,05	23,5	2,4
Córtex	Goethita	B1A	2,145	1,5	0,211	2,0	1,810	0,9	1,5	10,11	20,8	2,1
Córtex	Goethita	B1A	1,586	1,5	0,168	2,0	1,358	0,9	1,5	9,40	20,6	2,1
Córtex	Goethita	B1A	1,873	1,5	0,174	2,0	1,419	0,9	1,5	10,67	18,9	1,9
Córtex	Goethita	B1A	0,876	1,5	0,114	2,0	0,519	1,1	1,6	7,62	13,3	1,3
Córtex	Goethita	B1A	0,613	1,5	0,079	2,0	0,363	1,1	1,6	7,66	13,3	1,4
Córtex	Goethita	B1A	1,073	2,2	0,139	2,6	0,623	1,0	2,0	7,65	13,1	1,3
Média	Goethita	B1A	1,361	1,6	0,148	2,1	1,015	1,0	1,6	8,85	16,7	1,7
Crosta brechóide Fe-Al desenvolvida sobre o Grupo Alto Tapajós (Amostra C6)												
Pisólito	Hematita	C6	0,195	1,6	0,055	2,0	3,640	0,9	1,6	3,54	292,0	29,6
Pisólito	Hematita	C6	0,120	1,6	0,036	2,0	1,931	0,9	1,6	3,31	242,3	24,6
Pisólito	Hematita	C6	0,177	2,2	0,034	2,6	1,829	0,8	1,9	5,19	196,5	20,0
Pisólito	Hematita	C6	0,127	1,6	0,060	2,0	1,883	0,9	1,7	2,11	169,8	17,2
Pisólito	Hematita	C6	0,162	1,6	0,078	2,0	2,322	0,9	1,7	2,07	162,7	16,5
Pisólito	Hematita	C6	0,286	1,5	0,137	2,0	3,612	0,8	1,7	2,07	144,1	14,6
Média	Hematita	C6	0,178	1,7	0,067	2,1	2,536	0,9	1,7	3,05	201,2	20,4
Córtex	Goethita	C6	0,613	1,5	0,081	2,1	0,619	1,0	1,6	7,47	22,5	2,3
Córtex	Goethita	C6	0,562	2,2	0,057	2,5	0,396	1,2	2,1	9,76	17,2	1,8
Córtex	Goethita	C6	0,780	1,5	0,106	2,1	0,603	1,0	1,6	7,30	17,1	1,7
Córtex	Goethita	C6	0,846	1,5	0,097	2,1	0,596	1,0	1,6	8,68	16,6	1,7
Córtex	Goethita	C6	0,881	1,5	0,113	2,0	0,634	1,0	1,5	7,72	16,2	1,6
Córtex	Goethita	C6	0,627	2,2	0,075	2,6	0,404	1,1	2,0	8,34	14,9	1,5
Média	Goethita	C6	0,718	1,7	0,088	2,2	0,542	1,1	1,7	8,21	17,4	1,8

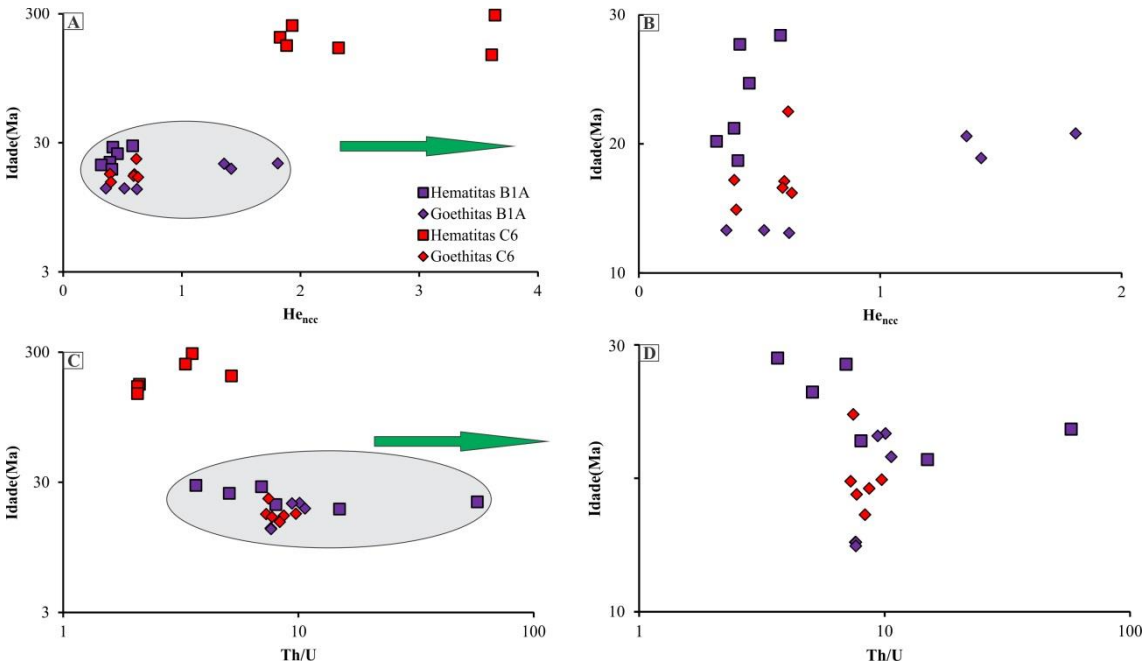

Figura 11: Relações He (ncc) vs Idade em Ma e Th/U vs idade em Ma das hematitas e goethitas datadas

8.1 Discussões das idades (U-Th)/He

O início da formação de lateritos em solos tropicais é comumente tomado como evidência de um grande evento de oxidação em 2,3 Ga, um passo importante na evolução da atmosfera da Terra (Rye & Holland, 1998; Retallack, 2010). Nesse contexto, o laterito mais antigo já catalogado em Sishen, África do Sul, data em 2,2 Ga (Gutzmer & Beukes, 1998). A formação de lateritos está condicionada também ao surgimento das florestas no Devoniano médio, uma vez que florestas tropicais produzem grandes quantidades de dióxido de carbono (CO_2), que em contato com moléculas de água resulta em ácido carbônico (H_2CO_3), um dos responsáveis por acelerar o intemperismo químico (Erhardt, 1965; Retallack, 2010). Soma-se a isto, a grande quantidade de gases estufa (metano e dióxido de carbono) nos limites Cretáceo-Terciário e Permiano-Triássico (Retallack, 2004). Esses eventos estufa do passado têm relação direta com o aumento nos níveis de metano e de dióxido carbono durante os eventos de bauxitização e lateritização (Retallack, 2002; 2009; 2010).

Segundo Tardy & Nahon (1985), Nahon (1986) e Théveniaut & Freyssinet (1999) a formação de crostas lateríticas pode ser interpretada como um modelo de multi camadas que envolvem remobilização do Fe nos pisólitos e reprecipitação de Fe como goethita. Tais fatores acarretam em agradação e degradação das crostas, de modo que formação de hematita e caulinita implicam em agradação e clima mais seco, enquanto que a geração de goethita, Al-goethita e gibbsita, aliadas à pedoturbação, apontam para

degradação, pois modificam o arcabouço original em condições mais úmidas (Beauvais, 1999, Anand & Paine, 2002, Bitom et al. 2003).

No sudeste do Amazonas, as idades U-Th/(He) obtidas em hematitas da crosta Fe-Al (C6) apontam intensa agradação de crosta ferruginosa (1° fase de agradação), num intervalo de 150 Ma que se iniciou em 292±29,6 Ma (Final Carbonífero/Início do Permiano), com intervalos bem definidos no fim do Permino/ início do Triássico e Triássico/Jurássico, e perdurou até 144,1±14,6 Ma (Final Jurássico/Início Cretáceo) (Figura 12A). Os resquícios desta crosta pretérita preservadas nos pisólitos ferruginosos indicam crosta com diminutos grãos angulosos de gibbsita (≤ 200μm) suportados por matriz hematítica maciça (Figura 10 D e E), tal qual observado por Théveniaut & Freyssinet (1999) e Bitom et al. (2003), na Guiana Francesa e Camarões. A gibbsita presente nesta crosta é anterior à formação da hematita (Final Carbonífero/Início do Permiano). Assim, o início do Carbonífero, com clima mais úmido e quente, temperatura média de 20ºC e CO_2 atmosférico médio de 1500 ppm é o cenário propício à formação de gibbsita (Berner & Kothavala, 2001).

Os diminutos grãos de gibbsita (≤ 200μm) se assemelham em tamanho e formato aos feldspatos potássicos (≥100 μm) das grauvacas do Grupo Alto Tapajós (Figura 10E, 13 A e B), o que indica que a gibbsita foi formada por intemperismo direto dos feldspatos potássicos e deu origem ao horizonte *"saprock"*, tal qual relatado por Anand & Butt (2003) na Austrália. A partir de então, o clima mais seco variando entre quente e frio perdurou do Permiano ao Triássico, e na interface Jurássico-Cretáceo tornou-se mais quente e úmido (Berner & Kothavala, 2001; Retallack, 2010), o que levou a consolidação da crosta maciça hematítica.

Relictos de crostas antigas são raros devido aos inúmeros eventos de erosão e retrabalhamento de crostas lateríticas ocasionados pelas mudanças climáticas, especialmente do fim do Cretáceo aos dias atuais, onde a formação de perfis lateríticos maturos ou imaturos foi alavancada (Costa, 1991; Retallack, 2010). Tais registros são relatados por Dammer et al (1999), Hécnoque et al. (1998), Ruffet et al. (1996), Vasconcelos et al. (1996), Théveniaut & Freyssinet (1999), Théveniaut & Freyssinet (2002), Pidgeon et al. (2004), Costa et al. (2005), Shuster et al. (2005), Spier et al. (2006), Lima (2008), Bonnet et al. (2014), Horbe (2014), Monteiro et al. (2014) e Riffel et al. (2015) via Ar-Ar, (U-Th)/He e paleomagnetismo realizadas no Brasil, Índia, Austrália, Burkina Faso. Esses dados mostram-se correlatos, e há registros marcantes de

“pulsos” da lateritização em 56, 53, 47, 40, 35, 20, 15 e 6 Ma, com algumas crostas ferruginosas com idade < 5Ma (Figura 12 A e B).

Na região sudeste do Amazonas, um segundo registro de agradação de crostas foi reconhecido pelas idades obtidas em hematitas da bauxita pisolítica (B1A), que dataram entre 28,4±2,9 e 18,7±1,9 Ma (Oligoceno médio ao início do Mioceno) (Figura 12). A partir de então, houve início da degradação das crostas ferruginosas em épocas mais úmidas que se estenderam desde o início ao fim do Mioceno (22,5±2,3 a 13,1±1,3 Ma) e proporcionaram a formação de goethita. Neste contexto, pode-se dizer que há dois intervalos distintos de formação de goethita, o primeiro entre 22,5±2,3 e 17,1±1,7 Ma e segundo entre 13,1±1,3 e 16.6 ±1,7 Ma. O primeiro está alinhado ao segundo evento de bauxitização ocorrido entre o fim do Oligoceno e início do Mioceno reconhecido por Kotschoubey et al. (2005) na região de Paragominas, Pará, apesar de Horbe (2014) via paleomagnetismo enquadra-lo entre 28 e 50 Ma.

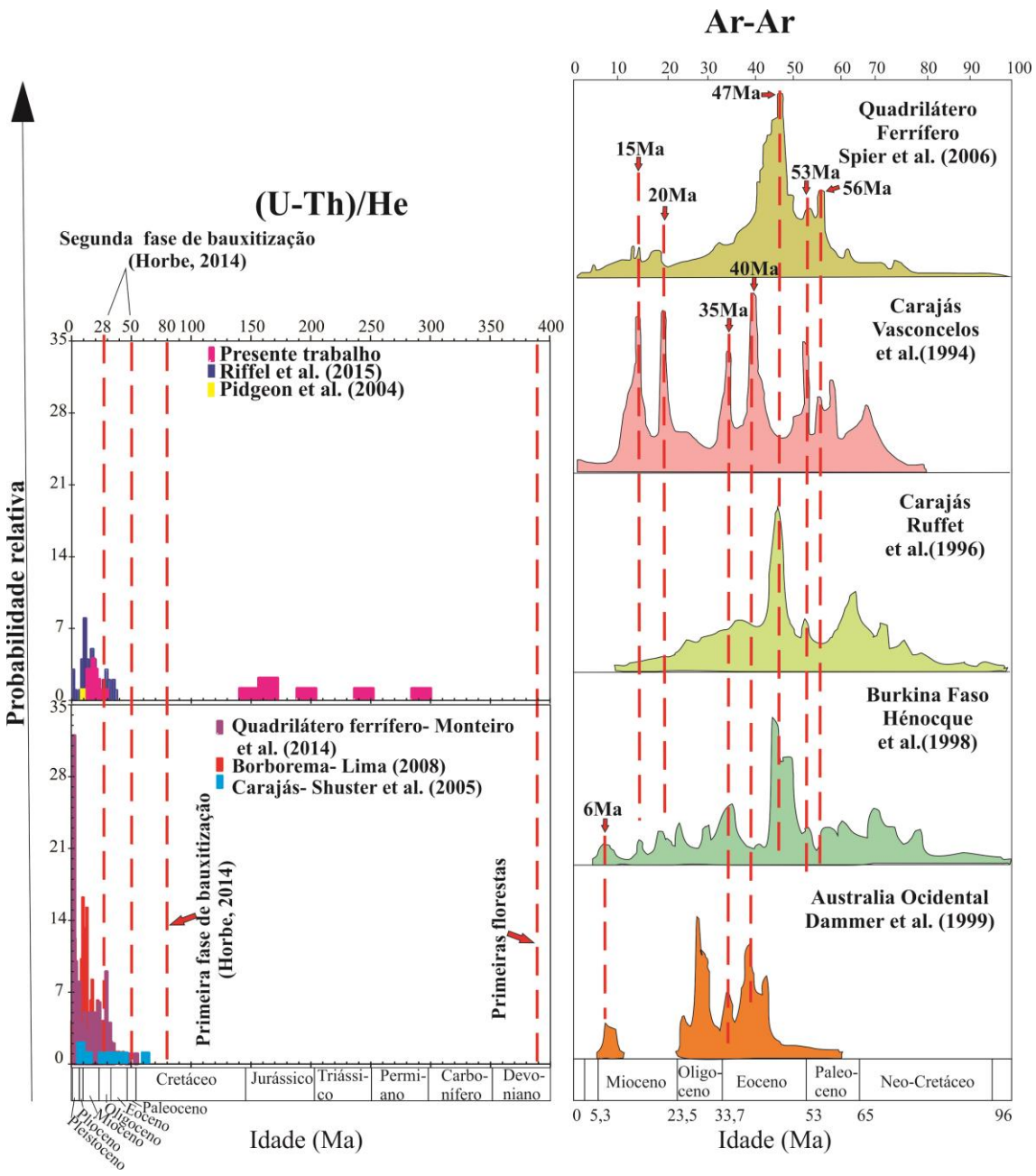

Figura 12: Idades obtidas em goethitas e hematitas por U-Th-He e em minerais do grupo da hollandita por Ar-Ar em diversas regiões do mundo

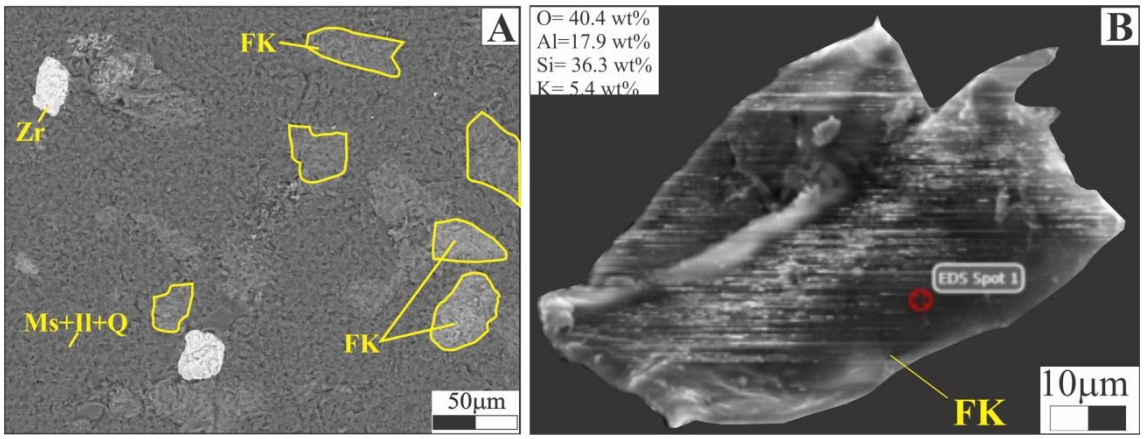

Figura 13: Arcabouço das grauvacas do Grupo Alto Tapajós compostas por matriz de muscovita (Ms), illita (Il) e quartzo (Q) com grãos de feldspato potássico (FK) e zircão (Zr).

CAPÍTULO VIII: CONSIDERAÇÕES FINAIS DA TESE E REFERÊNCIAS BIBLIOGRÁFICAS

O sudeste do estado do Amazonas é alvo de vários estudos de cunho geológico que envolvem revisão litoestratigráfica, prospecção mineral e estudo dos lateritos. A região é economicamente atraente em função das diversas ocorrências minerais relatadas desde a década de 1950 pela extração do minério de manganês em rochas sedimentares, crosta laterítica, colúvios e desmantelados e, recentemente, pelas ocorrências de ouro, fósforo, sulfetos e bauxitas (Liberatore et al. 1972; Araújo et al. 1976; Carvalho & Figueiredo, 1982; Brito et al. 2010; Silva et al. 2012; e Albuquerque & Horbe, 2015; CPRM, 2015).

Na área de estudo, o embasamento é vulcânico ácido (Grupo Colíder-1,80 a 1,78 Ga), seguido de duas sequências vulcano-sedimentares Proterozoicas, grupos Vila do Carmo (1,76-1,74 Ga) e Beneficente (1,43-1,08 Ga), enquadrados no Supergrupo Sumaúma; corpos graníticos reunidos nas suítes intrusivas Teodósia (1,756 Ga), Igarapé das Lontras (1,754 Ga) e Serra da Providência (1,57-1,53 Ga) e soleiras dos diábasio Mata-Matá (1,57Ga) e máficas indiferenciadas. Sobrepondo estas unidades há sucessão sedimentar Siluro-Devoniana do Grupo Alto Tapajós e depósitos Cenozóicos.

O Supergrupo Sumaúma têm alto conteúdo de MnO (13-40%) em grauvacas e siltitos, ao passo que o Grupo Alto Tapajós concentra P_2O_5 (0,44-2,26%) nas grauvacas, o que implica em fontes distintas. Além disso, arenitos do Supergrupo Sumaúma com grãos de quartzo bem esféricos e arredondados miram contribuição de fontes distais. Enquanto que grãos de quartzo subarredondados e menos esféricos dos arenitos do Grupo Alto Tapajós indicam menos abrasão e transporte. Some-se a isso, a abundância de microclínio, illita e alto teor de K_2O (3,9-8,5%) nas grauvacas do Grupo Alto Tapajós, ratificando fontes proximais.

Os isótopos de Nd (0,511539-0,512071) e TDM (1,81-3,4 Ga) demonstraram que o Supergrupo Sumaúma têm fontes atreladas à Província Rondônia Juruena, com maior influência do embasamento vulcânico do Grupo Colíder e suítes intrusivas Teodósia, Igarapé das Lontras e Serra da Providência. Além disso, as províncias Tapajós-Parima e Amazônia Central supriram o Grupo Vila do Carmo, e fontes distais relativas às províncias Carajás e Sunsás fomentaram sedimentos para as rochas do Grupo Beneficente. Tais dados confirmaram a utilização dos isótopos de Nd para estudos de proveniência, pois coadunam com as idades obtidas por Brito et al. (2010) e Reis et al. (2013). Vale ressaltar que o Grupo Vila do Carmo é potencial fonte do Grupo Beneficente, pois há discordância angular entre as unidades e os arenitos do Grupo

Beneficente mostraram altos conteúdos de Fe_2O_3, TiO_2, rutilo, Ti-magnetita (tal qual os tufos do Vila do Carmo) e população de zircão entre 1.76 e 1.74 Ga (idade inferida do Vila do Carmo) (Reis et al. 2013).

As mesmas fontes do Supergrupo Sumaúma foram identificadas pelos isótopos de Nd para o Grupo Alto Tapajós, contudo boas correlações entre $^{87}Sr/^{86}Sr$ vs CIA e $^{87}Sr/^{86}Sr$ vs Rb/Sr atestaram seu caráter autóctone e intraformacional. De modo que, após a incisão do Grabén do Cachimbo as rochas do Supergrupo Sumaúma juntamente com as vulcânicas do Colíder serviram de fontes do Grupo Alto Tapajós, de idade Siluro-Devoniana.

Estas rochas quando expostas formaram espessas crostas manganesíferas, bauxíticas e ferruginosas a ferro-aluminosas, recobertas por latossolos. Os protólitos manganesíferos com 13-40% de MnO estão relacionados às rochas dos grupos Vila do Carmo e Beneficente, Supergrupo Sumaúma. No entanto, há significativas diferenças mineralógicas e geoquímicas entre eles, enquanto os do Grupo Vila do Carmo têm maior diversidade de minerais de Mn (Pb-hollandita, coronadita e criptomelana) e altos conteúdos de Pb (17200-44000 ppm) e Cu (1446-2016 ppm), aqueles do Beneficente se caracterizam por romanechita como fase dominante e Ba elevado (107400- 112000 ppm).

As crostas de Mn e Mn-Al-Fe desenvolvidas sobre essas rochas são maciças, vermiformes, protopisolíticas e pisolíticas, há também colúvios manganesíferos. Crostas e fragmentos coluvionares também apresentam altos teores de MnO (5 e 63%) e BaO (612-205340 ppm). Assim como nos protólitos, crostas desenvolvidas sobre o Grupo Vila do Carmo têm maior diversidade de minerais de Mn (hollandita, Pb-hollandita, criptomelana e coronadita), assim como os maiores teores de K_2O, Ag, Cu, Pb e Tl.

A química mineral, permitiu distinguir a romanechita, hollandita, Pb-hollandita, coronadita e criptomelana uma das outras pelos conteúdos K_2O-BaO-PbO. Também, individualizou Pb-hollanditas, coronaditas e romanechitas primárias das secundárias por meio dos conteúdos das razões BaO/(CuO*CoO); (PbO/CuO)+(SiO_2/Al_2O_3); Mn_2O_3 e BaO/Fe_2O_3.

Associações geoquímicas também agruparam crostas e rochas desenvolvidas sobre estas duas unidades litoestratigráficas.

- **Crostas Mn-Al-Fe do Grupo Vila do Carmo (5-26% de MnO)**- Goethita, hematita, gibbsita, Al_2O_3, Fe_2O_3, Sc, Th, Y, U, LOI, Rb, Ce, Pr, Nd, Ho, Er, Tm e Yb→ Por se tratarem de crostas "bauxitizadas", em função do plasma gibbsítico

presente em seu arcabouço, estas crostas contém mais goethita (10-27%), hematita (5-38%) e gibbsita (6-40%), logo mais Al_2O_3 e Fe_2O_3. Sc e Th podem estar associados a goethita e hematita, ou concentrarem-se residualmente juntamente com o Y. A presença maciça de Ce, Pr, Nd, Ho, Er, Tm e Yb é justificada pela formação de cerianita. Neste ambiente oxidante, a redução de MnO_2 (Mn^{4+} para Mn^{3+} ou Mn^{2+}) atuou como catalisador para a oxidação Ce^{3+}. A redução de Mn^{4+} para Mn^{3+} também permitiu goethita e hematita fixarem Mn.

- **Protólitos e crostas Mn (54-63% de MnO) do Grupo Vila do Carmo**- Quartzo, coronadita, SiO_2, P_2O_5 e Pb; e Pb-hollandita, cryptomelana, pyrolusita, Ag, As, Cu, Ga, Sr, Tl, Sm, Eu, Gd, Tb e Dy, respectivemente. Coronadita e Pb-hollandita contêm PbO e CuO e criptomelana somente CuO. Estes minerais provém da remobilização e afinidade do Pb e Cu com Mn, o que resultou em várias gerações de minerais de Mn nos protólitos e crostas lateríticas. De mesmo modo, ocorreu com Dy, Tb, Sm, Eu, As, Ag, Cu, Sr e Tl que têm afinidades geoquímicas com esses minerais . A associação com o Ga se refere à sua imobilidade ou à associação com Al-fosfatos. Hollandita e coronadita também sequestram P_2O_5 ($\geq$ 0,37%) e quando formado nas porções fosfáticas da crosta Mn, alcançam até 1%.
- **Protólitos e crostas do Grupo Beneficente**- Romanechita, MnO, Ba, Co, Ni, Be, Zn e Mo→ A partir da dissolução da barita encontrada como resquícios na Mn-grauvaca do Grupo Beneficente, aliada à disponibilidade de MnO_8^{6-}, formou romanechita em ambiente aquoso. Em função da baixa capacidade de fixar elementos traços, alguns deles podem ter sido capturados na superfície da romanechita, ou o Ni^{3+} (0.57 Å), Co^{3+} (0.61 Å) e Mo^{4+} (0.65 Å) podem ter substituído o Mn^{3+} (0.643 Å) ou Mn^{4+} (0.60 Å). Esse processo também ocorreu nas crostas, uma vez que uma segunda geração de romanechita foi formada.
- **Todos os solos**- Anatásio, rutilo, caulinita, TiO_2, Zr, Hf, La e Nb devido à resistência do rutilo e do zircão, juntamente com a neoformação da anatásio, nas condições de intemperismo mais severas da Amazônia que promoveram a formação de caulinita.

A presença de galena, prata nativa, coronadita, Pb-hollandita, alto Cu, Tl e anomalias positivas de Gd (1,25-2,15) nas crostas Mn desenvolvidas sobre o Vila do Carmo são similares aos conteúdos de gossans, minérios sulfetados e depósitos de Mn de origem hidrotermal. Além do mais, a fonte hidrotermal do Mn do Grupo Vila do Carmo, a mesma que originou os sulfetos, é a ratificada indicada pelas relações

$^{206}Pb/^{207}Pb$ vs $^{208}Pb/^{206}Pb$, (Zn x Ni)/MnO_2 vs (Cu/Zn)/Fe_2O_3 e pelos altos teores de Cu, Pb e Zn similar aos Gossans Australianos do tipo SEDEX, e pode classificar o Mn supergênico como dubito. Essa atividade hidrotermal é reforçada pela presença de depósitos VMS de Ag, Au, Cu, Pb e Zn e gossans na região (Carvalho and Figueiredo, 1982; Leite et al., 2005 and Brito et al., 2010). Por outro lado, o Mn do Grupo Beneficente tem assinatura sedimentar e pode ser classificado como supergênico marinho.

Os isótopos de Sr e Nd foram utilizados para estabelecer diferenças entre perfis com protólitos de unidades diferentes (Vila do Carmo, Beneficente e Alto Tapajós), crostas (manganesíferas, bauxitas e crostas ferruginosas) e solos com composições químicas distintas.

Diferenças químicas e isotópicas marcantes foram observadas entre as rochas, crostas lateríticas e solos que se desenvolveram nos grupos Vila do Carmo, Beneficente e Alto Tapajós. Nesse contexto, a relação Rb/Sr vs εNd conseguiu agrupa-los de acordo com a unidade estratigráfica, o que ratifa o uso de crostas lateríticas no mapeamento de rochas mães.

As diferentes distribuições das razões isotópicas de Nd ao longo dos perfis indica efeito da lixiviação e, de modo geral, não mostraram correlação entre o Nd isótopo e o Nd elemento, ETR e P_2O_5 no balanço geoquímico. Assim, o primeiro critério adotado para analisar o comportamento das razões isotópicas de Nd ao longo do perfil laterítico, foi reconhecer os minerais que controlam os ETR. A razão ETR/(Zr+Hf) $\geq$1 indica controle por minerais de Mn e cerianita. Ao passo que, ETR/(Zr+Hf) $\leq$ 1 atesta que minerais pesados como zircão controlam a variação dos ETR ao longo do perfil laterítico, como acontece na maioria dos perfis estudados. Também ficou claro por meio de cálculos que os minerais de Mn e cerianita são responsáveis por 36,5 e 62% dos ETR nos perfis P1 e P2, enquanto que minerais pesados detém 38 e 64% dos ETR nos perfis 1 e 2. Por outro lado, o ^{143}Nd é principalmente atribuído a minerais pesados (85-95% nos perfis P1 e P2). Estes resultados, bem como o balanço de massa, ratificam que não há relação entre o comportamento das razões isotópicas de Nd e ETR em condições de intemperismo agressivo. Além disso, indicou que a redistribuição de minerais em todo o perfil laterítico com concentração residual de zircão ou lixiviação de minerais de Mn (coronadite, holandita e criptomelano) e fixação na cerianita, uma vez que ETR são imóveis durante o intemperismo, controlam a assinatura isotópica Nd.

As razões isotópicas de Sr apresentaram dois tipos de comportamento ao longo de quatro perfis. No primeiro, a razão $^{87}Sr/^{86}Sr$ aumenta em direção ao topo dos perfis onde predominam crostas de caráter Fe e Mn-Fe-Al, sugerindo a entrada de Sr proveniente da atmosfera, água da chuva, lençol freático. Por outro lado, a lixiviação mais severa, que resultou na formação de caulinita e gibbsita (perfis P2 e P5) liberou Sr dos protólitos em solução e diminuiu a razão $^{87}Sr/^{86}Sr$ em direção aos solos.

As razões isotópicas de Pb são mais elevados nas crostas lateríticas e solos do que nos protólitos, como não são afetados pelo intemperismo, essa diferença pode estar relacionado ao decaimento do ^{238}U para o ^{206}Pb ou misturas de fontes. Os perfis P1 e P2 ratificaram essa hipótese quando plotodas na curva de decaimento do Pb ao longo do tempo geológico. A excelente correlação entre $^{143}Nd/^{144}Nd$, $^{206}Pb/^{207}Pb$ e $^{208}Pb/^{206}Pb$ (r^2 = + 0.99; Tab. 6) no balanço de massa dos perfis P1 e P2 ratifica a imobilidade dos isótopos de Pb durante a intemperismo extremo e que os minerais pesados controlam as razões isótopicas Nd em condições de intemperismo agressivo da Amazônia.

A proveniência sedimentar, aliadas a relação crostas lateríticas e unidade litoestratigráfica sobre o qual se desenvolveram, juntamente com a gamaespectometria aérea, permitiu identificar as unidades litoestratigraficas da parte leste da área de estudo, no qual o mapeamento se encontra em andamento pela CPRM. A gammaespectometria aliada, a altimetria demarcada pelas crostas lateríticas e métodos estatísticos Booleano e Fuzzy, designaram áreas favoráveis às ocorrências de crostas lateríticas. O modelo Booleano, com índice kappa de 0.61, recobre uma área de 6500 Km^2 subdivididos de acordo com as três principais superfícies que abrigam crostas lateríticas. Os modelos Fuzzy, tais quais eTh Fuzzy, Fuzzy soma e produto, assim como o operador Fuzzy gamma mostraram forte correlação com os locais amostrados. O eTh Fuzzy cobre 3368 Km^2 e tem o maior grau de favorabilidade da ocorrência de crostas (Kp = 0,8), seguido pelo operador Fuzzy Sum e gamma (γ = 0,7), que cobrem 4737 a 4900 Km^2 e são classificados como substancialmente favorável (Kp entre 0,68 e 0,63). Por outro lado, o Fuzzy produto compreende cerca de 6050 Km^2, e apresenta o menor índice de kappa (K = 0,56).

Para o sucesso dos modelos Booleano e Fuzzy, a geomorfologia e a litoestratigrafia devem ser bem conhecidas, pois são balizadores e podem atestar ou descartar a ocorrência de crostas lateríticas. Nesse contexto, os dois modelos apresentaram boa relação para bauxitas, crostas manganesíferas e solos, apesar de o Booleano ser capaz de identificar 67% das crostas ferruginosas, 20% a mais que os

modelos Fuzzy. No entanto, os modelos Fuzzy foram eficientes em descartar pedras de ferro localizadas na porção oeste da área, pois estas não têm relação com a lateritização.

Por fim, a combinação relevo, eTh fuzzy (melhor índice Kappa-0.8), estratigrafia e mapa de solos permitiu identificar/sugerir 100 Km^2 de áreas propícias à ocorrências de Mn, 700 Km^2 de áreas propícias à ocorrências de bauxitas e 83 Km^2 de crostas fosfáticas.

Sumarizando, a região é ativa desde o Paleoproterozoico, quando rochas do Grupo Vila do Carmo com lentes e matrizes manganesífera foram depositadas sobre o embasamento vulcânico. Logo em seguida, a atividade magmática relativa às soleiras de diabásio Mata-Matá (1,57 Ga) criaram fraturas ao longo dessas rochas e permitiu a percolação de água (Albuquerque et al. 2017). A convecção da câmara magmática esquentou a água, liberando-a em direção ao fundo oceânico, lixiviando Au, Ag, Cu, Pb, Fe, Ba e Mn do embasamento e reprecipitando-os ao longo das fraturas, sob a forma de sulfetos e minerais de manganês. A partir disto, as soleiras do diabásio se instalaram e foram erodidas juntamente com parte do Grupo Vila do Carmo. Assim, o Grupo Beneficente foi depositado, e junto com ele manganês rico em Ba (Albuquerque et al. 2017). A incisão do grabém do cachimbo proporcionou a deposição do Grupo Alto Tapajós no Paleozóico.

O início da lateritização remete ao Permiano e se estende até o Jurássico-Cretáceo com agradação de crosta ferruginosa maciça. A ausência de dados Ar-Ar em crostas manganesíferas impede afirmar sua época precisa de formação, no entanto, por correlação de crostas manganesíferas em Burkina Faso, Carajás e Quadrilátero ferrífero, apontam para o fim do Cretáceo (~70 Ma) o início de formação dessas crostas, se estendendo até o fim do Mioceno. Neste contexto, na região de Apuí houve a segunda fase de agradação de crosta ferruginosa (Oligoceno médio ao início do Mioceno). A partir de então, dois intervalos distintos de degradação de crostas lateríticas (formação de goethita); o primeiro entre 22,5±2,3 e 17,1±1,7 Ma e segundo entre 13,1±1,3 e 16.6 ±1,7 Ma. O primeiro está alinhado ao segundo evento de bauxitização ocorrido entre o fim do Oligoceno e início do Mioceno reconhecido por Kotschoubey et al. (2005) na região de Paragominas, Pará.

Portanto, a utilização da mineralogia, geoquímica dos elementos maiores, menores e traços, química mineral, juntamente com isótopos de Pb, Nd e Sr das rochas, crostas e solos demonstraram extrema importância no que se refere à fonte das rochas sedimentares, ao reconhecimento da natureza do material parental, ambiente de

formação dos minerais de manganês e, comportamento dos isótopos de Pb, Nd e Sr em áreas de intemperismo extremo, como a Amazônia. A utilização da aerogeofisica designou áreas propenças à ocorrência de crostas lateríticas e regiões com potencial econômico para manganês, bauxita, fósforo e areias para construções civis. Além disso, um refinamento geológico foi proposto, no que tange a litoestratigrafia das rochas geradoras das crostas e a unidade "cobertura detrito-lateríticas" foi individualizada com mais precisão. Por fim, a evolução laterítica da região foi sustentada por aspectos mineralógicos, geoquímicos e geocronológicos (U-Th-He).

Sugestões para estudos futuros:

- Para o aperfeiçoamento da proveniência do Grupo Alto Tapajós, há necessidade de estudos da frequência de minerais pesados nas grauvacas e quartzo arenitos, bem como a utilização de dados geocronológicos com U-Pb e Lu-Hf. Além disso, em função da grande quantidade de K_2O, as grauvacas são passíveis de serem datadas por Rb/Sr, tal qual demonstrada por Da Silva et al. (2012) na bacia do Camamu, nordeste brasileiro. O fosfato relatado por Liberatore et al. (1972) e Araújo et al. (1976) devem ser caracaterizados e indicada sua proveniência
- Datação das crostas manganesíferas por Ar-Ar e comparação com os dados de U-Th-He obtidos, a fim de estabelecer relações entre as épocas de lateritização na Amazônia e no mundo.
- Datar mais crostas ferruginosas por U-Th-He e aumentar o potencial estatístico das idades com dados mais abrangentes e robustos. Há ainda, a possibilidade da datação de goethitas por U-Pb.
- Aplicar isótopos de Pb em mais perfis com o intuito de reconhecer o protólito e analisar seu comportamento.
- Propor mapa de índice de intemperismo/laterítico e índice máfico, tal qual proposto por Wilford (2012) e Iza (2017).
- Mapeamento em detalhe, com auxílio de furos de sondagens dos depósitos bauxíticos e fosfáticos recém-descobertos na região.

9 REFERÊNCIAS BIBLIOGRÁFICAS

Albuquerque, M.F.S., Horbe, A.M.C., 2015. Mineralogia, geoquímica e evolução da lateritização em Apuí, sudeste do Amazonas. Brazilian Journal Geology 45, 569–590.

Aleva, G.J.J., 1994. Laterites. Concepts, geology, morphology and chemistry, ISRIC, Wageningen.

Anand, R.R., Smith, R.E., Innes, J., Churchward, H. M., Perdrix, J. L., Grunsky, E. C., 1989. Laterite types and associated ferruginous materials, Yilgarn Block, WA: terminology, classification and atlas. CSIRO Division of Exploration Geoscience Report 60R.

Anand, R.R., Paine, M., 2002. Regolith geology of the Yilgarn Craton, Western Australia: implications for exploration. Australian Journal of Earth Sciences. 49, 3-162.

Anand, R.R., Butt, C.R.M., 2003. Distribution and evolution of 'laterites' and lateritic weathering profiles, darling range, Western Australia. Australian Geomechanics. 38 (4), 41-58.

Anand, R.R., Paine, M.D., Smith, R.E., 2002.Genesis, classification and atlas of ferruginous materials, Yilgarn Craton . Author. Australian Mineral Industries Research Association; CRC LEME (Australia). 90p

Anderson, W.L., Dyer, R.C., Torres, D.D., 1974. Ocorrências de manganês na Bacia do Rio Itacaiúnas, Centro Leste do Estado do Pará. Anais do XXVIII Congresso Brasileiro de Geologia. 6, 149-164.

Araújo, J.F.V., Montalvão, R.M.G., Lima, M.I.C., Fernandes, P.E.C.A., Cunha, F.M.B., Fernandes, C.A.C., Basei, M.A.S., 1976. Geologia da Folha AS-21 – Santarém. In: BRASIL, DNPM. Projeto RADAM BRASIL. Rio de Janeiro.10, 17-130.

Bähr, R., Lippolt, H.J., Wernicke, S., 1994. Temperature-induced 4He degassing of specularite and botryoidal hematite: a 4He retentivity study. Journal of Geophysical Research 99, 17695–17707.

Bardossy, G., Aleva, G.J.J., 1990. Lateritic bauxite. Elsevier,Amsterdam, 624p.

Beauvais, A., 1991. Paléoclimats et dynamique d'un paysage cuirasse´du Centrafrique. Morphologie, Pétrologie et Géochimie. Tese de doutorado, Universidade de Poitiers, França. 100p

Beauvais, A., 1999. Geochemical balance of lateritization processes and climatic signatures in weathering profiles overlain by ferricretes in Central Africa, Geochimica et Cosmochimica Acta. 63, 3939-3957.

Beauvais, A., 2009. Ferricrete biochemical degradation on the rainforest–savannas boundary of Central African Republic. Geoderma. 150, 379-388

Beauvais, A., Ruffet, G., Hécnoque, O., Colin, F., 2008. Chemical and physical erosion rhythms of the West African Cenozoic morphogenesis: The 39Ar-40Ar dating of supergene K-Mn oxides. Journal of geophysical research, 113.

Bello, R.M.S., 1978. Condições de metamorfismo de Buritirama, Pará e Serra do Navio, Amapá. Dissertação de mestrado, Universidade de São Paulo, São Paulo, 154p.

Berner, R.A., Kothavala, Z., 2001. GEOCARB III: A revised model of atmospheric CO2 over Phanerozoic time. American Journal Science. 301, 182-204

Betiollo, L.M., Reis N.J., Almeida, M.E., Bahia, R.C., Splendor, F., Costa, U.P., Luzardo, R., 2009. Magmatismo Máfico, Calimiano (Sill Mata-Matá), rio Aripuanã, Amazonas- Implicações Geológicas. In: XI Simpósio de Geologia da Amazônia, Resumos Expandidos.

Bitom D., Volkoff B., Abossolo-Angue M. 2003. Evolution and alteration in situ of a massive iron duricrust in Central Africa. Journal of African Earth Sciences, 37:89-101.

Bogatyrev, B.A.,Zhukov, V.V., 2009. Bauxite provinces of the world. Geology Ore Deposits. 51 (5), 339–355.

Bonnet, N.J., Beauvais, A., Arnaud, N., Chardon, D., Jayananda, M. 2014. First $^{40}Ar/^{39}Ar$ dating of intense Late Palaeogene lateritic weathering in Peninsular India. Earth and Planetary Science Letters, 386: 126–137.

Boschmann, W., 1986. Uran und Helium in Erzmineralien und die Frage ihrer Datierbarkeit. Heidelberger Geowissenschaftliche Abhandlungen, 4. University of Heidelberg, Heidelberg.

Boulangé, B., Carvalho, A., 1997. The bauxite of Porto Trombetas. In: Carvalho, A.; Boulangé, B.; Melfi, A. J.; Lucas, Y. (Eds.) Brazilian bauxites, USP/FAPESP/ORSTOM, Brazil. 55-73.

Brito R.S., Silveira F.V., Larizzati J.H., 2010. Metalogenia do distrito aurífero do rio Juma- Nova Aripuanã-AM. Informe recursos minerais. Série Ouro, 17, CPRM-Brasília, 35 p.

Carvalho, M.S., Figueiredo, A.J., 1982. Caracterização Litoestratigráfica da Bacia de Sedimentação do Grupo Beneficente no Alto Rio Sucundurí-AM. 1st Amazon Geology Symposium, Belém, Brazil, Extended Abstracts, 26–44.

Castro, R. T, 2015. A lateritização na Amazônia Ocidental: sul de Roraima e norte e noroeste de Rondônia. Dissertação de Mestrado em Geociências, Universidade Federal do Amazonas, Manaus, Amazonas. 74p.

Chisonga, B.C., Gutzmer, J., Beukes, N.J., Huizenga, J.M., 2012. Nature and origin of the protolith succession to the Paleoproterozoic Serra do Navio manganese deposit, Amapa Province, Brazil. Ore Geology Reviews. 47, 59–76.

Clarcke, J.D.A., Chenoweth, L., 1996. Classification, genesis and evolution of ferruginous surface grains. Journal of Australian Geology and Geophysic, 16:213-214.

Colin, F., Beauvais, A., Ruffet, G., Hécnoque, O. 2005. First $^{40}Ar/^{39}Ar$ geochronology of lateritic manganiferous pisolites: Implications for the Palaeogene history of a West African landscape. Earth and Planetary Science Letters, 238: 172– 188.

Correa, S. L. A., 1996. Evolução geoquímica das crostas lateríticas e dos sedimentos sobrepostos na estrutura de Seis Lagos (Amazonas). Tese (Doutorado) - Universidade Federal do Pará, Instituto de Geociências, Belém, Pará. 212p

Costa, M.L. 1991. Aspectos geológicos dos lateritos da Amazônia. Revista Brasileira de Geociências. 21, 146-160.

Costa, M.L., Fernandez, O.J.C., Requelme, M.E.R., 2005. O depósito de manganês do Azul, Carajás: Estratigrafia, mineralogia, geoquímica e evolução geológica. In: O.J. Marini, E.T. Queiroz, B.W. Ramos (eds.) Caracterização de Depósitos Minerais em Distritos Mineiros da Amazônia. Brasília, DNPM-CT/Mineral- ADIMB, 227-334p.

Costa, M.L.1990. Mineralogia, geoquímica, gênese e epirogênese dos lateritos fosfáticos de Jandiá, na região Bragantina (NE do Pará). Geochimica Brasiliensis. 4, 85-110.

Costa, M. L., Moraes, E. L., 1998. Mineralogy, Geochemistry and genesis of kaolins from the Amazon region. Mineralium Deposita, Alemanha. 33 (3), 283-297

Costa, M.L. 1997. Lateritization as major process of ore deposit formation in the Amazon Region. Exploration Mining Geology. 6,79-104.

Costa, M.L., 2007. Introdução ao intemperismo laterítico e à lateritização. In: Licht, O.A. B.; Mello, C.S.B.; Silva, C.R. (editores). Prospecção geoquímica de depósitos minerais metálicos, não metálicos, óleo e gás. São Paulo, SBGq, 788 p

Costa, M.L., Cruz, G.S., Almeida, H.D.F., Poellmann, H., 2014. On the geology, mineralogy and geochemistry of the bauxite-bearing regolith in the lower Amazon basin: Evidence of genetic relationships: Journal of Geochemical Exploration. 146, 58–74.

Costa, M.L., Do Carmo, M.S., Behling, H., 2005. Mineralogia e geoquímica de sedimentos lacustres com substrato laterítico na Amazônia brasileira. Revista Brasileira de Geociências. 35(2), 165-176

CPRM, 2013. Folha Sumaúma (SB.20-Z-D). Programa Geologia do Brasil. Carta geológica ao milionésimo-Escala 1:250.000. CPRM, Serviço Geológico do Brasil, Manaus.

CPRM, 2006. Mapa Geológico do Estado do Amazonas. Geologia e recursos minerais do Estado do Amazonas. Sistemas de Informações Geográficas – SIG, Programa Geologia do Brasil. Escala 1: 1.000.000. Rio de Janeiro, Ministério de Minas e Energia. 1 CD-ROM. Programa Geologia do Brasil.

CPRM, 2015. Folha Sumaúma (SB.20-Z-D). Programa Geologia do Brasil. Carta geológica ao milionésimo-Escala 1:250.000. Manaus, CPRM – Serviço Geológico do Brasil.

CPRM, 2010. Projeto aerogeofísico Aripuanã. Relatório Final do levantamento e processamento dos dados magnetométricos e gamaespectométricos. Ministério de Minas e Energia. Secretaria de Geologia, Mineração e Transformação Mineral. Serviço Geológico do Brasil. Brasília, Brasil. 207p

CPRM, 2010. Projeto aerogeofísico Sucunduri. Relatório Final do levantamento e processamento dos dados magnetométricos e gamaespectométricos. Ministério de Minas e Energia. Secretaria de Geologia, Mineração e Transformação Mineral. Serviço Geológico do Brasil. Brasília, Brasil. 295p

CPRM., 2014. Programa de Geologia do Brasil-PGB, Mutum, Folha S B.20-Z-B. Estado do Amaz onas, Carta Geológica. -Escala 1:250.000 Manaus: CPRM-Serviço Geológico do Brasil

Da Silva, D.R.A., Mizusaki, A.M.P., Milani,E.J., Pimentel,M., Kawashita, K., 2012. Whole-rock geochemistry and Sr-Nd isotopic composition of the pre-rift sequence of the Camamu Basin, northeastern Brazil. Journal of South American Earth Sciences. 39, 59-71

Dammer, D., McDougall, I., Chivas, A.R., 1999. Timing of weathering-induced alteration of manganese deposits in Western Australia: evidence from K/Ar and 40Ar/39Ar dating. Economic Geology. 94, 87–108.

Dantas, M.E., Maia, M.A.M., 2010. Compartimentação Geomorfológica. In: Maia, M.A.M & Marmos, J.L. (orgs). Geodiversidade do Estado do Amazonas. CPRM: Manaus, 27-44p.

Dennen, W.H.,Norton, H.A., 1977. Geology and geochemistry of bauxite deposits in the lower Amazon basin. Economic Geology. 72, 82–89.

Departamento Nacional de Produção Mineral. 2010. Anuário Mineral (http://www.dnpm.gov.br/assets/galeriaDocumento/AMB2010/ParteIII_2010.pdf).

Departamento Nacional de Produção Mineral. 2017. Anuário Mineral (http://www.dnpm.gov.br/assets/galeriaDocumento/AMB2017/ParteIII_2017.pdf).

Eggleton, R.A., 2001. Glossary of Regolith—Surficial Geology Soils and Landscapes. CRC LEME Publication, Perth.

Erhardt, H., 1965, Le temoinage paleoclimatique de quelques formations paleopediques dans leur rapport avec la sedimentologie: Geologische Rundschau. 54, 15-23.

Farley, K.A., 2002. (U–Th)/He dating: techniques, calibrations, and applications. Reviews in Mineralogy and Geochemistry. 47, 819–844.

Farley, K.A., Wolf, R.A., Silver, L.T., 1996. The effects of long alpha-stopping distances on (U–Th)/He ages. Geochimica et Cosmochimica Acta. 60, 4223–4229.

Gioia, S.M.C.L., Pimentel, M.M. 2000. The Sm–Nd isotopic method in the Geochronology Laboratory of the University of Brasília. Anais da Acadêmia Brasileira de Ciências, 72: 219–245.

Grubb, P.L.C., 1979. Genesis of bauxite deposits in the lower Amazon basin and Guianas coastal plain. Economic Geology. 74, 735-750.

Gutzmer, J., and Beukes, N.J., 1998, Earliest laterites and possible evidence for terrestrial vegetation in the early Proterozoic. Geology. 26, 263–266.

Hécnoque, O., Ruffet, G., Colin, F., Féraud, G. 1998. $^{40}Ar/^{39}Ar$ dating of West African lateritic cryptomelanes. Geochimica et Cosmochimica Acta. 62 (16), 2739–2756.

Horbe, A.M.C., 2014. Idades paleomagnéticas de crostas lateríticas da Amazônia. Boletim do Museu Paraense Emílio Goeldi. Ciências Naturais. 9, 93-104.

Horbe, A.M.C., Costa, M.L., 1999. Geochemical evolution of lateritic Sn, Zr, Th, Nb, Y and REE - bearing ore body derived from apogranite: the case of Pitinga, Amazonas - Brazil. Journal of Geochemical Exploration. 66, 339-351.

Horbe, A.M.C., Horbe, M.A., 2005. Linhas de pedra na região nordeste do Amazonas. In: Horbe A.M.C. & Souza V.S. (Org.) Contribuições à Geologia da Amazônia. Manaus, Sociedade Brasileira de Geologia. 4, 221-229.

Horbe, A.M.C., Costa, M.L., 2005. Lateritic crust and related soils in eastern Brazilian Amazonia. Geoderma. 126, 225–239.

Iza, E.R.H.F., Horbe, A.M.C., Silva, A.M. 2016. Boolean and fuzzy methods for identifying lateritic regoliths in the Brazilian Amazon using gamma-ray spectrometric and topographic data. Geoderma. 269, 27–38.

Klammer, G., 1971. Uber plio-pleistozãne Terrassen und ihre Sedimente in unteren Amazonasgebiet .Z. Geomorph. 15, 62-106.

Kotschoubey, B., Truckenbrodt, W., Calaf, J.M.C. 2005. Evolução Geológica da Porção Meridional da Província Bauxitífera de Paragominas durante o Neógeno/Pleistoceno (Noroeste da Bacia do Grajaú, Nordeste do Pará e Extremo oeste do Maranhão). Revista Brasileira de Geociências. 35, 263-272.

Kronberg, B.I., Couston, J.F., Stilianidi, B., Fyfe, W.S., Nash, R.A., Sudgen, D., 1979. Minor elements geochemistry of the Paragominas bauxite. Economic Geology. 75, 1869–1875.

Kronberg, B.I., Fife, W.S., Mckinnon, B.J., Couston, J.F., Stilianidi Filho, B., Nash, R.A., 1982. Model for bauxite formation: Paragominas (Brazil). Chemical Geology 35, 311 –320.

Lacerda Filho, J.V., Souza, J.O., Oliveira, C.C., Ribeiro, P.S.E., Villas Boas, P.F., Albuquerque, M.C., Frasca, A.A.S., Borges, F.R., Moreton, L.C., Martins, E.G., Camargo, M.A., Valente, C.R., Pimentel, M.M., Botelho, N.F. 2001. Geologia e Evolução Tectônica da Região Norte do Mato Grosso (Projeto Promin-Alta Floresta). In: SBG, Simpósio de Geologia da Amazônia, 7, Sessão temática VII, Belém.

Larizzatti, J.H., Oliveira, S.M.B., Butt, C.R.M., 2008. Morphology and composition of gold in a lateritic profile,Fazenda Pison ‘‘Garimpo’’, Amazon, Brazil. Journal of South American Earth Sciences. 25, 359-376

Leite, J.A.D., Sousa, M.Z.A., Saes, G.S., Macambira, M.J.B., Xavier, R.P., Siqueira, A.J., Batata, M.E.F., Oliveira, F.A., Silva Jr, J.G., Quadros, A.P., 2005. Caracterização do Depósito Polimetálico (Zn, Pb, Ag, Cu-Au) de Aripuanã, Mato Grosso. In: Marini, O. J., Queiroz, E. T., and Ramos, B.V. (Eds.), Caracterização de depósitos minerais em distritos mineiros da Amazônia, Brasilia, Departamento

Nacional de Producao Mineral, Fundo Setorial de Recursos Minerais-Agencia para Desenvolvimento Técnico da Industria Mineral Brasileira (ADIMB), 601–686p.

Liberatore, G., Alecrim, J.D., Medeiros, J.B., Malouf, R.F., Pinheiro, S.S., Achão, S.M., Santos, J.O.S., 1972. Projeto Aripuanã – Sucundurí, DNPM/CPRM, Manaus

Lima, M.G., 2008. A história do intemperismo na Província Borborema Oriental, Nordeste do Brasil: Implicações Paleoclimáticas e Tectônicas. Tese (Doutorado)-Centro de Ciências Exatas e da Terra, Universidade Federal do Rio Grande do Norte, Natal, Rio Grande do Norte.594p

Lucas, Y. 1997. The bauxite of Juriti. In: Carvalho, A.; Boulangé, B.; Melfi, A. J. & Lucas, Y. Brazilian bauxites, USP/FAPESP/ORSTOM, Brazil. 107-136.

Machamer, J.F., 1987. A working classification of manganese deposits. Mineral Magazine. 1, 348-351.

Monteiro, H.S., Vasconcelos, P.M., Farley K. A, Spier., C. A., Mello, C.L. 2015. (U–Th)/He geochronology of goethite and the origin and evolution of cangas. Geochimica et Cosmochimica Acta. 131, 267–289.

Nahon, D., 1986. Evolution of iron crusts in tropical landscapes. In: Colman, S.M., Dethier, D.P. (Eds.), Rates of ChemicalWeathering of Rocks and Minerals. Acad. Press, London. 169–192.

Nicholson, K., Nayak, V.K., Nanda, J.K., 1997. Manganese ores of the Ghoriajhor Monmunda area, Sundergarh District, Orissa, India: geochemical evidence for a mixed Mn source. In: Nicholson, K., Hein, J.R., Buhn, B., Dasgupta, S. (Eds.), Manganese Mineralization: Geochemistry and Mineralogy of Terrestrial and Marine Deposits. Geological Society, London. 117–121. Special Publication.

Oliveira, S. M., Trescases, J.J., Melfi, A.J., 1992. Lateritic nickel deposits of Brazil. Mineralium Deposita. 27, 137-146

Oliveira, S.B., Costa, M.L., Prazeres Filho, H.J., 2016.The lateritic bauxite deposit of Rondon do Pará: A new giant deposit in the Amazon region, northern Brazil. Economic Geology. 111, 1277–1290.

Ollier, C.D., Chan, R. A., Craig, M. A., Gibson, D. L., 1988. Aspects of landscape history and regolith in the Kalgoorlie region, Western Australia. BMR Journal of Australian Geology & Geophysics. 10, 309–321.

Peixoto, S.F., Horbe, A.M.C., 2008. Bauxitas do nordeste do Amazonas. Revista Brasileira de Geociências. 38, 406-422.

Pidgeon, R.T.; Brander, T.; Lippolt, H.J., 2004. Late Miocene (U+Th)/4He ages of ferruginous nodules from lateritic duricrust, Darling Range, Western Australia. Australian Journal of Earth Sciences. 51, 901-909.

Reis, N.J., 2006. Rochas carbonáticas da região de Apuí – Amazonas. Informes de Recursos Minerais. Série Insumos minerais para agricultura, 12. Manaus, CPRM – Serviço Geológico do Brasil, 60 p.

Reis, N.J., Bahia, R.B.C., Almeida, M.E., Costa, U.A.P., Betiollo, L.M., Oliveira, A.C., Splendor, F., 2013. O supergrupo Sumaúma no contexto geológico da Folha SB.20-Z-D (SUMAÚMA), sudeste do Amazonas: modo de ocorrência, discussão de idades em zircões detríticos e correlações no SW do Cráton do Amazonas. In: Wankler F.L., Holanda E.S., Vasquez M.L. (eds.). Contribuições à Geologia da Amazônia. Belém, Sociedade Brasileira de Geologia Núcleo Norte (SBG-NO). 8, 199- 222.

Retallack, G.J. 2010. Lateritization and bauxitization events. Economic Geology. 105, 655–667.

Retallack, G.J., 2002. Carbon dioxide and climate over the past 300 million years. Royal Society of London Philosophical Transactions. 360, 659–674.

Retallack, G.J., 2004. Soils and global change in the carbon cycle over geological time, in Holland, H.D., and Turekian, K.K., eds., Treatise on geochemistry, Oxford. 5, 581-605.

Retallack, G.J., 2009, Mesozoic greenhouse spikes. Geological Society of America Bulletin. 121, 1441–1455.

Riffel, S.B., Vasconcelos, P.M., Carmo, I.O., Farley, K.A., 2015. Combined 40Ar/39Ar and (U-Th)/He geochronological constraints on long-term landscape evolution of the Second Paraná Plateau and its ruiniform surface features, Paraná, Brazil. Geomorphology. 233, 52–63

Rodrigues, O.B., Kosuki, R., Coelho Filho, A., 1986. Distrito manganesífero de Serra do Navio, Amapá. In: Schobbenhaus, C., Coelho, C.E.S. (Eds). Principais Depósitos Minerais do Brasil, DNPM/CVRD, pp. 167–175.

Rosolen, V., Lamotte, M., Boulet, R., Trichet, J., Rouer, O., Melfi, A.J., 2002. Genesis of a mottled horizon by Fe-depletion within a laterite cover in the Amazon Basin. Comptes Rendus Geoscience. 334,187–195

Roy, S., Purkait, P.K., 1968. Mineralogy and genesis of the metamorphosed manganese silicate rocks (gondite) of Gowari Wadhona, Madhya Pradesh, India. Contrib. Mineral. Petr. 20, 86–114.

Ruffet, G.; Innocent, C.; Michard, A. Féraud, G. Beauvais, A.; Nahon, D.; Hamelin, B. 1996. A geochronological 40Ar/39Ar and 87Rb/87Sr study of K-Mn oxides from the weathering sequence of Azul, Brazil. Geochemical et Cosmochemical Acta. 60, 2219-2232.

Rye, R., and Holland, H.D., 1998, Paleosols and the evolution of atmospheric oxygen; a critical review: American Journal of Science. 298, 621–672.

Santos, J.O.S., 2003. Geotectônica dos Escudos das Guianas e Brasil Central. In: Bizzi, L.A., Schobbenhaus, C., Vidotti, R.M., Gonçalves, J.H. (Eds.). Geologia, Tectônica e Recursos Minerais Minerais do Brasil: texto, mapas e SIG. CPRM- Serviço Geológico do Brasil, pp. 169–226.

Santos, J.O.S., Hartmann, L.A., Faria, M.S.G. de, Riker, S.R.L., Souza, M.M. de, Almeida, M.E., McNaughton, N.J., 2006. A compartimentação do Cráton Amazonas em Províncias: Avanços ocorridos no período 2000–2006. In: SBG- Núcleo Norte, Simp. Geol. Amaz., 9, Belém, PA, Resumos Expandidos.CD-Rom.

Scandolara, J.E., Fuck, R.A., Dall'Agnol, R., Dantas, E.L., 2013. Geochemistry and origin of the early Mesoproterozoic mangerite-charnockite-rapakivi graniteassociation of the Serra da Providência suite and associated gabbros, centraleastern Rondônia, SW Amazonian Craton, Brasil. J. South America Earth Sciences. 45, 166–193.

Scarpelli, W., Horikava, E.H., 2017.Gold, iron and manganese in central Amapá, Brazil. Brazilian Journal of Geology. 47(4), 703-721.

Shuster, D.L., Farley, K.A., Sisterson, J., Burnett, D.S., 2004. Quantifying the diffusion kinetics and spatial distributions of radiogenic 4He in minerals containing protoninduced ^{3}He. Earth and Planetary Science Letters. 217, 19–32.

Shuster, D.L.; Vasconcelos, P.; Hein, J.A.; Farley, K.A. 2005. Weathering geochronology by (U-Th)/He dating of goethite. Geochimica et Cosmochimica Acta. 69, 659-673

Silva, P. J. M. 2009. Geologia, mineralogia e geoquímica de crostas manganesíferas, Bacia Alto Tapajós, Apuí - AM. Dissertação (Mestrado em Geociências) - Universidade Federal do Amazonas, Manaus, 70p.

Silva, P.J.M, Horbe A.M.C, Horbe M.A. 2012. Mineralogia e geoquímica de ocorrências manganesíferas da bacia Alto Tapajós, sudeste do Amazonas, Brasil. Boletim do Museu Paraense Emílio Goeldi. Ciências Naturais. 7 (1),11-28.

Sombroek, W.G., 1966. Amazonas Soils: A Reconnaissance of the Soils of the Brazilian Amazon Region. Centre for Agricultural Publications Document,Wagenigen, Holland. 292 p.

Spier, C.A., Vasconcelos, P.M., Oliveira, S.M.B. 2006. $^{40}Ar/^{39}Ar$ geochronological Constraints on the evolution of lateritic iron deposits in the Quadrilátero Ferrífero, Minas Gerais, Brazil. Chemical Geology. 234, 79–104.

Tardy, Y., 1993. Pétrologie des latérites et des sols tropicaux, Masson, Paris.

Tardy, Y., Nahon, D., 1985. Geochemistry of laterites. Stability of Al-goethite, Al-hematite and Fe-kaolinite in bauxites and ferricretes: an approach to the mechanism of concretion formation. American Journal Science. 285, 865–903.

Théveniaut, H. & Freyssinet, PH. 2002. Timing of lateritization of the Guiana Shield: synthesis of paleomagnetic results from French Guiana and Suriname. Paleogeography, Paleoclimatology, Paleoecology.178, 91-117.

Théveniaut, H., Freyssinet, P., 1999. Paleomagnetism applied to lateritic pro¢les to assess saprolite and duricrust formation processes : the example of the Mont Baduel pro¢le (French Guiana). Palaeogeogr. Palaeoclimatol. Palaeoecol. 148, 209-231.

Tripathy, G., Singh, S., Krishnaswami, S., 2012. Sr and Nd Isotopes as tracers of chemical and physical erosion. In: Baskaran, M. (Ed.), Handbook of Environmental Isotope Geochemistry. Advances in Isotope Geochemistry. Springer Berlin Heidelberg, 521-552p.

Truckenbrodt, W., Kotschoubey, B., 1981. Argila de Belterra – cobertura terciária das bauxitas amazônicas. Revista Brasileira de Geosciências. 11, 203–208.

Valarelli, J.V., 1967. O minério de manganês de Serra do Navio, Amapá. Tese de doutorado, Universidade de São Paulo, 149p.

Valeton, I., 1972. Bauxites. Development in Soil Science 1. Amsterdam, Elsevier, 244 p.

Varentsov, I.M., 1996, Manganese ores of supergene zone- Geochemistry of formation: Dordrecht, Netherlands, Kluwer Academic Publishers, 343 p.

Vasconcelos, P. M.; Renne, P.R.; Brimhall, G.H.; Becker, T.A., 1996. Direct dating of weathering phenomena by $^{40}Ar/^{39}Ar$ and K-Ar analysis of supergene K-Mn oxides. Geochemical et Cosmochemical Acta. 58, 1635-1665.

Vasconcelos, P.M., 1999. $^{40}Ar/^{39}Ar$ geocronology of supergene process in ore deposits. Reviews in Economic Geology. 12, 73-113.

Vasconcelos, P.M., Heim, J.A., Farley, K.A., Monteiro, H., Waltenberg, K., 2013. 40Ar/39Ar and (U-Th)/He - 4He/3He geochronology of landscape evolution and channel iron deposit genesis at Lynn Peak, Western Australia. Geochimica et Cosmochimica Acta. 117, 283–312

Wernicke, R.S., 1991. Botryoidal Hematite and its Potential for the Helium Isochron Dating Method. (Dr. rerumnaturalium Thesis) Ruprecht-Karls University Heidelberg, Heidelberg.

Wilford, J., 2012. A weathering intensity index for the Australian continent using airborne gamma-ray spectrometry and digital terrain analysis. Geoderma. 183–184, 124–142.